HYDRATION AND MICROSTRUCTURAL DEVELOPMENT OF PORTLAND LIMESTONE CEMENT-BASED MATERIALS

A Dissertation
Presented to
The Academic Faculty

by

Elizabeth I. Nadelman

In Partial Fulfillment
of the Requirements for the Degree
Doctor of Philosophy in the
School of Civil and Environmental Engineering

Georgia Institute of Technology
August 2016

HYDRATION AND MICROSTRUCTURAL DEVELOPMENT OF PORTLAND LIMESTONE CEMENT-BASED MATERIALS

Approved by:

Dr. Kimberly Kurtis, Advisor
School of Civil and Environmental Engineering
Georgia Institute of Technology

Dr. Carsten Sievers
School of Chemical and Biomolecular Engineering
Georgia Institute of Technology

Dr. Lawrence Kahn
School of Civil and Environmental Engineering
Georgia Institute of Technology

Dr. T. Russell Gentry
School of Architecture
Georgia Institute of Technology

Dr. Susan Burns
School of Civil and Environmental Engineering
Georgia Institute of Technology

Date Approved: June 14, 2016

ACKNOWLEDGEMENTS

A lot of time and effort went into the research presented in these pages, and I would be remiss if I did not acknowledge the contributions of a great many people to this work. First and foremost, I would like to express my utmost gratitude to my advisor, Dr. Kimberly Kurtis: thank you for pushing me beyond what I thought I was capable of achieving, for all your guidance and support, and for your thoughtful conversations over the last five years. Your advisement and mentorship has had a profound impact not only on this this work, but also on its author.

I would also like to thank Dr. Lawrence Kahn for his guidance and mentorship: thank you for serving as my "unofficial co-advisor" and for your advice and encouragement in both my academic and my professional pursuits. You was always reminded me of the bigger picture of my work and how my contributions – however small – could still advance knowledge and benefit society.

I would like to thank my committee members, Dr. Susan Burns, Dr. Carsten Sievers, and Dr. Russell Gentry for their thoughtful discussions, time, and support: this research was highly interdisciplinary, and I appreciate the variety of approaches and insights that each of you brought to the work.

This research was funded in part by the National Science Foundation (NSF) under grant number CMMI-0970049 and by the Georgia Department of Transportation (GDOT) under project number 02-127. I am especially grateful to Supriya Kamatkar, Jeff Carroll, and James Page at the GDOT Office of Materials and Research, for their time and advisement on this project, and to Gary Knight (Lehigh Hanson), Steve Wilcox (Argos USA), Wayne Wilson (LafargeHolcim), and Bill Goodloe (Cemex) for their time,

material donations, and insights provided during the course of this research effort. Additional thanks belong to Andy Chafin at the Heidelberg Cement Technology Center for conducting chemical analyses on all 11 cement samples. I am also grateful for the financial support provided by the American Concrete Institute (ACI) Georgia Chapter, the Georgia Institute of Technology, and the ARCS Foundation.

This research could not have been completed without the contributions of several collaborators. I would especially like to thank Behnaz Zaribaf and Ahmad Shalan, without whom much of this research would not have been possible, and Michel Badetti and Dr. Matthieu Vandamme (École des Ponts), who played integral roles in the salt crystallization component of this research. I would also like to thank my amazing group of undergraduate research assistants – Jamie Clark, Dylan Freas, Jonathan Bong, Molly Shinners, Daniella Remolina, Anat Revai, Kyle Manweiler, and Rachel Corbin – for their invaluable contributions to this research. Additional thanks belong to Jeremy Mitchell, who not only assisted with the logistics of conducting my research at the structures lab but also helped to keep me sane and grounded while doing it.

I would also like to thank the past and present members of the Kurtis research group who have made my time in graduate school an enjoyable one: Dr. Boyeon Lee, Dr. Amal Jayapalan, Dr. Chris Shearer, Dr. Passarin Jongvisuttisun, Dr. Nathan Mayercsik, Dr. Bradley Dolphyn, Dr. Álvaro Paul, Dr. Lisa Burris, Dr. Giovanni Loreto, Mitchell McKay, Marc Knapp, Ahmad Shalan, Behnaz Zaribaf, Mehdi Rashidi, Gun Kim, La Sasha Walker, Prasanth Alapati, Natalia Cardelino, Cole Spencer, and honorary group members Daniela Estrada, Falak Shah, and Dr. Guilherme Cordeiro. Thank you all for

your friendship, conversations, encouragement, game nights, and trivia shenanigans. Graduate school was a much richer and rewarding experience because of you.

Finally, I would like to thank my family for their unwavering support, love, and encouragement of me for the past 27 years: I could not have done any of this without you.

TABLE OF CONTENTS

LIST OF TABLES

LIST OF FIGURES

LIST OF SYMBOLS AND ABBREVIATIONS

Abbreviations

AASHTO	American Association of State Highway and Transportation Officials
ASTM	American Society for Testing and Materials
BET	Brunauer-Emmett-Teller
BJH	Barrett, Joyner, Halenda
BSE	Backscattered electron
COD	Crystallography Open Database
CSA	Canadian Standards Association
DOT	Department of Transportation
DTG	Thermogravimetric derivative
EPA	United States Environmental Protection Agency
GDOT	Georgia Department of Transportation
GHG	Greenhouse gas
HDPE	High-density polyethylene
NIST	National Institute of Standards and Technology
OPC	Ordinary portland cement
PLC	Portland limestone cement
RCP(T)	Rapid chloride permeability test
SCM	Supplementary cementitious material
SD	Standard deviation
SEM	Scanning electron microscopy
SR	Surface resistivity

SSA	Specific surface area
TGA	Thermogravimetric analysis
VP-SEM	Variable pressure scanning electron microscopy
XRD	X-ray diffraction

Cement Chemistry Abbreviations

AFm	Alumina-ferrite-monosulfate
AFt	Alumina-ferrite-trisulfate
C_2S	Dicalcium silicate ($2CaO \cdot SiO_2$)
C_3A	Tricalcium aluminate ($3CaO \cdot Al_2O_3$)
C_3S	Tricalcium silicate ($3CaO \cdot SiO_2$)
C_4AF	Tetracalcium aluminoferrite ($4CaO \cdot Al_2O_3 \cdot Fe_2O_3$)
$C\overline{C}$	Calcium carbonate ($CaCO_3$)
CH	Calcium hydroxide ($Ca(OH)_2$)
C-S-H	Calcium-silicate-hydrate
Hc	Hemicarboaluminate hydrate (hemicarbonate)
Mc	Monocarboaluminate hydrate (monocarbonate)
Ms	Monosulfoaluminate hydrate (monosulfate)

Symbols

a	Probe spacing
C/C_0	Degree of supersaturation (C = concentration)
D_{10}	10th percentile particle diameter

$D_{3,2}$	Surface area-weighted mean particle size
$D_{4,3}$	Volume-weighted mean particle size
D_{50}	50th percentile particle diameter
D_{90}	90th percentile particle diameter
D_a	Apparent diffusion coefficient
F	Formation factor
h	Height of capillary rise in a porous material
$H(t)$	Cumulative heat of hydration through time t
H_∞	Total heat of hydration upon complete hydration
H_{cem}	Total heat of hydration upon complete hydration of cement
H_{FA}	Total heat of hydration upon complete hydration of fly ash
h_s	Height of capillary rise at the surface of a porous material
H_{slag}	Total heat of hydration upon complete hydration of slag
I	Current (Chapter 7 only)
I	Total absorption (Chapter 8 only)
I_{eff}	Effective total absorption
J	Flux
k	Permeability
p	Initial volume fraction of water (Powers' model)
p_c	Crystallization pressure
p_{cap}	Capillary pressure
p_i	Mass fraction of phase i in system of interest
p_w	Pore wall pressure

Q_t	Total charge passed by RCP test
r	Pore radius
R	Universal gas constant, 8.314 J/mol·K
RH	Relative humidity
S	Sorptivity
SG	Specific gravity
SG_b	Specific gravity of binder
T	Temperature
V	Voltage (Chapter 7 only)
V_{cs}	Volume fraction of chemical shrinkage
V_{cw}	Volume fraction of capillary water (capillary porosity)
V_f	Volume fraction of filler
V_{hp}	Volume fraction of hydration product
V_{uc}	Volume fraction of unhydrated cement
w/b	Water-to-binder mass ratio, where the "binder" includes the cement and limestone
w/c	Water-to-cement mass ratio
w/cm	Water-to-cementitious material mass ratio, where the "cementitious materials" includes the cement, limestone, and any supplementary cementitious materials
α	Degree of hydration
α_u	Ultimate degree of hydration
β	Hydration shape parameter

γ	Surface energy
η	Viscosity
θ	Contact angle (of a liquid-solid interface)
κ	Curvature (of a crystal)
ρ	Density
ρ	Electrical resistivity (Chapter 7 only)
σ	Electrical conductivity
τ	Hydration time parameter
ϕ or φ	Porosity

SUMMARY

With more than 34 billion tonnes of portland cement concrete placed in 2015, the manufacture of portland cement is estimated to contribute 5-8% of all anthropogenic carbon dioxide (CO_2) emissions each year. While several strategies have been proposed to curb the CO_2 emissions associated with cement manufacture, one of the most immediately applicable and economically viable options is to reduce the amount of clinker in portland cement by replacing a portion of it with a widely available mineral filler, such as limestone. The objective of this research is to examine the relative influences of the limestone's composition, blending rate with portland cement, and particle size distribution on the hydration, microstructural development, and long-term durability of limestone-blended cement-based materials.

Investigation into the early-age hydration kinetics of portland limestone cements (PLCs) revealed that hydration rate was primarily dependent upon the fineness of the cement, with PLCs ground significantly finer than ordinary portland cements (OPCs) exhibiting increased rates and degrees of hydration as a result of heterogeneous nucleation effects, and PLCs ground to similar a fineness as OPCs exhibiting similar or decreased rates and degrees of hydration as a result of dilution effects. Experimental and computational studies of chemical shrinkage further found that the chemical shrinkage of finely ground PLCs increased at early ages due to the accelerated rate of hydration and at later ages and degrees of hydration due to chemical interactions between the limestone and the cement clinker. Such results suggest that concrete produced from PLCs –

especially those that are finely ground – may be more susceptible to cracking at early ages.

Assessment of microstructural development revealed that dilution of the clinker by limestone increased the total porosity of the cement paste matrix, while improvements to particle packing by filler effects reduced the average size of the pores. The net effect was that neat PLC concretes had similar permeabilities to neat OPC concretes. When combined with supplementary cementitious materials (SCMs), chemical interactions between the limestone and the SCMs further reduced the porosity of the PLC concretes, leading to additional reductions in permeability than compared to OPC-SCM blended concretes. Overall, the findings suggest that while hydration mechanics are altered in PLC-based materials, their long-term durability is comparable to those of OPC-based materials, provided that the increases to chemical shrinkage do not cause increased cracking at very early ages.

CHAPTER 1

INTRODUCTION

1.1 Motivation

Concrete is the most widely-used construction material in the world, with an estimated 34 billion metric tons produced worldwide in 2015 [1]. Of those 34 billion tons, approximately 12%, or 4.1 billion metric tons [1, 2], is portland cement, whose production is estimated to contribute 5-8% of all anthropogenic CO_2 emissions each year [2-4]. Worldwide, cement production ranks first among industrial processes in total greenhouse gas (GHG) emissions, with only fuel combustion ranking higher (Figure 1.1) [3]. Moreover, with more than 50% of the world's cement being produced in large, rapidly industrializing countries like India and China, global emissions from cement production are only expected to continue to rise with ongoing urbanization and industrialization (Figure 1.2 and Figure 1.3). Thus, there exists a need for more environmentally sustainable cement-based materials that can satisfy the global increase in construction demand while reducing the negative impacts of production-related CO_2 emissions.

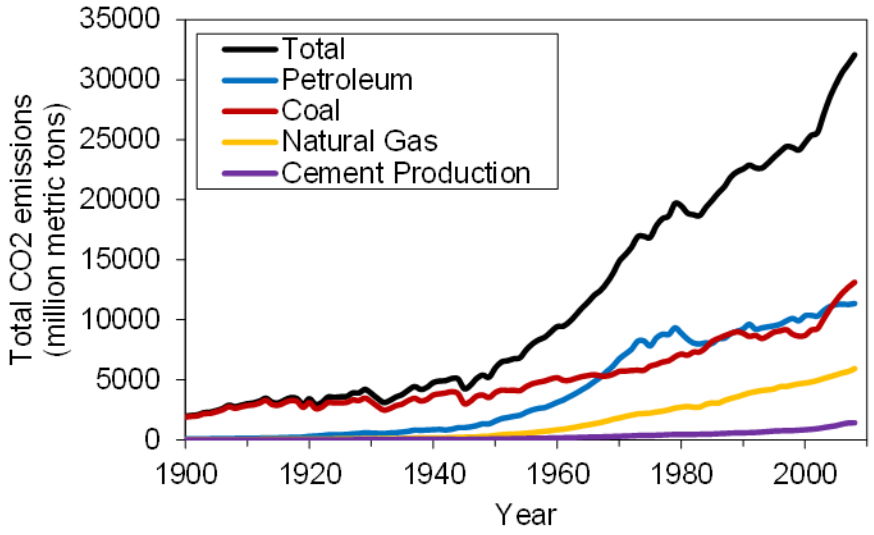

Figure 1.1 Global anthropogenic CO_2 emissions from four largest contributors, 1900-2009. [3]

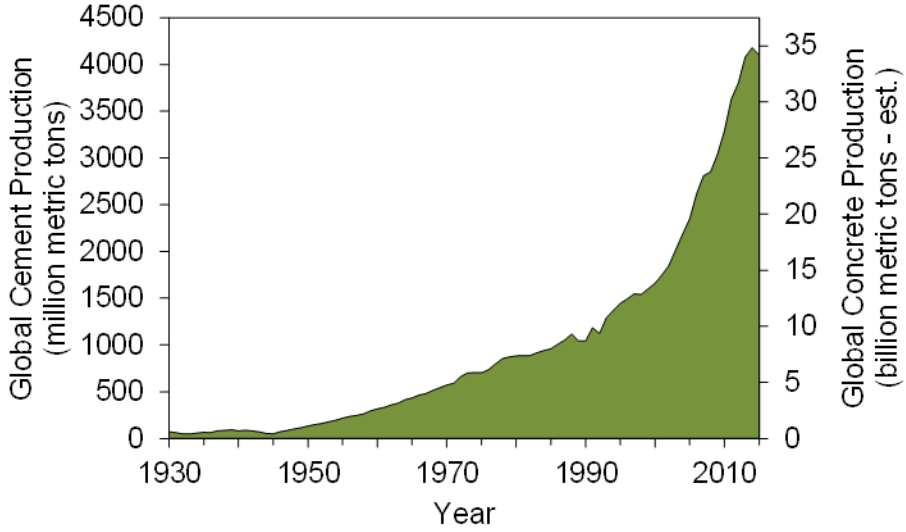

Figure 1.2 Global cement and concrete production, 1930-2012 [5]. Concrete projections are estimated assuming a cement content of 12% cement by mass.

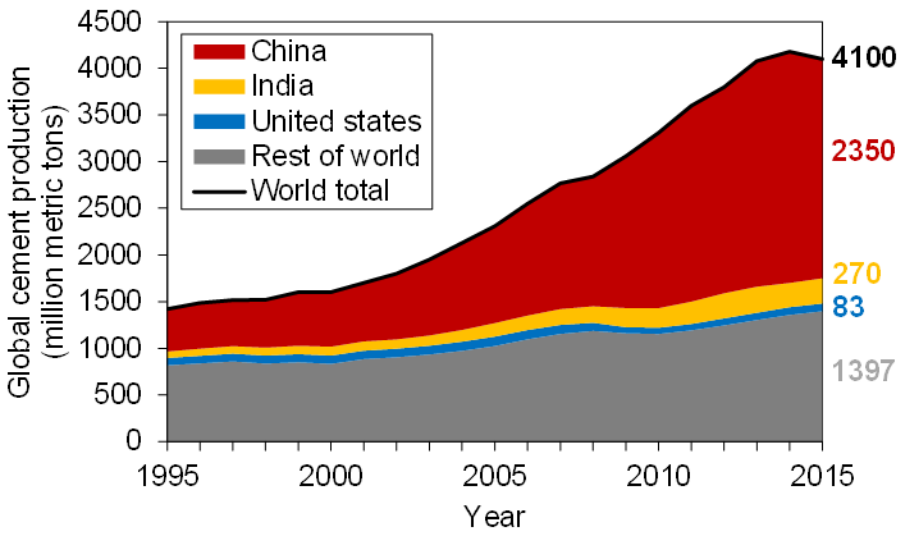

Figure 1.3 Contributions of China, India, and United States to global cement production, 1995-2015. 2015 production totals (million metric tons) are shown at the right. [1]

The CO_2 emissions attributed to portland cement production come from four primary sources – calcination, heating, electricity, and transportation – with over 90% of emissions the direct result of calcination and heating alone.

$$CO_2^{total} = CO_2^{calcination} + CO_2^{heating} + CO_2^{electricity} + CO_2^{transportation} \quad (1.1)$$

More than 50% of the total comes from calcination [6], in which the raw material limestone (primarily $CaCO_3$) is heated to produce lime (CaO).

$$CaCO_3 + heat \rightarrow CaO + CO_2 \quad (1.2)$$

One ton of calcined limestone produces approximately 0.56 tons of CaO, a key component of portland cement clinker, while the remaining 0.44 tons are converted into CO_2 gas. The EPA estimates that for every ton of clinker produced, 0.51 tons of CO_2 gas are emitted as a result of calcination [7].

Another 30-40% of the total emissions are attributed to the burning of coal and fossil fuels for heating the raw materials in the kiln [6, 8]. In order to produce clinker of

the proper chemistry, temperatures in the kiln must exceed 1450°C (2700°F) and often exceed 2000°C (3600°F), consuming large quantities of fuel in the process. Some reductions in CO_2 emissions may be achieved by switching to less CO_2-intensive fuels or by improving the efficiency of the kilns to reduce heating losses; however, with current kilns operating on 40-year service lives, it could take decades to fully implement such changes [6, 9].

Altogether, the production of one ton of portland cement releases between 0.65 and 0.95 tons of CO_2, with production in the United States averaging about 0.89 tons of CO_2 per ton of cement [6]. While long-term options to curb CO_2 emissions include improving the operating efficiency of the kilns and converting to less CO_2-intensive fuel sources for heating and energy, more immediate reductions in CO_2 emissions can be realized by (1) reducing the amount of cement used in concrete or (2) reducing the amount of clinker used in the cement. This research focuses on the latter of these two options, with a particular emphasis on portland limestone or limestone blended cements, which, in North America, contain nominally 80-90 wt.% portland cement clinker and 6-15 wt.% finely divided limestone powder [10].

1.2 Background

Portland limestone cements, or PLCs, originated in Europe in the 1960s [11, 12], but have only recently been considered for use in the United States and Canada. As early as 1960, Spanish standards permitted the use of cements containing up to 10% limestone by weight (later revised to 35%), while French standards adopted in 1979 allowed up to 35% limestone by weight [11]. The 35% upper limit still holds today for many European

countries under the EN 197-1 CEM II/A-L (6-20 wt.%) and CEM II/B-L (21-35 wt.%) designations [13].

The introduction of PLCs in Europe was driven in part by the energy crisis of the early 1970s, in which the cement industry came under pressure from the government to reduce the fraction of energy intensive clinker used in their portland cements [12]. By incorporating a finely ground "filler" material in place of a fraction of the traditional portland cement, the total amount of clinker produced – and therefore the total amount of energy consumed – could be reduced. Traditionally, this filler material would be a supplementary cementitious material (SCM), such as fly ash or slag, but with concurrent reductions in coal-based energy and steel production, the availability of such materials was constrained [12]. Limestone, however, was locally abundant and was already being used as a raw material in the manufacture of the clinker. It was therefore seen as a viable alternative to traditional SCMs, despite not having the same reactive properties as fly ash and slag. Since the 1970s, the use of blended cements in Europe has increased substantially to a current market share of about 75% [14]. In fact, approximately 30% of all cements consumed in Europe fall under the CEM II/A-L or CEM II/B-L designation – a greater share even than traditional portland cements [14].

As in Europe, the gradual introduction of portland limestone cements in the North American market has come about as a result of growing concerns over the environmental impacts of cement production – in terms of both its energy consumption and the CO_2 emissions generated during manufacture. However, unlike Europe, the acceptance of blended cements – and limestone blended cements, in particular – has been considerably more tepid. It was not until the early 2000s that limestone was permitted for use in

portland cements in the United States and Canada, and only at replacement levels shown to have a minimal impact on the strength of the concrete. In 2004, the American Society for Testing and Materials (ASTM) approved the inclusion of up to 5% limestone in all cements specified under its C150 standard [15], and in 2012 approved the inclusion of up to 15% limestone under its C595 designation [10]. Similar allowances were approved by the Canadian Standards Association (CSA) in 2006 (5% upper limit) and 2008 (15% upper limit) [16], and by the American Association of State Highway and Transportation Officials (AASHTO) in 2007 and 2012, respectively [9].

Yet despite recent provisions allowing their use, there is still widespread uncertainty regarding the performance and long-term durability of concretes made with limestone blended cements. PLCs originated during an era in which it was widely believed that suitable performance could be achieved through the design of high-strength concrete mixtures, and less consideration was paid to factors such as permeability and cracking resistance, which can have significant impacts on the service life of a structure. The focus has shifted in the last few decades, however, to a more performance-based philosophy, in which durability and service life are considered along with strength. Therefore, although PLCs have existed for more than 40 years, critical questions regarding their impact on durability and service life are only now being answered – and several key questions related to the role of the limestone in the development of early-age structure and properties still remain unanswered. Thus, this research serves to fill the gaps in the knowledge by investigating how the fundamental mechanisms of cement hydration and microstructural development are influenced by the presence of finely divided limestone powders.

1.3 Research objectives

The primary objective of this research is to understand how the chemistry and fineness of finely divided limestone influences the early-age structure and long-term durability of portland limestone cement-based materials. To that end, the experimental program focuses on the hydration and microstructural development in three primary limestone-blended systems of practical interest to the engineering community: (1) commercially-produced portland limestone cements with varying limestone contents and particle size distributions; (2) laboratory-produced portland limestone cements consisting of limestone with varying chemical compositions and geological sources; and (3) ternary blends of portland limestone cements and aluminum-rich supplementary cementitious materials (SCMs). By examining these three systems, greater insights are gained into how the limestone dosage rate, fineness, and composition influence the properties and performance of portland limestone cement-based materials.

Specifically, the objectives of this research are:

1. To understand the influence of finely divided limestone additions on the hydration and microstructural development of cement-based materials.
2. To examine the relative influences of limestone composition and fineness on cement hydration and microstructural development.
3. To investigate the interactions between limestone and aluminum-rich supplementary cementitious materials (SCMs).
4. To relate changes in early-age microstructural development to the long-term durability of portland limestone cement concretes, as assessed through

measurements of electrical resistivity, chloride permeability, and salt crystallization resistance.

1.4 Organization of dissertation

Keeping with the objectives of this research effort, the structure of the dissertation is outlined below:

- Chapter 2 presents a review of the literature regarding the physical and chemical effects of limestone fillers on the hydration and microstructural development of PLC-based materials. Dilution, filler, and nucleation effects are introduced and their influences on degree of hydration, early-age shrinkage, and permeability are discussed. Areas where additional research is needed are identified.
- Chapter 3 presents an investigation into the influence of limestone dosage and fineness on the hydration rate, chemical phase evolution, and microstructural development of commercially produced cementitious materials.
- Chapter 4 considers the influence of limestone fillers on the early-age chemical and autogenous shrinkage of commercially produced PLC-based materials. The applicability of Powers' model to the prediction of chemical shrinkage in PLC-based materials is assessed.
- Chapter 5 presents the results of hydration studies performed on laboratory-blended limestone cements. The influence of limestone mineralogy on hydration rate, chemical phase evolution, and early-age shrinkage are discussed.

- Chapter 6 investigates purported synergies between limestone and alumina-rich SCMs. Results from isothermal calorimetry and chemical and autogenous shrinkage tests are presented and discussed.
- Chapter 7 presents part one of a two-part investigation into the long-term durability of PLC-based materials. Permeability is assessed by electrical methods for concretes containing commercially produced PLCs and blends of PLCs with SCMs. Service life models are employed to predict the influence of limestone fillers on the long-term durability of PLC-based concrete structures.
- Chapter 8 presents part two of the investigation into the long-term durability of PLC-based materials. The susceptibility of PLC-based materials to damage by physical salt attack is assessed through a custom testing procedure and the results are discussed.
- Chapter 9 summarizes the research performed as part of this dissertation and presents the primary conclusions regarding the influence of limestone powders on the hydration, microstructural development, and long-term durability of PLC-based materials. Recommendations for practice and for future research are also presented.
- An appendix includes the derivation of a modified Powers' model for predicting the chemical shrinkage of materials containing inert fillers.

CHAPTER 2

LITERATURE REVIEW

2.1 Cement hydration in the presence of limestone fillers

When it was first incorporated into portland cements, finely divided limestone was believed to act as a chemically inert filler, occupying space that would otherwise be filled by either unhydrated cement grains or capillary porosity. However, recent research has shown that limestone "fillers" play several important roles in the early hydration of portland cement pastes, not only physically but chemically, as well. The combination of physical and chemical effects alters both the kinetics and the thermodynamics of cement hydration, changing the reaction rates of the raw cement phases and forming additional carbonate phases within the hydrated cement paste.

As a result, hydrated pastes of portland limestone cement have differences in physical microstructure – and consequently differences in performance – when compared to traditional portland cement pastes. The following sections discuss the influence of finely divided limestone on the hydration of portland limestone cements and the implications therein for their mechanical properties, dimensional stability, and ultimate durability.

2.1.1 Ordinary portland cement hydration

The most abundant mineral phases in ordinary portland cement clinker are tricalcium silicate (C_3S in cement chemistry notation[1]) or alite, dicalcium silicate (C_2S) or belite, tricalcium aluminate (C_3A) or aluminate, and tetracalcium aluminoferrite (C_4AF) or ferrite. During hydration, these primary phases react with water and other minor cement constituents such as gypsum ($C\overline{S}H_2$) to produce various hydration products, including calcium silicate hydrate (C-S-H), calcium hydroxide (CH, or portlandite), and ettringite ($C_6A\overline{S}_3H_{32}$), which together provide structure and mechanical strength to the hydrated cement paste.

C-S-H and CH form from the hydration of the calcium silicates, C_3S and C_2S. The C-S-H that is produced has a variable stoichiometry, with a C/S ratio typically in the range of ~1.2-2.3 [17]. When a stoichiometric C/S ratio of 1.5 is assumed [2], the reactions can be written as follows:

$$2C_3S + 6H \rightarrow C_3S_2H_3 + 3CH \quad (2.1)$$

$$2C_2S + 4H \rightarrow C_3S_2H_3 + CH \quad (2.2)$$

The C_3S dissolves readily in water, providing most of the early-age strength and structure to the hydrated cement paste. The C_2S, on the other hand, reacts over a much longer duration and contributes more to strength at later ages. As a result, most modern cement chemistries contain higher amounts of C_3S relative to C_2S.

[1] In cement chemistry notation, single capital letters are used to refer to elements in their oxide forms. In this naming convention, C = CaO, S = SiO_2, A = Al_2O_3, F = Fe_2O_3, H = H_2O, $\overline{S}$ = SO_3, and $\overline{C}$ = CO_2. The abbreviation C-S-H refers to non-stoichiometric calcium silicate hydrate.

The ettringite forms from the reaction of the C_3A with sulfate, largely derived from gypsum which is added to the cement to control the otherwise too rapid reaction of the C_3A. Ettringite is a metastable phase, however, and its stability depends on the availability of sulfate and aluminate ions in the pore solution. Once the sulfate ions have been consumed, any remaining C_3A will cause the ettringite to convert into a secondary hydration product called monosulfate ($C_4A\overline{S}H_{12}$). This sequence of reactions can be stated as follows for a system containing C_3A and gypsum:

$$C_3A + 3C\overline{S}H_2 + 26H \rightarrow C_6A\overline{S}_3H_{32} \quad (2.3)$$

$$2C_3A + C_6A\overline{S}_3H_{32} + 4H \rightarrow 3C_4A\overline{S}H_{12} \quad (2.4)$$

The conversion of ettringite to monosulfate typically begins after about 24 hours of hydration [18-20] and continues as long as there is sufficient alumina (in the form of C_3A) and sulfate (in the form of ettringite) available to react. A similar reaction occurs for the C_4AF phase, but more slowly, producing analogous AFt (alumina-ferrite-tri-sulfate) and AFm (alumina-ferrite-mono-sulfate) phases, $C_6(A,F)\overline{S}_3H_{32}$ and $C_4(A,F)\overline{S}H_{12}$, respectively.[2]

2.1.2 Portland limestone cement hydration

2.1.2.1 Chemical effects

In the presence of calcium carbonate ($C\overline{C}$), the hydration reactions are slightly altered. While the C_3S, C_2S, and the initial C_3A reactions all proceed in the same manner as in ordinary portland cements, thermodynamic models [20, 21] have suggested that the secondary conversion of ettringite into monosulfate will not occur when sufficient

[2] The notation (A,F) indicates aluminum oxide with a fractional substitution of iron oxide. The amount of iron oxide that is substituted depends on the composition of the C_4AF phase.

calcium carbonate is present. Rather, once the sulfate has been depleted, the remaining unhydrated C_3A will preferentially react with the calcium carbonate to form monocarbonate ($C_4A\bar{C}H_{11}$) and hemicarbonate ($C_4A\bar{C}_{0.5}H_{12}$) phases, in proportions that depend on the ratio of carbonate to alumina [20]:

$$C_3A + C\bar{C} + 11\ H \rightarrow C_4A\bar{C}H_{11} \quad (2.5)$$

$$C_3A + 0.5\ C\bar{C} + 0.5\ CH + 11.5\ H \rightarrow C_4A\bar{C}_{0.5}H_{12} \quad (2.6)$$

These models not only suggest that limestone stabilizes the ettringite that has already formed, preventing it from converting into monosulfate, but also that it replaces the monosulfate with a less soluble and more thermodynamically stable monocarbonate or hemicarbonate compound [19, 20]. The stabilization of the ettringite and the additional formation of carboaluminate phases is consequently believed to increase the volume of hydration products relative to ordinary cement pastes, leading to an overall reduction in the capillary porosity of the hydrated cement paste; however, such effects have not been experimentally demonstrated. Further work is needed not only to verify that the carboaluminate phases are formed in real cement systems, but also to quantify their effect on the overall microstructure of the hydrated cement paste.

2.1.2.2 Physical effects

The fineness of limestone powders and their dispersion throughout the cement paste also result in physical effects that may alter the kinetics of cement hydration. These physical effects include filler effects, nucleation effects, and dilution effects, each of which is illustrated in Figure 2.1.

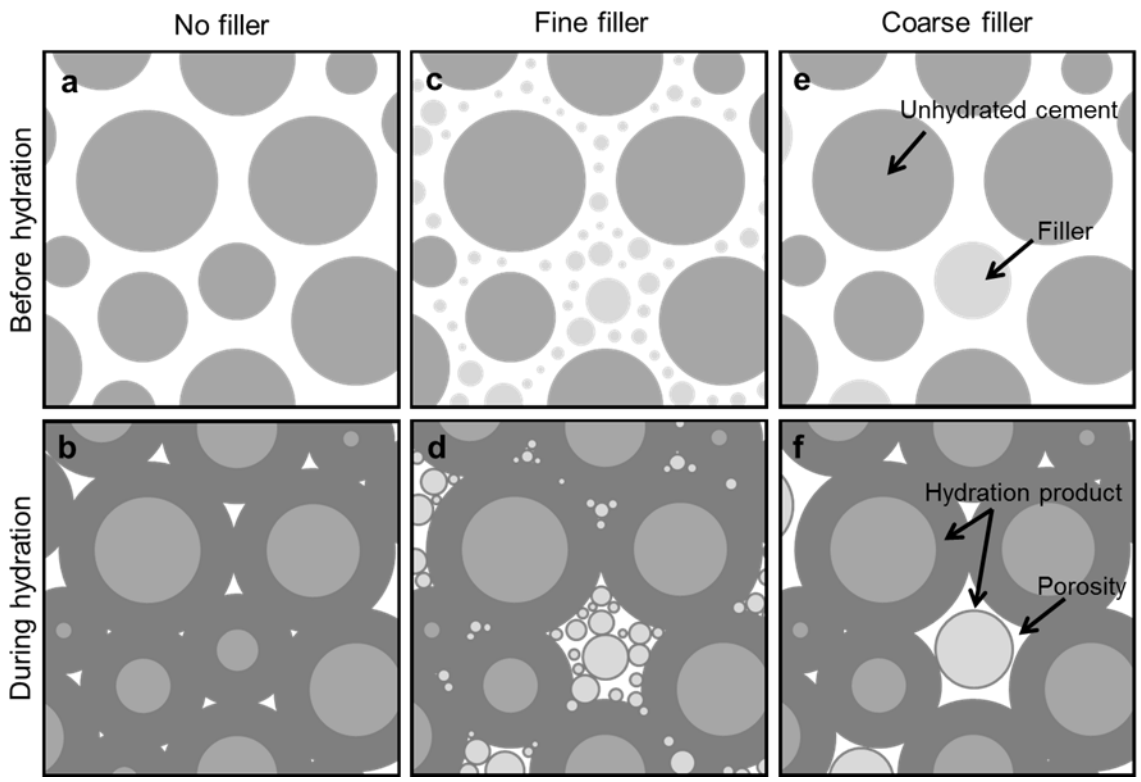

Figure 2.1 Schematic representation of the effect of a 10% volumetric filler replacement on cement hydration. Filler effects dominate in the presence of fine fillers (c & d), while dilution effects dominate in the presence of coarse fillers (e & f).

The filler effect, shown in Figure 2.1c and d, refers to the wider dispersion of the cement grains and the improved packing of the solid phases that result from the change in particle size distribution [22]. It is typically observed for cements in which the limestone filler is ground more finely than the cement clinker, resulting in a wider particle size distribution for the overall system [23]. The wider dispersion of the cement grains helps to improve material homogeneity by reducing flocculation, which in turn helps to improve the efficiency of the clinker dissolution and hydration. Additionally, the denser particle size distribution helps to fill the gaps in the hydrated cement paste, leading to overall decreases in porosity as will be discussed in Section 2.2.

Nucleation effects (Figure 2.1d and f) are caused by the increase in solid surface area due to the fine limestone addition. The increased surface area provides additional sites for the precipitation of hydration products (especially CH), which leads to a net acceleration of the hydration reaction [24, 25]. While nucleation effects are known to occur for many mineral fillers (e.g., quartz [24], TiO_2 [26, 27], and C-S-H [28]), they are especially pronounced for limestone additions [29, 30], which some researchers have attributed to the unique interfacial properties of limestone that significantly reduce the energy barrier (activation energy) for heterogeneous nucleation of cement hydration products [30]. As a result, limestone fillers may promote the hydration of cement clinker at earlier ages more effectively than other fillers.

Accompanying – and possibly counteracting – the filler and nucleation effects is the dilution effect (Figure 2.1e and f), which results from the substitution of the reactive cement clinker by a less reactive limestone filler. This substitution reduces or dilutes the amount of cement that is available for hydration and increases the effective water-to-cement ratio (*w/c*) of the cement paste. The increase in effective *w/c* may improve the efficiency of the hydration reaction by allowing a greater portion of the cement to hydrate, but the reduction in clinker content decreases the total volume of hydration products that may be formed, which could result in an increase in porosity and a decrease in strength. Some cement producers will compensate for this potential decrease in strength by increasing the fineness of the cement, effectively enhancing the nucleation effect and increasing strength at early ages. However, studies have shown that despite having higher early-age strengths, ordinary portland cements with higher fineness tend to

have lower strengths at later ages [31], and so it is unlikely that the nucleation effect can fully compensate for the dilution of the portland cement.

Finally, additional ancillary improvements in particle packing can occur as a result of the lower specific gravity of the limestone. Whereas portland cement clinker typically has a specific gravity of about 3.15, limestone has a specific gravity of only about 2.7 [32], which increases the volume of solids in the system when the limestone is used as a partial clinker replacement on an equivalent-mass basis. Replacing 10% of the clinker by mass, for example, will increase the solid volume of the system by approximately 1.6%. The increase in the solid volume creates a slightly denser packing of solid particles in the initial cement paste matrix, resulting in a secondary filler effect that is independent of particle size.

Analogously, when the limestone is substituted for cement on an equivalent-volume basis, the mass of cementitious "binder" in the system is decreased, leading to an increase in the water-to-binder ratio (*w/b*)[3] for the system. A portland limestone cement containing 10% limestone by volume, for instance, will weigh 1.4% less than an ordinary portland cement and increase the effective *w/b* by the same amount. The net result is a slight dilution effect, again independent of particle size.

2.2 Influence of limestone fillers on porosity

It is difficult to discuss the influence of finely divided limestone powders on cement hydration without also discussing their effect on microstructural development. Microstructure refers to the features of hydrated cement paste that are visible through the

[3] The "binder" refers to the aggregated cement, filler, and any supplementary cementitious materials (see section 2.4) that have been added to the system.

aid of a microscope, typically on the order of 200 μm or less. Such features can include solid hydration products, unhydrated cement particles, and voids. The products of cement hydration range in size and complexity, with CH crystals being the largest (on the order of 100 μm) and C-S-H being the smallest (with features on the order of 0.01 μm). The voids likewise exist over a range of sizes, as shown in Figure 2.2, with entrapped air voids visible on the macroscale (> 1 mm in size) and interlayer C-S-H space visible only at the nanoscale (~ 1 nm). In between those two extremes exists what is commonly referred to as porosity, which includes voids (or pores) ranging from about 2.5 nm to 10 μm in size. The larger pores (> 10 nm) are called capillary pores and house the water that is used to hydrate the cement, while the smaller pores (< 10 nm) are called gel pores and contain the water that is trapped between the C-S-H and other hydration products [2].

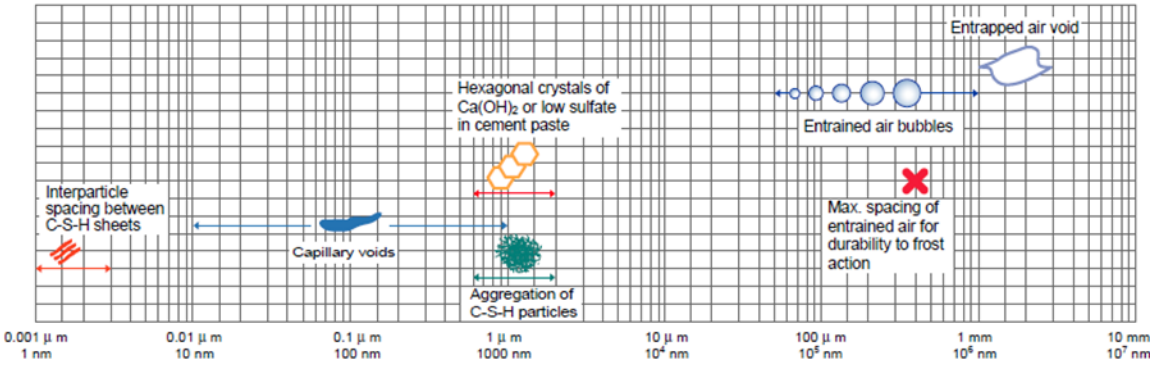

Figure 2.2 Dimensional ranges of microstructural features in hydrated cement paste. Dimensions are shown on a logarithmic scale, from 1 nm to 10 mm. (From Ref. [2])

Porosity has a profound influence on the properties of hydrated cement paste, influencing everything from strength to dimensional stability to ultimate durability. Increases in porosity are typically linked to lower strengths, greater creep and drying shrinkage, and poorer resistance to the ingress of contaminants [2]. Given that finely divided limestone powders have a variety of chemical and physical effects related to

cement hydration, it is therefore important to understand how such effects influence porosity and microstructural development, as well.

2.2.1 Powers' model for capillary porosity and chemical shrinkage

In 1948, T.C. Powers and T.L Brownyard [33] developed a simple model for understanding the influence of cement hydration on the structure of hydrated portland cement paste. After more than a decade of experimental work, they concluded that cement hydration can be expressed as a linear function of the fractional amount of cement that has reacted; that is, the total volume of hydration product can be linearly related to the degree of hydration, α, of the cement paste. The hydration product consists both of the solid products of cement hydration (e.g., calcium silicate hydrate (C-S-H), calcium hydroxide (CH), and AFt and AFm phases), as well as the water that is confined within its nanoscale porosity. Together, it occupies a volume approximately double that of the initial volume of cement that has reacted, but still less than the total volume of the cement plus water reacted, leading to an overall decrease in volume known as *chemical shrinkage* or *Le Châtlier contraction*. Since both the volumes of the reactants and the volumes of the hydration products vary linearly with α, it follows that chemical shrinkage – their difference – will also vary linearly with α. Thus, the model of Powers and Brownyard can be used to predict the chemical shrinkage of a hydrating cement paste at any degree of hydration by simply knowing its starting *w/c*, thereby providing a useful linkage between composition and microstructural development.

While Powers and Brownyard's original work lacks a truly "simple" model for cement hydration, later adaptations by both Powers [34] and others [35] have simplified

the model into a set of basic equations that are a function solely of the degree of hydration and the initial porosity, *p*, of the cement paste system. For a given initial porosity and degree of hydration, what is now commonly referred to as "Powers' model" can be used to predict the volume fraction of the *original system* that is occupied by water-filled capillary porosity, unhydrated cement, hydration product, and chemical shrinkage, according to Equation 2.7 [35]:

Capillary water: $$V_{cw} = p - 1.32(1-p)\alpha \quad (2.7a)$$

Unhydrated cement: $$V_{uc} = (1-p)(1-\alpha) \quad (2.7b)$$

Hydration product: $$V_{hp} = 2.12(1-p)\alpha \quad (2.7c)$$

Chemical shrinkage: $$V_{cs} = 0.20(1-p)\alpha \quad (2.7d)$$

Volume balance: $$V_{cw} + V_{uc} + V_{hp} + V_{cs} = 1 \quad (2.7e)$$

where $p = (w/c)/(w/c + 1/SG_c)$, and SG_c is the specific gravity of the cement. For portland cement, SG_c is typically assumed to be 3.15.

An example of Powers' model applied to a cement paste system with *w/c* = 0.40 is shown in Figure 2.3, for α = 0, 0.25, 0.50, 0.75, and 1. The model demonstrates that during hydration, 1 cm^3 of unhydrated cement combines with 1.32 cm^3 of water held within the capillary porosity of the material to produce 2.12 cm^3 of hydration product, leaving 0.2 cm^3 of volume unfilled as chemical shrinkage. As the volumes of unhydrated cement and capillary water continue to decrease, the volumes of hydration product and chemical shrinkage both increase proportionally. Hydration stops when all of the capillary water is consumed, or for a cement paste at *w/c* = 0.40, at a maximum degree of hydration of α = 0.955. For complete hydration to occur (α = 1, as shown), additional curing water must be provided to the system, either externally (e.g., by spraying the

surface with water or curing in 100% relative humidity) or internally (e.g., by incorporating saturated lightweight aggregates or superabsorbent polymers during mixing).

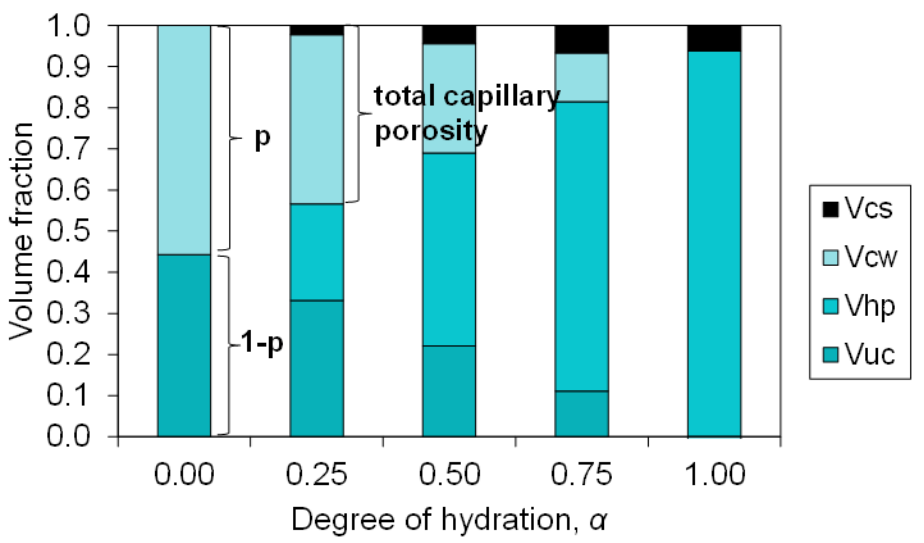

Figure 2.3 Powers' model applied to cement paste system at w/c = 0.40.

Examination of Powers' model reveals that for any *w/c* below 0.42, there is not enough capillary water available in the system to achieve complete hydration (α = 1) without additional sources of curing water being present. Furthermore, even if additional sources of curing water are available, complete hydration is *still* not possible for a *w/c* below 0.356 due to the volumetric limitations imposed on the system (i.e., V_{uc}, V_{cw}, $V_{cs} \geq 0$) [36]. Below this *w/c*, a portion of the cement will *always* remain unhydrated, essentially acting like an "inert" filler. Therefore, by replacing this unhydrated portion of cement by a less (environmentally and economically) expensive filler such as limestone, reductions in both economic cost and CO_2 emissions should be possible without significant impacts to performance.

A recent modification to Powers' model, proposed by Bentz, et al., [36] considers the partial replacement of cement by such an inert filler. In Bentz's model, the filler occupies a constant fraction of the system volume and does not participate in the hydration reaction, and so the volume fraction of reactants and products are simply reduced by the volume fraction of filler, V_f, in the system [36]:

Capillary water: $$V_{cw} = \left[p - 1.32(1-p)\alpha\right](1-V_f) \quad (2.8a)$$

Unhydrated cement: $$V_{uc} = (1-p)(1-\alpha)(1-V_f) \quad (2.8b)$$

Hydration product: $$V_{hp} = 2.12(1-p)\alpha(1-V_f) \quad (2.8c)$$

Chemical shrinkage: $$V_{cs} = 0.20(1-p)\alpha(1-V_f) \quad (2.8d)$$

Volume balance: $$V_{cw} + V_{uc} + V_{hp} + V_{cs} + V_f = 1 \quad (2.8e)$$

where now $p = (w/c)_{eff} / \left[(w/c)_{eff} + 1/SG_c\right]$, and $(w/c)_{eff}$ is the effective water-to-cement ratio of the mixture (mass ratio of the water to the clinker fraction of the portland limestone cement).

Essentially, the modified Powers' model differs from the original model only by a factor of $(1-V_f)$ in each of the volumetric terms and by the replacement of w/c by $(w/c)_{eff}$ in the equation for p. These two adjustments account simply for the reduction of the reacting materials in the system and do not assume any additional modifications to cement hydration. In other words, the modified Powers' model can be used to better understand the influence of limestone fillers on cement hydration in terms of the dilution effect, but other chemical and physical effects cannot be considered.

As previously discussed, the dilution effect reduces the amount of cement in the system, enabling pastes with low water-to-binder ratios (w/b) to achieve higher degrees

of hydration under sealed conditions. This can be illustrated using Powers' model, as shown in Figure 2.4. The model shows that at a *w/b* of 0.35, for example, an ordinary portland cement paste can achieve a theoretical maximum degree of hydration of 0.84, but when a portland limestone cement containing 20% limestone filler by mass is used instead, nearly complete hydration is possible (α = 0.98). It should be noted that in Figure 2.4, the filler replacement is given as a mass percentage rather than as a volume fraction, assuming a filler density ρ_f = 2700 kg/m^3.

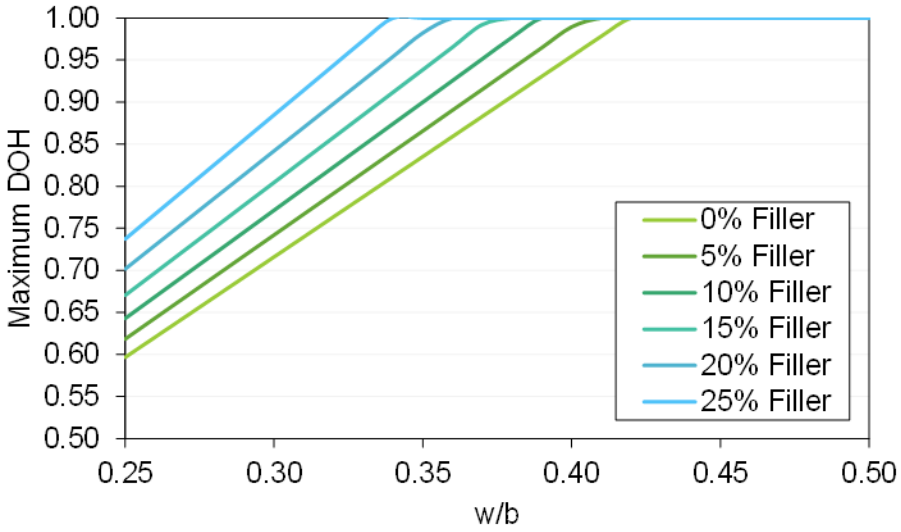

Figure 2.4 Theoretical maximum degree of hydration possible in a sealed cement paste system for a given *w/b* and filler replacement level (% by mass cement).

Experimental results from Bonavetti, et al., [37] corroborate these simulated results: they found that when limestone replacements of 0, 10, and 20% by mass were used, higher degrees of hydration could be observed at 28 days for cement pastes prepared at low *w/b* (0.25, 0.30, and 0.35), while no change was observed for cement pastes prepared at *w/b* = 0.50. For cement paste prepared at *w/b* = 0.40, a higher degree of hydration was observed when the limestone content increased from 0 to 10%, but not

when the limestone content increased from 10 to 20%, indicating that full hydration of the cement clinker was possible for a limestone content of less than 10%.

The modified Powers model can likewise be used to illustrate how the dilution effect changes the chemical shrinkage and final porosity of a fully hydrated cement paste. Figure 2.5 shows that for a cement paste that can hydrate fully under sealed conditions, the chemical shrinkage decreases with increasing filler content and with increasing *w/b*. Intuitively, this makes sense, since if the volume fraction of the cement in the system decreases, the volume change due to cement hydration should decrease correspondingly. Similarly, for a system that is unable to achieve complete hydration, there is no change in chemical shrinkage when the filler content increases since the same volume of cement is being reacted.

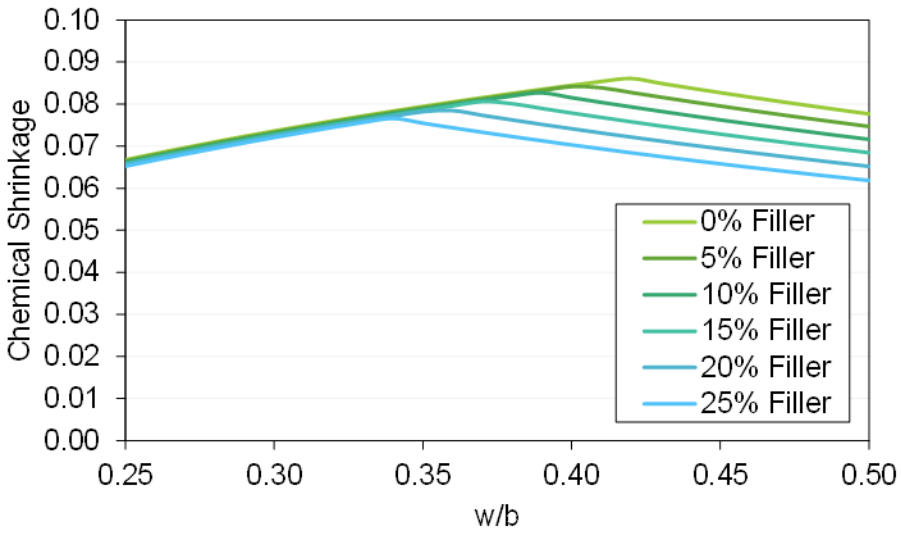

Figure 2.5 Theoretical volume reduction due to chemical shrinkage at the maximum degree of hydration possible for a given *w/b* and limestone filler content (% by mass of cement).

One caveat to these results is that by only considering dilution effects, the roles of the filler and nucleation effects are ignored. As previously discussed, filler and nucleation

effects can accelerate the hydration of cement, particularly if the filler material is finely ground. An increase in the rate of hydration will consequently increase the rate of chemical shrinkage at early ages. These effects were observed by Jayapalan, et al., for finely ground fillers consisting of TiO_2 nanoparticles [26] and 3μm-diameter limestone particles [38], but not for coarsely ground (20 μm) limestone fillers, which showed decreases in chemical shrinkage consistent with Powers' model.

Figure 2.6 illustrates how the dilution effect reduces the total amount of hydration product in a fully hydrated system, leading to increases in total capillary porosity (capillary water + chemical shrinkage). In the figure, solid lines are used to indicate a sealed curing condition, while dashed lines are used to indicate that additional sources of curing water are present. In both cases, it is apparent that the increase in filler content can result in substantial increases in final porosity when the system is allowed to hydrate fully. An ordinary portland cement paste with a *w/b* of 0.35, for example, can have theoretically zero capillary porosity when fully hydrated; however, when 25% of the portland cement (by mass) is replaced by a filler, the porosity increases to more than 9% by volume. These increases in capillary porosity can have adverse effects on the strength, dimensional stability, and durability of the concrete, so it is important to balance the cost and energy savings obtained with high filler dosages with the decreases in strength and durability that can also occur.

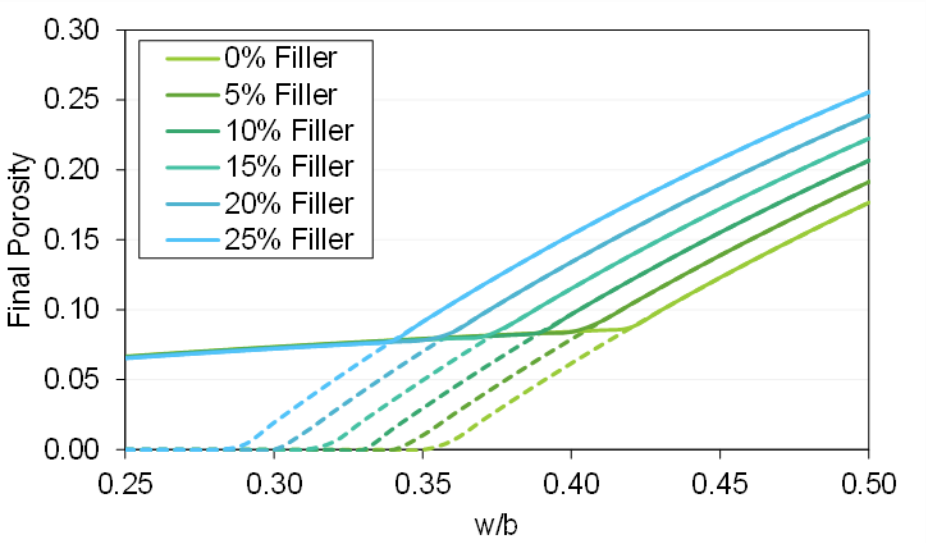

Figure 2.6 Theoretical final porosity of a fully hydrated cement paste system for a given *w/b* and limestone filler content (% by mass of cement). Solid lines indicate a sealed curing condition, while dashed lines indicate that additional curing water is available.

2.2.2 Influence of limestone substitution rate

Based on the previous discussion, an optimal limestone substitution rate is one which allows all of the cement in the system to achieve complete or nearly complete hydration without increasing the capillary porosity or chemical shrinkage of the hydrated cement paste. According to Powers' model, this optimal dosage would occur when the limestone filler content is equal to the theoretical unhydrated cement content of a plain portland cement paste at the maximum degree of hydration. It should be recalled, however, that Powers' model does not consider the potentially beneficial reduction in porosity that occurs as a result of a wider particle size distribution and the stabilization of the ettringite, nor does it consider potential increases in chemical shrinkage that can occur when fine fillers are used. It is therefore useful to examine three general scenarios for limestone replacement levels to better understand the influence of filler content on porosity and chemical shrinkage:

- *Case 1: Limestone filler (LF) < Unhydrated cement (UC)*

  In Case 1, the limestone filler content replaces less than the full unhydrated volume of cement in the paste, so a portion of the cement still remains unhydrated. As previously discussed, the dilution means that the cement can achieve a higher degree of hydration, but there is little change to the total porosity or capillary shrinkage of the overall system, even if additional physical and chemical effects are considered. Filler and nucleation effects may result in a slight decrease in porosity due to a wider particle size distribution (if applicable) and increased calcium hydroxide precipitation, but both of these effects will be minor due to the low filler content. Additionally, research by Matschei, et al., [20] and Lothenbach, et al., [21] show that at low limestone addition rates, the secondary reactions between the limestone and calcium aluminate phases favor the formation of hemicarbonate (and possibly monocarbonate, as well). Not only is hemicarbonate less dense than monosulfate, but it also stabilizes the ettringite, resulting in a greater volume of hydration product that is formed [19]. Overall, then, a minor decrease in porosity is expected to occur, but greater cost and energy savings can be realized with higher limestone contents.

- *Case 2: LF ≈ UC*

  In Case 2, the limestone replaces all of the theoretical volume of unhydrated cement at the maximum degree of hydration. This case is considered theoretically optimal, in that according to Powers' model, the cement can achieve complete hydration with no impact to porosity and shrinkage. When physical and chemical effects are considered, the optimal limestone addition rate turns out to be not

exactly equal to the unhydrated cement content, but nonetheless close to it. For instance, as in Case 1, chemical, nucleation, and filler effects will cause additional decreases in porosity beyond what is predicted by the Powers model, but increases in chemical shrinkage may additionally be observed if the limestone is ground significantly finer than the clinker. It is therefore expected that when the limestone filler is used to replace all – or nearly all – of the unhydrated cement, significant savings in cost and energy can be realized at the potential expense of slightly higher chemical shrinkage; strength and durability, however, should not be significantly impacted.

- *Case 3: LF > UC*

  When the limestone filler content is significantly higher than the original unhydrated cement content, the volume of hydrated cement is decreased. Although the filler effect increases calcium hydroxide precipitation, the decrease in overall calcium silicate content diminishes the efficiency of the filler effect. Likewise, although the calcite in the limestone results in more densifying and more stable products, their overall volume decreases as the carbonate ratio increases [20]. Thus, the dilution effect dominates cements in Case 3, resulting in a less dense pore structure and a higher capillary porosity, where the magnitude of the increase in porosity is directly related to the rate of filler addition.

Experimental results published in the literature support the analysis of these three general categories, but few studies have specifically focused on the influence of limestone substitution rate on the microstructural development and chemical shrinkage of

portland limestone cement pastes. In a study focused on the influence of limestone replacement rate on porosity and strength, Tsivilis, et al., [39] found that for concretes with *w/b*'s of 0.62 and 0.70 containing less than 15 wt.% finely ground limestone (Case 1), there were no significant impacts on strength or porosity relative to the ordinary portland cement mixture; however, when the limestone replacement increased to 20-35 wt.% (Case 3), reductions in strength and increases in porosity were observed. In a similar study conducted at lower *w/b*'s of 0.30 and 0.34, Bonavetti, et al., [37] observed a 8-12% reduction in the 28-day compressive strength of concrete when the fine limestone content was increased from 0 to 20 wt.%, due to the increased porosity of the cement paste at the higher filler levels (Case 3).

Despite the two studies generally corroborating the extreme classifications suggested by Powers' model (Case 1 and Case 3), there is no experimental evidence confirming the existence of an optimal Case 2 dosage. Furthermore, since the proposed relationships between limestone addition rate and capillary porosity are based largely on the empirical Powers' model for inert fillers, additional research is needed not only to confirm that Powers' model can be applied to portland limestone cement systems, but also to better understand the relative influence of the chemical and physical effects on the microstructural development of the pastes.

2.2.3 Autogenous shrinkage

A second type of shrinkage, called autogenous or self-desiccation shrinkage, can also result as a consequence of ongoing cement hydration and pore refinement after the initial setting of the paste. Prior to setting, cement paste exists in a fluid state, and

hydration and chemical shrinkage bring about a uniform contraction of the cement paste matrix. However, once the paste has set, continuing hydration consumes water from the capillaries, leading to a progressive emptying of the pores if no additional sources of curing water are available. As the pores empty, surface tension in the pore solution generates internal tensile stresses within the porosity, as illustrated in Figure 2.7. The magnitudes of the tensile stresses are inversely proportional to the radii of the pores being emptied, such that cement pastes with finer porosity will experience larger tensile stresses than cement pastes with coarser porosity. The net result is a contraction of the cement paste (autogenous shrinkage), as illustrated in Figure 2.8, which could cause extensive cracking if the material is restrained as in a structural member.

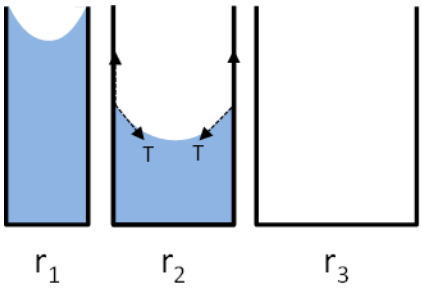

Figure 2.7 Capillary tension is inversely proportional to pore radius, with larger pores generating lower tensile stresses than smaller pores. Larger pores consequently empty before the smaller pores, but with less contraction of the paste.

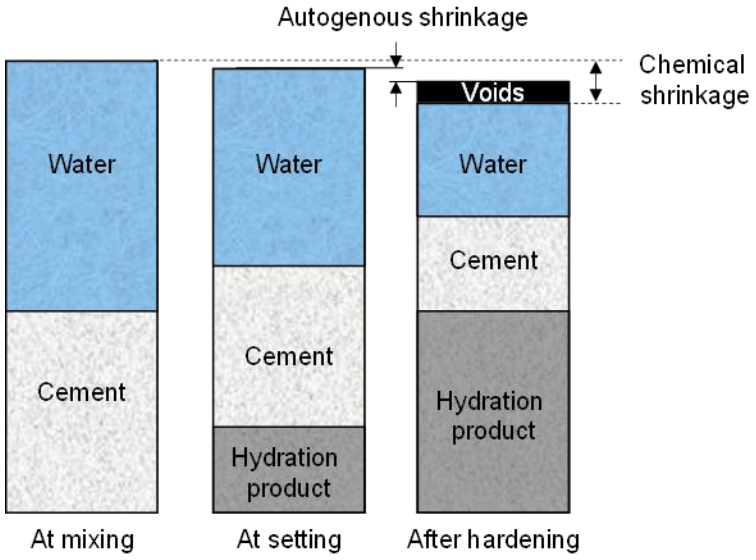

Figure 2.8 Schematic representation of autogenous and chemical shrinkage of portland cement pastes. Autogenous shrinkage refers to the external volume change after initial set, while chemical shrinkage refers to the total volume change, including internal voids. (Adapted from Ref. [31])

Autogenous shrinkage is typically most pronounced in cement pastes with *w/c* below about 0.42, for which less water is available than is required for complete hydration (α = 1). However, it can also be observed for cement pastes with denser microstructures, such as those containing SCMs and other fine mineral additions, for which even if sufficient water is available, the narrow pores restrict its mobility through the paste and create localized regions of low relative humidity [40]. Jayapalan [38] and Bentz and Peltz [41] observed increases in autogenous shrinkage for cement paste and mortar systems in which fine limestone was used as a partial substitute for cement clinker (at dosages of 5% and 10%, respectively), consistent with the previous discussion that nucleation and filler effects reduce the porosity of the cement paste. On the other hand, when coarse limestone was substituted at a 10% dosage rate, Bentz and Peltz observed a decrease in autogenous shrinkage, consistent with a dilution-dominant system. Few other authors have examined autogenous shrinkage in portland limestone cement systems, and

more work is needed in that regard. It is anticipated based on the previous discussion that autogenous shrinkage is higher for systems where nucleation and filler effects are dominant (i.e., systems with fine limestone additions) and lower for systems where dilution is dominant (i.e., systems with coarse limestone additions and high replacement rates), but further work is needed to validate this hypothesis.

2.3 Transport properties of portland limestone cement systems

The early-age hydration and microstructural development of a cement-based material are critical in determining its permeability and ultimate durability. Permeability is a function of the size, interconnectivity, and tortuosity of the porosity, so materials with high porosity are more likely to have large, interconnected pores through which contaminants, such as chlorides or sulfates dissolved in water, may flow.

Permeability is most strongly a function of the interconnectivity of the porosity. Theoretical simulations have demonstrated that the porosity of portland cement paste becomes disconnected for a capillary porosity of about 18% [42], while experimental observations have suggested that this threshold is somewhere in the range of 20-40% for real cement paste systems [2]. If a conservative percolation threshold of 18% is assumed, Powers' model can be used to show that an ordinary portland cement paste system can achieve disconnected porosity for *w/b* below about 0.51 [43]. This, again, assumes only the dilution effect and becomes more complicated as additional physical and chemical interactions are considered.

One interesting feature of the percolation threshold is that it is universal; that is, it does not depend on the presence (or absence) of fillers – reactive or inert, coarse or fine

[42]. This means that as the limestone addition rate increases, a portland limestone cement paste will require a lower *w/b* to achieve disconnected porosity as a consequence of the dilution effect previously discussed. For example, while less than 18% capillary porosity can be achieved in an ordinary portland cement paste with w/cm below 0.51, it cannot be achieved in a portland limestone cement paste containing 20% limestone (by mass) until the *w/b* drops below 0.42 [43]. Similarly, for limestone replacements of 5, 10, 20, and 35% by mass, a disconnected porosity may be obtained for maximum *w/b*'s of approximately 0.50, 0.48, 0.43, and 0.34, respectively [44]. Thus, for a constant *w/b*, an increase in limestone content should similarly increase the permeability of the cement paste.

In reality, permeability does not always increase with increasing limestone content due to the additional physical and chemical effects of the limestone fillers. Trends in porosity that were discussed previously can be applied again to trends in permeability because of the constant 18% threshold for disconnected capillary porosity. When the limestone content is less than or approximately equal to the unhydrated cement content, the possible decreases in capillary porosity that may occur will additionally reduce pore interconnectivity and overall permeability; however, when the limestone content is greater than the unhydrated cement content, the resulting increase in capillary porosity will further increase both interconnectivity and permeability.

These general trends are supported by water penetration and sorptivity experiments performed by Ramezanianpour, et al., [45] and Dhir, et al., [46] on concretes prepared over a range of typical *w/b*'s (0.37-0.79) and limestone contents (0-45 wt.%). In both studies, decreases in water penetration and sorptivity were observed after 28, 90, and

180 days of curing for low limestone replacement levels (5-15 wt.%, depending on the *w/b*), but marked increases were observed at higher levels (20-45 wt.%). On the other hand, when Tsivilis and colleagues [39] measured gas and water permeability on concretes prepared at *w/b* = 0.62 and 0.70, they found that although gas permeability was higher for concretes containing limestone, water permeability was lower at all limestone replacement levels.

One possible explanation for this seemingly anomalous behavior comes from the work of Pipilikaki and Beazi-Katsioti [47], who observed that although concretes with high limestone addition rates exhibited higher capillary porosities (related to gas permeability), they also tended to exhibit lower "threshold diameters", below which the pores are no longer continuous (related to water permeability). An ordinary portland cement paste with *w/b* = 0.50, for example, has a threshold diameter on the order of 1000 nm, while a paste with 35% limestone addition has a threshold diameter on the order of 100 nm [47]. This tenfold decrease in threshold diameter means that it is significantly more difficult for water to penetrate the 35% limestone mixture, since it may need to enter pores 100 nm in size – rather than 1000 nm – in order to percolate through the material. In other words, although the dilution effect may increase the total porosity of the cement paste matrix, particle packing and filler effects may still decrease the average size of the interconnected pores, making fluid penetration more difficult overall (this can be observed qualitatively in Figure 2.1d). It is therefore possible, as Tsivilis and others have observed, that gas permeability may increase with increasing limestone rate, but because of improvements in particle packing, water penetration may become more difficult. Additional study is needed to fully understand the influence of limestone on the

microstructural development – and interconnectivity of the porosity, in particular – of portland limestone cement pastes.

2.4 Interactions with supplementary cementitious materials (SCMs)

The preceding discussion has focused primarily on the influence of relatively inert mineral additions on the hydration, microstructural development, and durability of cement-based materials. However, it is often the case – particularly for high-performance and high-strength concrete mixtures – that additional reactive minerals called supplementary cementitious materials, or SCMs, will also be added to concrete as a partial replacement for cement. Not only does the incorporation of SCMs reduce the cement clinker fraction, thereby contributing to improved sustainability, but research has also shown that when used appropriately, SCMs can additionally be used to improve the strength and durability of concrete mixtures due to the pozzolanic and latent hydraulic properties that enable them to create additional C-S-H over time [2, 17].

Recent studies have additionally shown that when SCMs are used in combination with portland limestone cements, even greater improvements in strength, durability, sustainability, and economy may result. These so-called "synergetic" interactions between the limestone and SCMs are frequently attributed to the chemical reactions that occur between the calcium carbonate in the limestone and the alumina-containing phases in some SCMs [19]. Metakaolin, a highly reactive calcined clay, typically contains the highest alumina content among SCMs at 35-45% by mass; while fly ash, a byproduct of coal combustion, contains 5-35%, depending on the coal source; and slag, a byproduct of steel production, contains 5-15%. All three of these alumina-bearing SCMs have been

shown to have synergetic interactions with portland limestone cements, producing concrete that is stronger and less permeable than traditional portland-SCM blends [19, 48-51]. Silica fume, on the other hand, while a popular and highly reactive SCM, contains less than 1% alumina and consequently has not been shown to have the same synergetic relationship with portland limestone cement.

The primary mechanism by which it is believed the limestone interacts with the alumina-rich SCMs is analogous to the way in which it interacts with the C_3A phase in the clinker. Recent research has shown both theoretically and experimentally that the calcium carbonate combines with the alumina in the SCMs to produce additional carboaluminate hydration products in the paste and to stabilize the ettringite that has also formed [18, 48, 49]. As a result, the porosity of ternary blends of cement, limestone, and SCMs tends to be more refined than that of binary blends of cement and either limestone or SCMs alone, resulting in even greater improvements in strength, permeability, and long-term durability. These effects are especially pronounced for SCMs containing high amounts of alumina, such as metakaolin [48, 50], fly ash [19, 49], and slag [51], to the extent that some state Departments of Transportation (DOTs) will only permit the use of portland limestone cements in combination with an aluminum-rich SCMs [52].

Although several researchers have shown that limestone-SCM interactions can improve the strength and permeability characteristics of concrete mixtures, less research has been focused on their effects on chemical and autogenous shrinkage. As previously discussed, greater pore refinement often comes at the expense of greater autogenous shrinkage, which could lead to cracking that counteracts any improvements in durability caused by the decrease in permeability. Additional study is needed to investigate the

extent to which the limestone-SCM synergies influence early-age shrinkage and cracking potential of ternary PLC blends.

2.5 Summary

The current body of research regarding portland limestone cements indicates that, contrary to previous assumptions, limestone fillers can have a pronounced effect on the hydration of portland cements and on the development of early age properties and long-term durability. At cement replacement levels below 10-15% by mass, theoretical models suggest that a fine limestone powder can generate a more refined microstructure due to the preferential formation of hemi- and monocarbonate products, the subsequent stabilization of the ettringite, and the formation of additional hydration products on the surfaces of the limestone particles. Theoretically, this densification would result in decreased porosity and lower permeability, which suggests greater resistance to the ingress of chloride ions and other aggressive species. At high replacement levels (> ~10%) of a coarser limestone filler, theoretical models similarly indicate that decreases in C-S-H volume will arise as a consequence of the dilution effect, and can result in a significantly more porous and more permeable concrete. At these high replacement levels, aggressive ions may more easily permeate through the binder phase, leading to a greater risk of material degradation in the long-term.

While some experimental results from the literature corroborate these general conclusions, additional study is needed to verify (1) that the empirically derived Powers' model on which many of these conclusions are based can be applied to portland limestone cements, (2) that the formation of the carboaluminate phases and stabilization

of the ettringite creates a more complex hydrated microstructure, and (3) that the changes in microstructure resulting from the limestone-clinker interactions have the predicted effects porosity, permeability, and long-term durability.

Additionally, it has been shown that improvements to microstructure and long-term durability may be realized by blending portland limestone cements with alumina-containing SCMs, such as fly ash, slag, and metakaolin. Theoretical and experimental research has shown these SCMs to have "synergetic" interactions with the limestone that not only decrease porosity and increase strength, but also improve the overall sustainability of the concrete mixtures. Despite the improvements in permeability and strength, however, little attention has been paid to the potentially deleterious effect of finer porosity on the early-age shrinkage and crack resistance of PLC-SCM blends, and additional study is further warranted in that regard.

CHAPTER 3

EARLY-AGE HYDRATION: CHEMICAL EVOLUTION AND MICROSTRUCTURAL DEVELOPMENT

3.1 Introduction

As stated in Chapter 1, one of the primary objectives of this research is to understand the influence of finely divided limestone on the hydration and microstructural development of portland limestone cement-based materials. Prior research has shown that partial substitution of portland cement with limestone – even at dosages of less than 5% – can have pronounced effects on cement hydration through a combination of physical and chemical processes. The *dilution* of the cement clinker by a relatively inert filler reduces the amount of material available for reaction, effectively increasing the water-to-cement ratio (*w/c*) of the cement paste and consequently increasing the overall degree of hydration of the clinker [36]. The increase in surface area obtained with finer filler particles can encourage *heterogeneous nucleation* of hydration products on the surfaces of the limestone and lead to more rapid hydration rates and more refined microstructures at early ages [24, 25, 29, 30]. Changes to *particle packing* and *particle size distributions (filler effects)* resulting from the intergrinding of limestone with the cement clinker can lead to a wider dispersion of the cement grains for more complete hydration and reduced porosity [22, 23]. And finally, despite the relatively low solubility of calcium carbonate ($CaCO_3$), limited *chemical interactions* between the calcium carbonate in the limestone with the C_3A phase in the clinker can alter the secondary hydration products that are formed, with hemi- and monocarboaluminate hydrate (hemi- and monocarbonate) AFm

phases thermodynamically favored over the more commonly formed monosulfoaluminate hydrate (monosulfate) AFm phase [19-21].

In this chapter, the role of limestone is investigated in the hydration processes of eleven commercially produced portland and portland limestone cements. The relative influences of the limestone substitution rate and particle size distribution are traced throughout the hydration process, first with an emphasis on understanding their influence on hydration kinetics and chemical evolution, and later with an emphasis on understanding their implications for microstructural development.

3.2 Materials characterization

Eleven cements from five sources in the southeastern United States (Figure 3.1) were considered for this study. Sources were randomly assigned designations A-E to preserve anonymity. One ASTM C150 Type I/II ordinary portland cement (LS $\leq$ 5%) and at least one companion ASTM C595 Type IL portland limestone cement (LS $\leq$ 15%) produced from the same clinker were provided from each source. One Type IL cement was received from each source A-D, while two Type IL cements of identical composition and varying fineness (designated CG for more coarsely ground and FG for more finely ground) were received from source E. In the analysis and discussion that follows, Type I/II cements are indicated by their single letter source name (e.g., cement A), while Type IL cements are indicated by their single letter source name plus the letter "L" (e.g., cement AL).

Figure 3.1 Geographic sources for cements investigated. The dashed line between Calera, AL and Roberta, GA indicates that the Argos clinker was produced in Calera, AL and finished in Roberta, GA.

3.2.1 Chemical composition

The chemical compositions of each cement were obtained by oxide analysis (ASTM C114 [53]) and quantitative x-ray diffraction (XRD) (ASTM C1365 [54]). Primary phase distributions (i.e., the relative quantities of C_3S, C_2S, C_3A, and C_4AF phases) were determined either by application of the Bogue equations to oxide compositions or by Rietveld analysis of the x-ray diffraction patterns. While oxide analysis is more commonly used to estimate the primary phase distributions in cement, application of the Bogue equations to limestone cements requires *a priori* knowledge of the limestone composition and content [15]. For this reason, the Bogue potential compositions are only provided for the Type I/II cements. Complete results from the oxide and XRD analyses are provided in Table 3.1 and Table 3.2, respectively. The

similarities in chemical analyses between cements from the same source confirm that each of the paired cements likely originated from similar clinker, as had been planned by the producers. The differences between relative C_3S and C_2S quantities determined by the two methods can be partially attributed to the pure-phase assumptions implicit in the Bogue equations; since the XRD quantifications are based on the impure "alite" and "belite" phases of C_3S and C_2S, respectively (which are found in real cements), it is believed that they are more indicative of the true composition of the cement and will therefore be used in most future compositional inquiries [54, 55].

Table 3.1 Cement phase compositions as determined by Rietveld analysis of XRD patterns, % by mass. A non-zero portlandite content indicates that the cement is slightly pre-hydrated.

Component	Type I/II					Type IL				
	A	**B**	**C**	**D**	**E**	**AL**	**BL**	**CL**	**DL**	**EL**
C_3S	52.1	55.9	60.9	55.5	64.3	50.8	54.3	52.7	53.5	61.9
C_2S	24.2	21.6	16.4	17.4	13.1	17.3	15.3	17.9	15.3	7.6
C_3A	3.0	3.0	1.9	5.0	4.2	3.3	2.6	1.5	5.0	3.9
C_4AF	10.3	12.9	12.2	12.1	10.6	9.3	13.5	12.1	10.8	10.3
Calcite ($CaCO_3$)	3.2	1.0	4.2	4.2	2.4	12.2	7.9	10.8	10.5	9.8
Gypsum ($CaSO_4 \cdot 2H_2O$)	0.3	0.0	0.0	0.0	0.0	0.8	0.0	0.0	0.0	0.1
Hemihydrate ($CaSO_4 \cdot 0.5H_2O$)	2.0	3.2	2.5	3.9	1.6	1.6	3.3	3.0	2.9	1.1
Anhydrite ($CaSO_4$)	0.1	1.6	0.1	0.1	0.2	0.1	0.9	0.0	0.0	2.3
Arcanite (K_2SO_4)	0.3	0.3	0.0	0.3	1.1	1.1	1.3	0.2	0.4	1.8
Periclase (MgO)	3.1	0.2	0.8	0.3	1.0	2.2	0.3	0.5	0.1	1.4
Lime (CaO)	0.3	0.3	0.3	0.4	0.3	0.1	0.2	0.2	0.3	0.0
Quartz (SiO_2)	0.0	0.1	0.2	0.4	0.1	0.1	0.3	0.3	0.8	0.2
Portlandite ($Ca(OH)_2$)	1.3	0.0	0.6	1.7	1.2	1.2	0.2	0.8	1.5	1.3

Table 3.2 Cement oxide composition, % by mass. LOI is loss on ignition at 1000°C.

Component	Type I/II					Type IL				
	A	**B**	**C**	**D**	**E**	**AL**	**BL**	**CL**	**DL**	**EL**
C_3S	62.9	62.3	57.4	57.5	57.5	-	-	-	-	-
C_2S	7.6	10.5	13.6	13.6	14.0	-	-	-	-	-
C_3A	6.9	6.6	7.2	7.1	7.0	-	-	-	-	-
C_4AF	9.2	12.1	11.1	10.7	9.3	-	-	-	-	-
SiO_2	19.2	20.1	19.9	19.9	20.0	17.1	18.2	18.6	18.5	18.2
Al_2O_3	4.5	5.0	5.0	4.9	4.6	4.2	4.6	4.6	4.5	4.3
Fe_2O_3	3.0	4.0	3.6	3.5	3.1	2.9	4.2	3.5	3.3	3.2
CaO	62.8	64.7	63.4	63.8	63.0	62.1	62.9	62.4	63.3	62.2
MgO	3.6	1.1	1.5	1.1	2.5	3.1	1.1	1.5	1.0	2.8
Na_2O_e	0.5	0.4	0.5	0.4	0.5	0.4	0.3	0.4	0.4	0.5
TiO_2	0.3	0.3	0.3	0.3	0.3	0.3	0.3	0.3	0.2	0.2
Mn_2O_3	0.1	0.1	0.1	0.0	0.1	0.1	0.1	0.1	0.0	0.1
SO_3	3.1	3.1	2.9	3.2	3.2	3.3	3.2	3.1	3.2	3.0
Free CaO	0.9	0.1	0.7	1.0	0.7	0.6	0.1	0.2	0.9	0.6
LOI	2.6	0.8	2.3	2.5	2.4	6.3	4.7	5.1	5.2	5.3

In terms of chemical composition, all five portland cements conform to ASTM C150 Type I/II specifications [56], but contain a range of C_3S, C_2S, C_3A, and C_4AF contents. Based on the XRD analyses, the cements from source E contain the highest amount of C_3S (contributing to early strength and microstructural development), while the cements from sources A and B have more C_2S (contributing to later age strength and microstructural development). The cements from source D, meanwhile, have the most C_3A, possibly leading to more favorable conditions for carboaluminate formation, while the cements from source B have the most C_4AF. Given the range of compositions examined, it will be important to compare the behavior between pairs of cements to better understand the role of the limestone, as well as among all eleven cements to better understand the behavior of limestone cements as a whole.

The limestone content of each cement was additionally measured by thermogravimetric analysis (TGA) under nitrogen environment, using a Hitachi EXSTAR

TG/DTA 7300. Three replicate cement samples weighing approximately 20 mg were heated from ambient temperature to 900°C at a rate of 10°C/min, with a 30 minute hold at 105°C to remove any free moisture from the powder. $CaCO_3$ contents were calculated based on the mass loss between approximately 600°C and 750°C, wherein $CaCO_3$ thermally decomposes into CaO and $CO_2\uparrow$. The calculation is shown in Equation 3.1 below, where m_{600} indicates the mass of the sample at 600°C, and the molecular weights of $CaCO_3$ and CO_2 are taken to be 100.09 g/mol and 44.01 g/mol, respectively:

$$\%CaCO_3 = \frac{m_{600} - m_{750}}{m_{105}} \times \frac{MW_{CaCO_3}}{MW_{CO_2}} \tag{3.1}$$

The $CaCO_3$ contents as determined by TGA are shown in Figure 3.2. While the true "limestone" contents of the cements cannot be determined without also knowing the $CaCO_3$ contents of each interground limestone, it can nonetheless be observed that four of the five Type I/II cements contained small quantities of limestone as permitted under ASTM C150 specifications, while all five Type IL cements contained limestone contents within the 5-15% permissible range of ASTM C595.

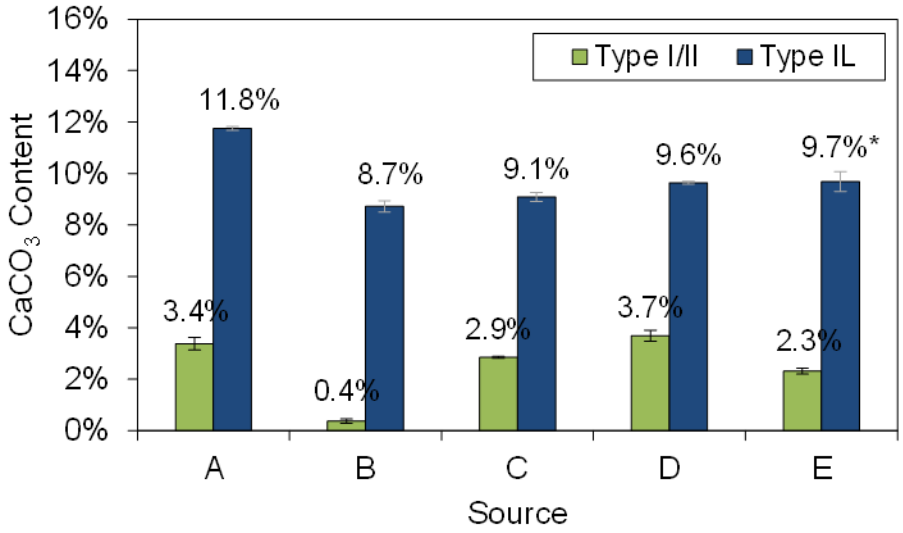

Figure 3.2 $CaCO_3$ contents of cements A-E determined by TGA. Error bars indicate one standard deviation. Values for cement EL represent the average of both CG and FG cements.

Finally, the specific gravity (SG) of each cement was measured by displacement in kerosene at 23 ± 2°C according to ASTM C188 (Table 3.3) [57]. The SG for cement is typically assumed to be 3.15, but values ranging from 3.04 to 3.17 were measured for the Type I/II cements considered in this study. Because limestone has a lower density than cement (typically ~2.7 g/cm^3 [32]), limestone substitutions of only a few percent by mass can cause significant reductions in the SG of the cementitious binder, accounting for the lower SGs for Type IL cements. If it is assumed that the limestone has SG = 2.7 and is composed 100% of the $CaCO_3$ measured by TGA, it can be further demonstrated that the Type I/II and Type IL cements for each source originate from clinkers having approximately the same specific gravity, and that they therefore likely originate from the same clinker.

Table 3.3 Specific gravities of cements A-E, measured according to ASTM C188.

	A	B	C	D	E
Type I/II	3.08	3.17	3.04	3.10	3.10
Type IL	3.05	3.11	3.01	3.07	3.05
Clinker (estimated)	*3.10*	*3.17*	*3.05*	*3.12*	*3.10*

3.2.2 Particle size distribution

Many of the physical effects of limestone fillers depend on the relative sizes of the cement and the limestone inclusions. It is therefore important to characterize the particle sizes of the Type I/II and Type IL cement pairs in order to better understand the role of nucleation, filler, and dilution effects in commercially produced cements. Several parameters can be used to describe relative particle size:

- Specific surface area (SSA): total surface area of material per unit mass, typically measured by laser diffraction (assuming smooth surfaces) or, more accurately, by gas adsorption [58].
- Blaine fineness: a specific surface area of material measured by Blaine air-permeability apparatus (ASTM C204 [59]).
- Surface-weighted mean particle size ($D_{3,2}$): the diameter of a spherical particle having a *surface area* equal to the mean surface area of the material. It can be calculated from a histogram divided into *n* discrete particle sizes as:

$$D_{3,2} = \frac{\sum_{i=1}^{n} D_i^3 v_i}{\sum_{i=1}^{n} D_i^2 v_i} \tag{3.2}$$

where D_i is the diameter of particles in bin *i* and v_i is the number of particles having in bin *i* [60].

- Volume-weighted mean particle size ($D_{4,3}$): the diameter of a spherical particle having a *volume* equal to the mean volume of the material; if the material is assumed to have uniform density, then $D_{4,3}$ is also equivalent to the mass-weighted mean particle size. It can be calculated from a histogram divided into *n* discrete particle sizes as:

$$D_{4,3} = \frac{\sum_{i=1}^{n} D_i^4 v_i}{\sum_{i=1}^{n} D_i^3 v_i} \tag{3.3}$$

  where D_i is the diameter of particles in bin *i* and v_i is the number of particles having in bin *i* [60].

- Percentile size (D_i): the i^{th} percentile of a cumulative distribution of particle sizes by volume (or equivalently, by mass); common percentiles are D_{10}, D_{50}, and D_{90}, where D_{50} is the median particle size and $D_{10} \leq D_{50} \leq D_{90}$.

In terms of the physical effects of limestone fillers, it is believed that parameters related to the surface area of the material (e.g., SSA and $D_{3,2}$) are likely to govern surface nucleation effects, while parameters related to the distribution of volumes (e.g., D_{10}, D_{50}, and D_{90}) are likely to govern filler and dilution effects.

With the exception of Blaine fineness, which was obtained according to ASTM C204 [59], all of the particle size parameters for the eleven cements were obtained by laser diffraction in ethanol using a Malvern Mastersizer 3000E. A small amount of each cement was dispersed in ethanol until a laser obscuration of approximately 7% was obtained. The dispersed material was sonicated for 1 min then stirred at a rate of 840 rpm for approximately 10 min to reduce agglomeration. Particle size distributions were determined as the average of five samples, each collected over a 60 s interval, assuming

smooth (but not necessarily spherical) particles and using Mie theory.[4] Refractive indices of 1.68 and 1.36 were selected for cement and ethanol, respectively, from the database included in the Mastersizer software. The resulting differential and cumulative particle size distributions for the eleven cements are shown in Figure 3.3 and Figure 3.4, respectively, with Type I/II cements shown in solid black lines and Type IL cements shown in colored dashed lines. A summary of relevant size parameters is given in Table 3.4.

Based on the particle size distributions, it can be observed that there are generally two categories of Type IL cements considered in this study: those with significantly finer particle size distributions than their Type I/II companion cements (cements AL, DL, and EL, both CG and FG), and those with broader but similar particle size distributions to their Type I/II companion cements (cements BL and CL). A working hypothesis is that Type IL cements in the former group will exhibit filler-dominated behavior, which would be evidenced by accelerated hydration rates and decreased porosity early ages, while Type IL cements in the latter group will exhibit dilution-dominated behavior, which would be evidenced by decreased hydration rates and increased porosity. Finally, since it was determined that all of the Type IL cements have higher specific surface areas and smaller surface-weighted mean particle sizes than their Type I/II companions, it is also hypothesized that nucleation effects will be observed at early ages for all six Type IL cements. This hypothesis is further supported by the Blaine fineness results, which similarly show higher relative specific surface areas for all six Type IL cements.

---

[4] The smooth-particle assumption most significantly affects the reported SSA. Measurements of SSA by gas adsorption are typically 3-5 times larger than those by laser diffraction, due to the irregular surface features on the cement particles [58]. While less accurate, the smooth-particle SSA measured by laser diffraction is still a useful summary parameter for the overall particle size distribution of the system.

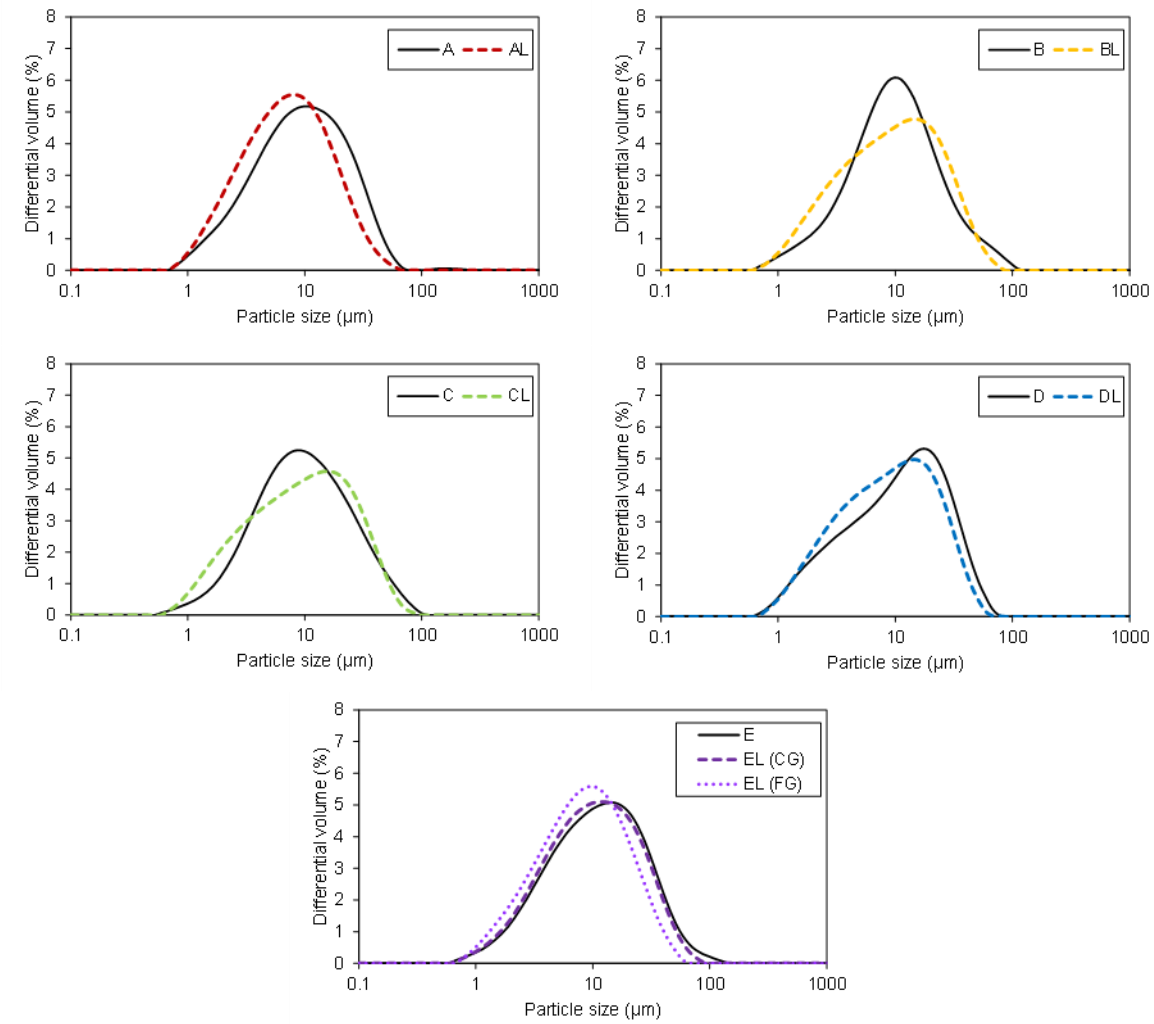

Figure 3.3 Differential particle size distributions for cements A-E.

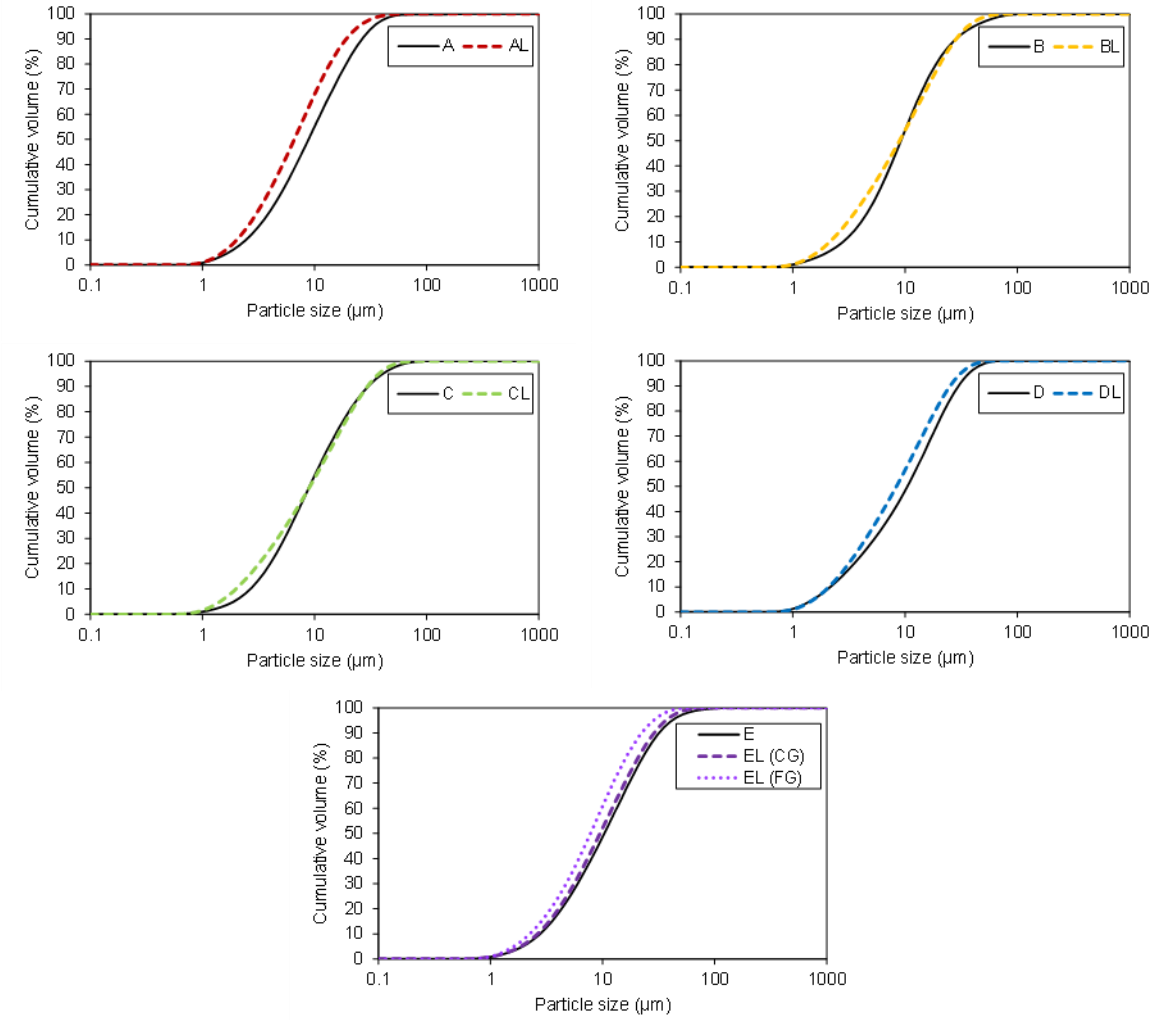

Figure 3.4 Cumulative particle size distributions for cements A-E.

Table 3.4 Summary of physical properties for Type I/II and Type IL cements.

Cement	D_{10} µm	D_{50} µm	D_{90} µm	$D_{3,2}$ µm	$D_{4,3}$ µm	SSA m^2/kg	Blaine m^2/kg
A	2.77	10.0	30.2	6.28	14.1	288	448
AL	2.29	7.5	21.8	5.09	10.2	356	597
B	3.17	10.4	31.9	6.71	15.1	282	416
BL	2.41	10.1	32.1	5.83	14.3	326	600
C	3.03	10.1	34.1	6.53	15.1	278	465
CL	2.25	10.2	33.6	5.60	14.6	324	606
D	2.45	11.9	34.0	6.19	15.5	293	460
DL	2.37	9.5	28.6	5.66	12.9	321	574
E	3.15	11.8	36.2	7.07	16.8	257	428
EL (CG)	2.99	10.8	32.8	6.69	14.9	271	511
EL (FG)	2.54	8.9	25.4	5.72	11.8	317	553

3.3 Hydration kinetics

As discussed in Chapter 2, the kinetics of cement hydration can be altered through changes to both the cement's chemistry and its physical properties. Just as small changes in the amount of C_3A, for example, in an ordinary portland cement can have a dramatic influence on the hydration rate, so, too, can changes to the amount, size, and (as will be discussed in Chapter 5) type of limestone incorporated into a portland limestone cement. In particular, prior research has demonstrated that the rate of hydration is sensitive to both nucleation and dilution effects arising from the incorporation of filler materials [11, 21, 25, 29, 30, 61]. In this section, hydration kinetics will be analyzed for pastes prepared from the eleven commercially produced Type I/II and Type IL cements. The roles of limestone particle size and material chemistry will be systematically analyzed in order to better understand which chemical and physical properties have the greatest influence on early-age hydration rates for portland limestone cement pastes.

3.3.1 Isothermal calorimetry

The kinetics of cement hydration were measured indirectly by isothermal calorimetry, by examining the rate of heat release for each cement paste as it hydrates. Three calorimetric peaks are typically observed during the hydration of a portland cement: the first corresponding to the dissolution of the clinker phases in the first ~30 minutes of hydration; the second corresponding to the hydration of the C_3S phase, after about 4-6 hours; and the third corresponding to the hydration of the C_3A phase, sometimes overlapping with the C_3S peak. A fourth broad shoulder may also appear after 24-36 hours, corresponding to the formation of AFm phases such as monosulfate and monocarbonate, but this peak is not always apparent [62]. By comparing the calorimetric heat profiles of the Type IL cement pastes to those of their Type I/II companions, the differences in hydration kinetics between Type I/II and Type IL cements can be assessed.

Isothermal calorimetry was performed in accordance with ASTM C1679 [63] on pastes prepared at a water-to-binder ratio (*w/b*) of 0.40, where the binder consists of both the cement and its interground limestone. The mixing procedure consisted of manual stirring of the cement in deionized water for 30 s, followed by mechanical mixing of the paste mixture with a 5-speed hand mixer at low speed for 60 s and at medium speed for 60 s. Two samples, each weighing 7.0 ± 0.5 g, were transferred to glass vials and then placed into the isothermal calorimeter (TA Instruments TAM Air). The rate of heat evolution and the cumulative heat released were measured at 25°C for the first 7 days of hydration.

The rates of heat evolution over the first 72 hr are shown in Figure 3.5, while the cumulative heats of hydration over the entire testing period are shown in Figure 3.6. The

rate of heat evolution and cumulative heat are both normalized with respect to the mass of the binder, such that dilution effects are indicated by a reduction in the amount of heat released. A summary of important calorimetric results is given in Table 3.5. For consistency, the "peak" heat release tabulated corresponds to the peak typically associated with C_3S hydration (second peak).[5]

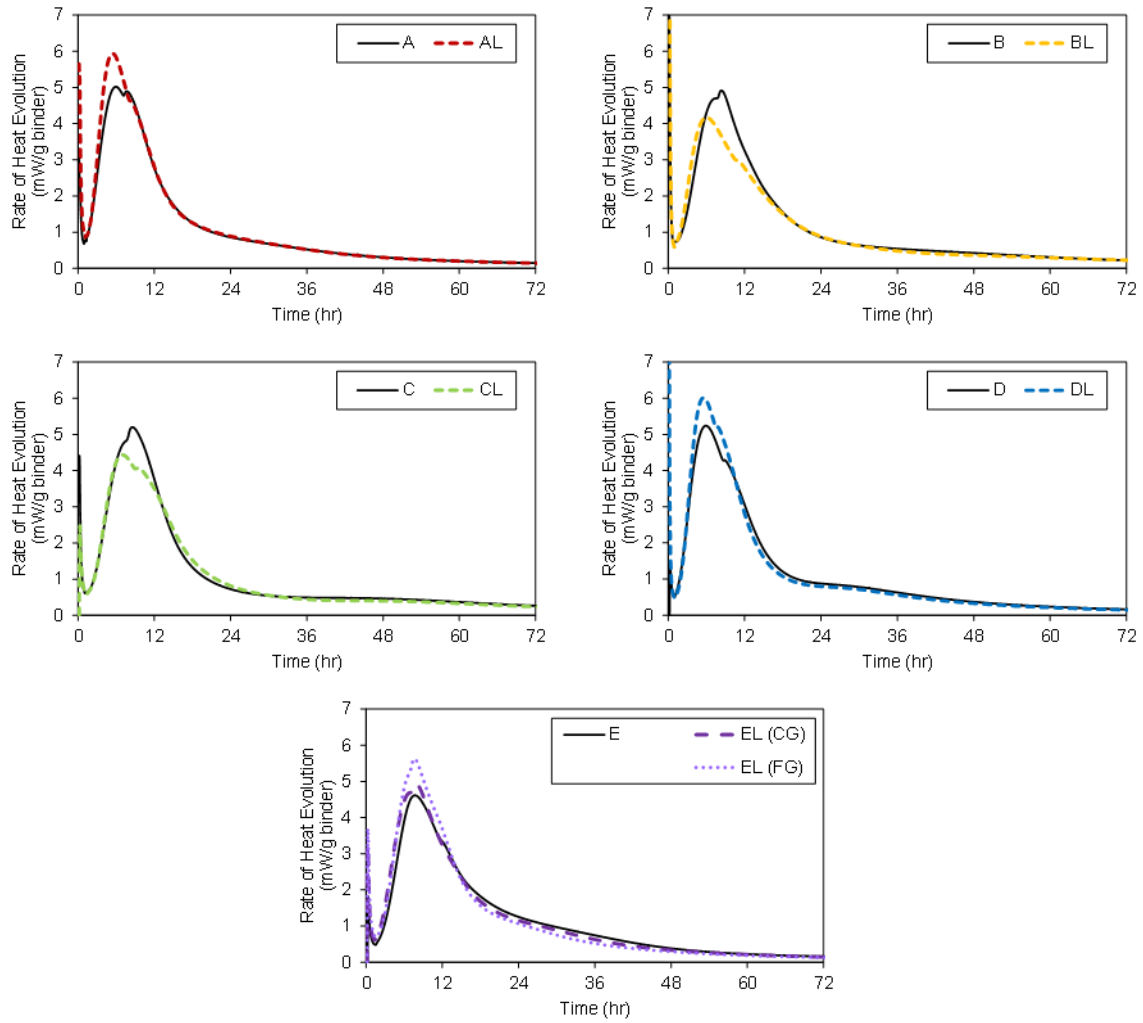

Figure 3.5 Heat evolution for cement pastes A-E at *w/b* = 0.40 and 25°C, through 72 hr.

[5] In some cements, such as cements B and C, the C_3A peak (third peak) has a greater magnitude than the C_3S peak. The height of the C_3A peak is sensitive to the SO_3/Al_2O_3 ratio of the cement, with lower ratios typically resulting in a greater amount of heat released by the C_3A hydration. Since SO_3 contents vary among cements, it is possible that the C_3A peak may be more prominent in one cement, but not in its companion, due to the different sulfate (e.g., gypsum) contents of the two cements.

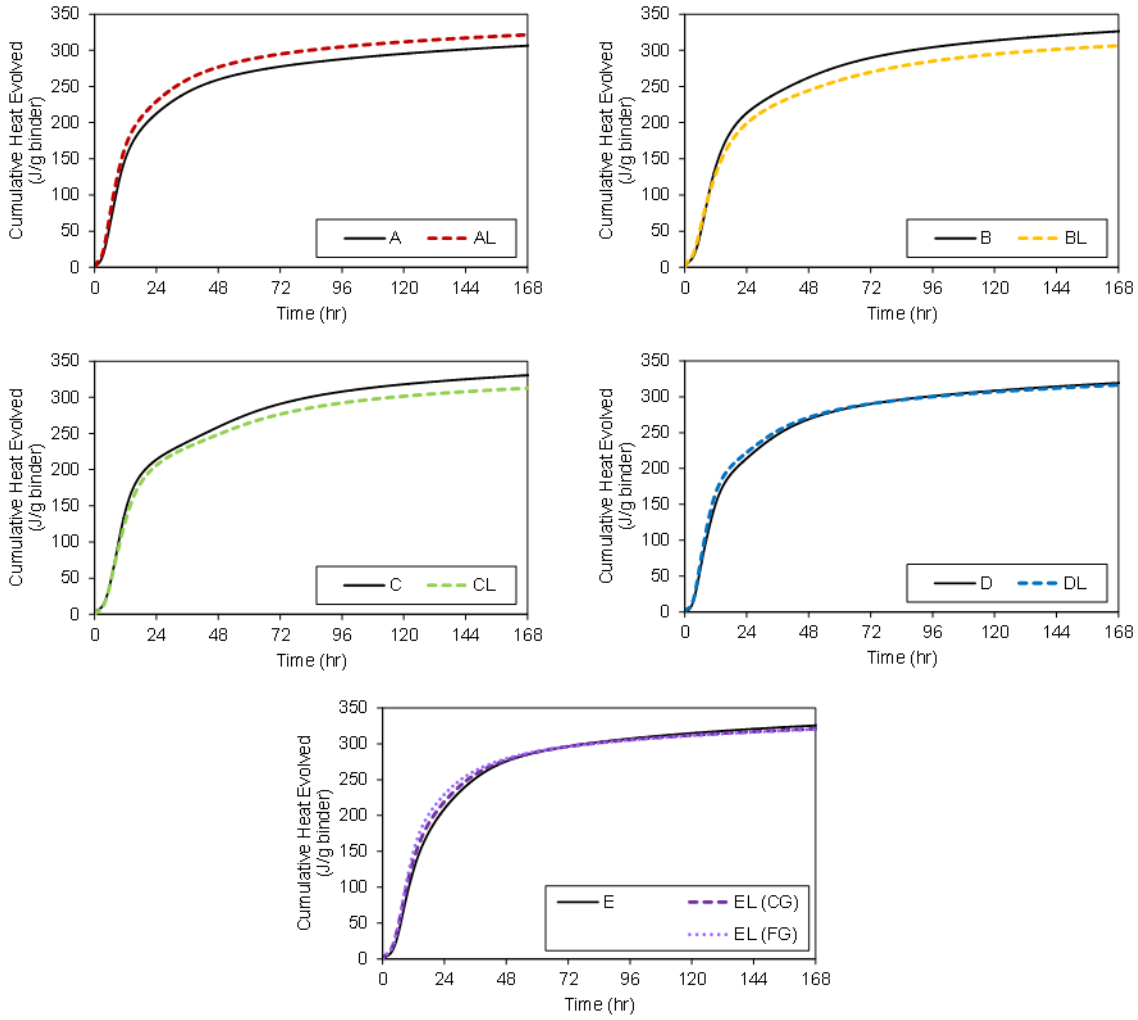

Figure 3.6 Cumulative heat evolved for cement pastes A-E at *w/b* = 0.40 and 25°C, through 168 hr (7 days).

Table 3.5 Summary of calorimetric results for cement pastes A-E with *w/b* = 0.4 at 25°C. Peak heat release parameters are given for the C_3S (second) peak.

Cement	Time to peak heat release (hr)	Peak heat release (mW/g)	Cumulative heat (J/g)			
			24 hr	48 hr	72 hr	168 hr
A	5.9	5.0	213	259	277	306
AL	5.4	5.9	230	277	295	321
B	7.5	4.7	213	262	290	326
BL	5.9	4.2	199	245	270	306
C	7.8	4.9	214	259	291	331
CL	7.0	4.4	306	249	277	313
D	5.9	5.2	214	269	290	319
DL	5.5	6.0	222	271	290	316
E	7.8	4.8	209	276	296	325
EL (CG)	7.5	4.8	219	277	296	321
EL (FG)	7.1	5.4	230	280	296	320

The results of the calorimetry experiments suggest that the rate of hydration in the first 24 hr is directly related to the relative fineness of the cement. When the Type IL cement is ground to a finer median particle size than its companion Type I/II cement (as illustrated by cements from sources A, D, and E), the peak heat release is increased, which indicates more rapid hydration rates, consistent with nucleation-dominated behavior [30]. Meanwhile, when the Type IL cement is ground to a similar median particle size as its companion Type I/II cement (as illustrated by cements from sources B and C), the peak heat release is reduced, consistent with dilution effect-dominated behavior [11]. Additionally, all six Type IL cement pastes show accelerated times to C_3S hydration, consistent with nucleation effects arising from the increase in surface area [30].

After the first 24 hr of hydration, the rates of heat evolution for all six Type IL cement pastes are lower than for their Type I/II counterparts due to the dilution of the cement. The consequences of the later-age dilution effects can be seen in the cumulative

heat curves (Figure 3.6). For the two dilution-dominated cements, BL and CL, an approximate 6% relative decrease in total heat release was observed at 7 days. For the four filler effect-dominated cements AL, DL, and EL (CG and FG), the early nucleation and filler effects were enough to overcome the later decreases in hydration rate, leading to a relative increase in total heat of 5% for cement AL, and only a 1% decrease in total heat release for the DL and EL cements by 7 days. Thus, while nucleation effects appear to have a potentially significant effect on hydration behavior in the first 24 hr, the dilution of the reactive clinker by the relatively inert limestone appears to have the more significant effect on the longer term heat of hydration.

3.3.2 Degree of hydration

Calorimetric data can be further used to investigate the influence of limestone addition on the degree of hydration of the cement, $\alpha(t)$ – that is, the fractional amount of cement that has reacted at a particular time t. Dilution and filler effects, because they respectively increase the effective water-to-cement ratio and improve the spatial distribution of cement grains, are both anticipated to increase degree of hydration in portland limestone cement pastes.

Research by Schindler, et al. [64], has demonstrated that the degree of hydration of a portland cement paste can be estimated from cumulative heat evolution curves according to Equation 3.4:

$$\alpha(t) = \frac{H(t)}{H_\infty} \tag{3.4}$$

where $H(t)$ is the cumulative heat evolved at time t, and H_∞ is defined as the cumulative heat evolved upon complete hydration (at $t = \infty$):

$$H_\infty = 500\,p_{C_3S} + 260\,p_{C_2S} + 866\,p_{C_3A} + 420\,p_{C_4AF} + 624\,p_{SO_3} + 1186\,p_{Free\,CaO} + 850\,p_{MgO} \quad (3.5)$$

The p_i terms in Equation 3.5 represent the mass fraction of phase *i* in the cement, indicated in Table 3.1. While p_i terms are typically taken from chemical oxide analyses and Bogue potential compositions, XRD with Rietveld analysis was used in this study due to its higher degree of accuracy in quantifying the primary clinker phases for Type IL cements, as previously discussed [54, 65]. The C_3S, C_2S, C_3A, C_4AF, free CaO (lime), and MgO (periclase) terms were all quantified in this manner, while the SO_3 term, because it originates from a variety of phases within the cement (e.g., gypsum, $CaSO_4{\cdot}2H_2O$, and arcanite, K_2SO_4), was instead quantified using chemical oxide analysis. Table 3.6 gives the total heat of hydration, H_∞, predicted for each cement by Equation 3.5.

Table 3.6 Predicted total heat of hydration, H_∞, J/g.

Cement	A	B	C	D	E
Type I	450.4	439.2	444.1	438.6	470.3
Type IL	414.5	415.0	401.1	413.2	441.3

The resulting degrees of hydration for each cement paste are shown in Figure 3.7 and are summarized in Table 3.7. For all eleven pastes, the presence of limestone leads to equivalent or increased degrees of hydration of the cement paste, with greater increases in α at a particular hydration age observed with increasing cement fineness. The increase in degree of hydration can be primarily attributed to the dilution of the clinker by limestone, as the increase in effective *w/c* provides more water for hydrating the clinker that remains. By 7 days, it can be observed that the interground limestone increases the total degree of hydration of the cement by an absolute 4.4 ± 3.0% (p = 0.10) for the six Type

IL cements investigated, or about 0.6 ± 0.4% per 1% limestone added to the binder. Therefore, while nucleation effects resulting from the inclusion of fine limestone appear to have a meaningful effect on the hydration rate of the system, it is the dilution of the cement by a relatively inert filler and the finer particle size distribution of the cement that appear to have the more significant impact on the degree of hydration of the clinker.

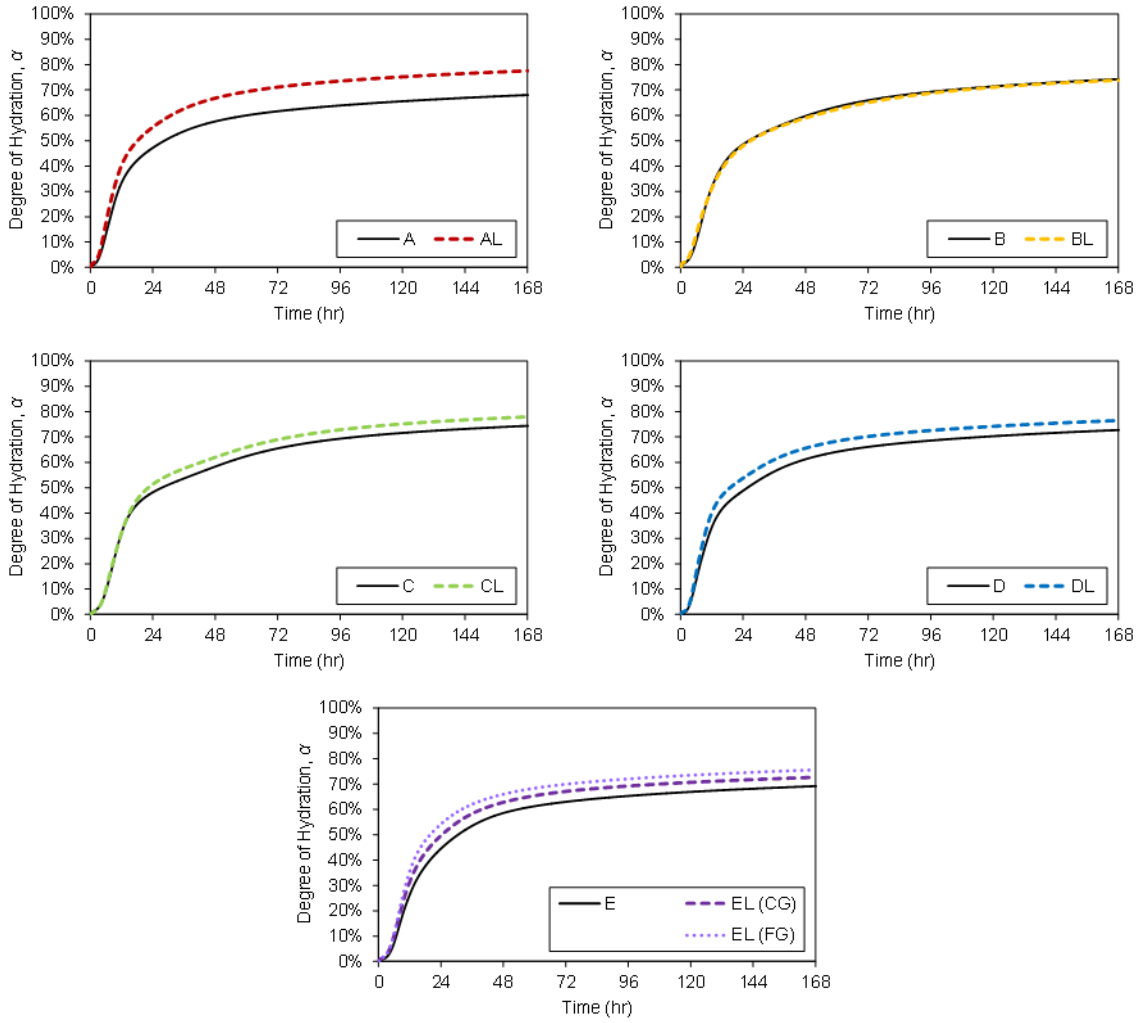

Figure 3.7 Degree of hydration for cement pastes A-E with *w/b* = 0.4 at 25°C, through 168 hr (7 days).

Table 3.7 Summary of degree of hydration results for cement pastes A-E with *w/b* = 0.4 at 25°C.

Cement	Degree of hydration (%)			
	24 hr	**48 hr**	**72 hr**	**168 hr**
A	47	58	62	68
AL	55	67	71	78
B	49	60	66	74
BL	48	59	65	74
C	48	58	66	74
CL	51	62	69	78
D	49	61	66	73
DL	54	66	70	77
E	45	59	63	69
EL (CG)	50	63	67	73
EL (FG)	54	66	70	76

3.3.3 Correlations to composition and particle size

In order to better understand which chemical and physical parameters most affect the hydration of Type IL cement paste systems, the compositions and particle sizes of the eleven cements were correlated to the hydration responses observed. All eleven cements were included in the analysis, with no distinctions made between Type I/II and Type IL cements due to limited sample sizes in each classification. The parameters and responses considered are listed in Table 3.8. Pearson correlation coefficients (ρ) were computed for each pair of variables to determine if an increase in parameter X was positively (or negatively) correlated with an increase in observed response Y. The statistical significance (p-value) of each correlation was assessed using a two-tailed t-test with n-2 = 9 (or, when only 4 mixes were considered, n-2 = 2) degrees of freedom and a null hypothesis H_0: $\rho = 0$ (i.e., X and Y are not linearly correlated to one another). The test statistic t^* is given in Equation 3.6:

$$t^* = \frac{\rho\sqrt{n-2}}{\sqrt{1-\rho^2}} \tag{3.6}$$

A value $p < 0.10$ indicates moderately strong evidence of correlation, $p < 0.05$ indicates strong evidence of correlation, and $p < 0.01$ indicates very strong evidence of correlation.

Table 3.8 Parameters and response variables for hydration correlation study.

Parameter variable, *X*	**Response variable, *Y***
Limestone (LS) content of binder	Time to peak heat release
SSA of binder	Magnitude of peak heat release
$D_{3,2}$ of binder	Degree of hydration of paste
$D_{4,3}$ of binder	
D_{10} of binder	
D_{50} of binder	
D_{90} of binder	
Blaine fineness of binder	

The statistical significance of the correlations found between the chemical and physical properties of the cements and their calorimetric responses are shown in Table 3.9. It was determined that an increase limestone content was strongly correlated with an increase in degree of hydration ($p < 0.01$), but that the strength of the correlation decreased with increasing time. The decreasing significance of the limestone content suggests that the limestone dosage may have a less significant influence on degree of hydration at later ages, as other parameters such as the clinker composition or the cement fineness take on more significant roles.

The physical properties of the eleven cements were generally found to be more strongly correlated to the initial rates of heat release. The analyses indicate that, for the cement pastes considered in this study, peak heat release is most significantly accelerated by an increase in cement fineness (increase in SSA, or decrease in D_{10} or $D_{3,2}$), while the magnitude of the peak heat release is most significantly decreased by an increase in the coarseness of the cement (increase in $D_{4,3}$ or D_{90}). These relationships support the previous assessment that the increase in surface area due to the partial replacement of

cement by a *less dense* limestone filler will encourage heterogeneous nucleation and accelerate cement hydration regardless of particle size, while the partial replacement of cement by a limestone filler of comparable size will make the cement more susceptible to dilution effects that decrease hydration rate.

Table 3.9 Statistical significance (*p*-value) of correlations between chemical and physical properties of Type I/II and Type IL cements and their calorimetric response at 25°C with *w/b* = 0.4. Sign of correlation is indicated in parentheses. Highlight colors indicate strength of significance.

Parameter	Rate of heat evolution		Degree of hydration			
	Time to peak	Peak heat release	24 hr	48 hr	72 hr	168 hr
LS content	0.19 (-)	0.33 (+)	0.00 (+)	0.01 (+)	0.01 (+)	0.04 (+)
SSA	0.01 (-)	0.24 (+)	0.00 (+)	0.03 (+)	0.02 (+)	0.01 (+)
$D_{3,2}$	0.01 (+)	0.15 (-)	0.00 (-)	0.02 (-)	0.01 (-)	0.01 (-)
$D_{4,3}$	0.06 (+)	0.03 (-)	0.00 (-)	0.00 (-)	0.01 (-)	0.06 (-)
D_{10}	0.01 (+)	0.32 (-)	0.03 (-)	0.07 (-)	0.05 (-)	0.05 (-)
D_{50}	0.19 (+)	0.09 (-)	0.00 (-)	0.03 (-)	0.03 (-)	0.06 (-)
D_{90}	0.08 (+)	0.02 (-)	0.00 (-)	0.01 (-)	0.03 (-)	0.15 (-)
Blaine	0.14 (-)	0.62 (+)	0.01 (+)	0.04 (+)	0.01 (+)	0.01 (+)

Legend:		$p < 0.01$
		$0.01 < p \leq 0.05$
		$0.05 < p \leq 0.10$

Finally, the relationships between the physical parameters and degree of hydration generally indicate that the particle size of the binder has a significant impact on the cement's degree of hydration. An increase in fineness by almost any measure (surface area or volume) results in a higher degree of hydration at all ages, likely due both to nucleation effects, which increase hydration rates at early ages, and to filler effects, which allow for better dispersion of the cement grains for more efficient dissolution and hydration in the pore solution. Interestingly, while SSA and $D_{3,2}$ were both strongly or

very strongly correlated to degree of hydration at all ages investigated, the Blaine fineness was always found to be less significantly correlated, suggesting that Blaine fineness is a less sensitive measure of surface area and is therefore a less accurate predictor of surface-area-related effects.

Based on the correlation analysis, it is therefore concluded that the hydration kinetics for portland limestone cements are strongly related to the limestone dosage and the relative fineness of the cements. The increase in limestone content is positively correlated with an increase in degree of hydration as a consequence of the dilution effect, while an increase in limestone fineness is correlated with an increase in both hydration rate and degree of hydration as a result of filler and nucleation effects occurring within the first 24 hr. Although dilution effects were observed to dominate the behavior of cements containing more coarsely ground limestone additions, the higher specific surface areas of all of the Type IL cements were found to positively correlate with an acceleration of the C_3S hydration, suggesting all six Type IL cements do in fact undergo nucleation effects, regardless of differences in their mean particle sizes.

3.4 Chemical evolution

Although isothermal calorimetry on its own does not give information about the chemical evolution of portland limestone cement pastes, preliminary insights into hydration reactions can be surmised based on changes to known heat release signatures. For example, since it was observed that cements with higher specific surface areas accelerate the hydration of C_3S, it would therefore be anticipated that the products of C_3S hydration, CH and C-S-H, would be more abundant at early ages in Type IL cement

pastes compared to their Type I/II counterparts. Similarly, in the heat evolution curves (Figure 3.5), a broad shoulder typically associated with AFm formation (e.g., monosulfate or moncarbonate) can be observed beginning around 36 hr for cements from sources A, D, and E and around 48 hr for cements from sources B and C; however, it is not possible to determine from isothermal calorimetry which of the AFm phases are actually forming in the pastes.

Therefore, to support the hydration studies conducted in Section 3.3, three additional chemical analyses – thermogravimetric analysis, x-ray diffraction, and Raman spectroscopy – were performed on a subset of the Type I/II and Type IL cement pastes, in order to gain further insights into the chemical evolution of portland limestone cement pastes over the first 28 days of hydration. Cements from sources A and B were selected for further study because they represent the extremes of composition and behavior for the eleven cements analyzed. Cements A and AL contained the greatest limestone addition rates among both the Type I/II and Type IL cements, were among the most finely ground of the Type I/II and Type IL cements, and exhibited the greatest increases in both hydration rate and degree of hydration, while cements B and BL contained the least amount of limestone (with cement B containing no interground limestone at all), were among the most coarsely ground of the Type I/II and Type IL cements, and exhibited the greatest reduction in hydration rate and the smallest increase in degree of hydration. Because of the extreme characteristics of the four cements pastes studied, it is expected that the seven cement pastes not selected for further study exhibit chemical evolutions that are bounded by the behavior discussed herein.

3.4.1 Thermogravimetric analysis

Thermogravimetric analysis (TGA) was used to quantify the amounts of calcium hydroxide (CH) and calcium carbonate ($CaCO_3$) in the hydrating cement pastes over time, as well as to qualitatively identify the AFm phases forming within the first 28 days of hydration. Cement paste samples with *w/b* = 0.40 were prepared using the same mixing procedure as for calorimetry, cast in sealed containers, and hydrated at 25°C for up to 28 days. After 1, 3, 7, 14, and 28 days of hydration, a portion of each specimen was removed and crushed into coarse particles (< 2.36 mm). Hydration of the particles was halted by solvent exchange, by soaking the particles in isopropanol[6] for 15 min then drying under vacuum for 5 min. The dried fragments were ground into a fine powder (< 150 μm) for analysis using a mortar and pestle. Because isopropanol is known to increase the likelihood of carbonation in cement pastes [66, 67], the resulting powders were stored in sealed bags under light vacuum until testing.

Thermogravimetric analyses (Hitachi EXSTAR TG/DTA 7300) were carried out on approximately 20 mg of each powder, heated under N_2 environment from 25 to 900°C at a rate of 10°C/min. CH and $CaCO_3$ contents were determined from thermal mass losses between approximately 400-450°C and 600-750°C, respectively, as given in Equations 3.7 and 3.8:

$$\%CH = \frac{m_{400} - m_{450}}{m_{25}} \times \frac{MW_{Ca(OH)_2}}{MW_{H_2O}} \tag{3.7}$$

$$\%CaCO_3 = \frac{m_{600} - m_{750}}{m_{25}} \times \frac{MW_{CaCO_3}}{MW_{CO_2}} \tag{3.8}$$

[6] Solvent exchange was selected rather than freeze-drying in order to preserve the hydrate phases, which can become damaged at the low temperatures and pressures used in freeze-drying [67].

where m_{400} is the mass of the sample at 400°C, m_{25} is the initial mass of the sample (at 25°C), and the molecular weights of $Ca(OH)_2$, and H_2O, $CaCO_3$ and CO_2 are taken to be 74.09 g/mol, 18.01 g/mol, 100.09 g/mol, and 44.01 g/mol, respectively. The exact bounds of the thermal decomposition for each phase were determined by examination of the thermogravimetric derivative (DTG) curves. Monosulfate and mono- and hemicarbonate could not be quantified due to overlapping decomposition ranges with ettringite and C-S-H, but were identified from the DTG curves by peaks occurring between ~130-150°C (monosulfate) and ~140-160°C (mono- and hemicarbonate).

The quantified CH and $CaCO_3$ contents are shown in Figure 3.8 and Figure 3.9, respectively. Values at an age of 0 days indicate the CH and $CaCO_3$ contents measured for the raw cements. The observed increase in $CaCO_3$ content between 0 and 1 days for cement B (and to a lesser extent for the other three cements) is believed to be due to incidental carbonation of the powder samples following solvent exchange, and does not necessarily reflect an increase in the $CaCO_3$ available during hydration.

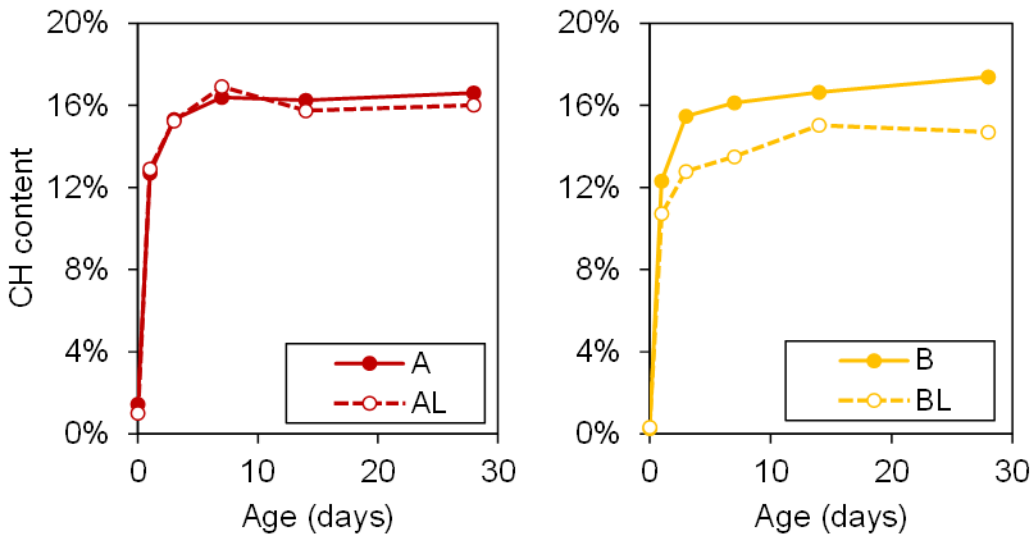

Figure 3.8 Calcium hydroxide (CH) contents measured by thermogravimetric mass loss between 400-450°C for cement paste samples with *w/b* = 0.4.

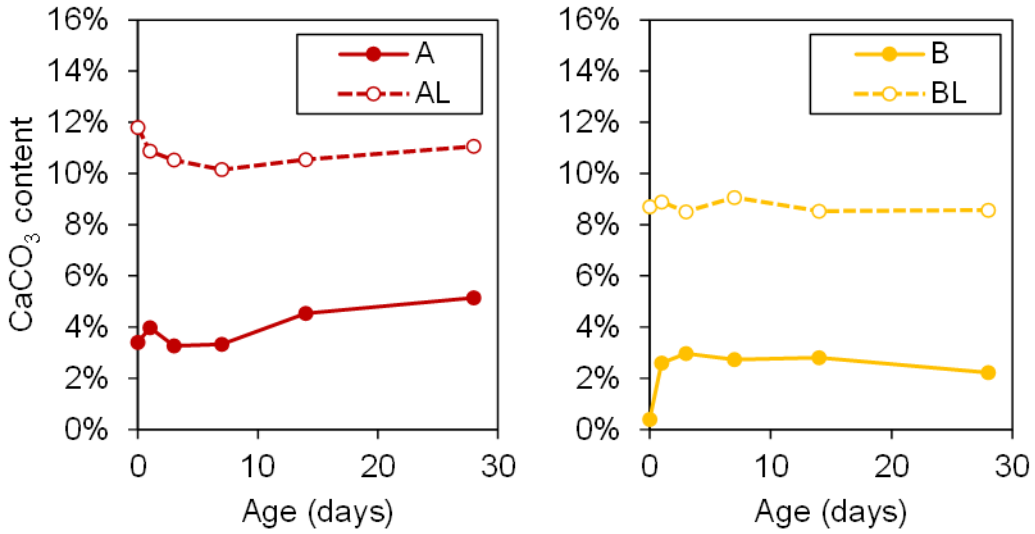

Figure 3.9 Calcium carbonate ($CaCO_3$) contents measured by thermogravimetric mass loss between 600-750°C for cement paste samples with *w/b* = 0.4.

From the results in Figure 3.8, it can be observed that the Type IL cement paste from source A exhibited comparable or slightly increased CH formation compared to its Type I/II companion within the first 7 days of hydration. This period of increased CH production coincides with the increased heat release observed by isothermal calorimetry,

and supports the idea that the fine limestone inclusions accelerate hydration by promoting nucleation of hydration products (CH) on their surfaces. At later ages, it was found that the Type IL cement paste from source A produced approximately 3% less CH than its Type I/II companion paste, indicating that although nucleation and filler effects enable more hydration at early ages, the dilution of the reactive clinker material ultimately leads to reductions in the amount of hydration product formed, potentially resulting in higher relative porosities at later ages.

For the cement pastes from source B, it was observed that despite the initial acceleration of the Type IL cement hydration, the overwhelming effect of the clinker dilution reduced CH contents by 10-15% at all ages investigated. This reduction is surprisingly larger than the 9% reduction in clinker content by the limestone filler, suggesting that the coarser average particle size of the Type IL cement may not be simply due to the inclusion of coarse limestone particles, but also due to a coarser grinding of the clinker itself. Such a coarse grind to the clinker would make dissolution of the cement grains more difficult, thereby reducing the overall amount of cement that is hydrated (lower degree of hydration) and, by extension, reducing the amount of hydration product formed [2, 68]. As a result, it is anticipated that the Type IL cement paste from source B will also have a much higher porosity relative to its Type I/II counterpart as a consequence of the significant reduction in its hydration product volume.

In Figure 3.9, it can be seen the $CaCO_3$ contents of cement pastes A and AL both decreased over the first 7 days of hydration and cement paste BL decreased between 7 and 14 days. In general, the decrease in $CaCO_3$ content suggests that some of the $CaCO_3$ is being consumed to form carboaluminate AFm phases. Although it was not possible to

quantify the amounts of hemi- and monocarbonate phases formed at these ages, it was possible to confirm their formation by examining the thermogravimetric derivative (DTG) curves (Figure 3.10 and Figure 3.11). The DTG curves confirm that the decrease in $CaCO_3$ contents for cements A and AL between 1 and 7 days of hydration coincide with the formation of mono- or hemicarbonate (whose peaks occur between approximately 130 and 150°C). The DTG curves for cement BL also indicate the presence of carbonate AFm phases, but the onset of their formation is delayed to 14 days, again consistent with the decrease in $CaCO_3$ content observed at that time. The delay in carbonate AFm formation may indicate that the more rapidly reacting C_3A phase is fully consumed by the sulfate-containing species within the first 3 days of hydration, such that mono- and hemicarbonate can only form once the more slowly reacting C_4AF phase has consumed the remaining sulfate ions. This hypothesis is supported by the composition of the cement reported in Table 3.1, where cement BL was found to have the highest combined gypsum-hemihydrate-anhydrite content of the Type IL cements (4.2%, by mass) despite having one of the lowest C_3A contents (2.6%).

As expected, since cement B contained no interground limestone, its DTG curves did not show any peaks corresponding to carbonate AFm phases through 28 days of hydration, but did show peaks for monosulfate (between approximately 150 and 170°C). Like the carbonate AFm phases detected for the other three cements, the formation of monosulfate was observed to initiate around 3 days and continue through the 28 day observation period. Since monosulfate does not consume limestone, no change in $CaCO_3$ content would be expected for cement B, and none was observed.

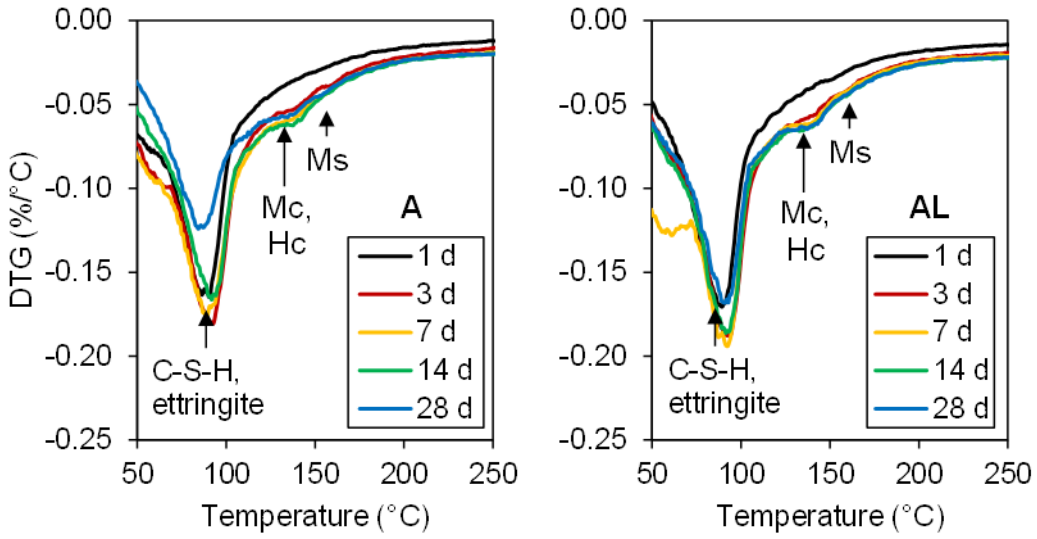

Figure 3.10 Thermogravimetric derivative (DTG) curves for cement pastes A and AL. (Mc = monocarbonate, Hc = hemicarbonate, Ms = monsulfate)

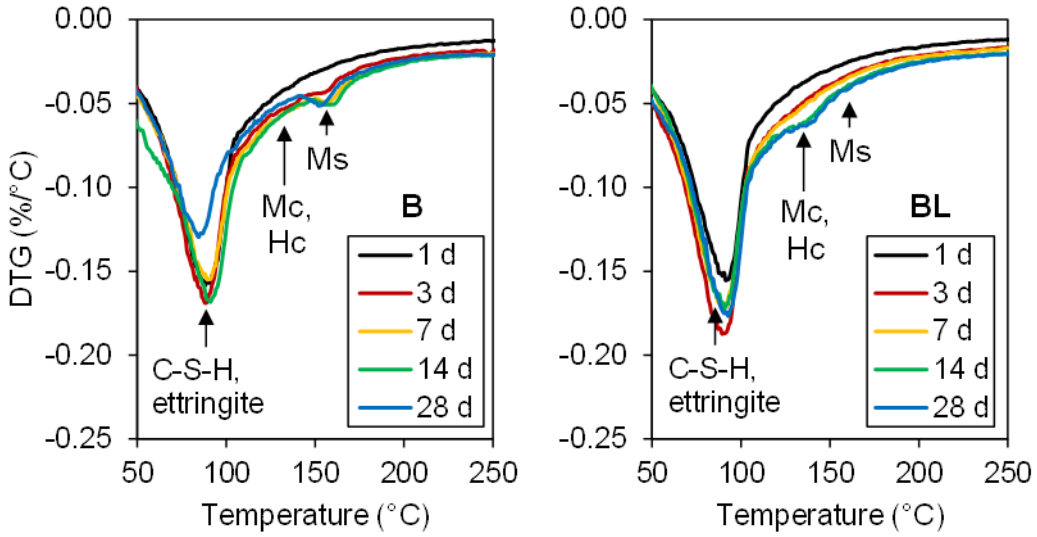

Figure 3.11 Thermogravimetric derivative (DTG) curves for cement pastes B and BL. (Mc = monocarbonate, Hc = hemicarbonate, Ms = monsulfate)

3.4.2 X-ray diffraction

Complementary compositional information for the hydrating cement pastes was also obtained by x-ray diffraction (XRD). Measurements were carried out on the same powderized cement paste samples used for TGA in order to identify additional phases

present in the cement pastes at the ages of interest. Samples weighing approximately 2 g were packed into sample holders, placed into a PANalytical X'Pert PRO Alpha-1 Empyrean x-ray diffractometer, and excited with Cu-Kα (λ = 1.54 Å) radiation. Scans were performed between 5° and 70° 2θ, using a PIXcel^{3D} detector and a sampling time of 30 seconds. Identification of crystalline phases was performed with PANalytical HighScore Plus software, using reference patterns found in the COD database [69-71].

Although the scans were collected between 5 and 70° 2θ, preliminary investigation of the resulting patterns revealed two regions of primary interest for subsequent analysis: one between 26 and 38° 2θ, where primary peaks for the clinker phases, CH, and ettringite are located, and another between 8 and 13° 2θ, where primary peaks for AFm hydration products are located. Patterns for each cement paste within the two regions of interest are shown in Figure 3.12 and Figure 3.13 below, with background signals from the amorphous content removed for clarity. Although the diffraction patterns outside of the two regions of interest are not shown, they were additionally used to aid in the identification of the cement paste phases.

Between 26 and 38° 2θ (Figure 3.12), the diffraction patterns demonstrate the consumption of the clinker phases and subsequent formation of the hydration products CH and ettringite. While quantification of individual phases was not possible due to the lack of an internal reference standard, observations regarding the relative rates of reaction could be made. For example, peaks corresponding to C_3A were observed to decrease in intensity more rapidly than peaks corresponding to C_3S or C_2S, and essentially disappear within the first 3 days of hydration, indicating that hydration of the C_3A phase and formation of C_3A-generated AFt and AFm phases occurs primarily during the first 3

days. Meanwhile, the C_4AF peak, shown magnified in Figure 3.13, does not show appreciable decreases in intensity over the first 28 days of hydration, suggesting that additional aluminate species will be available for AFt and AFm formation beyond 28 days of hydration.

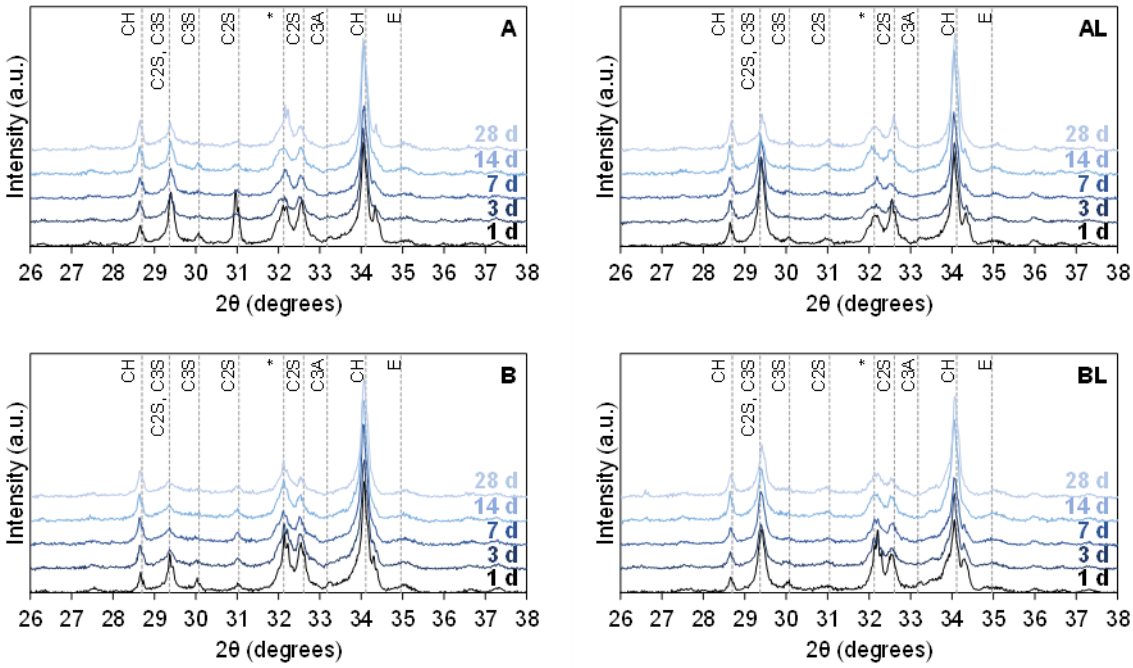

Figure 3.12 XRD patterns for cement pastes A, AL, B, and BL, between 26-38° 2θ. Peaks for CH, C_2S, C_3S, C_3A, and ettringite (E) are indicated. *: overlapping peaks for C_3S, C_2S, C_3A, and C_4AF.

Between the angles of 8 and 13° (Figure 3.13), the diffraction patterns indicate that as the C_3A is consumed, cements A and AL both form an ettringite AFt phase and hemi- and monocarbonate AFm phases. The rise of hemi- and monocarbonate peaks beginning at 3 days of hydration is consistent with observations made by TGA. Similar peaks for monocarbonate were observed for cement paste BL at 14 and 28 days, again consistent with the thermogravimetric results. According to the theoretical predictions by Matschei, et al., [20], the molar carbonate-to-alumina and sulfate-to-alumina ratios of the

three cements should all favor the coexistence of ettringite, monocarbonate, and excess calcium carbonate upon complete hydration, but no hemicarbonate should be observed. The observation of small amounts of hemicarbonate at 14 and 28 days suggests that hemicarbonate is an intermediate phase that will eventually convert to monocarbonate as hydration continues and the system approaches thermodynamic equilibrium.

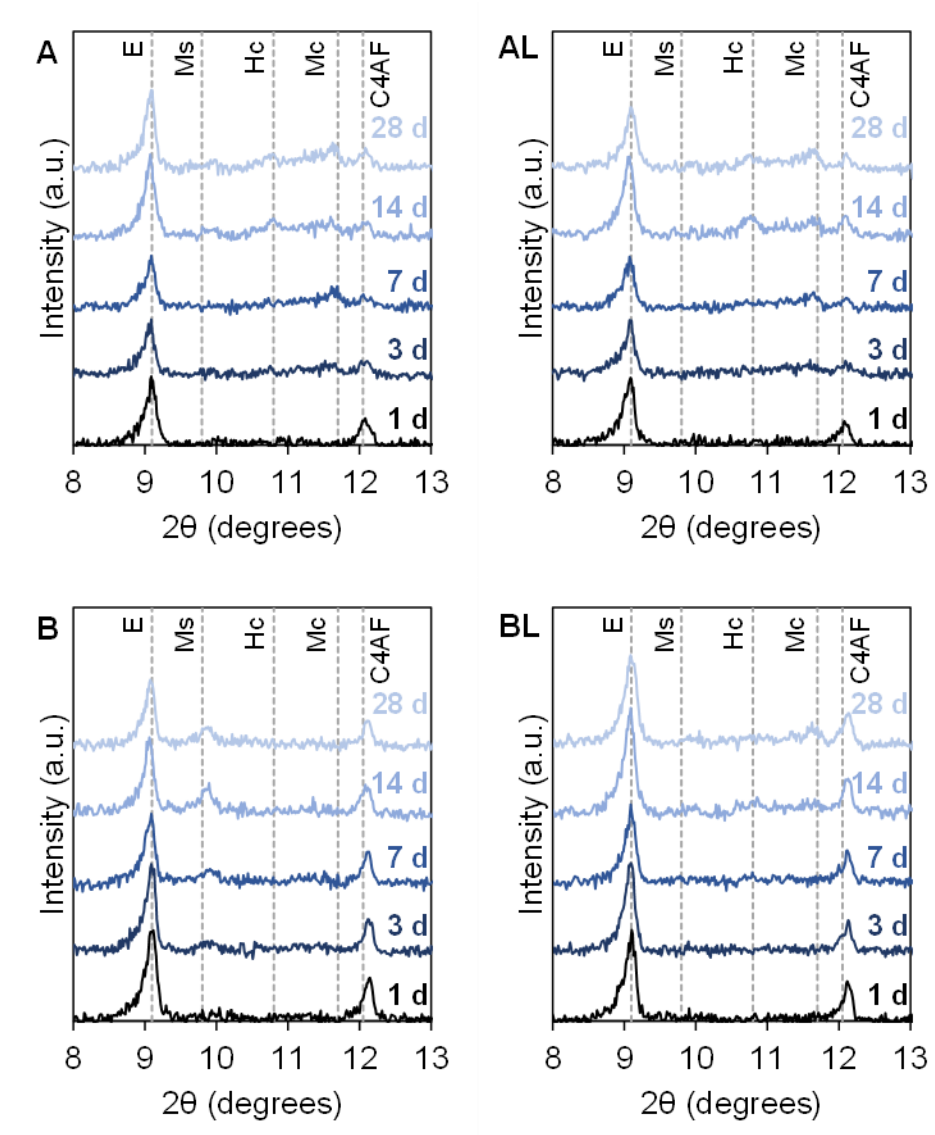

Figure 3.13 XRD patterns for cement pastes A, AL, B, and BL, between 8-13° 2θ. Peaks for ettringite (E), monosulfate (Ms), monocarbonate (Mc), hemicarbonate (Hc), and C_4AF are indicated.

The diffraction patterns for cement B between 8 and 13° similarly confirm observations from TGA that only monosulfate is formed in the first 28 days of hydration. The observations are again consistent with the models of Matschei, et al., which predict a combination of monosulfate and hemicarbonate phases present upon complete hydration; all of the ettringite should eventually convert to monosulfate, as is suggested in the analyses by the decreasing intensity of the ettringite peak over the first 28 days.

3.4.3 Raman spectroscopy

While a substantial amount of compositional information can be obtained via both thermogravimetry and x-ray diffraction, both of those techniques require extensive processing of the material prior to analysis. Samples cannot be tested *in situ*, and possible contamination of the samples by carbonation in air may affect the amounts of CH, $CaCO_3$ and carbonate AFm phases detected. Furthermore, TGA can only be used to uniquely identify three phases (CH, $CaCO_3$, and monosulfate), while XRD can only be used to identify highly crystalline phases, leaving gaps in information regarding chemical evolution of portland and portland limestone cement pastes.

To overcome some of the limitations of the TGA and XRD analyses, Raman spectroscopy was additionally used to perform *in situ* characterization of the cement pastes as they hydrated. Raman spectroscopy is an analytical technique in which photons of a particular energy (usually from a laser source in the visible or near-infrared range) interact with a material through molecular vibrations or other modes, and are inelastically scattered at a different energy and wavelength. The change in energy uniquely depends

on the molecular structure of the material so that specific chemical compositions can be determined. Carbonate and sulfate phases within the cement – including limestone, gypsum, monocarbonate, and monosulfate – are strongly Raman-active and appear as clear peaks within the spectra, making Raman spectroscopy potentially suitable for characterizing the hydration of portland limestone cements.

In this study, fresh paste specimens were prepared as described in Section 3.3. Approximately 2 g of each paste was placed into a shallow dish, which was subsequently stored in a vacuum desiccator to prevent carbonation. After 1, 2, 6, 12, 24, 48, 72, and 168 hr of hydration, the specimens were removed from the desiccator and the top surfaces were gently ground using 220 grit silicon carbide paper to remove surface carbonation; the same specimen was used for each testing age. Raman spectra were collected using a Thermo Nicolet Almega XR MicroRaman Spectrometer at 50× magnification, with a 488 nm excitation wavelength and a 100 μm pinhole aperture (~1.0 μm spot size). Nine scans were averaged for each specimen over a 200 μm × 200 μm grid to improve statistical representation and to reduce noise (Figure 3.14). Each scan consisted of 60 1.0 sec exposures. Peaks were assigned over the range of 300-1300 cm^{-1}, based on values reported in the literature, as shown in Table 3.10.

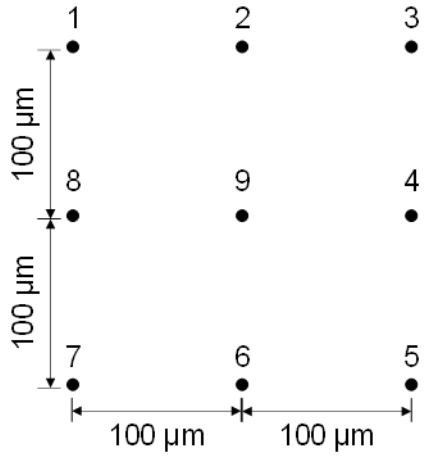

Figure 3.14. Sampling schematic for Raman spectroscopy.

Table 3.10 Possible assignments for peaks observed by Raman spectroscopy. Reference values are reported for excitation of 514 nm due to limited studies conducted at 488 nm.

Component	Raman shift (cm^{-1})	Ref.
C_3S	840-848	[72, 73]
C_2S	860-864	[72, 73]
C_3A	740-756	[72, 73]
C_4AF (Brownmillerite)	772, 506	[74]
Gypsum species	1008-1026	[72, 73]
Calcite ($CaCO_3$)	1085, 712	[72, 73]
C-S-H	600-700	[75]
CH	356	[72]
Ettringite	988	[76]
Monosulfate	982	[76]
Hemicarbonate	1068 (very weak)	[77]
Monocarbonate	1068	[77]

The averaged Raman spectra are shown in Figure 3.15 for cement pastes A and AL and in Figure 3.16 for cement pastes B and BL. For all four cement pastes, the Raman spectra clearly show the consumption of the unhydrated cement phases and the formation of the hydration products over time. With respect to the calcium silicate phases (C_3S and C_2S), a decreasing intensity can be observed over time in the calcium silicate band between 800-900 cm^{-1}. Initially, the calcium silicate peaks skew toward the C_3S signal

due to the higher proportions of C_3S in each cement, but with ongoing hydration, the peaks shift toward the C_2S signal, indicating the more rapid hydration of the C_3S phase relative to the C_2S phase. The overall decrease in peak intensity occurs concurrently with an increase in intensity of the C-S-H band (600-700 cm^{-1}) and the appearance of a faint calcium hydroxide (CH) peak at 356 cm^{-1}, further demonstrating Raman spectroscopy's unique ability to show the formation of both crystalline (CH) and amorphous (C-S-H) hydrate phases. It is suspected that the CH signal was weakened by carbonation at the sample surfaces, as the individual point scans having strong CH signals consistently showed strong $CaCO_3$ peaks at 1088 cm^{-1}, as well, regardless of the limestone content of the cement.

The dissolution of gypsum (~1010 cm^{-1}) and subsequent formation of ettringite (~988 cm^{-1}) can also be seen in the spectra, as early as 1 hr for all four cement pastes. For cement pastes A and AL, the gypsum dissolution occurs through 24 hr, at which point the signal disappears and the ettringite band begins to increase in intensity. The ettringite signals for cement pastes A and AL both continue to increase in intensity over the 7 day period, indicating that the ettringite is not being consumed to form monosulfate, and appropriately, no monosulfate peak (~982 cm^{-1}) was observed for either paste. Clear peaks indicating carboaluminate AFm phases (mono- and hemicarbonate) could not be detected around 1062 cm^{-1}, but a faint shoulder on the calcium carbonate peak may be visible in that region, beginning around 7 days hydration for cement paste A and around 3 days hydration for cement paste AL. More detailed investigation – perhaps looking at higher Raman shifts, where the O-H bond stretching produces stronger, more distinctive

signals for hemi- and monocarbonate – would be required to more adequately capture the early-age formation of carbonate AFm phases by Raman spectroscopy.

For cement pastes B and BL, the dissolution of the gypsum and subsequent formation of ettringite are also apparent; however, a clear gypsum peak can still be observed in both pastes beyond 24 hr of hydration, and in fact is still visible for cement paste BL by 7 days. The presence of a pronounced gypsum signal in cement paste BL after 7 days of hydration provides further support to the previously proposed hypothesis that the high gypsum and low C_3A content of that cement delays the onset of secondary AFm formation. Accordingly, neither carboaluminate AFm nor monosulfate AFm peaks were detected by Raman spectroscopy for cement paste BL. Although AFm peaks were also not detected for cement paste B, the ettringite peak was observed to nearly disappear for that paste by 7 days, suggesting that some of the ettringite is being consumed to form monosulfate. Longer testing durations would be required to confirm the formation of monosulfate by Raman spectroscopy, but evidence from TGA and XRD support the proposed hypothesis.

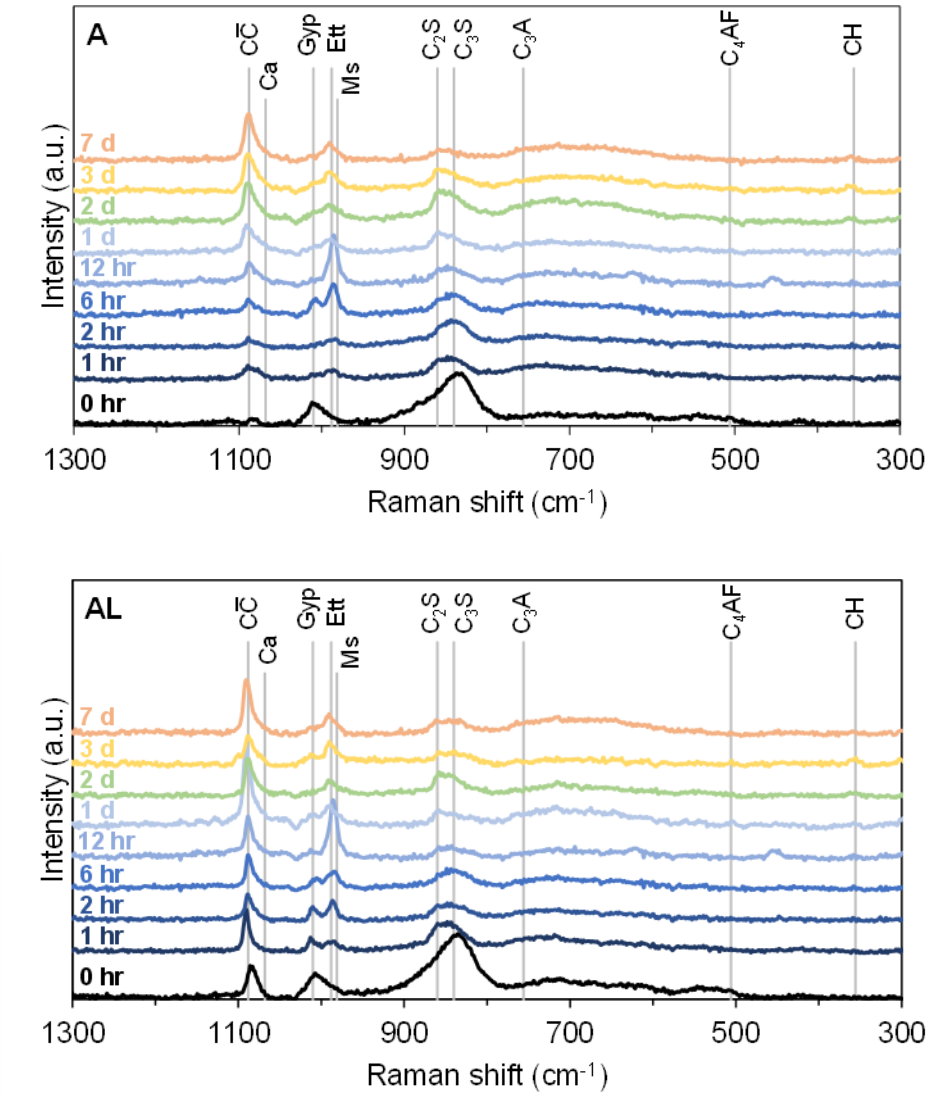

Figure 3.15 Raman spectra for cement pastes A and AL at *w/b* = 0.40. Raman shifts for calcium carbonate ($C\bar{C}$), carboaluminate AFm (Ca), gypsum (Gyp), ettringite (Ett), monosulfate (Ms), C_2S, C_3S, C_3A, C_4AF, and CH are indicated.

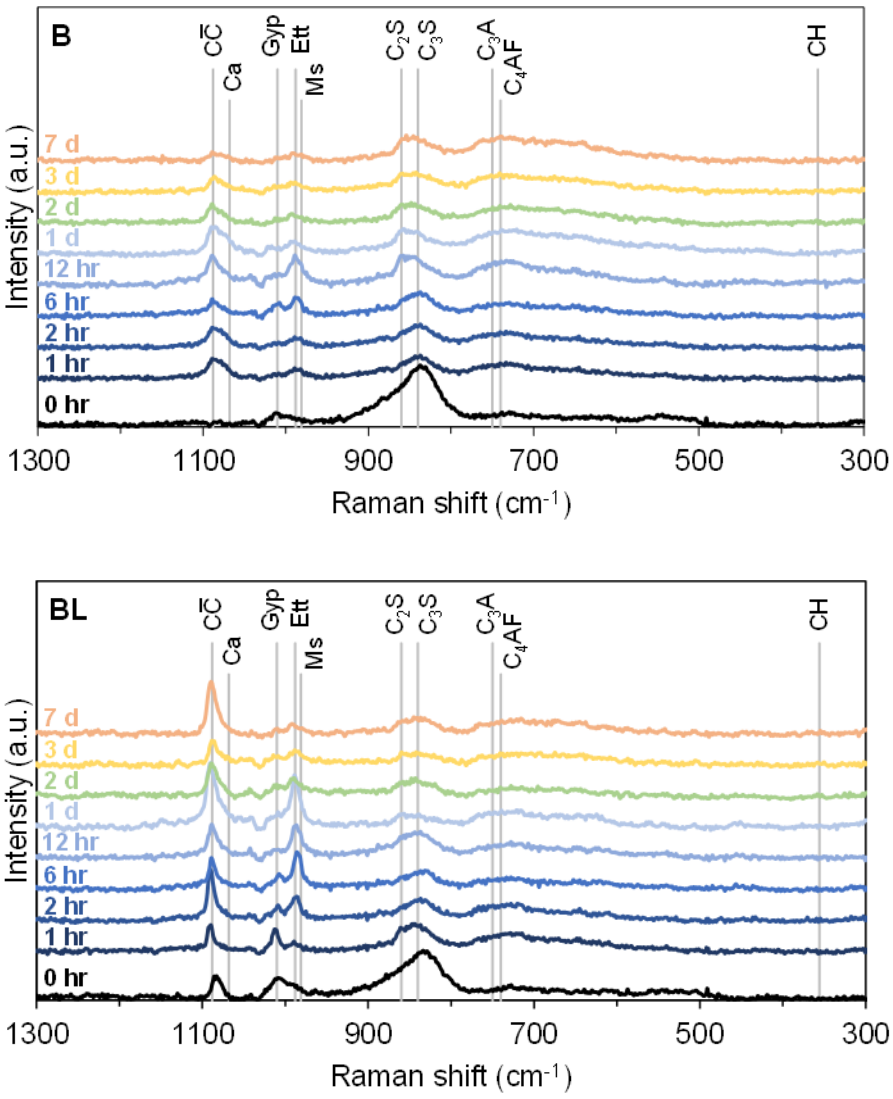

Figure 3.16 Raman spectra for cement pastes B and BL at *w/b* = 0.40. Raman shifts for calcium carbonate ($C\bar{C}$), carboaluminate AFm (Ca), gypsum (Gyp), ettringite (Ett), monosulfate (Ms), C_2S, C_3S, C_3A, C_4AF, and CH are indicated.

3.4.4 Discussion

The results of the three chemical evolution studies presented in this chapter provide greater support for theoretical hydration models proposed previously in the literature for Type IL cements [18-21]. Physically, limestone fillers were found to increase the rate and amount of CH precipitation at early ages for finely ground Type IL

cements (e.g., cement AL) and to dilute the overall amount of CH (and by extension, other hydration products) existing in the paste at later ages. The former effect can be attributed to increased heterogeneous nucleation of hydration products on the surfaces of the limestone, which results in an acceleration of the hydration reaction as observed by isothermal calorimetry. The latter effect can be attributed to the dilution of the cement by a less reactive filler, and additionally results in the lower cumulative heats of hydration observed by isothermal calorimetry for the Type IL cements.

Chemically, limestone fillers were found to have a more significant effect on the formation of AFt and AFm phases, preventing the ettringite from converting into monosulfate and instead forming hemi- and monocarbonate phases, which are not found in typical hydrated portland cements in the absence of limestone filler. Based on the results of this study, the chemical evolution of AFt and AFm phases in a hydrating portland limestone cement can be summarized as follows:

1) The initial dissolution of the clinker and calcium sulfate (e.g., gypsum) phases occurs rapidly, creating a system with a high sulfate-to-alumina ratio within a few hours. As the sulfate and alumina species are consumed to form ettringite (which can be observed by Raman spectroscopy), the sulfate-to-alumina ratio decreases, shifting to one that favors the formation of AFm phases within the first 72 hr (which can be observed by TGA and XRD).
2) Calcium carbonate is a poorly soluble compound, but was observed by TGA to partially dissociate into the pore solution within the first 24 hr of hydration for all three of the limestone-bearing cement pastes investigated. If a sufficient amount of carbonate is present in the pore solution when the sulfate-to-alumina ratio shifts

to favoring AFm formation, then carbonate AFm phases (mono- and hemicarbonate) will form, as was observed by both TGA and XRD for cements A, AL, and BL. If, on the other hand, an insufficient amount of carbonate is present at that time, the ettringite will begin to dissociate and sulfate AFm (monosulfate) phases will form instead, as observed by both TGA and XRD for cement B.

3) In cements with a high proportion of calcium sulfate phases relative to the C_3A, such as those from source B, the formation of secondary AFm phases may be delayed until the more slowly reacting C_4AF phase has begun to hydrate, since the initial calcium sulfate phases are not entirely consumed by the C_3A in the clinker (as observed by Raman spectroscopy). Such an effect would explain why the formation of mono- and hemicarbonate phases was delayed to 14 days for cement BL.

3.5 Microstructural evolution

Changes to the chemical evolution of portland limestone cement pastes will also affect their microstructural evolution. The accelerated and increased nucleation of hydration products (especially CH and C-S-H) at early ages can lead to reductions in pore volumes within the first few days of hydration, while the formation of carbonate – rather than sulfate – AFm phases can further reduce porosity by stabilizing the volume of ettringite that has already formed. In addition, dilution of the cement clinker by a comparatively less reactive filler material reduces the volume of cement hydration products formed at a given age, leading to potential increases in capillary porosity.

Finally, more subtle decreases in the total volume of large pores can also be generated by improvements in particle packing arising from changes to particle size distributions of the cements themselves. It is therefore important to investigate how both the chemical and physical properties of portland limestone cements influence the microstructural development of PLC-based materials.

In this study, two techniques will be used to characterize microstructural development: nitrogen gas adsorption, which can be used to quantify pore size distributions and specific surface areas (SSA_{BET}) of hydration products, and backscattered electron (BSE) microscopy, which can be used to qualitatively compare the volumes of hydration product, porosity, and unhydrated cement present in the hydrating cement pastes at various ages. As with the chemical evolution study, cements only two of the five sources – A and C – were selected for further microstructural characterization. Although cements from source B had been selected to provide a lower bound for chemical evolution studies (having the lowest limestone contents and among the coarsest particle size distributions), the cements from source C were selected for further microstructural studies due to their more similar rates of reaction to the other cements investigated. Because cements from source C, like the cements from source B, had more similar particle size distributions to one another, it is hypothesized that they will show rates of microstructural development more indicative of dilution-dominated behavior. Meanwhile, the cements from source A, which were more distinctive in particle size distribution, are hypothesized to show rates of microstructural development indicative of filler- and nucleation-dominated behavior.

3.5.1 Nitrogen gas adsorption

Nitrogen gas adsorption and desorption were used to measure the porosity of the cement pastes over the first 14 days of hydration. Paste specimens were prepared from cements A, AL, C, and CL, at *w/b* = 0.40, using the mixing procedure described in Section 3.3, and stored at 25°C in doubly sealed plastic bags. After 1, 3, 7, and 14 days of hydration, fragments of paste were removed from each specimen and crushed until they were 0.595-1.00 mm in size (passing No. 18 sieve and retained on No. 30 sieve). The crushed fragments were submerged in liquid nitrogen for 15 min to stop hydration, then freeze-dried at -48°C and 0.02 mbar pressure for 48 hr to sublimate the frozen pore water.

Approximately 1.5 g of crushed material was analyzed in a Micromeritics ASAP 2020 specific surface area gas analyzer. Specimens were degassed at 10 μmHg pressure and 105°C for 12 hr prior to analysis. Analysis was performed at 77 K (-196°C) using nitrogen gas adsorbate over a relative pressures range of 0.01 to 0.99. Specific surface area was determined by Brunauer, Emmett, Teller (BET) theory [78] using the adsorption isotherm between relative pressures of 0.05 and 0.30. Pore size distributions, total pore volume, and average pore diameter were determined using the Barrett, Joyner, Halenda (BJH) method [79] on data obtained from the desorption isotherm [80].

The evolutions of specific surface area, pore size, and pore volumes are shown in Figure 3.17 and Figure 3.18 for cement pastes A and AL and in Figure 3.19 and Figure 3.20 for cement pastes C and CL. Pore volumes are separated into small mesopores, having diameters between 1-10 nm, and large mesopores, having diameters 10-50 nm. The large mesopores primarily control transport properties and early-age shrinkage at high internal relative humidities (> 80%), while the small mesopores primarily control

long-term creep and early-age shrinkage behavior at lower relative humidities (50-80%) [40]. The durability implications of pores in each size range will be discussed in further detail in Chapters 4, 7, and 8, but in general, greater volumes of pores 10 nm and larger in diameter will increase early-age autogenous deformation (Chapter 4) and later-age permeability (Chapter 7), while greater volumes of pores in both size ranges can lead to increased crystallization pressures and physical salt attack-induced damages (Chapter 8).

For the cement pastes from source A, it was observed that the BET specific surface areas (SSA_{BET}) of both pastes (Figure 3.17a) increased slightly with hydration age, concurrent with a slight decrease in their average pore size (Figure 3.17b). The increase in SSA_{BET} and decrease in average pore size both indicate more complex microstructural evolution as a result of ongoing cement hydration. Comparing the two cement pastes to one another, it can be seen that for the first 7 days of hydration, cement paste AL has a larger volume of both small and large mesopores than its Type I/II companion (Figure 3.18), but with ongoing hydration, the total volumes of small and large mesopores both decrease for the Type IL paste to a greater extent than they do for the Type I/II paste. Such changes in pore size are likely due to the filler and nucleation effects arising from the finely ground limestone inclusion. The denser pore structures of the Type IL cement paste beyond 7 days suggest that materials made from the finely ground cement AL will experience reduced permeability and less shrinkage at later ages, although permeability and shrinkage may both be higher during the first 7 days, when the controlling pore volumes are greater.

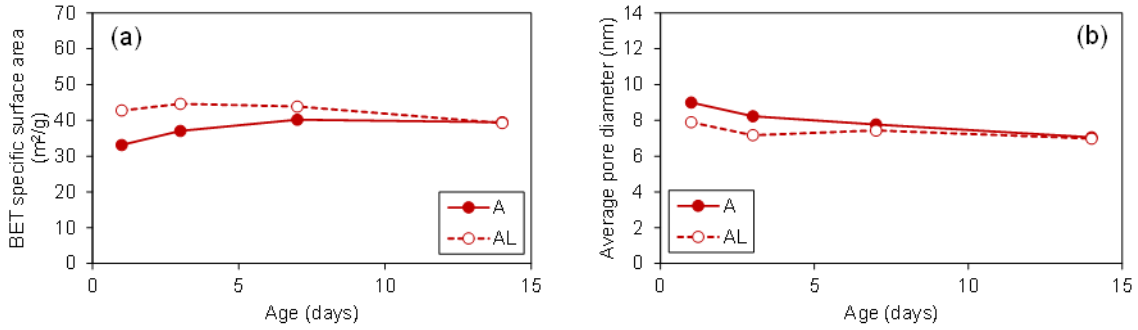

Figure 3.17 (a) BET specific surface area and (b) average pore size for pastes A and AL.

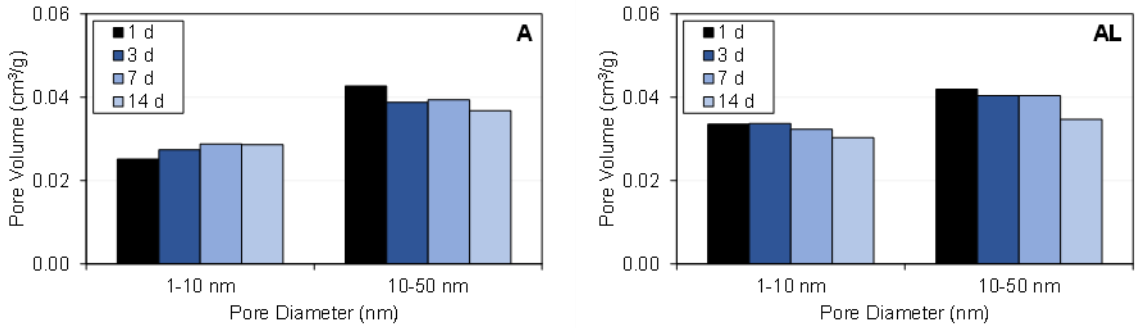

Figure 3.18 Capillary porosity in small (1-10 nm) and large (10-50 nm) mesopore size ranges for cement pastes A and AL.

Looking at the cement pastes from source C, it was likewise observed that the SSA_{BET} of both pastes (Figure 3.19a) increased with hydration age, concurrent with a decrease in their average pore size (Figure 3.19b), again indicative of more complex microstructural evolution with time. Comparing the two cement pastes to one another, it was found that despite having lower initial hydration rates as a consequence of its coarser mean particle size, the Type IL cement paste had a higher SSA_{BET} than its Type I/II counterpart at all ages investigated. Two possible effects could explain this increase in surface area: (1) the increase in the surface area of the binder by the incorporation of the less dense limestone, or (2) the more refined microstructure occurring as a result of

improved particle packing (filler effect). While an increase in specific surface area by the limestone filler *could* increase SSA_{BET} measurements in the paste, the effect is not expected to be on the same scale as the differences observed, as the binder was found by laser diffraction to have specific surface area two orders of magnitude smaller than the specific surface area of the cement paste. The second possibility – further refinement of the porosity as a consequence of filler effects – is more likely the source for the increased specific surface area of the Type IL paste, and has been observed in past studies by Jayapalan and others [26] to occur in cement pastes containing blended limestone filler.

The influence of the filler effect on the microstructural development of cement paste CL is further illustrated by the BJH pore volumes shown in Figure 3.20. As hydration continues, the volume of pores between 1-10 nm in diameter increases substantially for the Type IL cement paste, and even exceeds the volume of pores in that size range for the Type I/II paste. At the same time, the volume of pores 10-50 nm in diameter remains approximately constant with time, suggesting that although some of the capillary pores are being reduced in size by ongoing hydration, much of the pore refinement is occurring in pores already smaller than 10 nm in diameter. It is therefore hypothesized that the Type IL cement paste from source C will undergo more early-age shrinkage than its Type I/II counterpart owing to its larger volume of small mesopores, and that it will also have slightly greater permeability at later ages as a result of its larger relative volume of large mesopores. These predictions will be re-evaluated in Chapters 4 and 7.

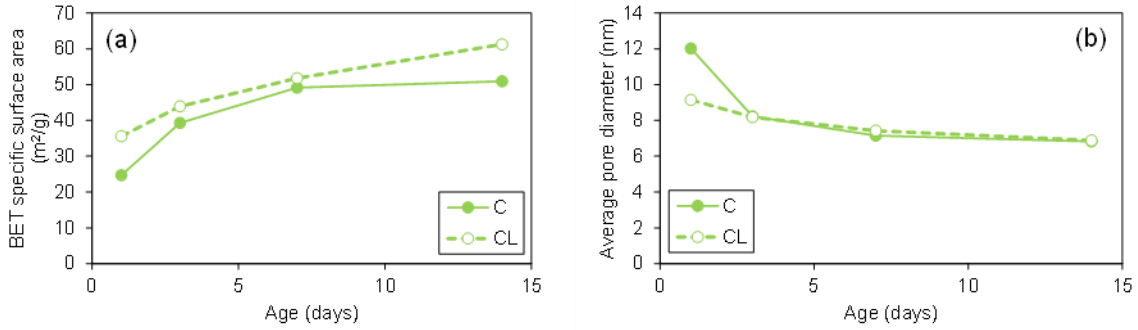

Figure 3.19 (a) BET specific surface area and (b) average pore size for pastes C and CL.

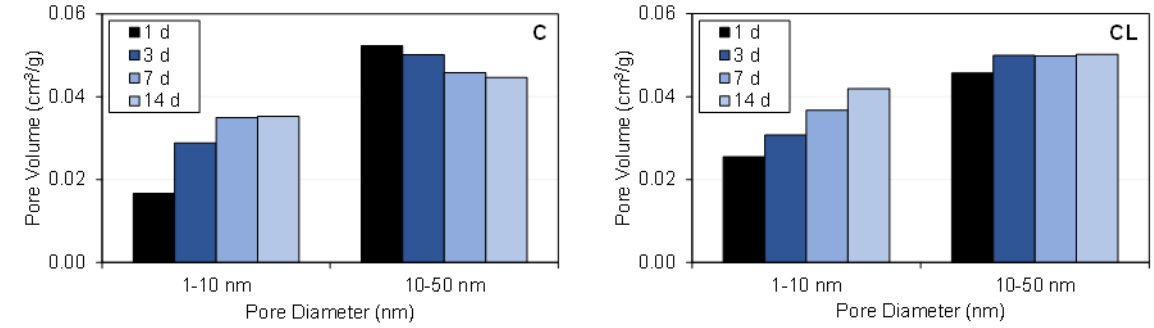

Figure 3.20 Capillary porosity in small (1-10 nm) and large (10-50 nm) mesopore size ranges for cement pastes C and CL.

3.5.2 Electron microscopy

Cement paste microstructure was also qualitatively investigated using variable pressure scanning electron microscopy (VP-SEM) with backscattered electrons. VP-SEM was selected instead of traditional low-pressure SEM because it can be used on non-conductive materials like cement paste without requiring the application of a conductive surface coating [81].

Paste specimens were prepared again from cements A, AL, C, and CL, at *w/b* = 0.40, using the mixing procedure described in Section 3.3. Prismatic bars with a 1" square cross-section were cast for each paste and cured in a bath of saturated limewater at 25°C until the designated testing age. After 1 and 7 days of hydration, a section

measuring approximately 5 mm in thickness was cut from each of the bars using an isopropanol cooled diamond saw at 30 rpm. Debris was gently removed from the cut surfaces by ultrasonically cleaning in isopropanol for 30 seconds. The cut samples were submerged isopropanol for 48 hr to halt hydration [81], then stored under vacuum for an additional 24 hr to allow the isopropanol vapors to evaporate. The degassed sections were impregnated in epoxy, cured for 24 hr, then ground with successively finer grits of silicon carbide paper (220, 320, and 600 grit) and polished with successively finer diamond suspensions (6, 3, 1, and 0.25 μm). Samples were ultrasonically cleaned in an isopropanol bath for 30 seconds in between sizes. The polished sections were analyzed using a Hitachi S-3700N VP-SEM with a 15 kV accelerating voltage and 30 Pa chamber pressure. Backscattered electron (BSE) images were acquired at 200×, 500×, and 1000× magnification. Specimens were stored under vacuum when not being analyzed to prevent contamination of the surface by carbonation or moisture.

The SEM images acquired for cements A and AL are shown in Figure 3.21 through Figure 3.23, at 200×, 500×, and 1000× magnification, respectively. The images for cements C and CL are shown at the same respective magnifications in Figure 3.24 through Figure 3.26. The backscattered electron intensities are related to the atomic number of the atoms in the sample, which allows for easy visual identification of the basic components of the hydrated cement paste: unhydrated cement grains appear as the brightest gray phases, hydration products (primarily C-S-H and CH) appear in dark and medium shades of gray, and porosity appears in black [81-83].

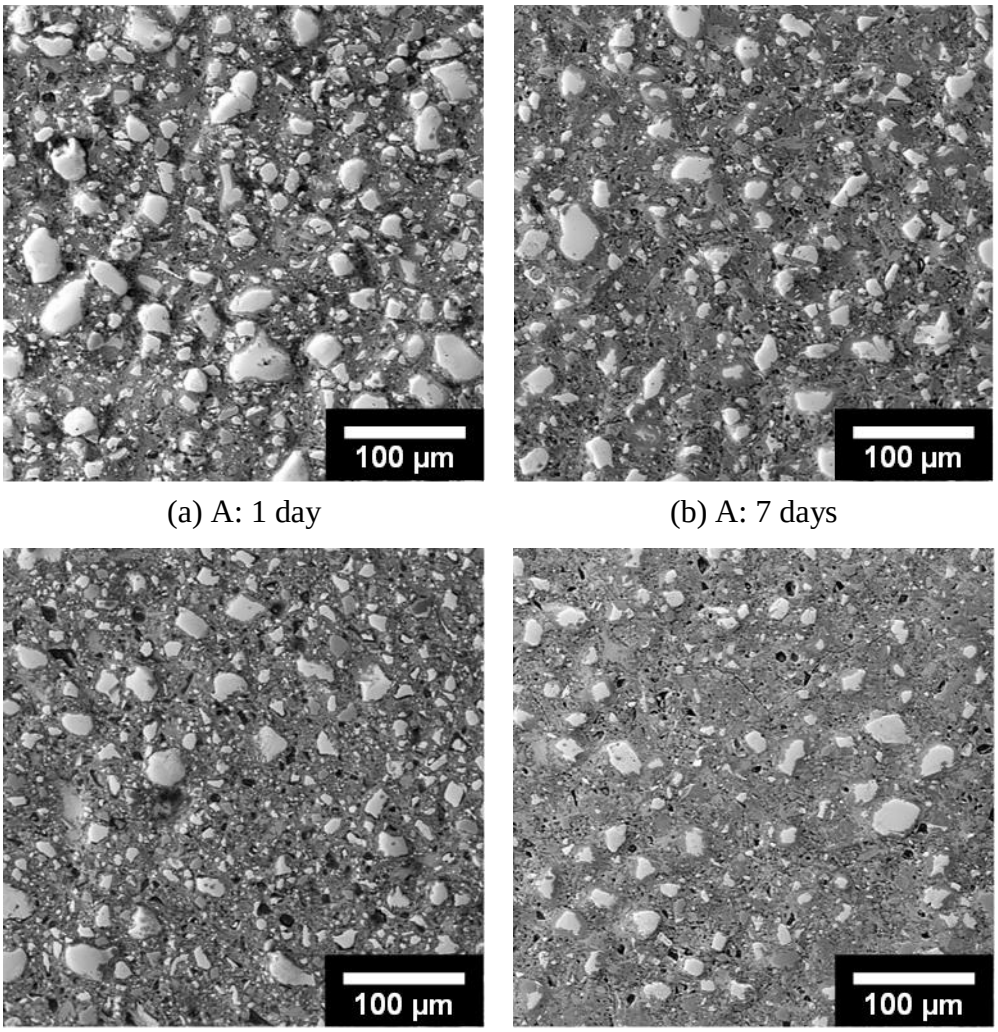

(a) A: 1 day (b) A: 7 days

(c) AL: 1 day (d) AL: 7 days

Figure 3.21. BSE images for cement pastes A and AL at 200× magnification.

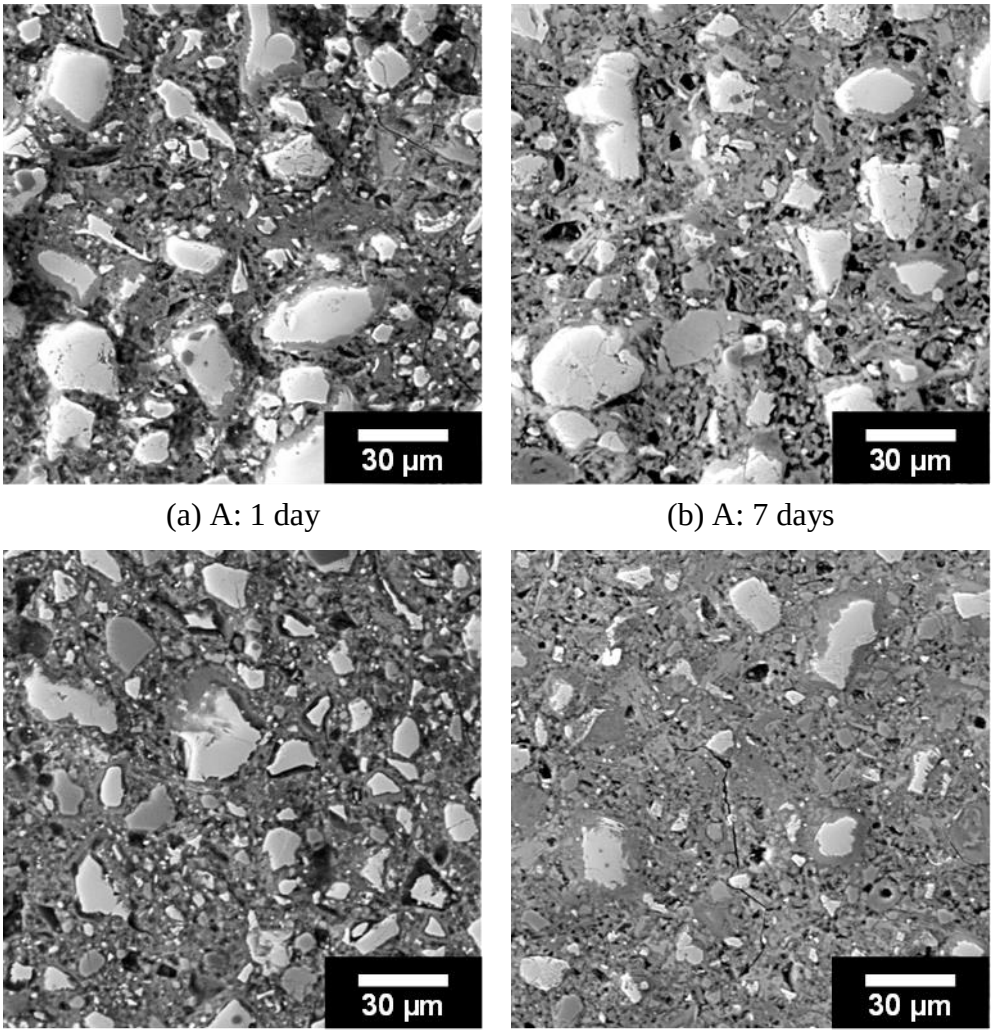

(a) A: 1 day (b) A: 7 days

(c) AL: 1 day (d) AL: 7 days

Figure 3.22. BSE images for cement pastes A and AL at 500× magnification.

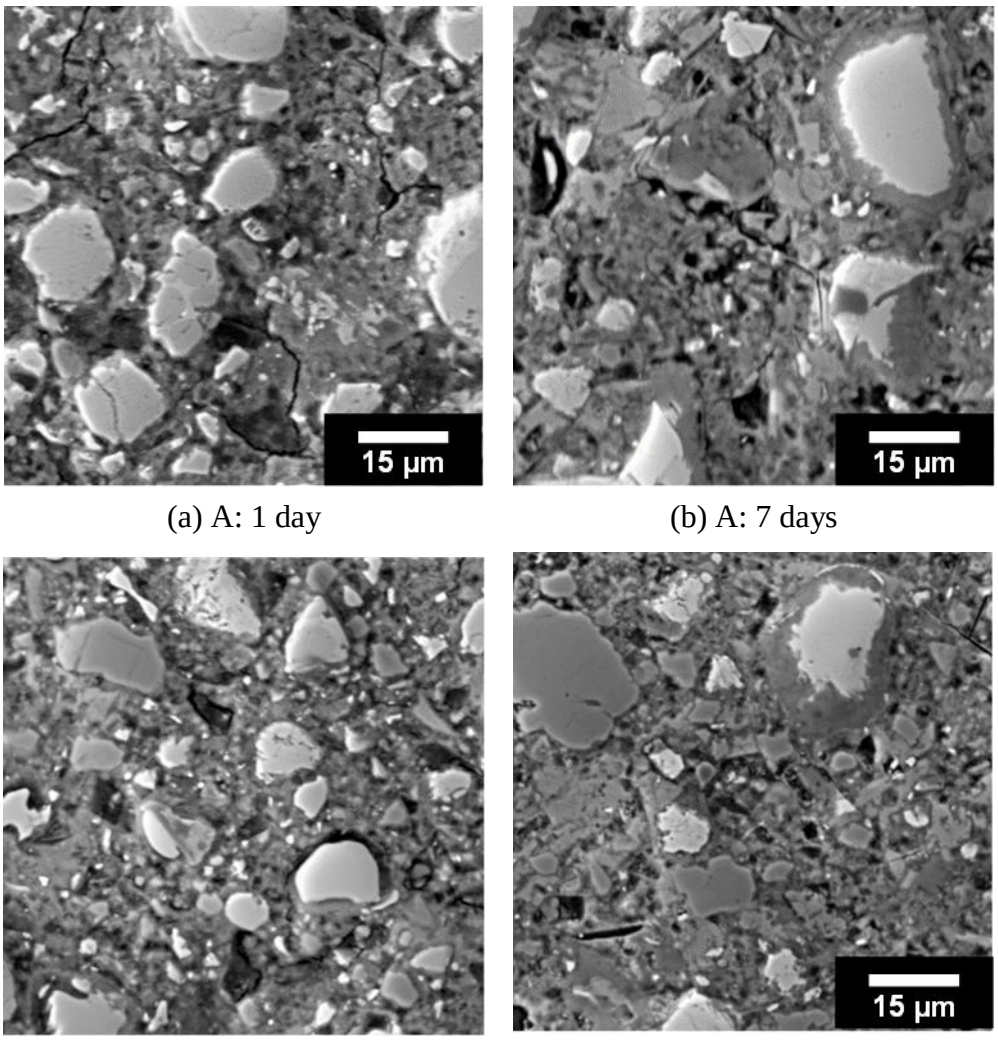

(a) A: 1 day (b) A: 7 days

(c) AL: 1 day (d) AL: 7 days

Figure 3.23. BSE images for cement pastes A and AL at 1000× magnification.

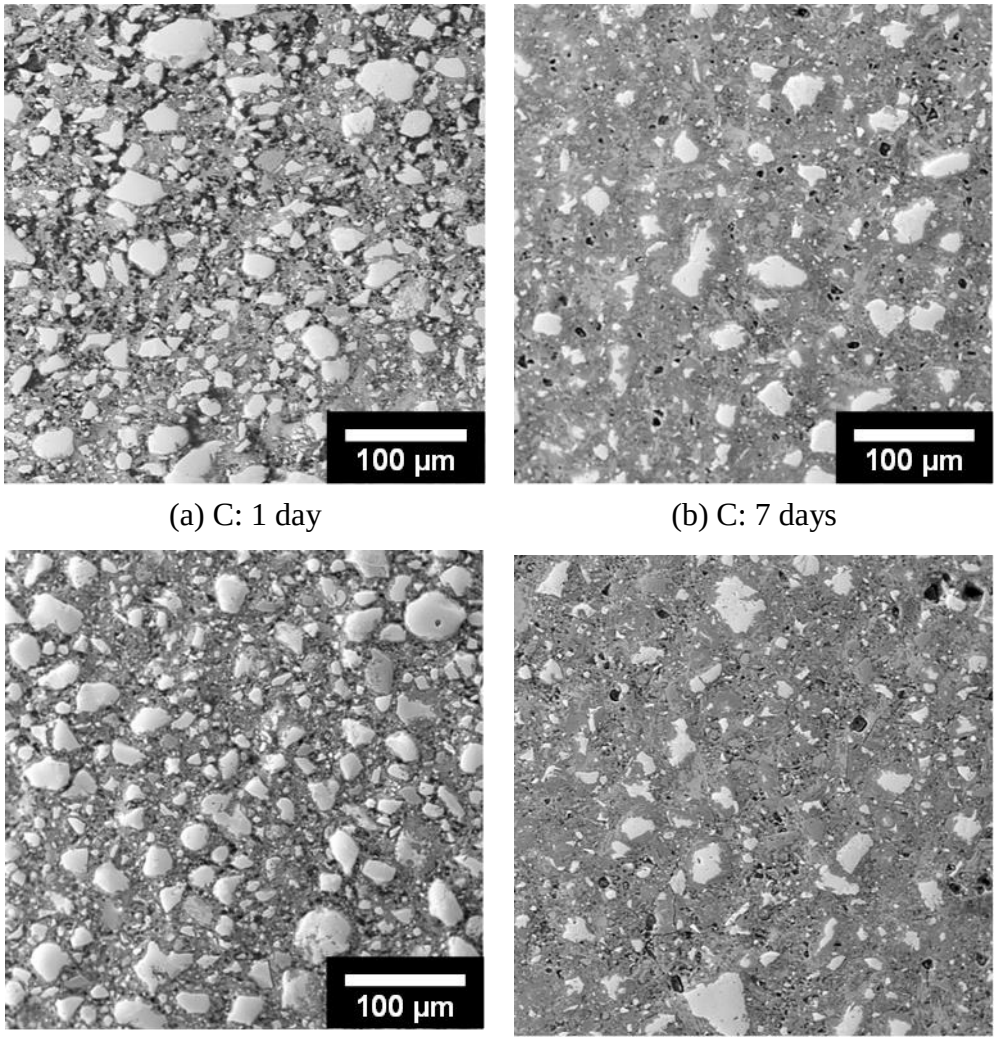

(a) C: 1 day (b) C: 7 days

(c) CL: 1 day (d) CL: 7 days

Figure 3.24. BSE images for cement pastes C and CL at 200× magnification.

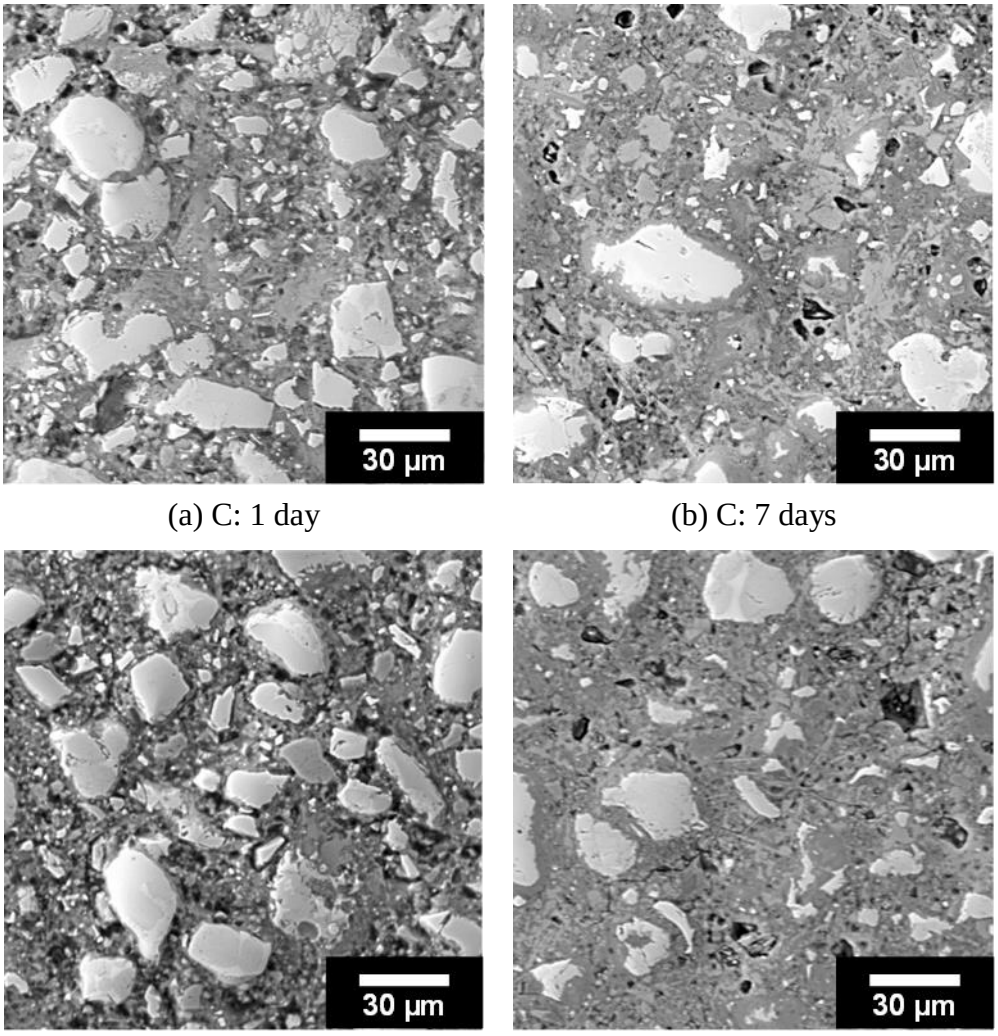

(a) C: 1 day (b) C: 7 days

(c) CL: 1 day (d) CL: 7 days

Figure 3.25. BSE images for cement pastes C and CL at 500× magnification.

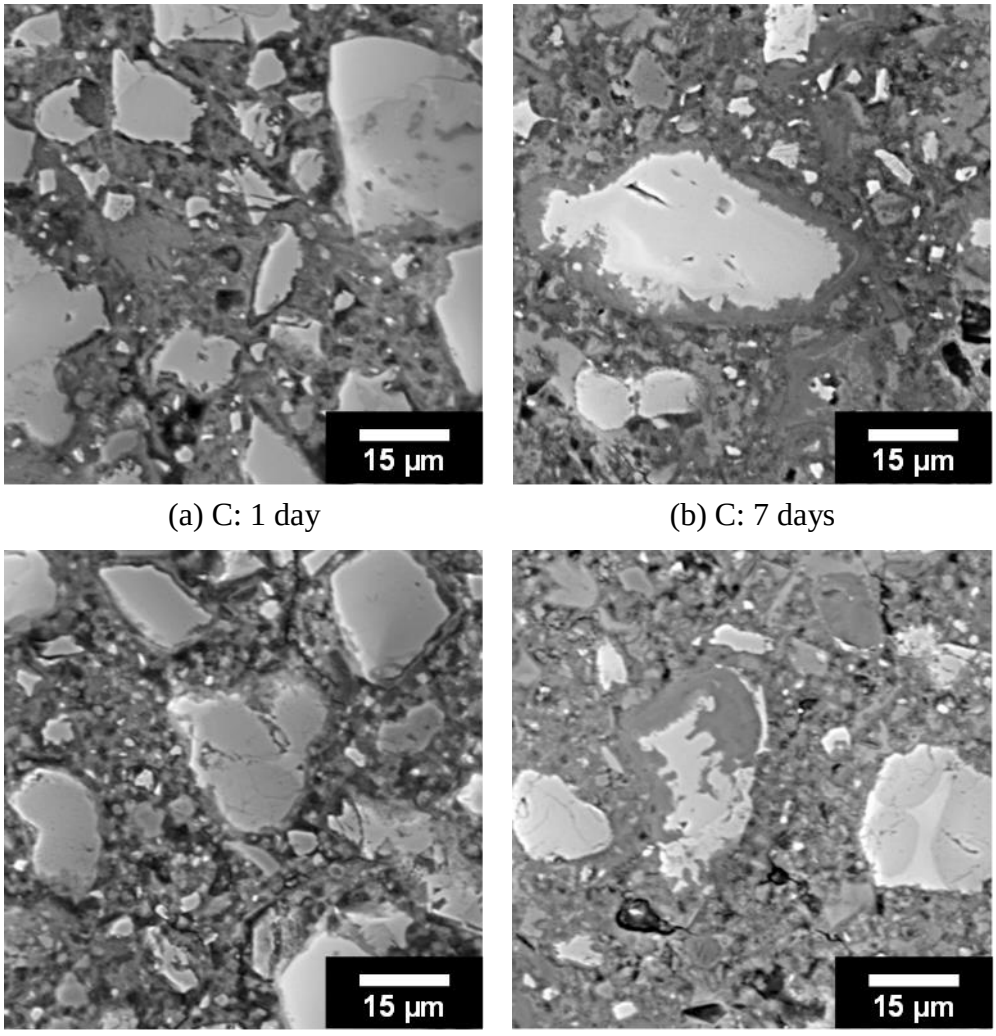

(a) C: 1 day (b) C: 7 days

(c) CL: 1 day (d) CL: 7 days

Figure 3.26. BSE images for cement pastes C and CL at 1000× magnification.

At the coarsest magnification, the differences between the degrees of hydration for the Type I/II and Type IL cement pastes are readily apparent. After 1 day of hydration, cement paste A appears to have slightly more unhydrated cement and a similar porosity to cement paste AL (Figure 3.21), which is consistent with the degrees of hydration (47% and 55%) and total nitrogen-accessible pore volumes (0.095 and 0.103 cm^3/g) measured by isothermal calorimetry and nitrogen gas adsorption, respectively. At 1 day, cement paste AL also appears to have smaller unhydrated cement grains than

cement paste A, which could be due to the greater degree of hydration, but is more likely the result of the finer particle size distribution of cement AL. By 7 days of hydration, both cement pastes show further reductions in the amounts of unhydrated cement and porosity, as would be expected given their continued hydration and microstructural development. Comparing the two cement pastes to one another, it is clearly evident from the SEM images that cement paste AL contains less unhydrated cement than cement paste A, which is again consistent with previous measurements from isothermal calorimetry (68% and 78% degrees of hydration).

Cement pastes C and CL, by comparison, show far more similar BSE images to one another at 200× magnification (Figure 3.24). At 1 day, there is visually little difference between the two cement pastes in terms of the quantity and size of unhydrated cement grains observed, consistent with the more similar 48% and 51% degrees of hydration (C and CL, respectively) and the nearly identical particle size distributions measured previously. Cement paste C appears to have greater porosity than cement paste CL, but at higher magnification levels, it is evident that much of the perceived increase in porosity is due to relief damage from polishing through the weaker hydrate phases [81, 83], rather than to true differences in porosity. At 7 days, there are again similar proportions of unhydrated cement grains observed for cement pastes C and CL (consistent with the measured 74% and 78% degrees of hydration, respectively), but it appears as though cement paste CL contains slightly more porosity than cement paste C. No significant relief damage was observed in the polished sections of cement pastes C and CL, suggesting that the observed differences in porosity are reflective of true

differences in microstructural development. The measured nitrogen-accessible pore volumes of 0.109 cm^3/g and 0.128 cm^3/g, respectively, further support these observations.

At 500× and 1000× magnification, the role of clinker particle size on cement hydration can be observed. At 1 day, most of the unhydrated cement particles were measured to be about 5 μm or larger, implying that clinker particles smaller than 5 μm can fully hydrate within 24 hr. These fully hydrated cement grains contribute to the bulk hydration product matrix surrounding the unhydrated cement particles and provide most of the initial microstructure for the paste [82]. The rest of the microstructure in the 1 day old pastes is provided by the hydration products emanating out from the surfaces of the larger cement grains; although the interiors of the grains remain unhydrated, most of the large particles are surrounded by thin shells of outer hydration product, which can be observed for some of the particles at 1000× magnification. By 7 days, hydration of the larger cement grains moves inward, as demonstrated by the formation of a 3-5 μm thick ring of "inner-product" C-S-H around the interior edges of the particles. Hydration will continue to progress inward for these larger grains, but may never fully reach completion due to their large size.

In the context of PLC-based materials, the observations made at 500× and 1000× magnification suggest that it is not only the relative size of the limestone particles in the PLC but also the relative size of the *clinker* particles which can have a significant impact on degree of hydration and microstructural development. Prior research has demonstrated that when limestone and clinker are interground to produce Type IL cement, the limestone will be ground to a finer particle size than the clinker due to its relative softness [23, 84]. Therefore, if a Type I/II and a Type IL cement have similar overall particle size

distributions to one another (e.g., cements from sources B and C), then the Type IL cement will have coarser clinker particles than the Type I/II cement, and will consequently hydrate more slowly due to the larger clinker size. Thus, Type IL cements ground to similar particle size distributions as their Type I/II counterparts will not only experience reduced hydration product volumes and increased porosities as a consequence of the dilution effect, but will also experience further reductions in hydration rate due to the larger size of the clinker particles [84]. Such an effect is suggested visually by the BSE images for cement paste CL (Figure 3.25) and was observed by TGA for cement paste BL.

If, on the other hand, the Type IL cement is ground to a much finer particle size distribution than the Type I/II cement in order to compensate for the size-induced reductions in hydration rate, it is possible that the clinker portion of the cement will have finer particle size in the Type IL cement than it does in the Type I/II cement. Such an effect can be demonstrated by considering cements A and AL. According to the particle size distributions shown in Figure 3.4, approximately 30% of cement A and 40% of cement AL are finer than 5 μm, the maximum particle size observed to fully hydrate within 24 hr. Since the fine limestone replacement in the Type IL cement can account for at most 8% of that 10% difference, cement AL must also contain a higher fraction of finely ground clinker due to the intergrinding process used to combine the limestone with the clinker. As a result, the clinker fraction of cement paste AL would be expected to hydrate more fully, contributing – in part – to the greater degree of hydration and denser hydration product matrix observed during the first 24 hr. (Heterogeneous nucleation,

improved particle packing, and formation of carboaluminate phases contribute to the additional increases in degree of hydration and hydration product volume.)

3.6 Conclusions

This chapter investigated the early-age hydration and chemical and microstructural evolutions of eleven commercially produced Type I/II and Type IL cement pastes. The results demonstrated that finely ground Type IL cements promote the nucleation of hydration products (especially CH) and accelerate hydration within the first few hours of mixing, which, in turn, lead to finer microstructures at the earliest ages of hydration. Coarsely ground Type IL cements were also shown to experience nucleation effects at very early ages due to their increased specific surface area, but these effects were largely overcome by more the dominant dilution effects and slower clinker hydration rates within only a few hours of hydration. The dilution effects and coarser clinker sizes were shown to decrease the rate of hydration, leading to lower hydration product volumes and increased porosities, especially at later ages (beyond 7 days). Such dilution behavior was observed to dominate the hydration and microstructural development of both the coarsely ground and the finely ground cements after the first 3-7 days of hydration.

The research further demonstrated that limestone is not simply an inert filler, and, in addition to altering hydration and microstructural development through physical means, it also has a significant impact on chemical evolution. In particular, it was demonstrated that even small substitutions of limestone (< 5% by mass) can result in the formation of carbonate AFm phases and the indirect stabilization of ettringite. When

limestone was not present, as for cement B, ettringite instead was converted into sulfate AFm (monosulfate) and no carbonate AFm phases were detected. While these changes to chemical evolution were not found to have a significant impact on microstructural development as measured by nitrogen adsorption, they could still have a significant impact on other durability-related phenomena such as chemical shrinkage. The implications of these altered chemical and microstructural development rates for early-age shrinkage will be investigated in the next chapter.

CHAPTER 4

EARLY-AGE HYDRATION: IMPLICATIONS FOR CHEMICAL AND AUTOGENOUS SHRINKAGE

4.1 Introduction

Changes to cement hydration and microstructural development have important implications for the early-age shrinkage of cement-based materials. Two types of shrinkage – chemical and autogenous – are considered in this chapter. Chemical shrinkage, as described in Chapter 2, is the volumetric contraction of the cement paste caused by the relative differences in volume between the original cement and water system and the resulting hydration products. Upon complete hydration (α = 100%), a typical portland cement paste will contract by about 7% of its original volume due chemical shrinkage [2]. Partial replacement of the cement with an inert filler can reduce the total amount of chemical shrinkage experienced by the paste at a rate roughly proportional to the dilution of the cement volume, provided that no other chemical or physical effects occur. However, when fine, partially reactive fillers such as limestone are used, the amount of chemical shrinkage experienced at a particular age (or degree of hydration) can actually increase as a function of the chemistry, dosage rate, and fineness of the filler. For example, since chemical shrinkage is a direct consequence of cement hydration, an increase in hydration rate due to nucleation effects should also increase the rate of chemical shrinkage experienced by the paste.

A second type of early-age shrinkage that depends on the rates of hydration and microstructural development in portland cement pastes is autogenous, or self-desiccation,

shrinkage. Autogenous shrinkage is the volumetric contraction of the cement paste generated by the consumption of capillary pore water during hydration.[7] Contraction of the cement paste matrix is directly a function of the internal relative humidity (RH) of the paste (Equation 4.1) inversely a function of the size of the pores being emptied (Equation 4.2) [40]:

$$p_{cap} = \frac{\ln(RH)}{K} \tag{4.1}$$

$$p_{cap} = \frac{2\gamma \cos(\theta)}{r} \tag{4.2}$$

where p_{cap} is the tensile pressure generated in the capillary pores, γ is the surface energy of the pore solution, θ is the contact angle between the pore solution and the pore walls, r is the radius of the pore being emptied, and K is a constant related to temperature and the molar volume of the pore solution. Based on equations 4.1 and 4.2, it is proposed that cement pastes with more rapid rates of reaction (i.e., more rapid rates of water consumption) and with finer porosities will experience greater amounts of autogenous deformation at early ages. In the context of Type IL cements, this implies that pastes of the more finely ground Type IL cements, whose hydration and microstructural development are dominated by nucleation effects, are more likely to undergo increased autogenous deformation at early ages.

[7] Autogenous shrinkage is a special case of a more general type of shrinkage called "drying shrinkage," which is caused by a loss of pore water within the paste. Practically, drying shrinkage and autogenous shrinkage are differentiated from one another by the mechanism by which pore water is lost: traditionally, drying shrinkage considers water lost both physically to evaporation and chemically to ongoing hydration, while autogenous shrinkage considers only water lost chemically to ongoing hydration. Since this research is primarily concerned with hydration mechanisms, only the autogenous form of drying shrinkage is considered in this dissertation.

Since it was established in Chapter 3 that limestone inclusions alter the rates of hydration and microstructural development in PLC-based materials, it is important to consider the implications of such changes on early-age shrinkage and cracking potential. To that end, this chapter investigates the relative influences of limestone addition rate and cement fineness on the early-age chemical and autogenous shrinkage of portland limestone cement pastes. The two shrinkage mechanisms are first analyzed separately, to isolate differences arising from changes to hydration rate and microstructural evolution, and then compared to one another, to determine which physical and chemical properties, if any, are strong predictors of early-age shrinkage. Finally, the experimentally measured chemical shrinkage is compared to theoretical predictions obtained from the model of Powers and Brownyard [33] to determine if traditional models for cement hydration and early-age shrinkage can still be used to predict early-age behavior of cement pastes containing limestone substitutions of up to 15%, by mass.

4.2 Materials and methods

Cement pastes with w/b = 0.40 were prepared from each of the eleven commercially produced cements discussed in Chapter 3, where again the mass of the binder was taken to be the mass of the cement as received, including interground limestone. The mixing procedure consisted of manual stirring of the cement in deionized water for 30 s, followed by mechanical mixing of the paste mixture with a 5-speed hand mixer at low speed for 60 s and at medium speed for 60 s. Specimens were cast immediately after mixing and hydrated in their respective environments at 25°C.

Chemical shrinkage was measured by dilatometry according to ASTM C1608 [85]. 9.5 ± 0.5 g of paste was added to each of at least three glass vials, which were then filled with de-aerated deionized water and capped with a rubber stopper fitted with a capillary pipette. A colored droplet of hydraulic oil was added to the top of each pipette, so that the change in water volume over time, which indicated the amount of chemical shrinkage in the paste, could be easily monitored. The capped vials were placed into a water bath maintained at 25°C, and measurements were recorded at 30 minute intervals for 7 days, using an automated camera acquisition system as shown in Figure 4.1. For each set of tests performed, one additional set of empty vials – containing only de-aerated deionized water – was also placed into the water bath to measure incidental volume changes due to evaporation of water from the capillary tubes; the average evaporation-induced volume change at each sampling age was subtracted from the raw testing data prior to analysis.

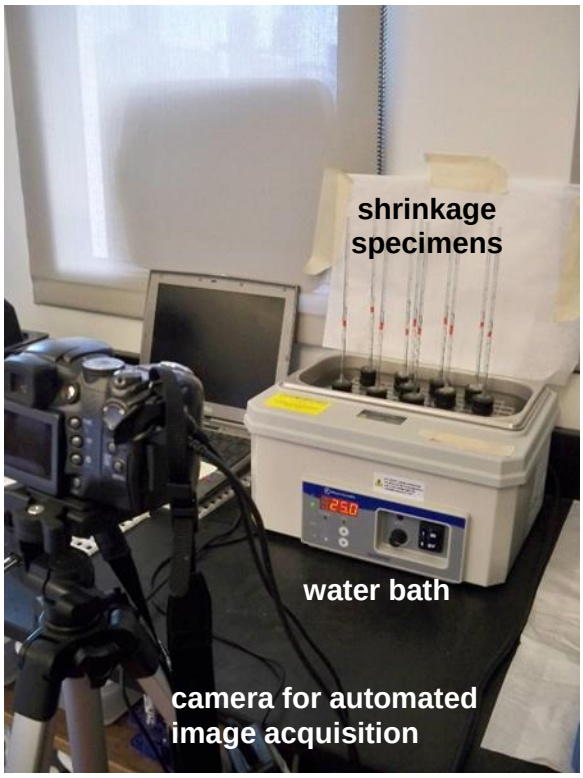

Figure 4.1 Experimental set-up used for chemical shrinkage test. Shrinkage was monitored by tracking the heights of red oil droplets atop the water within the capillary pipettes. Image acquisition software was used to automatically record images at 30 min intervals.

Autogenous shrinkage was measured for each cement paste in accordance with ASTM C1698 [86]. Three specimens were cast for each mixture in corrugated tube molds and stored in their sealed conditions in an environmental chamber at 25°C. The length change of each sample was measured by dilatometry, as shown in Figure 4.2, from the time of final setting to an age of 56 days. The time of final setting was determined by penetration of a Vicat needle in accordance with ASTM C191 [87]. Measurements of autogenous deformation were taken every 2 hr for the first 6 hr, once daily until 7 days, bi-weekly until 28 days, and then weekly until 56 days.

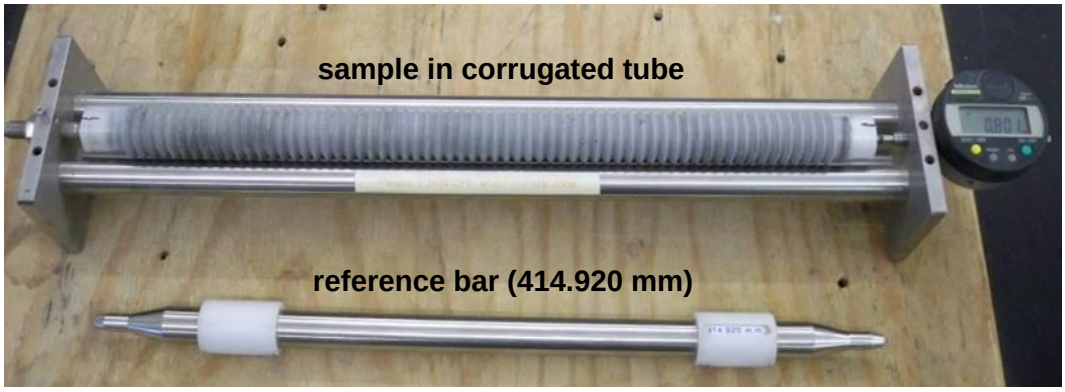

Figure 4.2 Autogenous deformation measured on a corrugated tube specimen, in accordance with ASTM C1698.

4.3 Experimental results

4.3.1 Chemical shrinkage

The results of the chemical shrinkage test, in units of mL shrinkage per g binder, are presented in Figure 4.3. For clarity, error bars are not shown, but the average coefficient of variation over the 7 day testing period was less than 5% for each of the pastes examined.

The chemical shrinkage results showed behavior consistent with heat of hydration (Figure 3.6), in which the more finely ground Type IL cements from sources A, D, and E exhibited greater amounts of chemical shrinkage relative to their Type I/II counterparts, while the more coarsely ground Type IL cements from sources B and C exhibited lesser amounts of chemical shrinkage relative to their Type I/II counterparts. Intuitively, this makes sense, as an increase in hydration rate would imply an increase in the rate of hydration product formation and, by extension, an increase in the rate of volume loss (due to chemical shrinkage), as well. Therefore, it is not surprising that the four cements that exhibited nucleation-dominated behavior in calorimetric studies also exhibited a higher degree of chemical shrinkage during that period [88]. Neither is it surprising that the two

Type IL cements that exhibited dilution-dominated hydration behavior (cements BL and CL) also exhibited a lower degree of chemical shrinkage than their Type I/II counterparts, since the reduction in reactive material implies a reduction in the relative volume of hydration product and therefore a reduction in chemical shrinkage, as well.

Interestingly, although the trends in chemical shrinkage were generally consistent with what was observed through isothermal calorimetry, the relative magnitudes of chemical shrinkage were not as significantly different between Type I/II and Type IL cement pastes as were the relative magnitudes of cumulative heat. In particular, it was observed that at 7 days the cumulative heats of hydration for cement pastes BL and CL were approximately 6% lower than for their companion cement pastes, while the chemical shrinkages for the same two cement pastes were only 2% lower than their Type I/II counterparts. Such a result suggests that the limestone addition may have a greater impact on chemical shrinkage than it does on heat of hydration, which has important implications, for example, for the prediction of chemical shrinkage of Type IL cements by Powers' model.

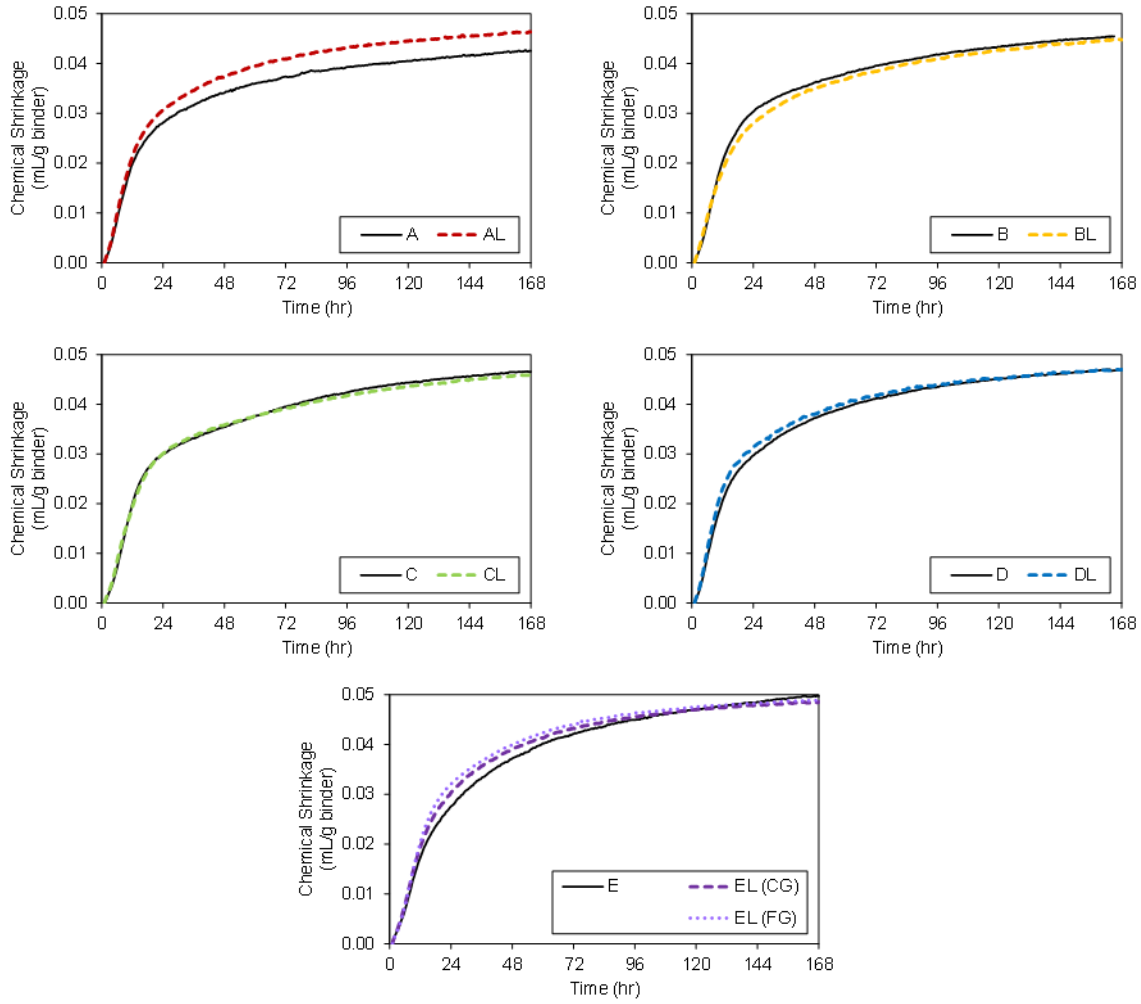

Figure 4.3 Chemical shrinkage measured, in mL/g binder, for cement pastes A-E at *w/b* = 0.40 and 25°C for 7 days (168 hr).

4.3.2 Autogenous shrinkage

The autogenous shrinkage results (Figure 4.4) also indicate that the more finely ground Type IL cements (from sources A, D, and E) tend to experience greater degrees of autogenous shrinkage when compared to Type I/II cements of the same clinker composition. Linear strains were increased by as much as 200 μm/m by 56 days for cement pastes AL, DL and EL, suggesting that the more refined microstructures (Section 3.5) and more rapid rates of hydration (Section 3.4) for the finely ground Type IL cement

pastes result in greater contractions than would be expected for conventional Type I/II cement pastes at the same age.

For the cements from sources B and C, the autogenous deformation of the more coarsely ground Type IL cement pastes was lower in magnitude than the autogenous deformation of the Type I/II companion pastes through the first 7 days of hydration. According to Equation 4.1 and 4.2, these lower magnitudes of autogenous shrinkage can be attributed to the slower rates of hydration and larger porosities for these pastes [41], as were observed in Chapter 3.

After 7 days of hydration, however, although the autogenous deformation of cement paste CL continued to be of lower magnitude compared to its Type I/II counterpart, the autogenous deformation of cement paste BL was found to increase in magnitude relative to its Type I/II counterpart. The cements from sources B and C had nearly identical particle size parameters to one another (Table 3.4), so the differences between the autogenous deformations of the two Type IL cements suggest that particle size alone is not a suitable predictor for autogenous deformation. Rather, the results suggest that significant hydration and microstructural changes are still occurring in cement paste BL due to primary (AFt-producing) and secondary (AFm-producing) reactions of the more slowly hydrating C_4AF phase, which was previously proposed to alter later-age chemical and microstructural evolution (Sections 3.4 and 3.5) for cement paste BL. Thus, it cannot be predicted on the basis of particle size alone whether a Type IL cement will be more or less susceptible to autogenous deformation compared to a traditional Type I/II cement – both chemical and physical properties must be considered.

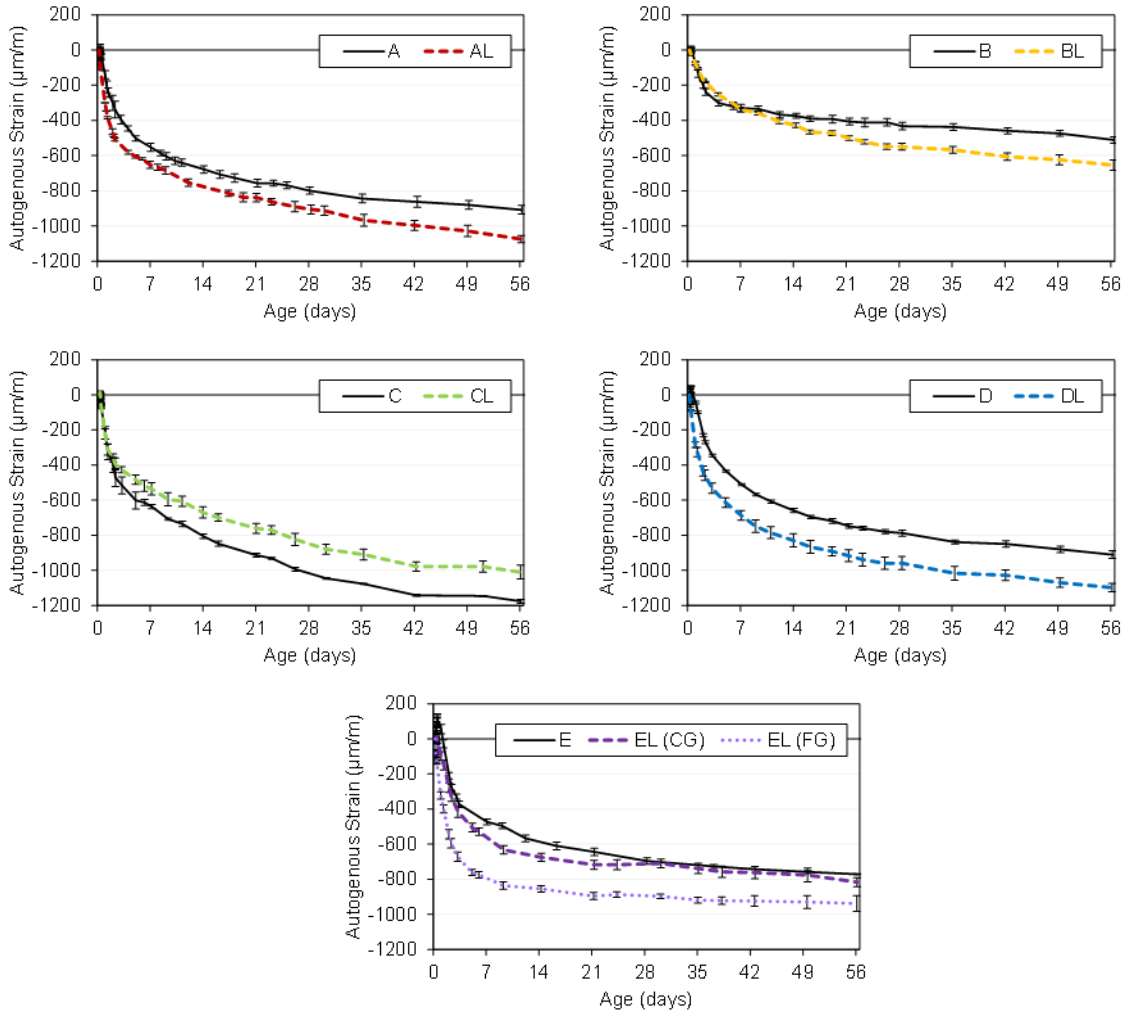

Figure 4.4 Autogenous deformation of cement pastes A-E at 25°C with *w/b* = 0.40.

4.3.3 Examining correlations to composition and particle size

In order to better understand which specific compositional and size parameters most affect the early-age shrinkage of Type IL cement paste systems, the compositions and particle sizes of the eleven cements were correlated to the measured chemical and autogenous shrinkage responses. As in Chapter 3, all eleven cements were included in the analysis, with no distinctions made between Type I/II and Type IL cements due to limited sample sizes in each classification. The parameters and responses considered are listed in

Table 4.1. Pearson correlation coefficients (ρ) were computed for each pair of variables to determine if an increase in parameter X was positively (or negatively) correlated with an increase in observed response Y. The statistical significance (p-value) of each correlation was assessed using a two-tailed t-test with n-2 = 9 degrees of freedom and a null hypothesis H_0: $\rho = 0$ (i.e., X and Y are not linearly correlated to one another). The test statistic t^* is given in Equation 4.3:

$$t^* = \frac{\rho\sqrt{n-2}}{\sqrt{1-\rho^2}} \tag{4.3}$$

A value $p < 0.10$ indicates moderately strong evidence of correlation, $p < 0.05$ indicates strong evidence of correlation, and $p < 0.01$ indicates very strong evidence of correlation. The results of the correlation study are shown in Table 4.2 (chemical properties) and Table 4.3 (physical properties).

Table 4.1. Parameters and response variables for shrinkage correlation study.

Parameter variable, *X*	**Response variable, *Y***
Limestone (LS) content of binder	Chemical shrinkage of paste
Clinker composition	(at 1, 2, 3, and 7 days)
Molar SO_3/Al_2O_3 and CO_2/Al_2O_3 of binder	Autogenous shrinkage of paste
SSA of binder	(at 1, 3, 7, 14, and 28 days)
$D_{3,2}$ of binder	
$D_{4,3}$ of binder	
D_{10} of binder	
D_{50} of binder	
D_{90} of binder	
Blaine fineness of binder	

Although chemical shrinkage appeared to follow similar trends as cumulative heat and degree of hydration in Chapter 3, the measured values for chemical shrinkage did not correlate significantly with any of the cement's physical parameters beyond the first 24 hr of hydration. During the first 24 hr, the relative "coarseness" of the cement (as evidenced

by a larger $D_{4,3}$ or D_{90}) was found to correlate with decreased chemical shrinkage, implying that more coarsely ground Type IL cements will exhibit less chemical shrinkage over the first 24 hr due to their comparatively slower rates of reaction. Beyond 24 hr, chemical shrinkage is more strongly influenced by the chemical composition of the clinker than by any direct contribution of the limestone itself. In particular, it can be observed that the two calcium silicate phases, C_3S and C_2S, are strongly correlated to chemical shrinkage by 7 days, which makes sense given that they comprise more than 70% of the clinker, by mass, and therefore contribute significantly to the total hydration product volume and chemical shrinkage of the paste (see Section 4.4.2). Additionally, it was found that C_3A content has its most significant impact on chemical shrinkage between 2 and 3 days of hydration, where it was previously determined that AFm phases begin to form (see Section 3.4). Such a correlation could point to the formation of AFm phases having a more pronounced effect on chemical shrinkage than on degree of hydration, since clinker composition was found to correlate to chemical shrinkage but not to degree of hydration at that age. However, such a correlation could also be an artifact caused by the small range of C_3A contents examined (1.5-5.0%), since it was also found that neither the CO_2/Al_2O_3 nor the SO_3/Al_2O_3 molar ratios – factors previously determined to predict the type of AFm products formed [20] – were significant predictors of chemical shrinkage at those early ages.

With respect to autogenous shrinkage, during the first 24 hr, strong correlations were found between the magnitude of autogenous shrinkage and the relative fineness of the cement. As was observed experimentally, an increase in cement fineness by almost any measure was either strongly or very strongly correlated to an increase in autogenous

deformation, likely due to the more rapid rates of hydration (decrease in internal RH) and decreased average pore size experienced by those cement pastes. Moreover, an increase in limestone content was also found to correlate with an increase in autogenous deformation over the first 24 hr, suggesting that the improved particle packing and generally smaller pore sizes (greater capillary stresses) of Type IL cements outweigh the effect of cement dilution when it comes to early-age autogenous deformation of PLC-based materials.

Beyond the first 24 hr, fineness effects again become less significant. An increase in the relative coarseness of the cement (as measured by $D_{4,3}$ and D_{90}) was once again found to reduce autogenous deformation, but the significance of the effect is only meaningful through the first 7-14 days of hydration. More meaningful for later-age autogenous deformation appears to be the C_4AF content of the cement. The correlation study seems to present strong evidence that later-age autogenous deformation is a function of the C_4AF content of the cement, with higher-C_4AF cements exhibiting lower amounts of autogenous deformation through 28 days of hydration; however, upon closer examination, it can also be shown that the C_4AF content is itself positively correlated to the mean particle size ($D_{4,3}$) of the cement ($p = 0.14$), suggesting that the influence of the C_4AF content may be confounded with the influence of the coarser particle size distribution. The slow reactivity of the C_4AF phase does likely contribute to a reduction in autogenous deformation at early ages, but since the similarly slowly reacting C_2S phase did not show any significant correlation to autogenous deformation, the effect is likely not as strong as the correlations presented here suggest. It was previously hypothesized that the increased autogenous deformation for cement BL at ages beyond 7

days is due to the slower reaction of the C_4AF, but in light of the correlation study it may additionally be proposed that cement pastes B and BL exhibited less overall autogenous shrinkage than the other nine cement pastes due to their coarser grind combined with their higher relative amounts of slowly-reacting clinker phases.

Table 4.2. Statistical significance (p-value) of correlations between chemical properties of Type I/II and Type IL cements and their early-age shrinkage response at 25°C with w/b = 0.4. Sign of correlation is indicated in parentheses. Highlight colors indicate strength of significance.

Parameter	Chemical shrinkage				Autogenous deformation				
	1 d	2 d	3 d	7 d	1 d	3 d	7 d	14 d	28 d
LS content	0.23 (+)	0.28 (+)	0.45 (-)	0.86 (-)	0.03 (+)	0.13 (+)	0.12 (+)	0.15 (+)	0.22 (+)
C_3S content	0.40 (+)	0.52 (+)	0.24 (+)	0.03 (+)	0.06 (-)	0.58 (-)	0.69 (-)	0.69 (-)	0.67 (-)
C_2S content	0.75 (+)	0.06 (+)	0.03 (+)	0.00 (+)	0.98 (+)	0.50 (-)	0.41 (-)	0.46 (-)	0.52 (-)
C_3A content	0.73 (+)	0.06 (+)	0.04 (+)	0.14 (+)	0.45 (-)	0.96 (-)	0.68 (+)	0.73 (+)	0.94 (-)
C_4AF content	0.44 (+)	0.11 (+)	0.11 (+)	0.43 (+)	0.31 (-)	0.04 (-)	0.02 (-)	0.02 (-)	0.05 (-)
SO_3/Al_2O_3	0.89 (+)	0.41 (+)	0.52 (+)	0.87 (+)	0.39 (+)	0.52 (+)	0.44 (+)	0.51 (+)	0.59 (+)
CO_2/Al_2O_3	0.19 (+)	0.21 (+)	0.35 (+)	0.78 (+)	0.03 (+)	0.11 (+)	0.10 (+)	0.14 (+)	0.23 (+)

Legend:		$p < 0.01$
		$0.01 < p \leq 0.05$
		$0.05 < p \leq 0.10$

Table 4.3. Statistical significance (*p*-value) of correlations between physical properties of Type I/II and Type IL cements and their early-age shrinkage response at 25°C with *w/b* = 0.4. Sign of correlation is indicated in parentheses. Highlight colors indicate strength of significance.

Parameter	Chemical shrinkage				Autogenous deformation				
	1 d	2 d	3 d	7 d	1 d	3 d	7 d	14 d	28 d
SSA	0.26 (+)	0.98 (+)	0.67 (-)	0.33 (+)	0.02 (+)	0.33 (+)	0.43 (+)	0.44 (+)	0.42 (+)
$D_{3,2}$	0.21 (-)	0.90 (+)	0.76 (+)	0.35 (+)	0.01 (-)	0.16 (-)	0.21 (-)	0.20 (-)	0.18 (-)
$D_{4,3}$	0.06 (-)	0.40 (-)	0.68 (-)	0.63 (+)	0.00 (-)	0.03 (-)	0.05 (-)	0.10 (-)	0.18 (-)
D_{10}	0.49 (-)	1.00 (+)	0.72 (+)	0.40 (+)	0.08 (-)	0.41 (-)	0.39 (-)	0.30 (-)	0.25 (-)
D_{50}	0.12 (-)	0.75 (-)	0.94 (+)	0.45 (+)	0.00 (-)	0.05 (-)	0.11 (-)	0.17 (-)	0.23 (-)
D_{90}	0.07 (-)	0.32 (-)	0.57 (-)	0.70 (+)	0.01 (-)	0.05 (-)	0.08 (-)	0.16 (-)	0.29 (-)
Blaine	0.39 (+)	0.75 (+)	1.00 (+)	0.75 (-)	0.04 (+)	0.32 (+)	0.35 (+)	0.36 (+)	0.35 (+)

Legend:		$p < 0.01$
		$0.01 < p \leq 0.05$
		$0.05 < p \leq 0.10$

In summary, it was observed that although chemical shrinkage appeared to follow the same particle-size dependent trends as cumulative heat and degree of hydration, particle size alone was not an adequate predictor of chemical shrinkage for Type IL cement pastes at *w/b* = 0.40. It was similarly observed that while a relative increase in cement fineness increased autogenous deformation at *w/b* = 0.40, a relative *decrease* in cement fineness did not necessarily decrease autogenous deformation. Recommendations to limit early-age shrinkage in PLC-based materials, therefore, cannot rely solely upon limiting the fineness of the cement, as the chemistry of the clinker also has an important impact on the early-age deformation of PLC pastes that must be considered.

4.3.4 Combined effects of chemical and autogenous shrinkage

To examine the combined effects of the two types of early-age shrinkage during the first 7 days of hydration, the volumetric chemical deformations obtained by ASTM C1608 (in units of mL shrinkage per g binder) and the linear autogenous deformations obtained by ASTM C1698 (in units of μm shrinkage per m length) were first converted to consistent units. Chemical shrinkage was converted from units of mL (cm^3) shrinkage per g binder to consistent units of cm^3 shrinkage per cm^3 paste using the relationship,

$$1\,\text{g binder} \rightarrow \frac{1}{\rho_w}\left(\frac{1}{SG_b} + w/b\right)\text{cm}^3\ \text{paste} \tag{4.3}$$

where ρ_w is the density of water (assumed to be 1 g/cm^3) and SG_b is the specific gravity of the portland or limestone cement binder given in Table 3.3. Autogenous shrinkage was converted from units of 10^{-6} m shrinkage per m length to consistent units of 10^{-6} cm^3 shrinkage per cm^3 paste assuming linear isotropic deformations, in which [89]:

$$\varepsilon_{vol} = 3\varepsilon_{lin} \tag{4.4}$$

where ε_{lin} is the linear strain and ε_{vol} is the volumetric strain. The resulting amounts of chemical and autogenous shrinkage were reported as a percentage of the original paste volume. Since the sign conventions for the two tests are opposite one another, with a positive chemical shrinkage and a negative autogenous strain both indicating contraction of the paste, a consistent sign convention was adopted for the purposes of comparison, wherein a positive amount of "shrinkage" indicates contraction of the paste volume.

The normalized values of chemical and autogenous shrinkage over the first 7 days of hydration are shown in Figure 4.5. For ease of comparison, chemical shrinkage is only shown at ages where a corresponding autogenous shrinkage measurement was also made.

The results indicate that, over the first 7 days of hydration, autogenous deformation reduces the volume of the cement paste by an average of 0.2%, while chemical shrinkage reduces the volume by an average of 6.4%. The order of magnitude difference between the two shrinkage types is consistent with values reported elsewhere in the literature for portland cement pastes [88-90], further suggesting that, for *w/b* = 0.40, chemical shrinkage has a much greater impact on early-age shrinkage than autogenous shrinkage does. In fact, chemical shrinkage accounts for nearly 97% of all early-age volume change experienced by the eleven cement pastes over the first 7 days of hydration. (The same observations may not necessarily hold at very low *w/b*, where autogenous shrinkage is typically larger [89-91].) Thus, it can be postulated that hydration models such as the Powers' model [33] may provide reasonable predictions of early-age shrinkage for both Type I/II and Type IL cement pastes, without considering the effects of autogenous deformation at a *w/b* of 0.40.

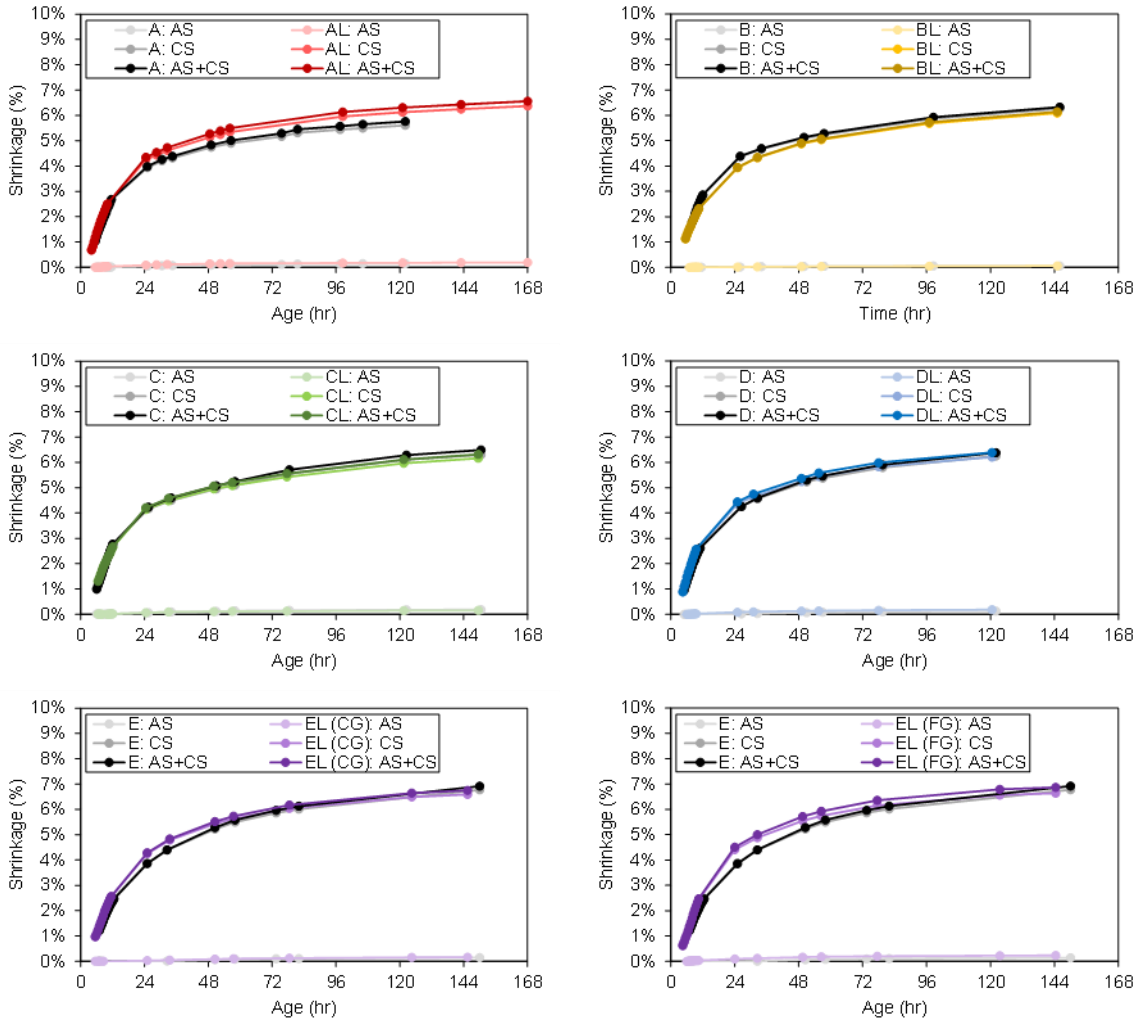

Figure 4.5 Chemical and autogenous shrinkage, in volume % units, for cement pastes A-E at *w/b* = 0.40 and 25°C for first 7 days (168 hr) of hydration.

4.4 Prediction of chemical shrinkage by Powers' model

In 1948, T.C. Powers and T.L Brownyard [33] developed a simple model for understanding the influence of cement hydration on the structure of hydrated portland cement paste. After more than a decade of experimental work, they concluded that cement hydration can be expressed as a linear function of the fractional amount of cement that has reacted; that is, the total volume of hydration product can be linearly related to the degree of hydration, α, of the cement paste. Since the volumes of cement and water

also decrease as a linear function of α, it follows that chemical shrinkage – the difference between the hydration product volume and the initial reactant volume – will also vary linearly with α. Thus, the model of Powers and Brownyard can be used to predict the chemical shrinkage of a hydrating cement paste at any degree of hydration by simply knowing its starting *w/b*, thereby providing a useful linkage between composition and microstructural development.

In the nearly seven decades since Powers and Brownyard's original publication, what is now commonly referred to as "Powers' model" has undergone only minor revisions [34-36], despite significant changes in the chemical and physical properties of portland cements. In particular, the chemical and physical effects occurring as a result of the incorporation of up to 5% limestone in traditional portland cements and up to 15% in portland limestone cements (PLCs) have been largely ignored. A common approach to considering limestone cements has been to simply "dilute" the volume of reactive cement used in the model [36], but this assumes that the limestone has no other effect on hydration beyond simple dilution. As a result, the diluted model may under-predict the amount of chemical shrinkage expected from a PLC paste, leading to unexpected shrinkage and potentially cracking in field applications. It is therefore necessary to evaluate the appropriateness of using such a modified Powers' model to predict the chemical shrinkage of both modern portland cement pastes (with < 5 wt.% limestone) and blended limestone cement pastes (with up to 15 wt.% limestone), to determine if the constant linear relationship assumed by Powers and Brownyard remains applicable.

4.4.1 Theoretical background: Powers' model

The original model of Powers and Brownyard came as part of a landmark study [33] that systematically explored for the first time the hydration of portland cement. Through careful experimentation, Powers and Brownyard were able to develop a simple model for determining relative volumes of hydration product, capillary porosity, and chemical shrinkage for a given cement paste [33, 35, 55, 92-94]. Although their original work lacks a truly "simple" model for cement hydration, later adaptations by both Powers [34] and others [35] have simplified the model into a set of basic equations that are a function solely of the degree of hydration and the initial porosity, *p*, of the cement paste system. For a given initial porosity and degree of hydration, Powers' model can be used to predict the volume fraction of the *original system* that is occupied by water-filled capillary porosity, unhydrated cement, hydration product, and chemical shrinkage, according to Equation 4.5 [35]:

Capillary water: $$V_{cw} = p - 1.32(1-p)\alpha \quad (4.5a)$$

Unhydrated cement: $$V_{uc} = (1-p)(1-\alpha) \quad (4.5b)$$

Hydration product: $$V_{hp} = 2.12(1-p)\alpha \quad (4.5c)$$

Chemical shrinkage: $$V_{cs} = 0.20(1-p)\alpha \quad (4.5d)$$

Volume balance: $$V_{cw} + V_{uc} + V_{hp} + V_{cs} = 1 \quad (4.5e)$$

where $p = (w/c)/(w/c + 1/SG_c)$, and SG_c is the specific gravity of the cement. For portland cement, SG_c is typically assumed to be 3.15.

A recent modification to Powers' model, proposed by Bentz, et al., [36] considers the partial replacement of cement by an inert filler. In Bentz's model, the filler occupies a constant fraction of the system volume, and does not participate in the hydration reaction,

and so the volume fraction of reactants and products are simply reduced by the volume fraction of filler in the system.

Bentz's model, however, only applies to systems in which the filler has been dosed on an equivalent volume basis; that is, if the binder is said to contain 10% filler, then 10% of the cement has been replaced with an equivalent *volume* of filler. In the case of commercially produced blended cements and in ASTM standards describing limits on cement composition, however, filler (e.g., limestone) content is expressed on an equivalent *mass* basis, such that for a binder containing 10% filler, 10% of the clinker has been replaced with an equivalent *mass* of filler. If the filler has a different specific gravity than the cement that it is replacing, then a different set of equations, considering changes to the binder volume, must be used (see Appendix A for a detailed derivation). For a binder containing filler dosed on an equivalent-mass, Powers' model takes on the form:

Capillary water: $$V_{cw} = p - 1.32(1-p)(\alpha)(1-V_f) \quad (4.6a)$$

Unhydrated cement: $$V_{uc} = (1-p)(1-\alpha)(1-V_f) \quad (4.6b)$$

Hydration product: $$V_{hp} = 2.12(1-p)(\alpha)(1-V_f) \quad (4.6c)$$

Chemical shrinkage: $$V_{cs} = 0.20(1-p)(\alpha)(1-V_f) \quad (4.6d)$$

Volume balance: $$V_{cw} + V_{uc} + V_{hp} + V_{cs} + V_f = 1 \quad (4.6e)$$

where V_f is the volume fraction of filler in the binder, and the initial porosity p is now expressed in terms of the water-to-binder ratio, *w/b*, and the specific gravity of the binder, SG_b (which may be different from the 3.15 typically assumed for portland cement): $p = (w/b)/(w/b + 1/SG_b)$. If the specific gravity of the filler, SG_f, is known, then the volume fraction V_f can be determined from the mass fraction of filler in the cement, M_f, by the relationship:

$$V_f = M_f \cdot \frac{SG_f}{SG_b} \tag{4.7}$$

The adjustments to Powers' model in Equation 4.6 account simply for the reduction of the reacting materials in the system and do not consider any additional alterations to cement hydration. Therefore, if the adjusted Powers' model were to be applied to the hydration of a cement containing *limestone* filler, it would only be able to account for the dilution of the cement, and not the other chemical and physical phenomena introduced by the limestone. The relative impact of these other effects is currently not known and warrants further investigation. Thus, the research presented in the remainder of this chapter aims to investigate the applicability of the modified Powers' model, particularly its prediction of chemical shrinkage, to modern portland and portland limestone cement pastes containing up to 15% limestone by mass.

4.4.2 Experimental comparison

To fully investigate the influence of limestone fillers on the relationship between chemical shrinkage and degree of hydration, it is necessary to parametrically combine the experimental data to generate Powers' model curves ("Powers curves") for each cement paste. This is accomplished by plotting the measured chemical shrinkage at age *t* (Figure 4.3) against the derived degree of hydration at the same age *t* (Figure 3.7), for all ages *t* of interest. The modified Powers' model given in Equation 4.6 was used to predict the total amount of chemical shrinkage for each paste upon complete hydration (Table 4.4). The experimental results are shown in Figure 4.6 along with the theoretical Powers' model curves ("Powers' curves").

Table 4.4 Chemical shrinkage predicted by Powers' model for α = 100%, cm^3/cm^3.

Cement	A	B	C	D	E
Type I	0.087	0.087	0.087	0.085	0.088
Type IL	0.079	0.083	0.081	0.081	0.082

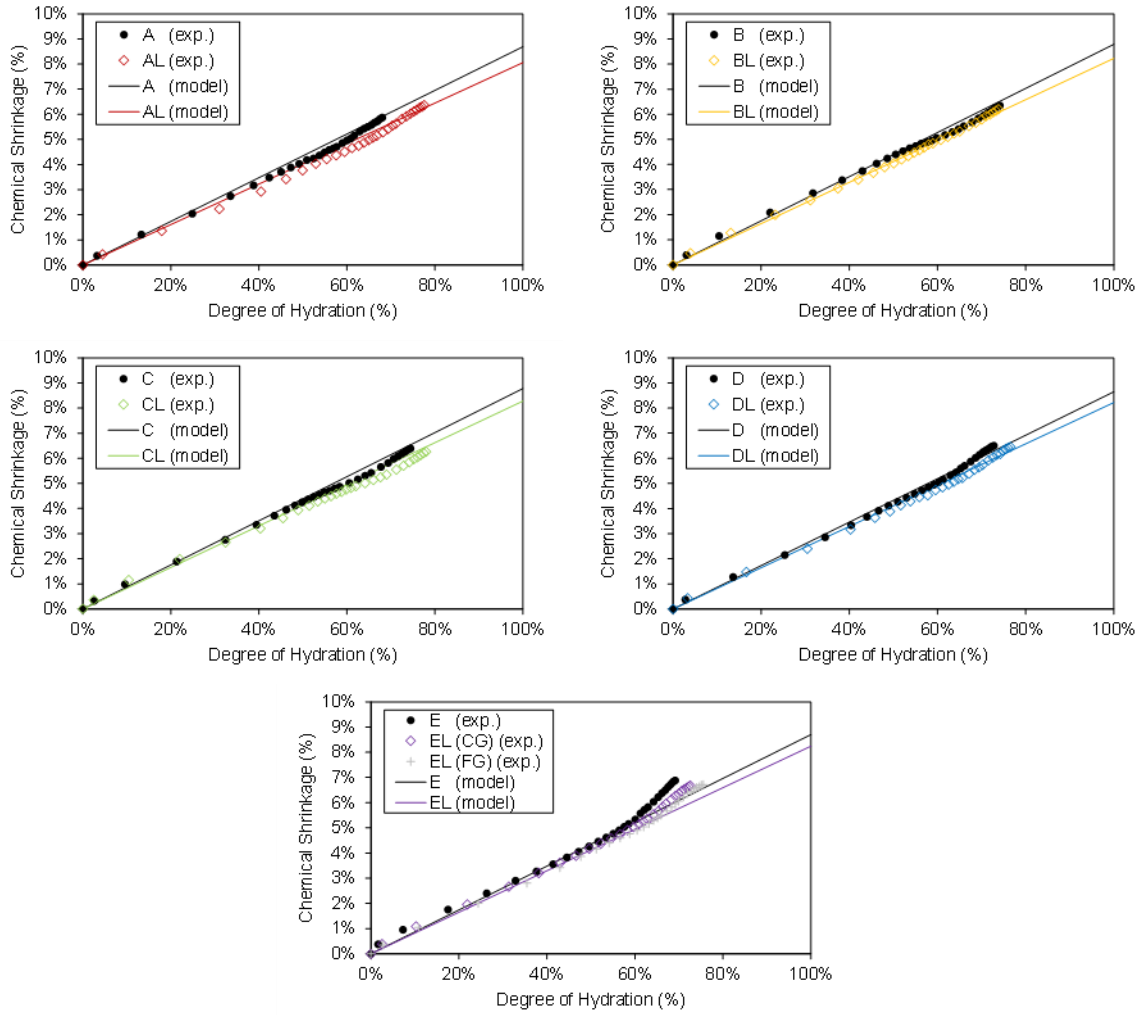

Figure 4.6 Comparison of experimental chemical shrinkage to that predicted by Powers' model. For clarity, data points are shown once every 3 hr through 48 hr, once every 6 hr through 72 hr, and once every 12 hr through 168 hr.

Until $\alpha \approx 60\%$, the experimental results for all 11 cements are in good agreement with Powers' model, and generally exhibit linear increases in chemical shrinkage with increasing degree of hydration. Beyond this point, 9 of the 11 cements (excepting

cements B and BL) begin to show further increases in chemical shrinkage that are not accounted for by the model. These increases are evident by a bilinear knee-bend shown in Figure 4.6. The slopes of the experimental Powers curves were found by least squares approximation to generally match the slopes predicted by Powers' model over the entire 7 day testing period (Figure 4.7), but when only the secondary "knee-bend" portion of the curves were examined, the slopes were found to exceed the predicted values by 25-40% for cements from sources A, C, D, by 15-20% for cements from source B, and by 60-100% for cements from source E.

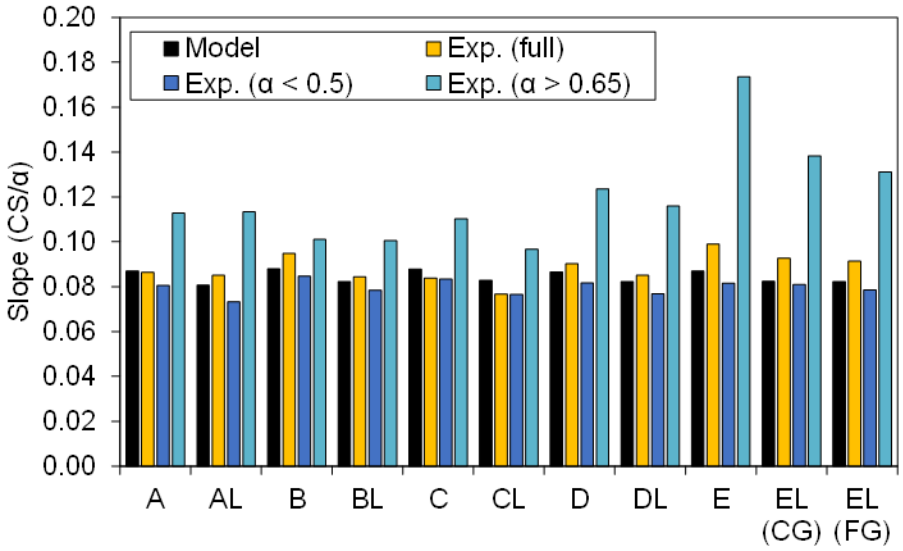

Figure 4.7 Slopes of experimental Powers curves over entire testing range and for degrees of hydration below 0.5 and above 0.65.

Interestingly, the bilinear behavior is exhibited by both Type I/II and Type IL cements, suggesting that it is not unique to cements containing a high mass fraction of limestone. Neither does it appear to be a direct function of the cement fineness, as the two Type IL cements from source E, cements EL (CG) and EL (FG), show nearly identical slopes to one another before and after the knee-bend. The deviant behavior furthermore does not appear to be an artifact of the two test methods, as any potential artifacts were

removed prior to analysis by subtracting heat losses (apparent decrease in α) and evaporation (apparent increase in chemical shrinkage) measured from testing vials containing only water (no cement paste). Finally, the apparent increase in shrinkage is also not likely due to the self-desiccation of the chemical shrinkage specimens, as autogenous shrinkage (1) was found to be most rapid during the first 48 hr of hydration (corresponding to degrees of hydration of less than 50% for most of the cement pastes investigated), and (2) was found to be less than 800 microstrain, or, assuming linear isotropic deformation, less than 0.25% by volume after 7 days of hydration.

Thus, it is believed that the onset of bilinear behavior is due to the presence of the limestone filler. Three potential limestone-related causes will be presented in the remaining discussion: (1) the limestone content (dilution effect), (2) the limestone fineness (nucleation effect), and (3) the limestone mineralogy (chemical effect).

4.4.2.1 Physical effects: Dilution

The modified Powers' model used to predict chemical shrinkage in this study considers limestone to be a filler or diluent. Dilution reduces the volume fraction of cement in the system while holding the volume fraction of water constant. As a consequence, the effective water-to-cement ratio of the system is increased, thereby increasing the degree of hydration and decreasing the total amount of chemical shrinkage occurring in a hydrating cement paste at a particular age. Taken together, these two effects imply that for a dilution-dominated system, the slope of the Powers curve will be shallower than that of the original undiluted system. This effect is demonstrated qualitatively in Figure 4.8. Therefore, while the dilution effect does, explain the

shallower initial slopes of the Powers curves for the six Type IL cement pastes, it does not explain the secondary increase in slope beyond $\alpha = 0.60$.

4.4.2.2 Physical effects: Nucleation

Heterogeneous nucleation of hydration products on the surfaces of the limestone particles also had a notable effect on the early-age hydration behavior of the Type IL pastes. Nucleation effects are known to increase the rate of hydration during the nucleation and growth stage [28] (occurring primarily between 2 and 6 hr for the pastes considered in this study [62]), which consequently gives rise to increased degree of hydration and chemical shrinkage at early ages. Such increases in degree of hydration and chemical shrinkage were observed for all four of the finely ground Type IL cements (AL, DL, and EL (CG and FG)), with greater increases observed as the cements were ground more finely (e.g., cement EL (FG) vs. cement EL (CG)). However, since both degree of hydration and chemical shrinkage are linearly related to the rate of hydration [95], it follows that a nucleation phenomenon should not alter the relationship between chemical shrinkage and degree of hydration. Consequently, the slope of the Powers curve should not change with a change in surface area or particle size distribution, as illustrated qualitatively in Figure 4.8. Appropriately, no significant deviations in slope were observed for the finely ground Type IL cements from sources A, D, and E during the first 24 hr ($\alpha < 0.5$), where nucleation-dominated behavior was observed, and likewise, no significant differences were observed between the bilinear slopes for cements EL (FG) and EL (CG), which differed from one another only in particle size. Thus, nucleation effects can also not explain the secondary increase in the slope observed beyond $\alpha = 0.60$.

If nucleation effects do not affect the slope of the Powers' model curves, and dilution effects cause a shallowing of the curve, then the net effect of these physical phenomena should be a decrease in slope, as predicted by the modified Powers' model. While the experimental results were found to adhere to these predictions for the first several hours of hydration (up to $\alpha \approx 0.60$, or between 36-72 hr of hydration, according to Figure 3.7), they do not continue to follow the expected trends beyond that point. Thus, the physical effects of limestone fillers alone cannot predict the chemical shrinkage of the cement paste; chemical effects must also be considered.

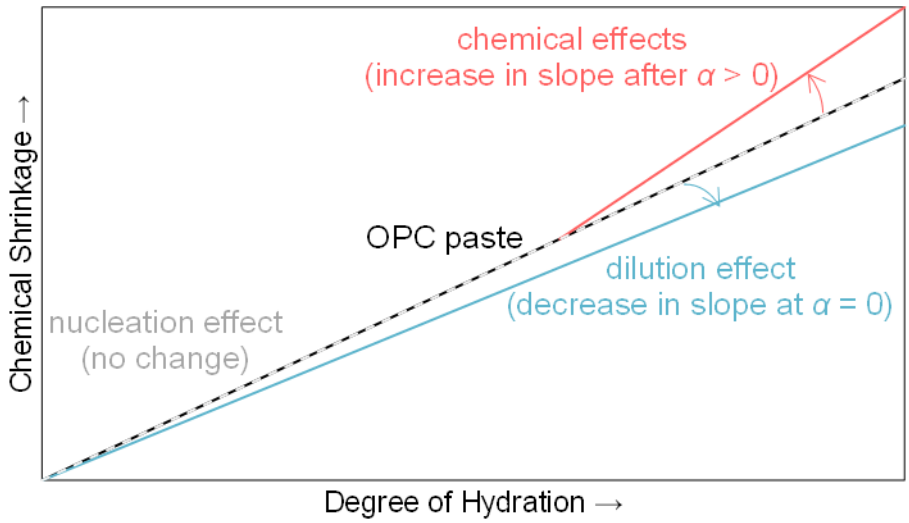

Figure 4.8 Qualitative illustration depicting physical and chemical effects of limestone fillers on Powers' model for chemical shrinkage.

4.4.2.3 Chemical effects

In terms of material chemistry, Powers' model is primarily concerned with the primary products of hydration – calcium silicate hydrate (C-S-H), calcium hydroxide (CH), and ettringite ($C_3A\overline{S}_3H_{32}$) – which occupy a substantial portion of the hydrated cement paste volume. Secondary reaction products like monosulfate hydrate ($C_4A\overline{S}H_{12}$) are less important to the model, not only because they occupy a relatively small fraction

of the hydrated cement paste volume, but they are also more similar in density to the reactants from which they form, and therefore do not cause significant volume changes. Consider the secondary reaction of the C_3A and ettringite to form monosulfate, as described in Equation 4.8:

$$2C_3A + C_6A\bar{S}_3H_{32} + 4H \rightarrow 3C_4A\bar{S}H_{12} \quad (4.8)$$

$$178.34 + 705.91 + 72.08 \rightarrow 926.83\,(\text{-}3.1\%)$$

On a molar volume basis, and assuming the pure-phase densities provided by Balonis and Glasser [32] (Table 4.5), this idealized reaction has 956.33 cm^3/mol of reactants combining to produce 926.83 cm^3/mol of monosulfate, a reduction of only 3.1% by volume. Compared to the 7-10% reduction in volume accompanied by the formation of C-S-H, CH, and ettringite from the primary phase reactions (Equation 4.9-4.11), this 3% secondary volume reduction can be considered negligible – especially when considering the fact that typically less than 5% of the cement paste volume participates in this reaction[8]. In total, it can be expected that the formation of monosulfate reduces the overall system volume by only about 0.15%, or approximately 2% of the total chemical shrinkage expected for a typical, fully hydrated portland cement paste.

[8] The volume fraction of material participating in the reaction was estimated from the volume fractions of each phase in the paste, assuming that the reactions given by Equations 4.9-4.11 each proceed to completion before the reaction given by Equation 4.8 initiates. Thus, for cement paste A at *w/b* = 0.4, approximately 9.2 cm^3 of a 226 cm^3 system will participate in this reaction, or about 4% of the total volume of the system.

Table 4.5 Molecular weights and densities of selected clinker phases and hydration products, from Balonis and Glasser[32].

Phase	Chemical Formula	Molecular Weight, g/mol	Density, g/cm^3
C_3S	$3CaO{\cdot}SiO_2$	228.32	3.120
C_2S	$2CaO{\cdot}SiO_2$	172.24	3.326
C_3A	$3CaO{\cdot}Al_2O_3$	270.19	3.030
C_4AF	$4CaO{\cdot}Al_2O_3{\cdot}Fe_2O_3$	485.96	3.708
$C\bar{C}$	$CaCO_3$	100.09	2.710
$C\bar{S}H_2$	$CaSO_4{\cdot}2H_2O$	172.17	2.311
$C\bar{S}H_{0.5}$	$CaSO_4{\cdot}½H_2O$	143.14	2.733
$C\bar{S}H$	$CaSO_4$	136.14	2.968
$C_3S_2H_3$	$3CaO{\cdot}2SiO_2{\cdot}3H_2O$	342.45	2.645
CH	$Ca(OH)_2$	74.09	2.251
$C_3A\bar{S}_3H_{32}$	$3CaO{\cdot}Al_2O_3{\cdot}3SO_3$	1255.11	1.778
$C_4A\bar{S}H_{12}$	$3CaO{\cdot}Al_2O_3{\cdot}CaSO_4{\cdot}12H_2O$	622.52	2.015
$C_4A\bar{C}H_{11}$	$3CaO{\cdot}Al_2O_3{\cdot}CaCO_3{\cdot}11H_2O$	568.29	2.175
$C_4A\bar{C}_{0.5}H_{12}$	$4CaO{\cdot}Al_2O_3{\cdot}½CO_2{\cdot}12H_2O$	564.45	1.985

C_3S hydration: $2C_3S + 6H \rightarrow C_3S_2H_3 + 3CH$ (4.9)

40-50% system vol. $146.36 + 108.12 \rightarrow 129.47 + 98.74\,(-10.3\%)$

C_2S hydration: $2C_2S + 4H \rightarrow C_3S_2H_3 + CH$ (4.10)

10-12% system vol. $103.57 + 72.08 \rightarrow 129.47 + 32.91\,(-7.6\%)$

C_3A primary hydration: $C_3A + 3C\bar{S}H_2 + 26H \rightarrow C_6A\bar{S}_3H_{32}$ (4.11)

10-12% system vol. $89.17 + 223.50 + 468.52 \rightarrow 705.91\,(-9.6\%)$

Consider, instead, the secondary reaction of C_3A and calcium carbonate ($C\bar{C}$) to form monocarbonate ($C_4A\bar{C}H_{11}$) or hemicarbonate ($C_4A\bar{C}_{0.5}H_{12}$), as described by Equations 4.12 and 4.13, respectively:

Monocarbonate: $C_3A + C\bar{C} + 11H \rightarrow C_4A\bar{C}H_{11}$ (4.12)

$$89.17 + 36.93 + 198.22 \rightarrow 261.28 \text{ (-19.4\%)}$$

Hemicarbonate: $$2C_3A + C\overline{C} + CH + 23H \rightarrow 2C_4A\overline{C}_{0.5}H_{12} \quad (4.13)$$

$$89.17 + 18.47 + 16.46 + 207.23 \rightarrow 284.36 \text{ (-14.2\%)}$$

Now a significant volume reduction occurs as a result of to the formation of these denser secondary hydration products: 19.4% for monocarbonate and 14.2% for hemicarbonate. Again, considering that approximately 5% of the original system volume is available to participate in this reaction, now the secondary phases can contribute up to 1% additional volume loss, or a relative increase in chemical shrinkage of about 15% for a typical, fully hydrated portland cement paste.

Such an increase would necessarily cause a change in slope of the Powers' model curve, and because the secondary reaction does not initiate until after the primary sulfate-rich phases (e.g., gypsum) have been substantially depleted, the change in slope would occur at a time and degree of hydration > 0, as experimentally observed. Therefore, it is proposed that the formation of these secondary mono- and hemicarbonate hydration phases is responsible for the bilinear trends seen in the experimentally derived chemical shrinkage versus degree of hydration curves. (Although the magnitude of the slope increase was experimentally found to be approximately double that of that caused by the carboaluminate AFm phases, the calculated values are based on idealized stoichiometric relationships and pure-phase reactants and products, which may vary considerably in real cement paste systems. Additionally, the contributions of the C_4AF and other calcium aluminate phases in the cement – which can account for another ~10% of the system volume – are also not considered due to the more complex nature of their reactions. Thus,

the true contribution of the carboaluminate AFm phases to chemical shrinkage is expected to be higher than the approximate 15% derived.)

4.4.3 Validation by chemical analysis

To confirm that the change in slope of the Powers chemical shrinkage curves is due to the formation of mono- and hemicarbonate phases, additional TGA and XRD analyses were performed for Cements A and AL, which contained 3.2 and 12.2% $CaCO_3$ by mass, respectively, and for Cements B and BL, which contained < 1.0 and 7.9% $CaCO_3$ by mass, respectively. Specimens were cast in sealed containers and stored at 25°C until the designated age of testing. Every 24 hours after mixing until 7 days, a portion of each specimen was removed and crushed into coarse particles (< 2.36 mm). Hydration of the particles was halted by solvent exchange in isopropanol for 15 minutes followed by drying over vacuum for 5 minutes. The dried fragments were further ground into a fine powder (< 150 μm) for analysis using a mortar and pestle.

Thermogravimetric analysis (Hitachi EXSTAR TG/DTA 7300) was carried out on approximately 20 mg of powder heated under N_2 environment from 25 to 900°C, at a rate of 10°C/min. X-ray diffraction analyses were carried out on approximately 2 g of powder, using a PANalytical X'Pert PRO Alpha-1 Empyrean with Cu-Kα (λ = 1.54 Å) radiation. Samples were scanned between 5° and 70° 2θ with a PIXcel^{3D} detector and a sampling time of 30 seconds.

The Powers curves for cements A and AL both showed bilinear knee-bends beginning between 48 and 72 hr of hydration, while the Powers curves for cements B and BL remained relatively linear throughout the 7 day testing period. If the theory that the

bilinear behavior is caused by the formation of monocarbonate is to be confirmed, then it would be expected that cement A and AL both form moncarbonate beginning between 2 and 3 days of hydration, while cements B and BL form either monosulfate or no AFm phase within the first 7 days.

The results from the TGA and XRD analyses are shown in Figure 4.9a-b and Figure 4.10a-b, respectively, for cement pastes A and AL, and in Figure 4.9c-d and Figure 4.10c-d, respectively, for cement pastes B and BL. In both the TGA and XRD analyses for cements A and AL, signature peaks corresponding to monocarbonate were observed beginning at 3 days of hydration for *both* the Type I/II and the Type IL cement paste. Monosulfate, which typically forms in Type I/II cement pastes [20], was only faintly observed in the TGA and not observed in XRD analyses. The small limestone substitution in the Type I/II cement (3.2%) was therefore determined to be significant enough to favor the formation of a monocarbonate AFm phase over the formation of monosulfate. The onset of the monocarbonate formation around 72 hr in both cement pastes coincides with the bilinear knee-bend of the experimental chemical shrinkage curve in Figure 4.6a. It is therefore likely that the change in slope observed for these pastes is related to the chemical influence of the limestone addition and to the increased chemical shrinkage caused by the formation of these secondary AFm products. Given their compositional similarities, it would likewise be expected that the small limestone substitution in the Type I/II cements from sources C, D, and E would be enough to favor hemi- or monocarbonate formation at around 72 hr in those pastes. At higher limestone inclusion rates, such as those found in the Type IL cements, monocarbonate formation

would continue to be favored, and likely form in larger quantities, as demonstrated by the more pronounced peaks in the TGA and XRD results for cement AL.

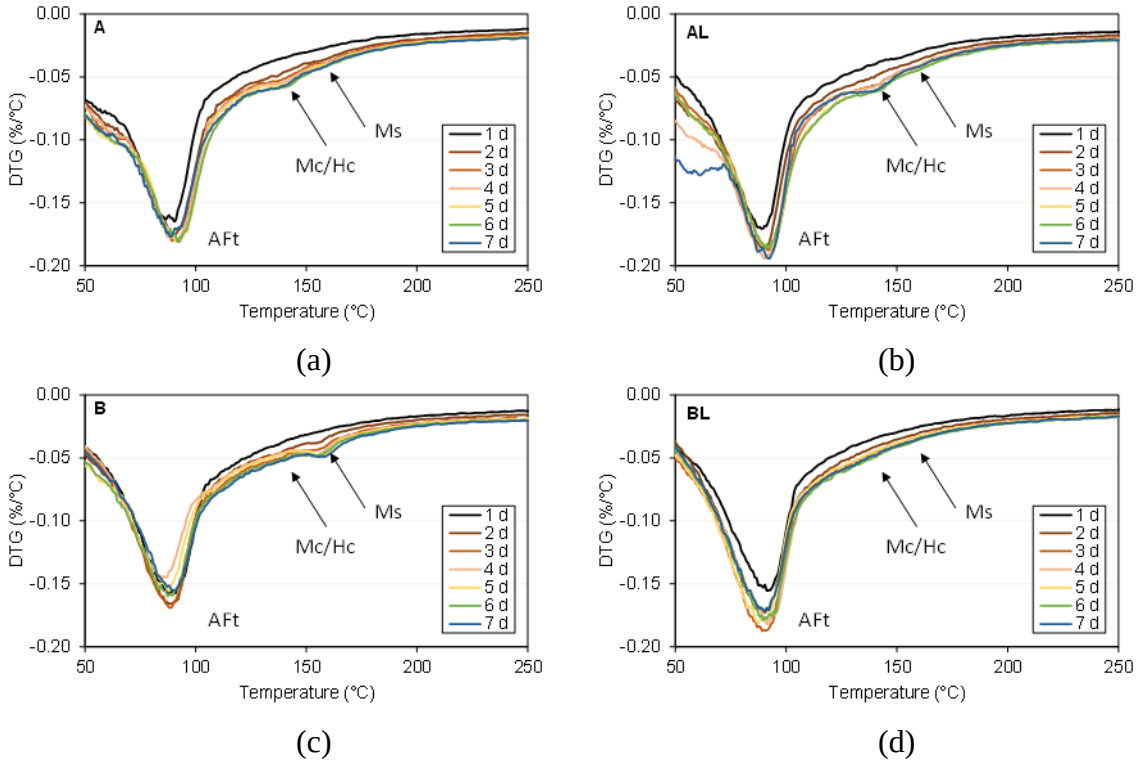

Figure 4.9 Derivative DTG curves for (a) Cement A, (b) Cement AL, (c) Cement B, and (d) Cement BL. Thermal mass loss around 130°C is assumed to correspond to the decomposition of monocarbonate, while the mass loss around 150°C is assumed to correspond to the decomposition of monosulfate.

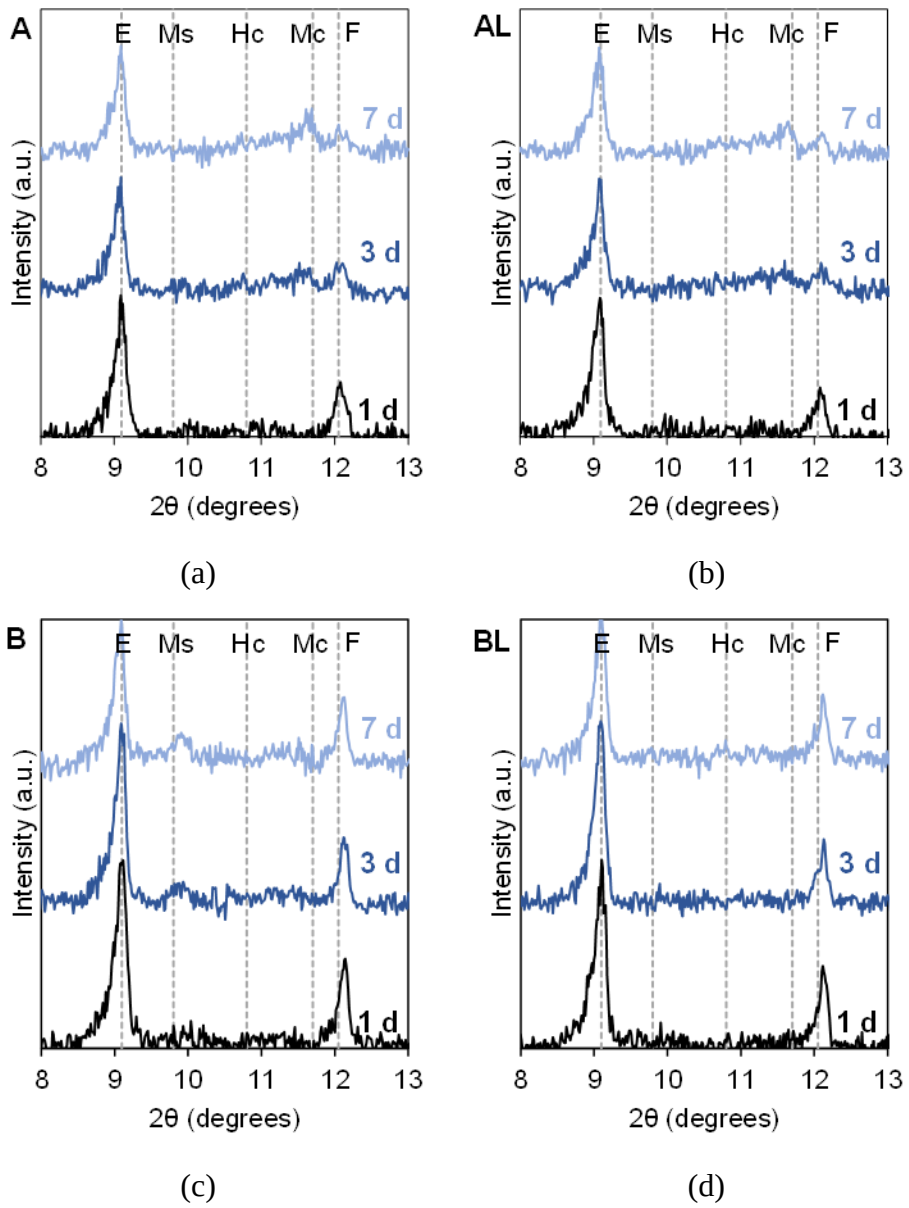

Figure 4.10 XRD patterns for (a) Cement A, (b) Cement AL, (c) Cement B, and (d) Cement BL. (E = ettringite, Ms = monosulfate, Hc = hemicarbonate, Mc = monocarbonate, F = C_4AF)

Cement pastes B and BL were the only two pastes which did not exhibit a significant bilinear behavior. Moreover, cement B was the only cement paste with a negligible limestone content (< 1% $CaCO_3$, by mass of cement). With limited calcium

carbonate available to produce carbonate AFm phases, it was primarily monosulfate that was observed to form by TGA (Figure 4.9c) and XRD (Figure 4.10c) analyses. Since the contributions of monosulfate to chemical shrinkage are considerably smaller than the contributions of the primary phases, they do not cause a significant change in slope for the chemical shrinkage Powers curves, as the experimental data in Figure 4.6b confirm. It is only when the partially reactive limestone fillers are included in significant quantities that it becomes apparent the model is inadequate for the prediction of chemical shrinkage of portland limestone cement pastes.

Thus, Powers' model is incapable of fully predicting the contribution of limestone fillers to chemical shrinkage in modern ordinary portland and portland limestone cement pastes. Because the model assumes that all reactions initiate at $\alpha = 0$, only the physical effects of the limestone fillers can be incorporated into the model. Time- and rate-dependent effects, such as the onset of secondary reactions, cannot be considered and therefore appear as experimental deviations from the expected linear behavior. If the secondary reactions were to be properly considered, the chemical shrinkage versus degree of hydration curve would exhibit a change in slope at some degree of hydration $\alpha > 0$, signifying the formation of the mono- and hemicarbonate AFm phases. Once the reactions reach completion, the slope of the curve would then be expected to return to its predicted value. However, because the secondary hydration products form over a range of degrees of hydration particular to the cement's unique composition, it is not currently possible to predict the points at which the line changes slope, and more research into C_4AF-derived AFm phases is needed to predict the magnitude of each slope change.

4.5 Conclusions

The research presented in this chapter examined the relative influence of limestone particle size and dosage rate on the early-age chemical and autogenous shrinkage of portland and portland limestone cement pastes. The experimental results support previous findings in the literature that limestone fillers primarily modify early-age shrinkage through both physical and chemical means, with dilution, nucleation, and chemical effects having the most significant impacts on the parameters investigated in this study. Cement pastes made from finely ground Type IL cements exhibited the greatest relative increases in chemical and autogenous shrinkage, which were attributed to their increased rates of hydration and microstructural development as a result of filler and nucleation effects. On the other hand, cement pastes made from the more coarsely ground Type IL cements initially exhibited a relative decrease in early-age shrinkage as a consequence of dilution-dominated hydration, but were found to show potential increases in shrinkage beyond 7 days of hydration due to contributions from more slowly reacting clinker phases such as C_4AF. Based on the results, it was suggested that restrictions on particle size may not be sufficient to limit early-age shrinkage of PLC-based materials, since the chemistry of the cement itself (clinker composition and limestone dosage rate) was found to significantly affect early-age chemical and autogenous shrinkage, as well.

The research additionally demonstrated that, at a *w/b* of 0.40, chemical shrinkage accounted for approximately 97% of the early-age shrinkage experienced by the eleven cement pastes considered in this study, leading to the hypothesis that Powers' model for chemical shrinkage may be used to adequately predict early-age shrinkage for portland and portland limestone cement based materials. The experimental results, however,

indicated that while the modified Powers' model can adequately account for the physical influences of limestone fillers on chemical shrinkage and degree of hydration, it cannot sufficiently predict the influence of the secondary reactions (i.e., those occurring at $\alpha > 0$) between the C_3A and calcium carbonate phases. In this sense, the modified Powers' model can be used satisfactorily for cement paste systems containing inert filler materials such as quartz, or cementitious filler materials such as nano-C_3S [28], for which hydration is only altered through physical means, but it should not be used for cement paste systems containing reactive or partially-reactive fillers such as limestone or supplementary cementitious materials, where secondary reactions may contribute significantly to chemical shrinkage in mature pastes. A new model, taking into account the delayed onset of these secondary reactions, would be required to adequately and sufficiently account for the influence of limestone fillers on the chemical shrinkage of modern portland and portland limestone cement pastes.

CHAPTER 5

INFLUENCE OF LIMESTONE GEOLOGY ON PLC HYDRATION

5.1 Introduction

The previous two chapters focused primarily on the influence of limestone addition rate and particle size distribution on the hydration and early-age shrinkage of portland limestone cement pastes. Dilution, nucleation, and filler effects arising from changes to the particle size distribution were thoroughly examined, with coarsely ground fillers exhibiting slower hydration rates and reduced shrinkage as a result of dominant dilution effects, and finely ground fillers exhibiting accelerated hydration rates and increased shrinkage as a result of dominant nucleation and filler effects. Chemical effects resulting from the incorporation of partially reactive $CaCO_3$ were also examined, relying on the assumption that the source or variations mineralogy of the limestone addition could be neglected. In that prior investigation, because each cement producer uses a unique combination of raw materials and processing methods, chemical effects could only be examined between pairs of cements produced from the same clinker source. Furthermore, because each of the cements examined contained a different limestone addition rate and particle size distribution, their chemical effects could not be examined in isolation from their physical effects.

To specifically examine how the source and resulting variations in mineralogy of limestone affect cement hydration in PLCs, it is therefore desirable to create custom limestone cement blends – which can control for differences in clinker chemistry and particle size distribution – in order to better understand the chemical role of the limestone

in the hydration of portland limestone cement-based materials. Few studies in the literature have focused exclusively on the chemical effects of limestone fillers on cement hydration, leaving a gap in the fundamental knowledge about limestone's role in cement-based systems. Recent studies looking at limestone chemistry have focused almost exclusively on AFm reactions, with little investigation into the implications therein for early-age properties such as degree of hydration and chemical shrinkage. Several researchers [19, 20, 95-97] have demonstrated through thermodynamic models and experimental investigations that even small quantities of limestone can cause significant changes to the secondary hydration of the calcium aluminate phases (C_3A and C_4AF), forming mono- and hemicarboaluminate hydrate (mono- and hemicarbonate) instead of monosulfoaluminate hydrate (monosulfate). Such reactions were also demonstrated for the commercially produced cements studied in Chapter 3, but as the results of Chapter 4 indicate, the consequences of altered hydration could have potentially significant impacts on chemical shrinkage, as well.

Fewer studies yet have focused specifically on the mineralogical contributions of the limestone. Sprung and Siebel [98] performed a comprehensive study of 33 different limestones with varying calcite ($CaCO_3$), dolomite ($CaMg(CO_3)_2$), and clay (illite, montmorillonite, and kaolinite) contents, but only characterized performance on the basis of compressive strength and frost-resistance. A subsequent study by Tsivilis, et al., [99] investigated three different limestone powders in combination with two different clinkers, but they, too, primarily focused their analysis on compressive strength. Furthermore, the two studies also provided contradictory conclusions regarding the influence of limestone mineralogy on compressive strength development: Sprung and Siebel found no

significant impact on strength due to varied limestone geology, while Tsivilis, et al., found that dolomitic limestone decreased strength while clayey limestone increased it. No studies specifically considering the effect of limestone mineralogy on cement hydration could be found in a search of the literature.

Consequently, the objectives of this study are (1) to investigate the chemical influence of limestone powders on cement hydration in isolation from their physical effects, and (2) to investigate the relative contributions of limestone mineralogy on early-age hydration and chemical evolution of PLC-based materials. Custom limestone-blended cements are developed using limestone powders from four different geological sources and compared to two custom quartz-blended cements to isolate the chemically-induced effects from the physically-induced ones [22]. Hydration kinetics, chemical evolution, and early-age shrinkage are investigated for pastes prepared from each blend to provide greater insights into the chemical effects of limestone fillers.

5.2 Materials

In order better understand the role of limestone mineralogy in early-age hydration and microstructural development, custom blends of limestone cements must be developed to control for the clinker chemistry and cement fineness. To create such blends, a single cement source containing no interground limestone is combined with various limestone powders, each ground to a similar particle size distribution and dosed at the same percentage, by weight. To control for the physical effects arising from the incorporation of the limestone particles, additional blends of a chemically inert quartz powder, also ground to a similar particle size distribution and dosed at the same percentage, by weight,

are prepared. The differences in hydration behavior between the limestone and quartz blended cement pastes will reveal the chemical influence of the limestone itself [22], while differences between the various limestone blended cement pastes will reveal the chemical influence of the limestone mineralogy.

5.2.1 Cement

The base cement selected for this study was an ASTM C150 Type I/II portland cement (Cement B) containing a nominal 0% interground limestone.[9] The composition of the cement was determined by both oxide analysis (ASTM C114 [53]) and x-ray diffraction (ASTM C1365 [54]). Full compositional data can be found in Chapter 3, but a summary of the primary phase composition is provided in Table 5.1.

Table 5.1. Composition of portland cement determined by Rietveld analysis.

Component	Oxide Analysis (%)	XRD (%)
C_3S	62.3	55.9
C_2S	10.5	21.6
C_3A	6.6	3.0
C_4AF	12.1	12.8
$CaCO_3$	0.4[†]	1.0

[†] Determined by thermogravimetric analysis (TGA).

5.2.2 Fillers

Limestone was received from four different sources, each having a different primary mineralogy, as indicated in Table 5.2. The calcitic and dolomitic limestones were provided by local cement producers from their feedstock and were selected for this study as representative materials for use in limestone-blended cements. Some sources of

[9] Although it contained no interground limestone, cement B did contain a small fraction of $CaCO_3$ (<1%) as a result of carbonation in air.

dolomitic limestone are known to react with alkalis in the cement to form an additional hydrate phase brucite, $Mg(OH)_2$ [100, 101], but the particular geological source used in this study is not believed to be reactive in that way. The siliceous limestone (Spratt) is not a common feedstock for cement production, but was selected for further study due to its potential reactivity with alkalis in the cement. It is well-established that the amorphous silica within the siliceous limestone reacts with alkalis in the cement to form a gel-like product [100, 101], which can cause damaging expansion in concrete when used as a coarse aggregate, but can serve instead as a pozzolanic additive when ground to a fine powder [102, 103]. A fourth feedstock limestone, calcitic marl, was also provided by a local cement producer and included in this study to investigate the potential effects of its aluminosilicate clay impurities on hydration and microstructural development. Finally, a commercially produced inert quartz powder (MIN-U-SIL, U.S. Silica), was also used in order to isolate the physical effects of the limestone fillers from their chemical effects.

Table 5.2. Fillers listed by primary geology and source.

Filler Type	Source
Calcitic limestone	Calera, AL, USA
Dolomitic limestone	Clinchfield, GA, USA
Siliceous limestone	Ottawa, ON, Canada
Calcitic marl	Holly Hill, SC, USA
Quartz	U.S. Silica Company, USA

5.2.3 Material processing

The four limestone materials were processed into powders, each having approximately the same particle size distribution; the quartz was received in powderized form and did not require further processing. The as-received limestones were first crushed in an industrial aggregate crusher into fragments measuring approximately 4 mm

in size or less. Each limestone was then ground further into a fine particle size (< 150 μm) using a Retsch PM100 planetary ball mill. Slurries were prepared from 20 g of limestone and 10 mL of deionized water to minimize agglomeration of the ultrafine particles in the ball mill. Each batch of slurry was placed into a 50 mL stainless steel grinding jar along with 10 stainless steel balls, 10 mm in diameter. The jars were spun in the planetary mill at a rate of 250 rpm for 30 minutes, after which time the slurry was passed through a No. 30 sieve (595 μm opening) to remove any remaining coarse particles, then oven dried over low heat (50°C) for approximately 24 hours. The coarse particles separated from the slurry were returned to the grinding jars and ground with the next batch of material. This process was repeated until approximately 200 g of each limestone had been ground.

The dried material was lightly pulverized with a mortar and pestle to separate into a fine powder. The powder was passed through a No. 100 sieve (150 μm opening) and stored for further use. Any particles not passing the No. 100 sieve were discarded, amounting to less than 1 g of discarded material.

5.3 Filler characterization

The limestone and quartz powders were characterized on the basis of particle size distribution and chemical composition. Particle size analyses were conducted to verify that the limestone powders were ground to similar particle size distributions, as well as to determine the appropriate blend of quartz powders to use in order to match the size of the limestone powders. Chemical analyses were conducted to verify the primary mineralogy

of each limestone as indicated by the materials suppliers, as well as to identify the unique mineralogical components of each limestone powder.

5.3.1 Particle size distribution

Laser particle size analyses were conducted using a Malvern Mastersizer 3000E to verify that each material had approximately the same particle size distribution. A small amount of each powder was dispersed in ethanol until a laser obscuration of approximately 7% was obtained. The dispersed material was sonicated for 2 minutes then stirred at a rate of 840 rpm for approximately 10 minutes prior to analysis to reduce particle agglomeration. Particle size distributions were determined as the average of five samples, each collected over a 60 second interval.

The differential and cumulative size distributions for the four ground limestone powders are shown in Figure 5.1 and Figure 5.2, respectively. The particle size distributions for the cement, determined by the same method, are also shown for comparison. All four limestones had similar size distributions to one another, with median particle sizes (D_{50}) between 5-8 μm and surface mean particle sizes ($D_{3,2}$) between 3-4 μm (Table 5.3). These parameters were significantly lower than the D_{50} and $D_{3,2}$ for the base cement, signifying that nucleation effects could dominate the early-age hydration behavior of the cements, as were observed in the commercially produced PLC pastes.

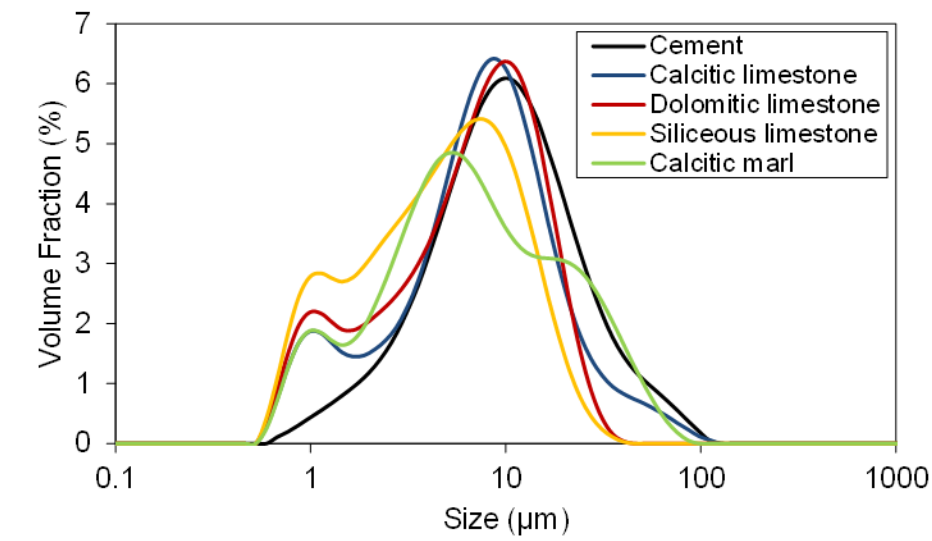

Figure 5.1. Differential particle size distribution (by volume) for cement and limestone powders.

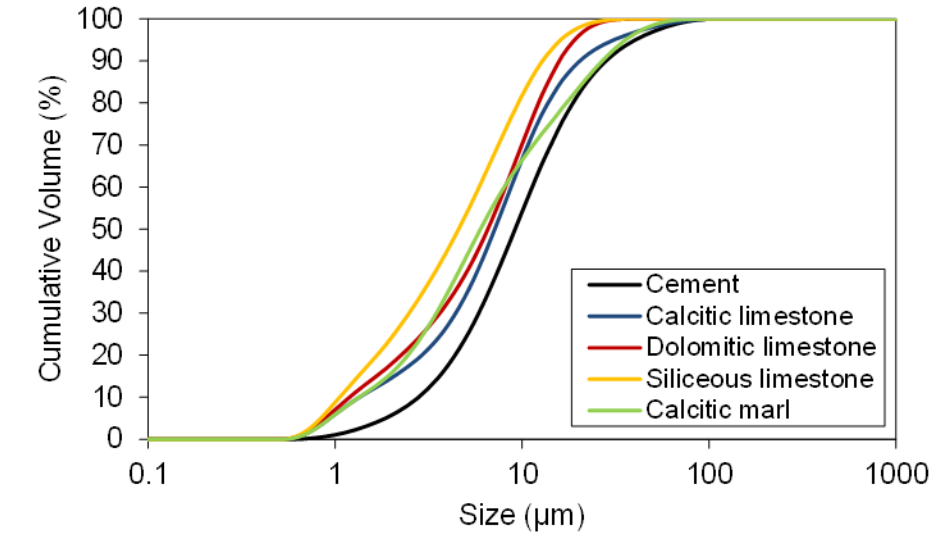

Figure 5.2. Cumulative particle size distributions (by volume) for cement and limestone powders.

The quartz powder was received in three different gradations, having maximum particle sizes of 30, 15, and 5 µm. Each gradation was characterized individually in order to develop a blend that most closely resembled the size distributions of the limestone powders. The cumulative size distributions of all three powders are shown in Figure 5.3,

with the cement also shown for comparison. As can be seen from the figure, the 30 µm top-size quartz powder was similar in size to the cement, making it too coarse for comparison with the limestone powders. The 15 µm top-size powder was similar in gradation to the calcitic limestone, dolomitic limestone, and calcitic marl, and was used to isolate physical effects for those three powders; it was given a designation "15" to indicate its top-size. The 15 µm top-size powder, however, was still coarser than the siliceous limestone powder, so an additional 4:1 blend of the 15 µm and 5 µm powders, respectively, was used to generate a finer gradation for comparison with that powder; this finer blend was given a designation "15/5" to indicate that it was a blend of the two 15 and 5 µm top-size powders. As can be seen in Figure 5.4 and Table 5.3, the two quartz powders reasonably approximate the particle size parameters of the four limestone powders.

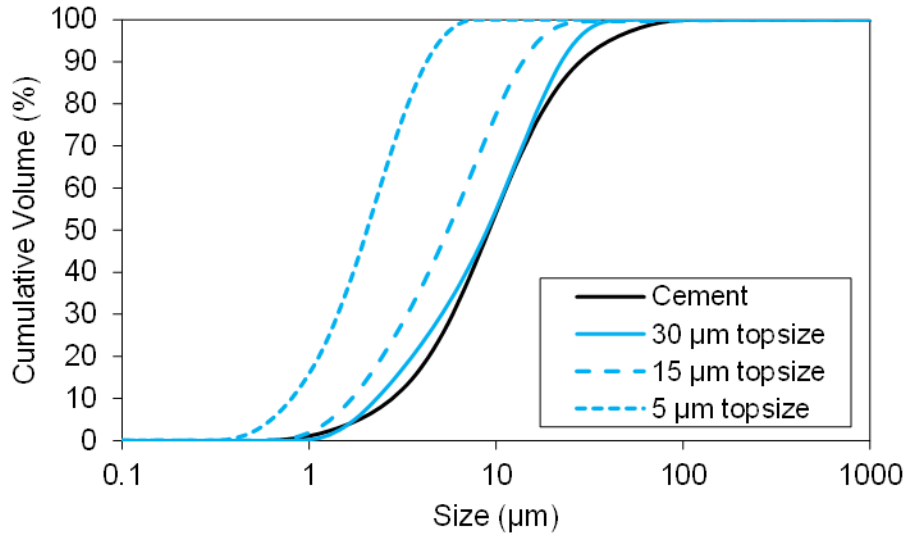

Figure 5.3. Comparison of particle size distributions for commercially produced quartz powders.

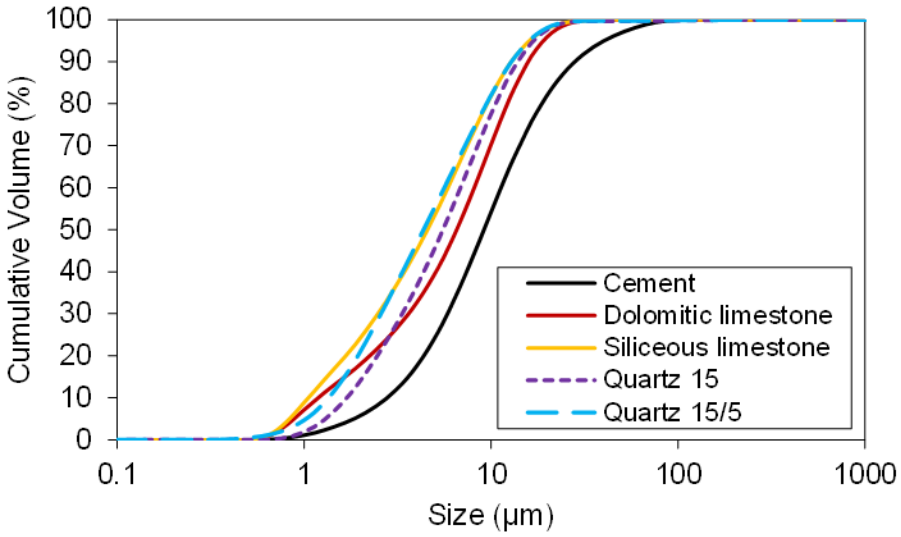

Figure 5.4. Particle size distributions for quartz powders, compared to a subset of limestone powders.

Table 5.3. Particle size distribution parameters for cement and filler powders. 10th, 50th, and 90th percentile diameters (by volume) and surface mean particle size ($D_{3,2}$) are given.

Material	**D_{10} (µm)**	**D_{50} (µm)**	**D_{90} (µm)**	**$D_{3,2}$ (µm)**	**SSA (m^2/kg)**
Cement	3.17	10.40	31.90	6.71	282
Calcitic limestone	1.53	8.11	23.20	4.28	518
Dolomitic limestone	1.35	7.44	18.00	3.77	587
Siliceous limestone	1.52	6.80	30.40	4.01	721
Calcitic marl	1.20	5.20	14.60	3.07	552
Quartz 15	1.92	6.28	15.8	4.26	531
Quartz 15/5	1.61	5.33	15.1	3.59	630

5.3.2 Mineralogical characterization

The mineralogical characterization of the limestone powders was performed using x-ray diffraction (XRD), to determine the limestone's crystalline mineralogy, and thermogravimetric analysis (TGA), to determine the limestone's CO_2 content. The mineralogy of the quartz powder had been provided by the supplier, and was determined to be 99.4% crystalline SiO_2.

XRD analyses were performed on approximately 2 g of powder, using a PANalytical X'Pert PRO Alpha-1 Empyrean with Cu-Kα (λ = 1.54 Å) radiation, scanned

between 5° and 70° 2θ. Results were analyzed using PANalytical HighScore Plus software with reference patterns selected from the COD database [69-71]. The relative proportions of the crystalline phases were determined by Rietveld analysis.

Thermogravimetric analyses were performed on approximately 20 mg of powder, in a Hitachi EXSTAR TG/DTA 7300, under N_2 environment. Samples were heated from 25°C to 105°C at a rate of 10°C/min, held at 105°C for 30 minutes to drive off any moisture, then heated further 10°C/min to a maximum temperature of 900°C. The CO_2 content of each limestone was determined from the mass loss between 600-750°C, normalized by the mass of the sample at 105°C (following the removal of moisture).

The combined results of the XRD and TGA analyses were used to determine the amorphous content of each limestone powder. The total percentage of crystalline material in each limestone was estimated by dividing the measured CO_2 content by the theoretical CO_2 content of a 100% crystalline material having the same relative proportions of calcite and dolomite as obtained by Rietveld analysis. Calcite ($CaCO_3$) was assumed to have a CO_2 content of 44.0%, and dolomite ($CaMg(CO_3)_2$) was assumed to have a CO_2 content of 47.7%:

$$\%\,\text{crystalline} = \frac{\%CO_2^{TGA}}{\%CaCO_3^{XRD} \times 44.0\% + \%CaMg(CO_3)_2^{XRD} \times 47.7\%} \tag{5.1}$$

The amorphous content was estimated by subtracting the crystalline content from 100%. Contributions from amorphous carbonate phases were assumed to be negligible and were not considered.

The diffraction patterns for each limestone sample are shown in Figure 5.5, and the mineralogy determined by Rietveld analysis is given in Table 5.4. The final estimated limestone compositions, adjusted for amorphous content, are given in Table 5.5. While

each limestone received was primarily composed of calcite, crystals of dolomite and quartz were also observed. Amorphous material was also found in all four limestone sources, with the siliceous limestone and calitic marl having the highest percentages, at 7.3 and 4.0%, respectively. Suppliers of the siliceous limestone indicated that highly reactive opal (amorphous SiO_2) had been detected by petrographic analysis, likely accounting for much of the 7.3% amorphous content for that material. Based on its geological origins, the amorphous content of the calcitic marl is believed to be an aluminosiliceous clay of unknown composition.

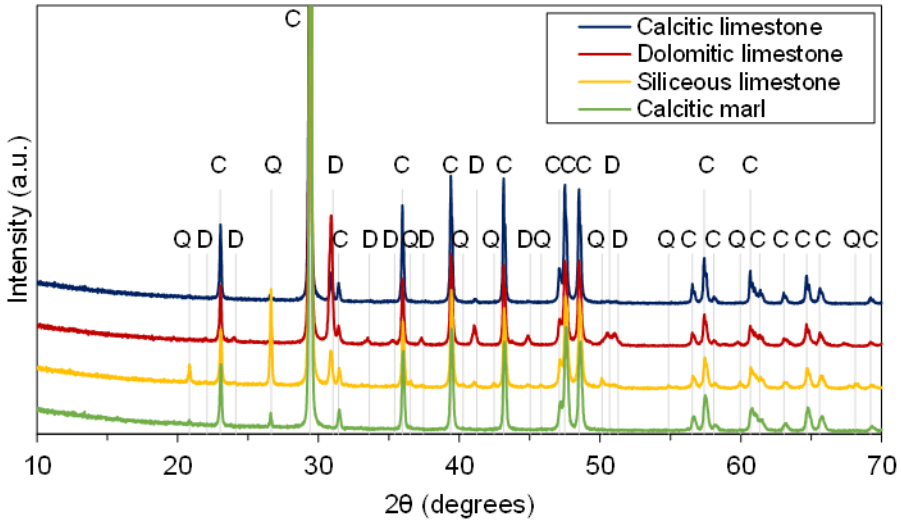

Figure 5.5. XRD patterns for limestone samples. (C = calcite, D = dolomite, Q = quartz)

Table 5.4. Crystalline limestone mineralogy, as determined by Rietveld analysis of XRD patterns.

Component	Chemical Formula	Calcitic Limestone	Dolomitic Limestone	Siliceous Limestone	Calcitic Marl
Calcite	$CaCO_3$	99.6%	74.8%	91.0%	99.6%
Dolomite	$CaMg(CO_3)_2$	0.4%	25.1%	5.4%	--
Quartz	SiO_2	--	< 0.1%	3.6%	0.4%

Table 5.5. Estimated limestone composition, adjusted for amorphous content.

Component	Chemical Formula	Calcitic Limestone	Dolomitic Limestone	Siliceous Limestone	Calcitic Marl
CO_2 content	CO_2	43.1%	43.6%	39.5%	42.0%
Calcite	$CaCO_3$	97.7%	72.7%	84.4%	95.6%
Dolomite	$CaMg(CO_3)_2$	0.4%	24.4%	5.0%	--
Quartz	SiO_2	--	< 0.1%	3.3%	0.4%
Amorphous	--	1.9%	2.8%	7.3%	4.0%

5.3.3 Specific gravity

Finally, the specific gravity (SG) of each powder was determined by displacement in kerosene at 23°C, according to ASTM C188 [57]. The measured specific gravities for the limestone, shown in Table 5.6, were found to be approximately 2.70, a typical value for limestone due to its high calcite content (SG = 2.71) [32]. Quartz was found to have a specific gravity of 2.65, as indicated by the supplier.

Table 5.6. Specific gravity of filler materials , measured by ASTM C188.

Cement	Calcitic Limestone	Dolomitic Limestone	Siliceous Limestone	Calcitic Marl	Quartz
3.17	2.70	2.70	2.69	2.70	2.65

5.4 Methods

5.4.1 Mix preparation

Seven cement pastes, each with *w/b* = 0.40, were prepared in small batches to investigate the influence of limestone mineralogy on hydration and early-age microstructural development. Four of the pastes contained a 10% mass substitution of cement by limestone, two contained a 10% mass substitution of cement by quartz, and one contained no added filler.

The cement, water, and filler were each weighed and added separately to the mixing vessel. The filler and water were combined first and sonicated for 5 minutes to ensure uniform dispersion of the material in the water. The filler solution was further agitated using a five-speed hand mixer at medium speed for 60 seconds. (These two steps were omitted when no filler was used.) Cement was then added to the solution, stirred by hand for 30 seconds, and then stirred mechanically with the hand mixer at low speed for 60 seconds and at medium speed for 60 seconds.

5.4.2 Isothermal calorimetry

The influence of the limestone fillers on hydration kinetics was investigated using isothermal calorimetry (ASTM C1698 [86]). Cement pastes were prepared in 70 g batches using the mixing procedure previously described. 7.0 ± 0.5 g of each paste was added to a high-density polyethylene (HDPE) ampoule and inserted into the calorimeter (TA Instruments TAM Air), which was maintained at a constant 25°C. The heat released from each ampoule was recorded at 1 minute intervals for 7 days. The results were integrated to determine the cumulative heat of hydration for each cement paste, which was then used to estimate the degree of hydration using the method of Schindler and Folliard (Equations 3.4 and 3.5) [64]. For the control OPC paste, the total cumulative heat of hydration, $H_{\infty,}$ was taken to be 439.2 J/g, and for the six blended cement pastes, H_{∞} was taken to be 90% of the OPC value, 395.3 J/g.

5.4.3 Chemical shrinkage

The influence of limestone fillers on early-age chemical shrinkage was investigated using the ASTM C1608 chemical shrinkage test [85]. Cement pastes were prepared in 84 g batches using the mixing procedure previously described. 9.5 ± 0.5 g of paste was added to each of at least three glass vials, which were assembled and tested as described in Section 4.2. A control set of empty vials, containing only de-aerated water, was also monitored so that any incidental effects related to evaporation of water from the vials could be subtracted prior to analysis of the pastes.

5.4.4 Thermogravimetric analysis

Chemical evolution of the hydrating cement pastes was monitored using thermogravimetric analysis (TGA). Cement pastes were prepared in 70 g batches and cast into 6 cubes measuring approximately 1 cm on each side. After 24 hr, the cubes were removed from their molds and cured in sealed bags at 25°C for up to 28 days. After 1, 3, 7, 14, and 28 days of hydration, one of the cubes was removed from the environmental chamber and crushed into a coarse powder (< 2.36 mm). Hydration of the powder was halted by solvent exchange in isopropanol for 15 minutes, followed by drying over vacuum for 5 minutes. The powder was further ground using a mortar and pestle until it passed a No. 100 sieve (< 150 μm).

20 mg samples of each powderized cement paste were heated under N_2 environment in a Hitachi EXSTAR TG/DTA 7300. The temperature of the samples was gradually increased from 25°C to 900°C at a constant rate of 10°C/min. The mass

fraction of calcium hydroxide was determined from the mass lost between 400-450°C, normalized by the mass of the sample at 25°C:

$$\%\ \mathrm{Ca(OH)_2} = \frac{m_{400} - m_{450}}{m_{25}} \times \frac{MW_{Ca(OH)_2}}{MW_{H_2O}} \times 100\% \tag{5.2}$$

where the molecular weights of $Ca(OH)_2$ and H_2O were taken to be 74.09 g/mol and 18.01 g/mol, respectively. The mass fraction of unreacted limestone remaining in the sample was determined from the CO_2 content of the cement paste (taken as the mass lost between 600-750°C, normalized by the mass of the sample at 25°C), divided by the CO_2 content of the raw limestone given in Table 5.5:

$$\%\ \mathrm{CO_2\ in\ paste} = \frac{m_{600} - m_{750}}{m_{25}} \times 100\% \tag{5.3}$$

$$\%\ \mathrm{limestone} = \frac{\%\mathrm{CO_2\ in\ paste}}{\%\mathrm{CO_2\ in\ limestone}} \times 100\% \tag{5.4}$$

5.5 Experimental results

The hydration kinetics, chemical evolution, and early-age shrinkage were evaluated for the six blended cement pastes in order to determine the chemical effects of limestone fillers in general, and the relative influence of the limestone's specific geological source and mineralogical composition. The physical effects of limestone fillers can be isolated from their chemical effects by comparing the results obtained for each limestone blended cement paste to an inert quartz blended cement paste having a similar particle size distribution. The effects of limestone mineralogy can be assessed by comparing the four limestone-blended cement pastes to each another, with the calcitic limestone source serving as a control mixture.

5.5.1 Hydration kinetics

The influence of limestone geology on hydration kinetics was investigated using isothermal calorimetry. The rates of heat evolution for the four limestone blended cement pastes (Figure 5.6) indicate that all four limestone powders accelerate hydration relative to the control OPC paste mixture. The acceleration of the reaction, as measured by the time to the inflection point between the C_3S and C_3A peaks, ranged from 44 min (calcitic limestone) to 88 min (siliceous limestone), with an average acceleration of 70 min. Such an acceleration was anticipated due to the finer grinding of the limestone powders (see Chapter 3); however, the extent of the acceleration was much greater than for the quartz powders, which, despite their similar fineness to the limestone powders, only accelerated the C_3S and C_3A hydration by 27 min (Quartz 15) and 28 min (Quartz 15/5). Oey, et al., [30] found similar trends in their investigation of filler and nucleation effects for limestone and quartz powders and suggested that limestone accelerates hydration more than quartz because its surface chemistry provides more favorable sites for heterogeneous nucleation of hydration products. However, their analyses did not consider potential differences in the morphologies of the limestone and quartz powders, which could also contribute to such an enhancement of the surface nucleation effect.

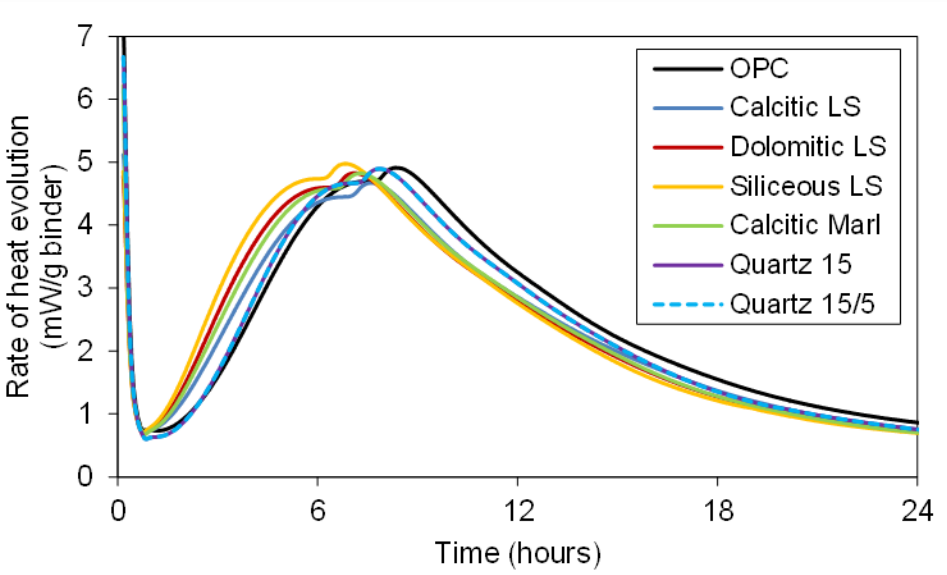

Figure 5.6. Rate of heat evolution for custom blended cement pastes at *w/b* = 0.40 and 25°C, through 24 hr. All fillers were dosed at a 10% substitution of cement, by mass.

To determine whether differences in surface morphology may have additionally influenced the heterogeneous nucleation potential of the limestone and quartz powders, each of the six powders was further examined using a Hitachi S-3700N variable pressure scanning electron microscope (VP-SEM) with a 15 kV accelerating voltage and 25 Pa chamber pressure. Representative backscattered electron (BSE) images acquired for each powder are shown in Figure 5.7 (limestone) and Figure 5.8 (quartz). The BSE images indicate that each of the limestone powders is composed of irregular, textured particles, characterized by substantial cleavage and surface roughness, while the quartz powders are composed instead of comparatively smoother particles, characterized by conchoidal fracture surfaces, as is typical for quartz [104]. The morphological differences between the two types of filler suggest that the enhanced heterogeneous nucleation potential of limestone fillers may be at least partially influenced by their increased surface roughness, and not strictly to differences in surface chemistry, as originally proposed. The increased

roughness of the limestone powders would provide additional sites for heterogeneous nucleation to occur – much more than would be suggested from their laser diffraction specific surface area estimates (which are based on a spherical particle assumption). Thus, it is possible that the enhanced "nucleating ability" of the limestone powders that was observed by Oey, et al., may be due – at least, in part – to the increased specific surface area of the limestone powders, and not strictly due to the limestone having a more favorable surface chemistry.

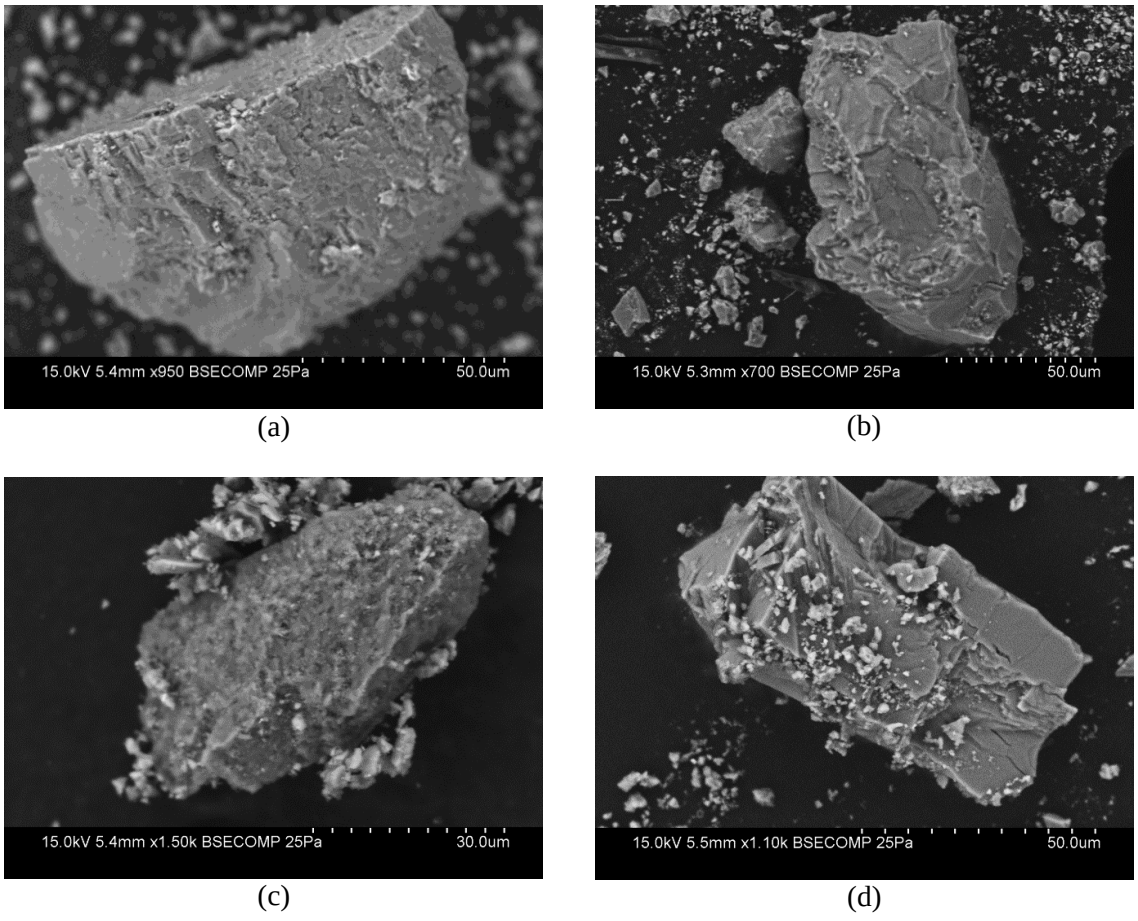

Figure 5.7. SEM images of limestone powders. (a) Calcitic limestone (950× magnification), (b), dolomitic limestone (700×), (c) siliceous limestone (1500×), and (d) calcitic marl (1100×).

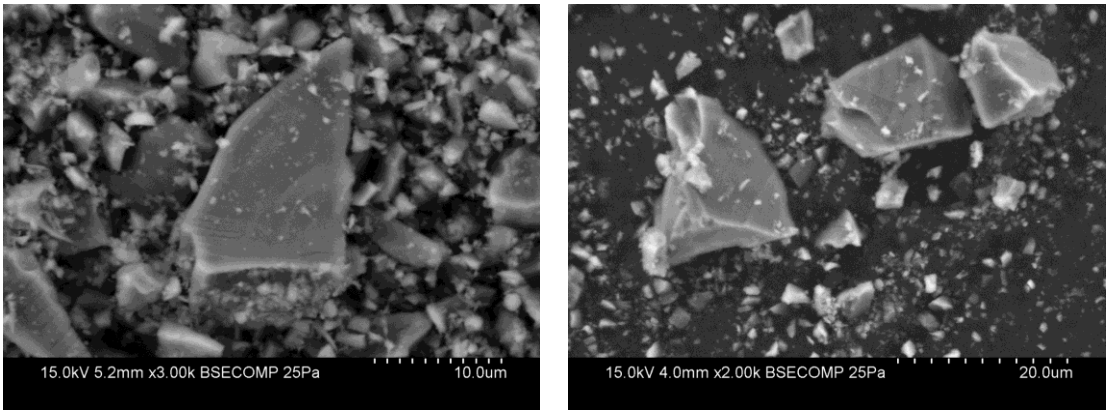

(a) (b)

Figure 5.8. SEM images of quartz powders at (a) 3000× and (b) 2000× magnification.

Comparing the four limestone powders to one another, it can also be observed in Figure 5.6 that each of the powders accelerates the C_3S and C_3A hydration to a different extent. The siliceous limestone has the most accelerating effect, while the calcitic limestone has the least accelerating effect. Based on the findings already presented in this section and in Chapter 3, it is proposed that the differences in acceleration are either a function of (1) the slightly different finenesses of the limestone powders, or (2) the slightly different surface properties (i.e., surface chemistry and roughness) of the limestone powders.

To determine if the different accelerations of the four limestone blended cement pastes is related to slight variations in limestone fineness, the magnitude of each acceleration was plotted against the powders' median particle size (Figure 5.9). The peak acceleration was found to increase with increasing limestone fineness (decreasing median particle size), with all four limestones following approximately the same linear trend. The quartz powders also followed a linear trend, but one that was separate from that exhibited by the limestone powders, further supporting the observation that quartz powders have different surface nucleation properties than the limestone powders. However, since all

four limestone powders follow a trends to one another, it is possible that the surface properties of the four limestones are all similar to one another such that the observed differences in hydration behavior at early ages is primarily related to the overall increase in surface area for the system, rather than to any changes in limestone morphology or surface chemistry.

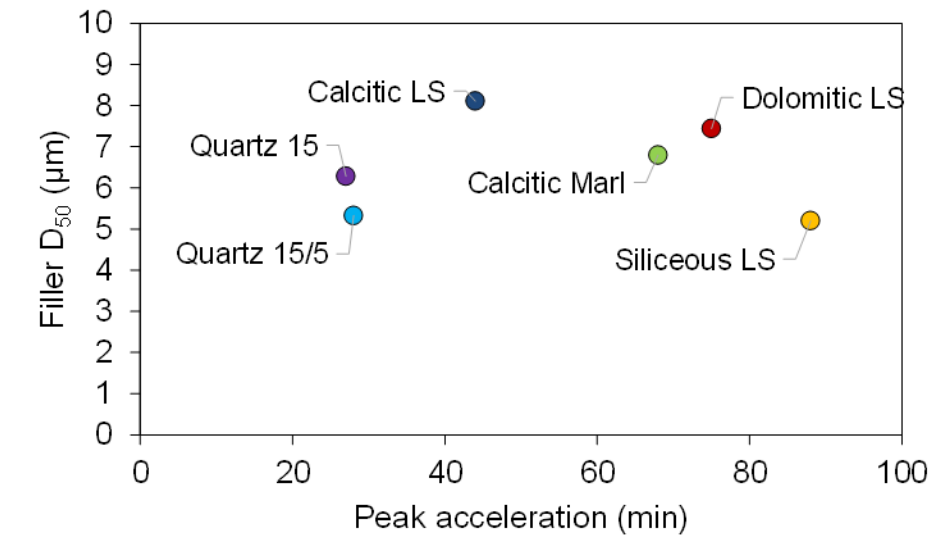

Figure 5.9. Hydration acceleration versus median particle size (D_{50}) of filler.

While the hydration at very early ages appears to be primarily a function of the size and surface properties of the filler used, after about 24 hr of hydration, it is the relative lack of reactivity of the filler that appears to play a more significant role in hydration behavior. In the cumulative heat curves shown in Figure 5.10, all six of the blended cement pastes showed a reduction in total heat release at 7 days, with the limestone blends showing an average 7.8% decrease in cumulative heat release and the quartz blends showing an average 5.5% decrease in cumulative heat release, relative to the control OPC paste. The heats of hydration for the four limestone cement pastes were all within one standard deviation (0.5%) of the mean, suggesting that the later-age

hydration *rate* for the four limestone cement pastes is primarily dominated by dilution effects rather than any differences arising from the compositions of the limestones themselves.

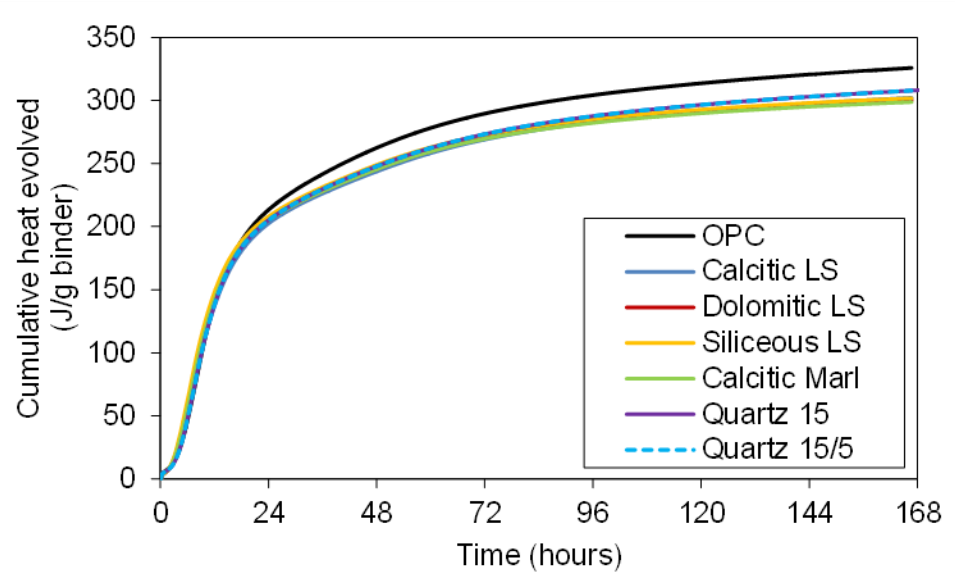

Figure 5.10. Cumulative heat of hydration for custom blended cement pastes at *w/b* = 0.40 and 25°C, through 7 days (168 hr). All fillers were dosed at a 10% substitution of cement, by mass.

Finally, the degree of hydration results shown in Figure 5.11 indicate that all six fillers increase the degree of hydration of the clinker relative to the OPC control paste. Each of the four limestone powders increased degree of hydration by an average of 1.8% (SD = 0.4%), while the quartz powders increased degree of hydration by an average of 3.7%. As discussed in Chapter 3, the increase in degree of hydration for the blended cement pastes can be attributed primarily to the greater availability of water for hydration as a result of the dilution effects. It is hypothesized that the quartz powders show slightly greater increases in degree of hydration than the limestone powders as a consequence of secondary AFm reactions. For each mole of C_3A that reacts to form secondary AFm

phases, 11 and 11.5 moles of water are consumed to form mono- and hemicarbonate, respectively, while only 4 moles of water are consumed to form monosulfate. Although the quantities of AFm phases formed by 7 days are typically small, the decreased availability of water in the limestone cement pastes relative to the quartz cement pastes could slightly reduce the ability of other clinker phases to hydrate, leading to a smaller increase in degree of hydration when compared to purely a diluted (quartz-blended) system.

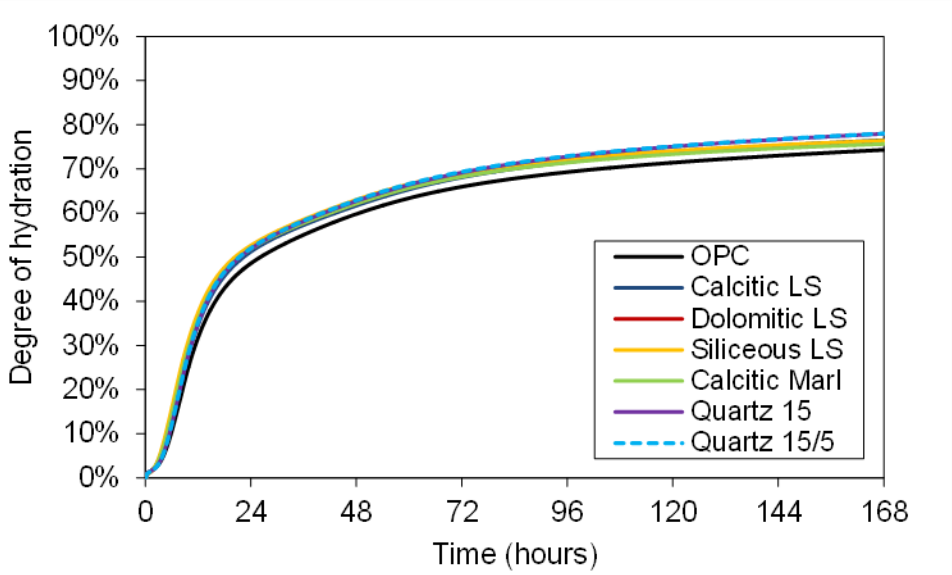

Figure 5.11. Degree of hydration for custom blended cement pastes at *w/b* = 0.40 and 25°C, through 7 days (168 hr). All fillers were dosed at a 10% substitution of cement, by mass.

5.5.2 Chemical shrinkage

The results of the chemical shrinkage test, in both measured units of mL per g binder and derived units of percent of original paste volume (see Section 4.3), are shown in Figure 5.12 and Figure 5.13, respectively. For clarity, error bars are not shown, but the average coefficient of variation for each cement paste over the 7 day testing period was found to be less than 3.4%.

Like cumulative heat, all six blended cement pastes experienced a reduction in chemical shrinkage relative to the OPC control mixture as a consequence of the binder dilution. A 10% mass substitution by each of the four limestone powders reduced the 7-day chemical shrinkage by an average of 0.29% (SD = 0.09%) of the starting volume, or about 4.6% (SD = 1.5%) of the total chemical shrinkage observed for the control OPC paste over the first 7 days. The calcitic marl showed the greatest reduction in chemical shrinkage, experiencing 0.4% less chemical shrinkage by volume (or a relative 6.5% of the total) compared to the OPC paste. By comparison, the siliceous limestone and the quartz powders both reduced chemical shrinkage by only 0.2% of the starting volume (a relative decrease of 3.0%) compared to the OPC control mixture.

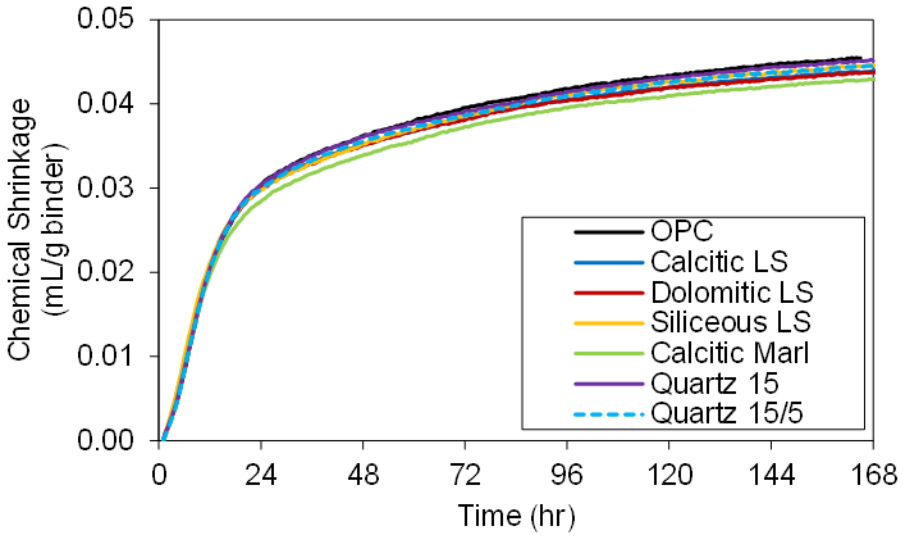

Figure 5.12. Chemical shrinkage of blended cement pastes at *w/b* = 0.40 and 25°C, through 7 days (168 hr). All fillers were dosed at a 10% substitution of cement, by mass.

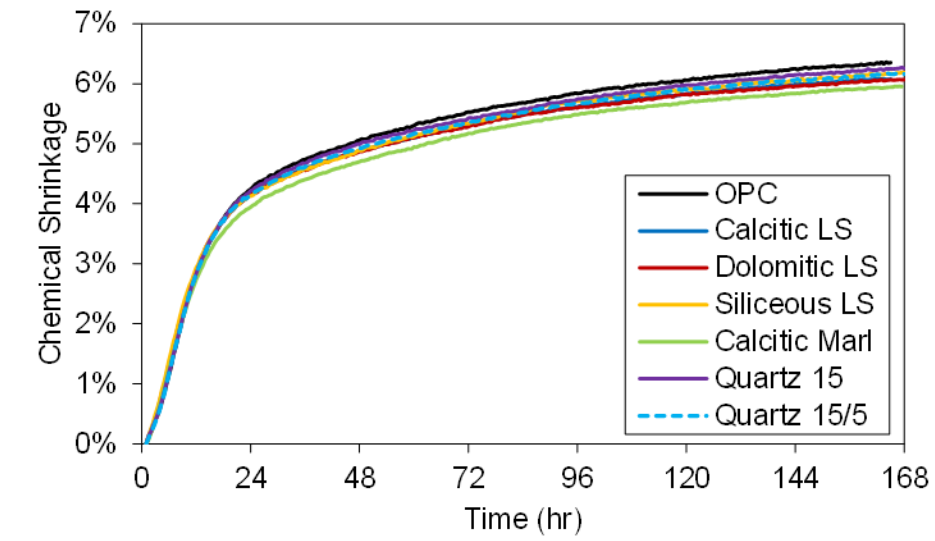

Figure 5.13. Chemical shrinkage of blended cement pastes as percentage of initial paste volume.

The trends in chemical shrinkage are roughly proportional to the median particle size of the filler (Figure 5.14), suggesting that the primary differences between the chemical shrinkages are related to physical effects such as nucleation and dilution, rather than to chemical effects arising from the different limestone mineralogies. The one visible exception to this observed trend is the calcitic marl, which shows less chemical shrinkage than would be expected based on the physical properties of the limestone alone. It is hypothesized that the chemistry of the calcitic marl – perhaps its purported clay impurities – produce additional "dilution-like" effects that reduce the ability of the cement to hydrate.

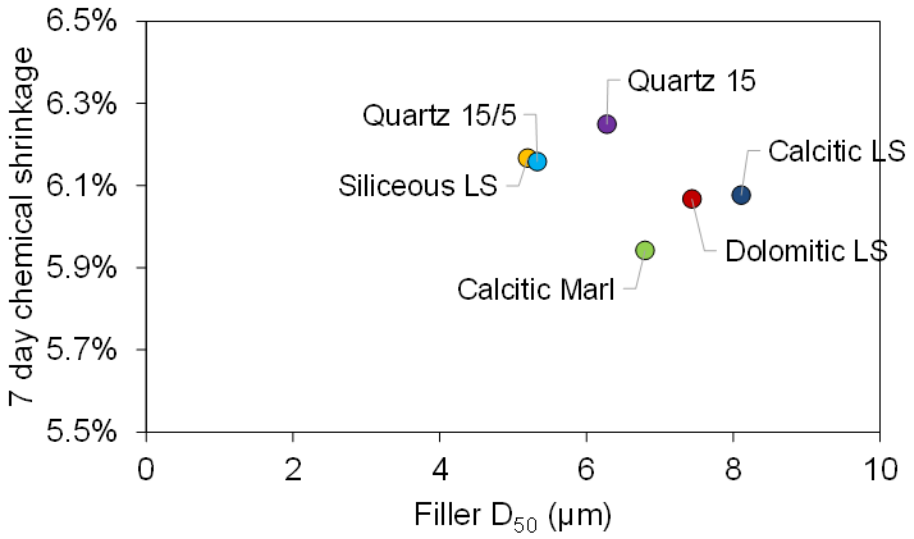

Figure 5.14. 7-day chemical shrinkage versus median particle size of filler, dosed at 10% by mass of cement.

5.5.3 Comparison to Powers' model

Chemical shrinkage was also plotted versus degree of hydration for each of the blended cement pastes to obtain Powers' model curves similar to the ones produced in Chapter 4. Theoretical values were computed according to Equation 4.6d, where the specific gravity of the binder was calculated from the measured specific gravities (Table 5.6) using the inverse rule of mixtures. The experimental results are compared to the theoretical Powers' model relationship in Figure 5.15.

Several observations can be made from the experimental Powers' curves regarding the physical and chemical influences of the different limestone powders. First, it was proposed in Chapter 4 that the dilution effect is evidenced by a decrease in the overall slope of the Powers' model curves; thus, the shallower slopes of the six blended cement pastes can be attributed to the dilution of the clinker by a relatively less reactive filler. While most of the paste mixtures show decreased slopes that are consistent with theoretical predictions, the calcitic marl mixture shows a much shallower slope than is

predicted by Powers' model, again suggesting a possible "dilution-like" effect related to the aluminosiliceous phases in the marl.

It was additionally proposed in Chapter 4 that secondary reactions of the clinker generate bilinear "knee-bends" in the experimental Powers' curves, such that the slope of the curve increases at some degree of hydration, $\alpha > 0$. For the commercially produced cements investigated in Chapter 4, a change in slope around $\alpha \approx 60\%$ was attributed to the formation of mono- and hemicarbonate AFm phases, and was experimentally validated through thermogravimetric and XRD analyses. For the custom blended cement pastes considered in this chapter, only the siliceous limestone blended cement paste showed a pronounced knee-bend, beginning around 70% hydration. The dolomitic limestone and calcitic marl showed very subtle upturns, also around 70% hydration, and the calcitic limestone and two quartz powders showed no upturn at all, suggesting that these powders either did not produce carbonate AFm phases or did not did not produce large enough quantities of carbonate AFm phases during the first 7 days of hydration to significantly change the slope of the curve. The increase in slope for the siliceous limestone powder does suggest a secondary reaction; however, since that limestone contains two potentially reactive components, further chemical analysis is required to determine if the secondary reaction indicated by the knee-bend is the reaction of the limestone to form carbonate AFm phases or the reaction of the opal within the limestone to form pozzolanic C-S-H.

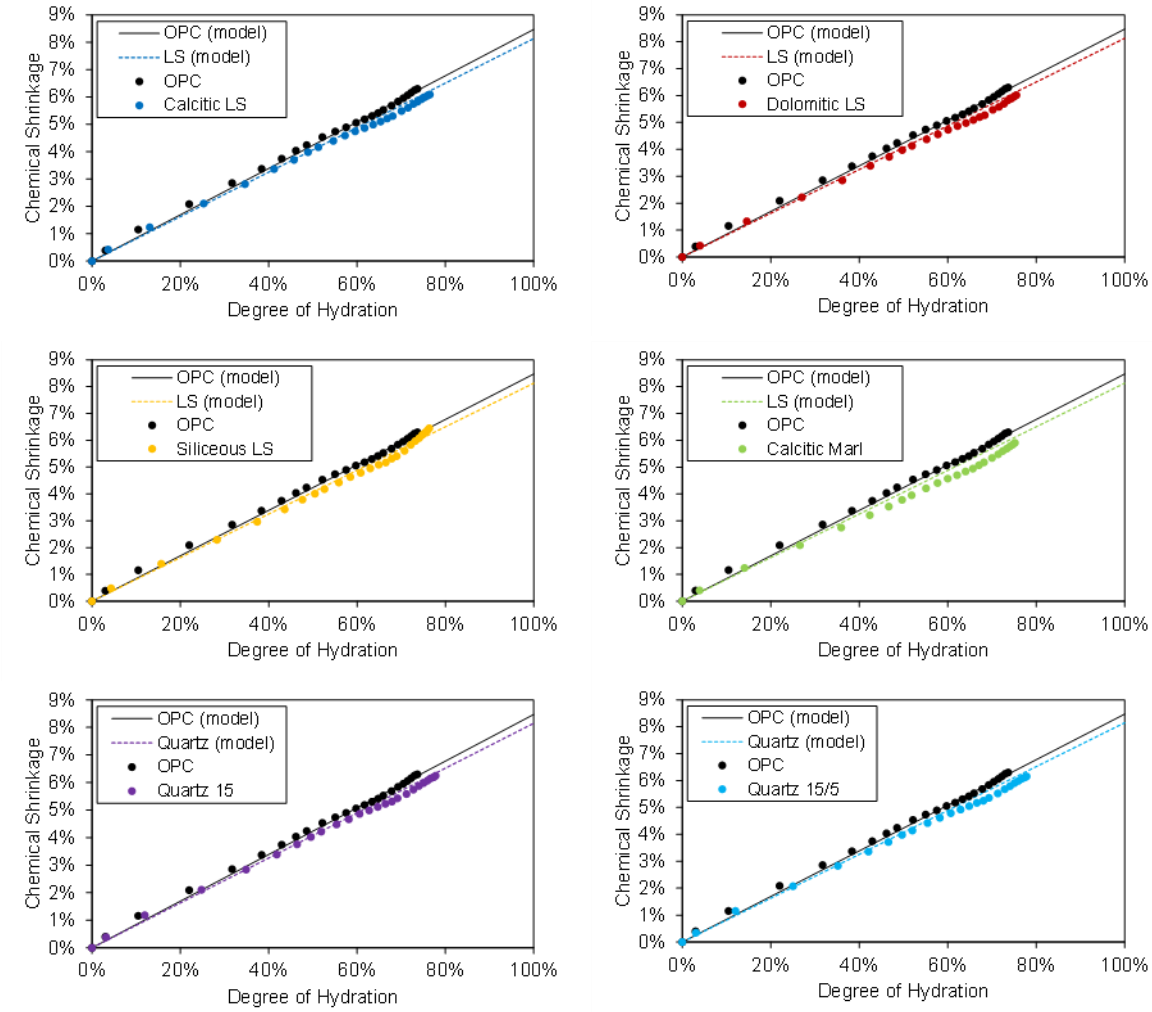

Figure 5.15. Comparison of experimental results to theoretical predictions made by Powers' model for custom blended cement pastes with *w/b* = 0.40, through 7 days (168 hr). All fillers were dosed at a 10% substitution of cement, by mass.

5.5.4 Chemical evolution

Chemical development of the cement pastes – focusing specifically on limestone reactivity and AFm formation – was assessed by TGA. It was determined that all four of the limestone powders exhibited partial reactivity with the cement clinker, as evidenced by their reduced quantities over time (Figure 5.16) and the subsequent formation of carbonate AFm phases (Figure 5.17). The siliceous limestone showed the greatest rate of

consumption (27% decrease in mass over 28 days), while the calcitic limestone showed the smallest rate of consumption (16% decrease in mass over 28 days). Most of the consumption occurred within the first 3 days of hydration, which was found in the thermogravimetric derivative (DTG) curves in Figure 5.17 to correspond to the initiation of carbonate AFm formation. In the OPC and the two quartz blended cement pastes, there was no carbonate AFm detected, but rather monosulfate was found to form instead. The formation of hemi- and monocarbonate phases in the four limestone blended cement pastes therefore indicates that the 10% substitution of limestone powder is sufficient to shift the thermodynamic equilibrium toward carbonate rather than sulfate AFm phases for the particular clinker chemistry investigated in this study.

By 28 days, not only is there a distinctive carbonate AFm peak for the four limestone pastes and a distinctive sulfate AFm peak for the OPC and quartz pastes, but there is also a clear difference in the height of the peak between approximately 50 and 100°C for the two groups of cement pastes. The region between 50 and 100°C primarily corresponds to the thermal decomposition of C-S-H and ettringite [66], and the difference in peak height is likely due to a difference in the amount of ettringite present in the two types of paste. In pastes without limestone, ettringite is consumed as it converts into monosulfate, decreasing the ettringite content with time and consequently reducing the height of the peak. In pastes with limestone, the calcium carbonate reacts instead to form mono- and hemicarbonate, leaving the ettringite content relatively unchanged. Thus, the relative differences in peak height may be indicative of the indirect stabilization of the ettringite by the calcium carbonate in the limestone.

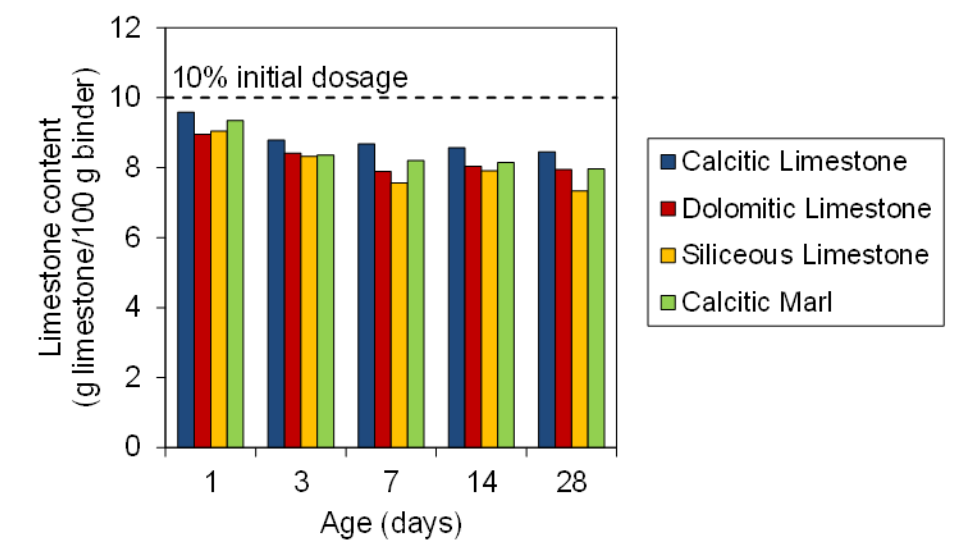

Figure 5.16. Limestone content of blended cement pastes, as determined by TGA.

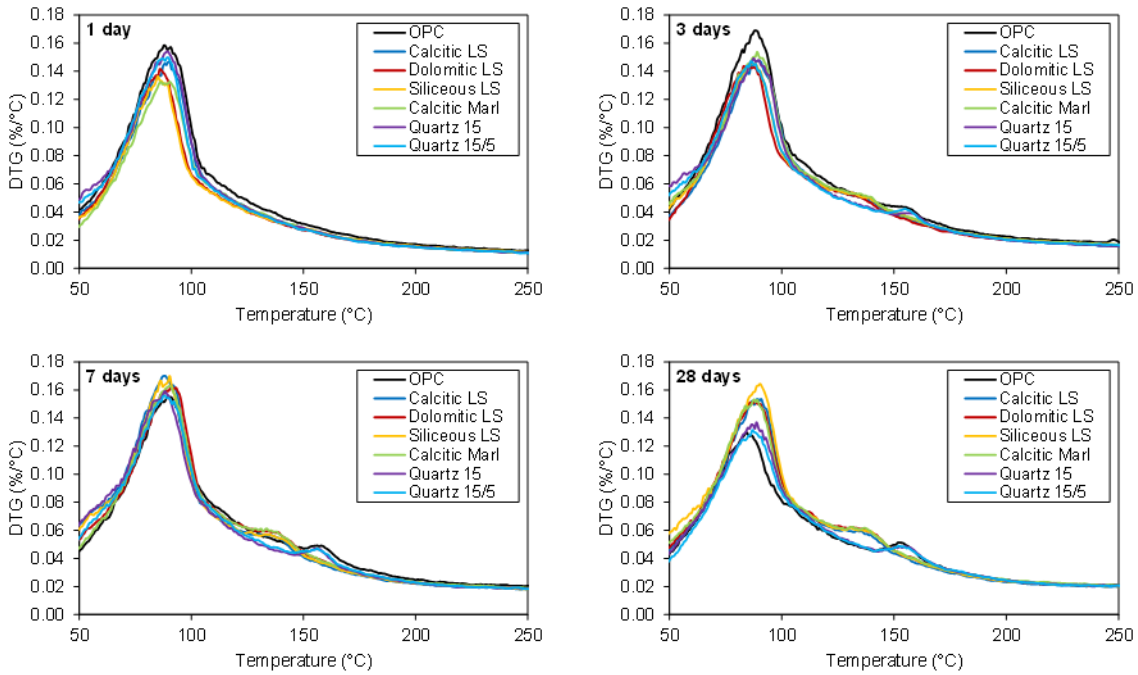

Figure 5.17. Thermogravimetric derivative (DTG) curves for laboratory-blended cement pastes at 1, 3, 7, and 28 days of hydration.

Figure 5.18 shows the measured calcium hydroxide (CH) contents for the seven cement pastes, normalized by the mass of cement in each paste to account for the dilution

of the clinker. Through the first 28 days, the CH contents of the OPC paste and the blended cement pastes show no significant differences from one another, indicating that nucleation effects and secondary hydration reactions have a minimal impact on the overall CH content of the blended cement pastes considered in this study. Most differences fall within the ± 0.4% CH error introduced by rounding masses to the nearest 0.01 g. The one exception is the 28 day CH content for the siliceous limestone, which is a full 1% less than the CH content for the quartz 15/5 blend. Since both blended cements had nearly identical particle size distributions, the difference in CH content at 28 days hints at pozzolanic reactivity for the siliceous limestone, but the evidence at early ages is inconclusive and warrants further investigation.

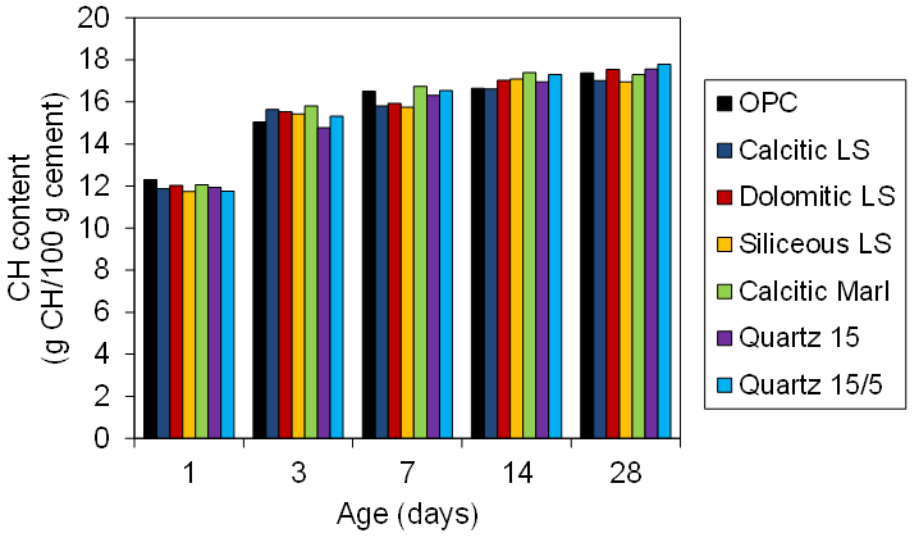

Figure 5.18. Calcium hydroxide (CH) content of blended cement pastes, as determined by TGA.

5.6 Discussion

The research presented in this chapter has two primary objectives: first, to examine the influence of limestone chemistry on cement hydration, and second, to

determine if limestones of different mineralogical composition affect cement hydration in significantly different ways.

With respect to the first objective, the calorimetric results provide compelling evidence that it is not only the increased fineness of the binder but also the unique surface properties of the limestone powder that makes it a more favorable site for heterogeneous nucleation of hydration products. Quartz fillers ground to a similar gradation as the limestone accelerated hydration by 30 minutes or less, while the limestone powders, on average, accelerated hydration by more than an hour. The trends observed for the four limestone powders in this study are consistent with trends observed by Oey, et al., [30] for blends made from pure calcite, providing additional support to the theory that nucleation phenomena are influenced both by the physical size (surface area) of the limestone powders and by the surface properties (surface energy and surface roughness) of the limestone itself.

The results further demonstrate that the presence of limestone favors the formation of AFm phases hemi- and monocarbonate over monosulfate. Although several researchers have previously shown that carbonate AFm phases form in limestone-blended cement pastes [19, 20, 61, 95-97], the consequences of such formation on degree of hydration and chemical shrinkage have largely been ignored. In this study, however, it was found that the two quartz blended cement pastes increased degree of hydration by a factor more than double that of the four limestone blended cement pastes by 7 days (3.7% for quartz versus only 1.8% for limestone). Since the particle size distributions among the six powders were similar, the relatively reduced degree of hydration for the limestone blended cement pastes must be related to the composition of the limestone filler. It is

proposed that the increased degree of hydration arising from the dilution of the clinker (as shown by the two quartz pastes) is offset in the limestone cement pastes by the nearly three-fold increase in water uptake by the carbonate AFm phases relative to monosulfate. The greater consumption of water by the hemi- and monocarbonate reduces the amount of water available for later hydration of other clinker phases, and consequently reduces the maximum degree of hydration achievable for limestone-blended cement pastes. Thus, degree of hydration does not change simply as a function of the physical dilution of the cement paste as previously assumed, but is also influenced by the chemical changes to secondary AFm formation caused by the limestone inclusions.

Similarly, the results from this study also demonstrate that formation of carbonate AFm products has a subtle but potentially significant impact on chemical shrinkage. As was discussed at length in Chapter 4, the formation of hemi- and monocarbonate phases beginning around 3 days of hydration (Figure 5.17) generates approximately 5 times more chemical shrinkage than the formation of monosulfate does. Because approximately the same amount of the clinker has reacted, yielding the same degree of hydration, the increase in chemical shrinkage causes an upturn in the Powers' model curves for chemical shrinkage, as shown in Figure 5.15. Most of the limestone-blended cement pastes showed such an upturn, although the magnitude of the upturn was less than was observed in Chapter 4 for the commercially produced cements. The presence of the upturn suggests that chemical shrinkage is, in fact, increased due to the formation of hemi- and monocarbonate, but the smaller magnitude suggests that there is less carbonate

AFm forming by 7 days for these particular blends than was observed for the commercial cements.[10]

With respect to the second objective of this study, the limestone mineralogy appears to play only a subtle role in the early-age hydration of the limestone blended cement pastes. Overall, the differences between the four limestone powders were minimal and primarily found to be a function of the subtly different gradations obtained for each powder. The predominant chemistry of the limestone ($CaCO_3$) and the physical artifacts arising from the various particle sizes appeared to be, on average, significantly more impactful on early-age hydration than were any of the more subtle differences in surface chemistry (nucleation effects) or reactivity (AFm formation).

The most distinct effects can be observed in the Powers' model curves of Figure 5.15, wherein the siliceous limestone exhibits the most pronounced change in slope after about 70% hydration and the calcitic marl exhibits a more pronounced dilution effect than predicted by the model. The siliceous limestone is known from previous laboratory and field studies to react with the alkalis within the cement to produce a gel-like product [100, 101], but when alkali-reactive materials are finely ground, like the limestone in this study, the gel-like product can be similar to pozzolanic C-S-H [103]. The slight decrease in CH content for the siliceous limestone at 28 days could indicate a pozzolanic reaction, but the difference is comparable in magnitude to the sensitivity of the test and cannot firmly establish whether a pozzolanic reaction is occurring. Although pozzolanicity cannot be confirmed, it is nonetheless evident from both the Powers' model analysis and

[10] Cement BL, which used the same base cement as this particular study, was found in Chapters 3 and 4 to exhibit a delayed AFm formation as a result of its comparatively higher gypsum content and lower C_3A content. It was hypothesized then that most of the AFm phase formed from secondary hydration of the slowly reacting C_4AF, rather than C_3A, phase.

the limestone contents measured by TGA that the siliceous limestone is more reactive than the other three limestone powders.

The Powers' model curves also indicate that calcitic marl has an increased "dilution-like" behavior compared to the other three more traditional limestones. Although it appears as though a similar proportion of the calcitic marl participates in the hydration reaction as for the other three powders, the magnitude of the chemical shrinkage is lower than would be expected for a limestone having that particular particle size distribution. Previous research has found that clay minerals can absorb water from the atmosphere or from the mixing water, leading to decreased workability and potentially delayed hydration [105, 106]. Both the cumulative heat and degree of hydration results for the calcitic marl were approximately one standard deviation below the mean for the four limestone powders, suggesting that the clay content may have slightly inhibited cement hydration, leading to the additional "dilution-like" behavior exhibited by the powder. However, since the differences are once again within the range of error for each test, further research examining a broader range of marls with varying clay contents would be necessary to provide additional support for this hypothesis.

5.7 Conclusions

This research examined the role of limestone mineralogy on early-age hydration of limestone cement-based materials. The physical effects of limestone fillers were isolated from their chemical effects by comparing the results obtained for each limestone blended cement to an inert quartz blended cement having a similar particle size distribution. By isolating the chemical effects, it could be observed that limestone has not

one, but two, primary effects on cement hydration related to its mineralogy. First, it was observed that the limestone encourages heterogeneous nucleation of hydration products to a greater extent than for quartz fillers, suggesting that the "nucleation effect" described in previous chapters is not purely physical in nature, but also dependent on the type and chemistry of the filler. While prior research by other authors suggested that this enhanced nucleation effect is due to the preferential surface chemistry of the limestone fillers, additional research conducted in this study suggests that increased roughness of the limestone surfaces due to cleavage during grinding could also contribute to the apparent affinity of hydration products to precipitate on the surfaces of the limestone particles. Second, the bulk chemistry of the limestone – and in particular, its $CaCO_3$ content – changes the chemical evolution of hydrated limestone cement pastes by forming mono- and hemicarbonate instead of converting ettringite into monosulfate. While this particular chemical effect is well-established in the literature, its implications into degree of hydration and chemical shrinkage had not been thoroughly explored. This study demonstrated that the chemical changes to the AFm hydration products can offset the increased degree of hydration arising from dilution effects and simultaneously increase the chemical shrinkage experienced by the paste at a particular degree of hydration.

Finally, it was found that mineralogy does have an impact on the early-age hydration of limestone blended cement pastes, but the chemical effects introduced by the mineralogical impurities tended to be small in comparison to the overall chemical and physical effects of the limestone fillers. While the siliceous limestone showed increased secondary reactivity and the calcitic marl showed decreased hydration rate beyond what was predicted by physical effects, their deviations from the mean behavior were not

statistically significant, and thus, no firm conclusions regarding mineralogical effects could be made. Additional research would be needed to clearly establish the pozzolanic potential of the siliceous limestone and the hydration inhibiting potential of the calcitic marl, but it is anticipated, based on the results of this study, that such effects are minimal in comparison to the other chemical and physical effects already established.

CHAPTER 6

INTERACTIONS WITH SUPPLEMENTARY CEMENTITIOUS MATERIALS

6.1 Introduction

The previous five chapters investigated the influence of finely divided limestone powders on the hydration and microstructural development of neat portland limestone cement systems – that is, systems that contain only the PLC and water. In practice, however, cements are frequently blended with supplementary cementitious materials (SCMs) such as fly ash and slag, which react with the products of cement hydration to yield concrete with higher strengths, more refined porosities, and longer service lives in aggressive environments [100, 107]. Since portland limestone cements are intended to be used as direct alternatives to ordinary portland cements in concrete applications, it is therefore necessary to investigate how interactions between SCMs and limestone affect the hydration rate, early-age shrinkage, and microstructural development in PLC-SCM systems.

Supplementary cementitious materials fall into two general categories, based on their reactivity: pozzolanic materials, which contain reactive (glassy) silicates and produce additional C-S-H by reacting with the calcium hydroxide product of cement hydration; and latent hydraulic (or self-cementing) materials, which contain reactive calcium silicates or that produce additional C-S-H by their own reaction with water [2, 40]. Most SCMs exhibit some combination of both pozzolanic and latent hydraulic reactivity. Low-calcium (Class F [108]) fly ash, for example, is primarily pozzolanic due to its high concentration of aluminosilicate glass, while high-calcium (Class C) fly ash is

both pozzolanic and latent hydraulic due to its high concentrations of aluminosilicate and calcium aluminosilicate glasses. Blast-furnace slag is similar to high-calcium fly ash and exhibits primarily hydraulic behavior due to its high concentrations of calcium silicate and calcium-aluminosilicate glass [2, 100].

In typical portland cement-SCM systems, the pozzolanic and latent hydraulic reactions produce additional C-S-H beyond what is produced by cement hydration. This secondary C-S-H further densifies the microstructural skeleton created by the cement hydration, leading to reductions in porosity and corresponding increases in strength and impermeability. Additionally, the consumption of CH by the pozzolanic reaction, the improved alkali-binding of the secondary C-S-H [2, 40], and the more efficient particle packing of finer SCMs [22] all further enhance the ability of SCM-blended systems to resist degradation, such that blends containing SCMs are often recommended (or required) for use in applications where the concrete may be exposed to aggressive environments [100].

Recent studies have shown that when SCMs are combined with portland limestone cements, even greater improvements in durability will result from further refinements in porosity and increases in strength and impermeability [19, 49-51]. It is believed that these enhancements (commonly referred to as “synergies” in the literature) occur as a result of chemical reactions between the limestone and the aluminosilicate and calcium aluminosilicate phases in the SCMs [19, 48, 109], with higher alumina loadings hypothesized to yield greater “synergetic” interactions between PLCs and SCMs. Although several researchers have shown that limestone-SCM interactions can improve the strength and permeability characteristics of concrete mixtures, less research has been

focused on their effects on early-age hydration rate and chemical and autogenous shrinkage. Since greater pore refinement often comes at the expense of greater autogenous shrinkage (Chapter 4), these SCM-limestone "synergies" could lead to increased potential for cracking that counteracts any improvements in durability caused by the decrease in permeability. The objective of the research presented in this chapter is therefore to evaluate combinations of portland limestone cements and alumina-bearing SCMs in order to better understand how synergies between the limestone and the SCMs affect the early-age hydration and microstructural development of PLC-SCM blends.

6.2 Materials

For this study, 33 cement paste mixtures and 12 concrete mixtures were developed using the eleven commercially produced cements discussed in Chapter 3, combined with either Class F fly ash, Class C fly ash, or blast-furnace slag. Since it was desirable to investigate portland limestone cements in combination with SCMs for real structural applications, each SCM was dosed at the maximum replacement levels currently permitted by local Georgia Department of Transportation (GDOT) specifications for concrete structures [110]: 15%, by weight, for each of the two fly ashes and 50%, by weight, for the slag.[11]

[11] GDOT Section 500 specifications permit replacements of fly ash at variable rates of 1.0-1.5 lb of fly ash to 1.0 lb of cement. Since an equivalent-mass substitution was used for this study in order to maintain a consistent *w/cm* for all mixes, 1.0 lb of fly ash was substituted for 1.0 lb of cement.

6.2.1 Composition

The oxide compositions (ASTM C114 [53]) for the three SCMs are shown in Table 6.1; trace amounts of Mn_2O_3, P_2O_5, SrO, and BaO were also found, but are not shown in the table. The high SiO_2 and low CaO content of the Class F fly ash suggest that it is primarily a pozzolanic material and will not hydrate until sufficient CH has been produced from primary cement hydration. Meanwhile, the SiO_2 and CaO contents of the Class C fly ash and the slag suggest that they are both primarily hydraulic materials, which can hydrate independently of the cement but more once sufficient CH has been produced. With respect to limestone synergies, the Class F fly ash contains the highest alumina (Al_2O_3) content at 23.3%, followed by the Class C fly ash at 18.8%, and the slag at 7.6%. Taking into account the different dosages used for the three SCMs, the total alumina loadings of the SCMs are found to be 3.5 g per 100 g cementitious material for the Class F fly ash, 2.8 g per 100 g cementitious material for the Class C fly ash, and 3.8 g per 100 g cementitious material for the slag. It is hypothesized that the higher alumina loadings for the Class F fly ash and slag blends will yield the greatest differences in early-age behavior for the Type I/II and Type IL cements.

Table 6.1. Chemical oxide analyses for SCMs. LOI indicates loss on ignition at 1000°C.

Component	Fly Ash (Class F)	Fly Ash (Class C)	Slag
SiO_2	51.30	34.57	38.77
Al_2O_3	23.32	18.78	7.62
Fe_2O_3	13.31	5.52	0.75
CaO	2.75	26.41	36.81
MgO	1.03	6.60	12.08
Na_2O	0.82	1.92	0.19
K_2O	2.43	0.47	0.48
TiO_2	1.25	1.39	0.26
SO_3	0.48	1.98	2.29
LOI	2.89	0.22	0.12

6.2.2 Particle Size

The particle size distributions of the three SCMs, as measured by laser diffraction in ethanol (Section 3.2.2), are shown in Figure 6.1 (differential) and Figure 6.2 (cumulative); cement A is shown in each figure for comparison. A summary of relevant parameters is given in Table 6.2.

The Class F fly ash was found to be the coarsest of the four materials, having a median particle size 50% larger than that of cement A and nearly double those of the Class C fly ash and slag. It has similar surface area parameters ($D_{3,2}$ and SSA) to the cement when smooth particles are assumed for both materials, but has roughly half the specific surface area of the other two SCMs. The slag was found to be the finest of the three SCMs, having a median particle size nearly 30% finer than cement A and almost twice the specific surface area. Some of the increase in specific surface area can be attributed to the lower density of the slag compared to the cement; however, much of the increase is due to the finer size of the slag particles, as further evidenced by the 40% reduction in surface mean particle size ($D_{3,2}$). Based on the particle size distributions, it is hypothesized that the finer Class C fly ash and slag blends will likely exhibit further microstructural refinements due to the physical influence of filler effects [22], but since the SCMs are chemically reactive, these physical effects are not anticipated to dominate the hydration behavior like they did for the neat PLC systems.

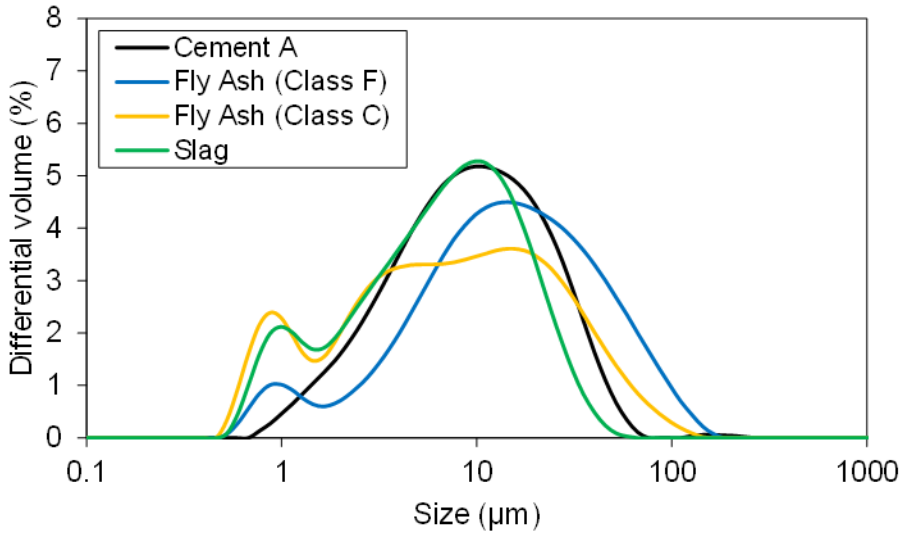

Figure 6.1. Differential particle size distributions for the three SCMs. Cement A is shown for comparison.

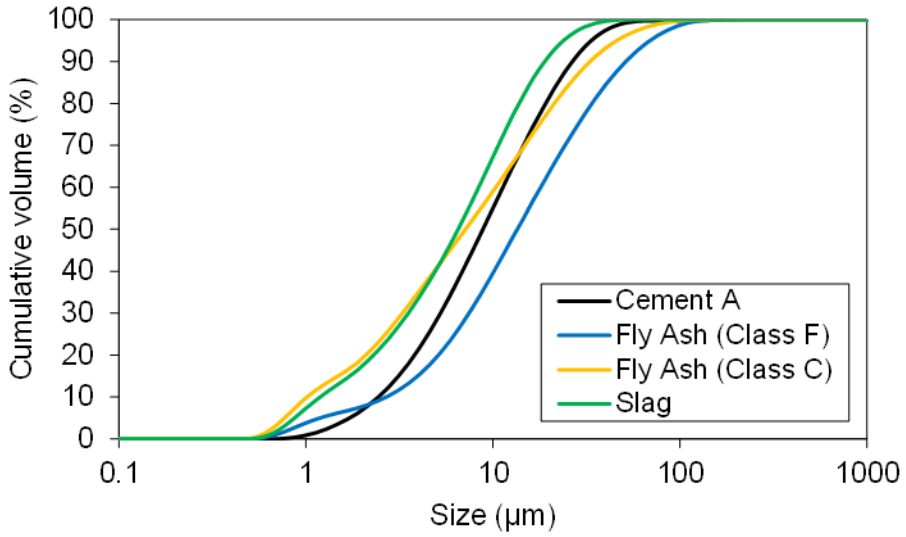

Figure 6.2. Cumulative particle size distributions for the three SCMs.Cement A is shown for comparison.

Table 6.2. Particle size distribution parameters for SCMs.Cement A is shown for comparison.

Parameter	Cement A	Fly Ash (Class F)	Fly Ash (Class C)	Slag
D_{10}, µm	2.77	3.05	1.15	1.35
D_{50}, µm	10.0	15.3	8.08	7.38
D_{90}, µm	30.2	58.3	37.5	21.4
$D_{3,2}$, µm	6.28	6.67	3.58	3.79
$D_{4,3}$, µm	14.1	24.3	15.0	9.78
SSA, m^2/kg	288	337	627	566

6.2.3 Specific gravity

The specific gravities of the three SCMs were measured by displacement in kerosene (ASTM C188 [57]) to be 2.35, 2.66, and 2.82 for the Class F fly ash, the Class C fly ash, and the slag, respectively. All three SCMs are lower in specific gravity than the Type I/II and Type IL cements (Table 3.3), indicating that an equivalent mass substitution will increase the volume of the binder phase in the cement paste. The SCM blended cement pastes are therefore hypothesized to exhibit some reductions in average particle size due to ancillary particle-packing/filler effects in addition to the reductions generated by their pozzolanic and hydraulic reactions [22].

6.3 Experimental methods

6.3.1 Preparation of cement paste

Thirty-three cement paste mixtures were prepared from the eleven cements and three SCMs at a water-to-cementitious materials ratio (*w/cm*) of 0.40, where the cementitious material was taken to be the combined Type I/II or Type IL cement and any SCM substitutions. The SCMs were first blended with the cement, then added to deionized water (18.2 MΩ-cm) and mixed following the procedures outlined in Chapter

3. Cement paste specimens were used for the investigation of hydration kinetics (isothermal calorimetry) and chemical and autogenous shrinkage.

6.3.2 Isothermal calorimetry

Isothermal calorimetry (ASTM C1679 [63]) was used to characterize the SCM-induced changes to hydration kinetics. Tests were performed on 7.0 ± 0.5 g of cement paste contained within high-density polyethylene (HDPE) ampules. Two replicate specimens of each mix were placed into a TAM Air isothermal calorimeter, held at 25°C for 72 hr. The rate of heat evolution was measured at 1 min intervals, and results were integrated to determine the cumulative heat of hydration over the 72 hr period.

The cumulative heat results were used to indirectly measure the degree of hydration of the SCM-blended cement pastes, using a similar procedure to that described in Section 3.3.2. For cement pastes containing additions of fly ash or slag, Equation 3.3 for the total heat of hydration at α = 100% (H_∞) was modified as follows [64]:

$$H_\infty = H_{cem} p_{cem} + H_{FA} p_{FA} + H_{slag} p_{slag} \quad (6.1)$$

where H_{cem} is the total heat of hydration for the cement, given in units of J/g by Equation 3.3; H_{FA} is the total heat of hydration of the fly ash, in units of J/g; H_{slag} is the total heat of hydration of the slag, assumed to be approximately 461 J/g [64]; and p_{cem}, p_{FA}, and p_{slag} are the mass fractions of cement, fly ash, and slag, respectively in the total cementitious binder. The total heat of hydration of fly ash depends on the mass fraction of CaO in the fly ash (p_{FACaO}), and can be approximated in units of J/g as [64]:

$$H_{FA} = 1800\, p_{FACaO} \quad (6.2)$$

The estimated values for H_∞ for the 33 blended cement pastes are given in Table 6.3; the values for neat cement pastes are shown for comparison, and are generally similar to

those of the blended cement pastes, with the exception of the Class F fly ash mixture, which releases less heat due to its lower CaO content.

Table 6.3. Predicted total heats of hydration, H_∞, for SCM-blended cement pastes, J/g cementitious material.

	A	AL	B	BL	C	CL	D	DL	E	EL
No SCMs	450.4	414.5	439.2	415.0	444.1	401.1	438.6	413.2	470.3	441.3
15% Fly Ash (Class F)	390.3	359.8	380.7	360.2	384.9	348.4	380.2	358.6	407.2	382.5
15% Fly Ash (Class C)	454.1	423.6	444.6	424.1	448.8	412.2	444.1	422.5	471.1	446.4
50% Slag	455.7	437.8	450.1	438.0	452.6	431.1	449.8	437.1	465.7	451.2

6.3.3 Chemical and autogenous shrinkage

Chemical shrinkage (ASTM C1608 [85]) was measured for the 33 blended cement pastes at 25°C, using the procedure described in Section 4.2. Measurements were recorded on a minimum of three replicate specimens, twice per hour for at least 48 hr, then once every 2 hr until 7 days. Units were converted from measured units of mL shrinkage per g of cementitious material to dimensionless % volume units, using Equation 4.3, where the specific gravity of the binder was found using the inverse rule of mixtures for the cements and SCM additions.

Autogenous shrinkage (ASTM C1698 [86]) was measured by monitoring the length change of three replicate corrugated tube specimens cast as described in Section 4.2. Testing was performed on pastes made with cements from sources A and C only, due to the longer duration of the test. Length change was recorded at 2 hr intervals from the time of final set until 12 hr of hydration, then once daily until 7 days, bi-weekly until 28 days, and weekly until 56 days.

6.3.4 Preparation of concrete specimens

Twelve concrete mixtures were also prepared using the cements from sources A and C, blended with the three SCMs at the replacement levels prescribed in Section 6.2. Mixtures were designed to meet the "worst-case" specifications for GDOT Class AA structural concrete [110], and were therefore mixed with the maximum permissible *w/cm* of 0.445, and the minimum total cementitious materials content of 635 lb/yd^3 (375 kg/m^3). Crushed granite coarse aggregates (Lithia Springs, GA; #67 stone, dry-rodded unit weight = 98 lb/ft^3, SG = 2.61) and natural sand fine aggregates (Byron, GA; fineness modulus = 2.4, SG = 2.65) were proportioned at 1889 lb/yd^3 (1120 kg/m^3) and 1260 lb/yd^3 (750 kg/m^3), respectively, for each of the 12 mixtures. A mid-range water reducer (Sika SikaPlast-300GP) was used at dosages of 10-14 fl.oz./100 lb of cementitious material to ensure adequate workability.

The raw materials were mixed in 5 ft^3 batches in a 9 ft^3 rotating drum mixer, following ASTM standard practices [111]. Twenty cylindrical specimens measuring 4 in. (diameter) by 8 in. (length) were cast from the mixtures for compressive strength testing. Specimens were removed from their molds 24 hr after casting and cured in a saturated calcium hydroxide (limewater) solution at 70 ± 3°F until testing.

6.3.5 Compressive strength

Compressive strength was measured for the concrete specimens after 1, 7, 28, 56, and 90 days of hydration, following the ASTM C39 testing specification [112]. Four specimens were tested at each age. Results were used to evaluate the purported "synergetic" effect of PLCs on the physical properties of SCM-blended mixtures.

6.4 Results

The interactions between PLCs and SCMs were monitored through a combination of hydration, shrinkage, and mechanical property studies. Hydration kinetics and chemical shrinkage were characterized to better understand how the interactions between the limestone and alumina-containing SCMs and affect early-age hydration processes, while autogenous shrinkage and compressive strength were characterized in order to indirectly evaluate how the limestone-SCM interactions affect microstructural development.

6.4.1 Hydration

The rates of heat evolution for the 33 cement pastes over the first 48 hr are shown in Figure 6.3, and the cumulative heats of hydration over the first 72 hr are shown in Figure 6.4; the calorimetric results for the eleven neat cement pastes are also shown for comparison. The results indicate that for all 33 mixtures, the partial substitution of cement by either fly ash or slag reduces the heat evolved relative to the neat cement paste mixtures throughout the first 72 hr of hydration, which would be expected given the slower rates of reaction of the three SCMs compared to the cement. By 72 hr, the cumulative heats released by the mixtures containing 15% Class F fly ash, 15% Class C fly ash, and 50% slag are reduced by an average of 10%, 5%, and 24%, respectively, when compared the neat cement paste controls. The reductions in heat evolution are less than the reduction in cement content, indicating that the three SCMs participate to some degree in the early-age hydration reactions.

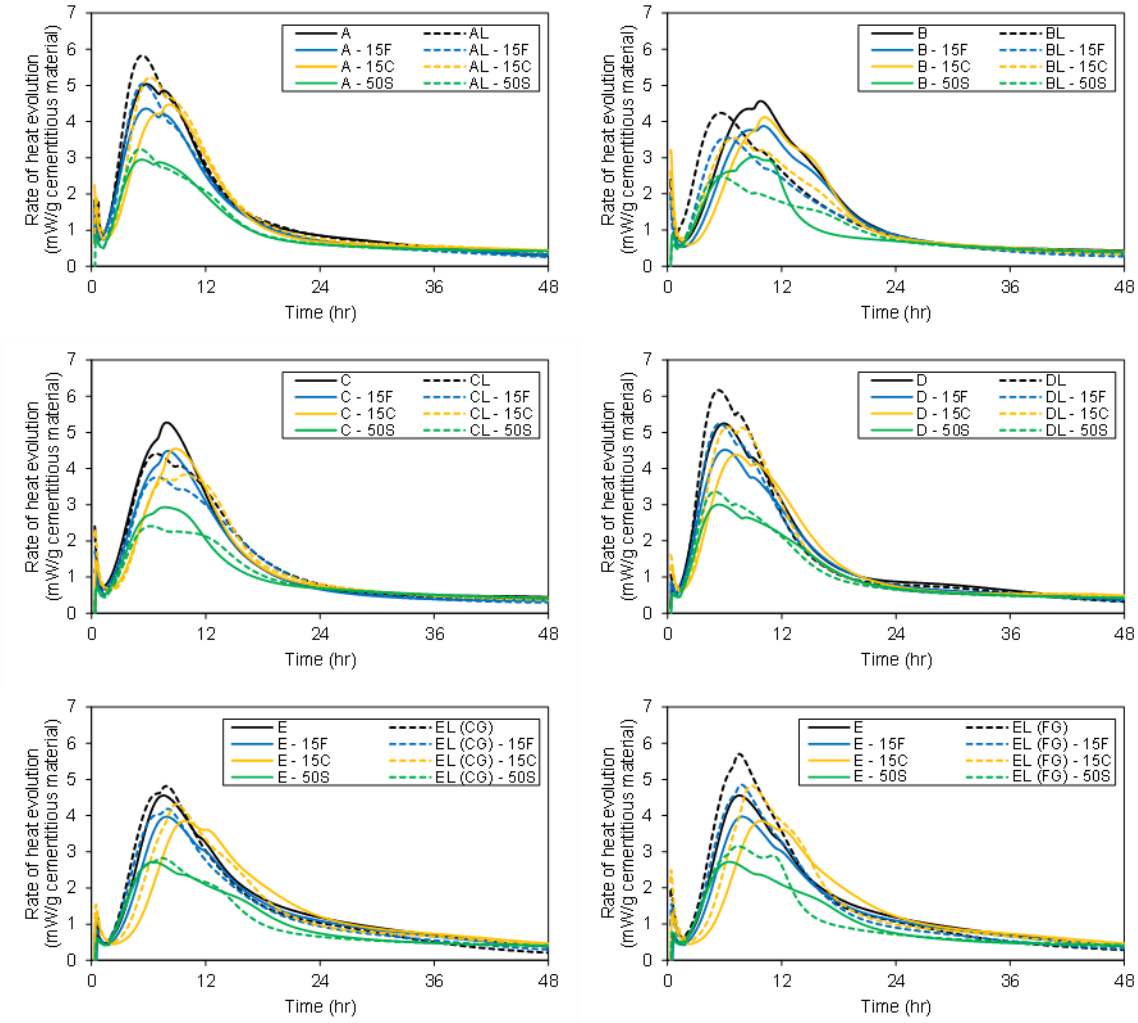

Figure 6.3. Rate of heat evolution for SCM-blended cement pastes, normalized by the mass of cementitious material.

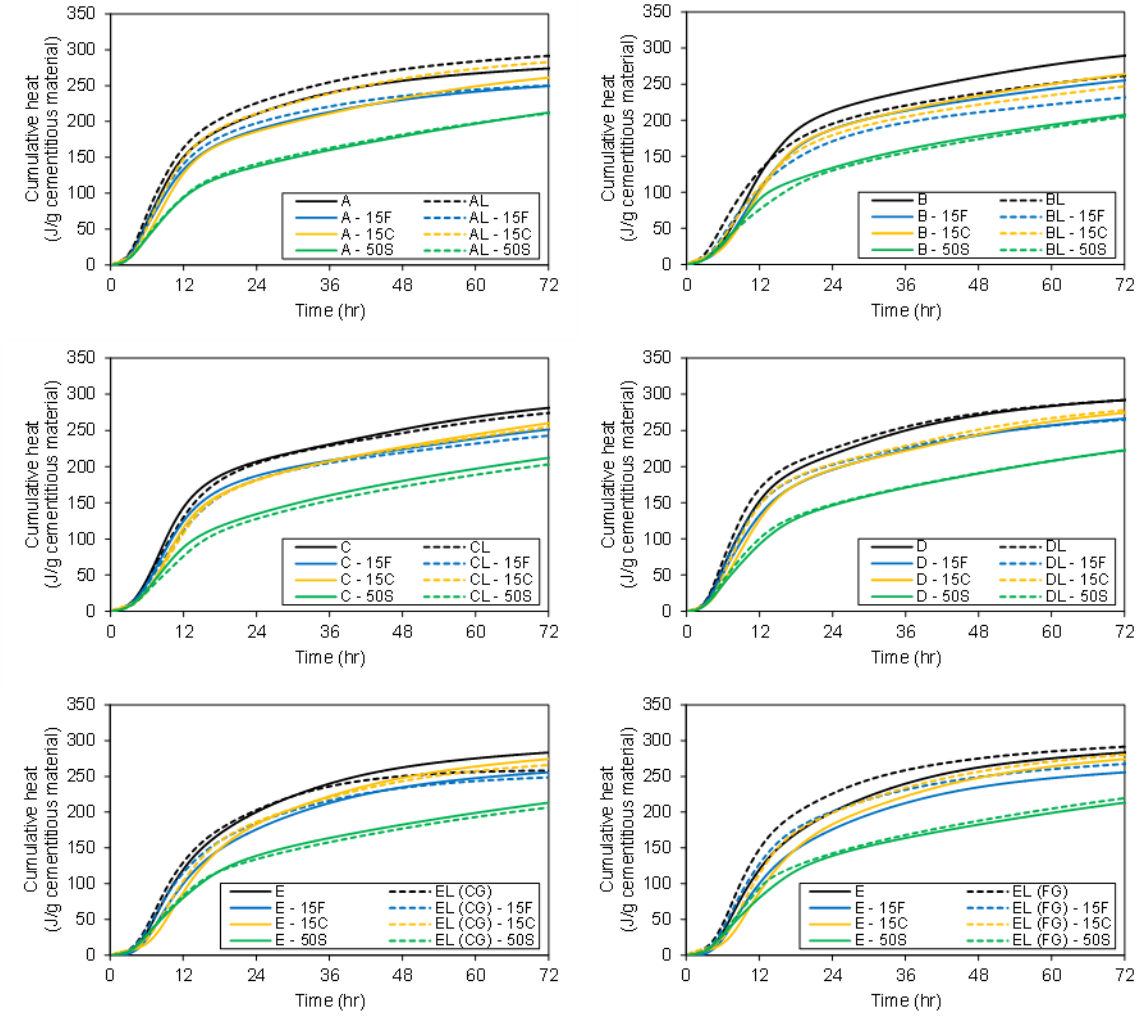

Figure 6.4. Cumulative heats of hydration for SCM-blended cement pastes, normalized by the mass of cementitious material.

The SCM-induced dilution effects can removed by normalizing the heat by the mass of Type I/II or Type IL cement in the paste, rather than by the total mass of cementitious material. It can be seen from the resulting curves in Figure 6.5 that slag increases the rate of heat release per gram of cement by 15.4% (SD = 6.8%), while the Class F and Class C fly ash have no significant effects on rate of heat release (increases of 0.8 ± 1.2% and 1.7 ± 3.2%, respectively). Thus, while most of the overall differences in hydration for the fly ash blended cement pastes appear to be related to the dilution of the cement by the more slowly reacting fly ash, the hydraulically reactive slag is found to contribute to the heat of hydration at early ages.

It can also be seen that the three SCMs each have a different accelerating or decelerating effect on hydration, as determined by the time to peak heat release. On average, it was found that a 15% substitution of cement by Class F fly ash delayed the time to peak heat release by less than 10 min, while a 50% substitution of cement by slag accelerated the time to peak heat release by approximately 25 min. By comparison, a 15% substitution of cement by Class C fly ash was found to have a significant retarding effect, delaying the time to peak heat release by more than 1 hour, on average. Since the slag and the Class C fly ash had similar (fine) particle size distributions, the retardation of the Class C fly ash mixtures is likely related to the chemistry of the fly ash, rather than to its particle size distribution.

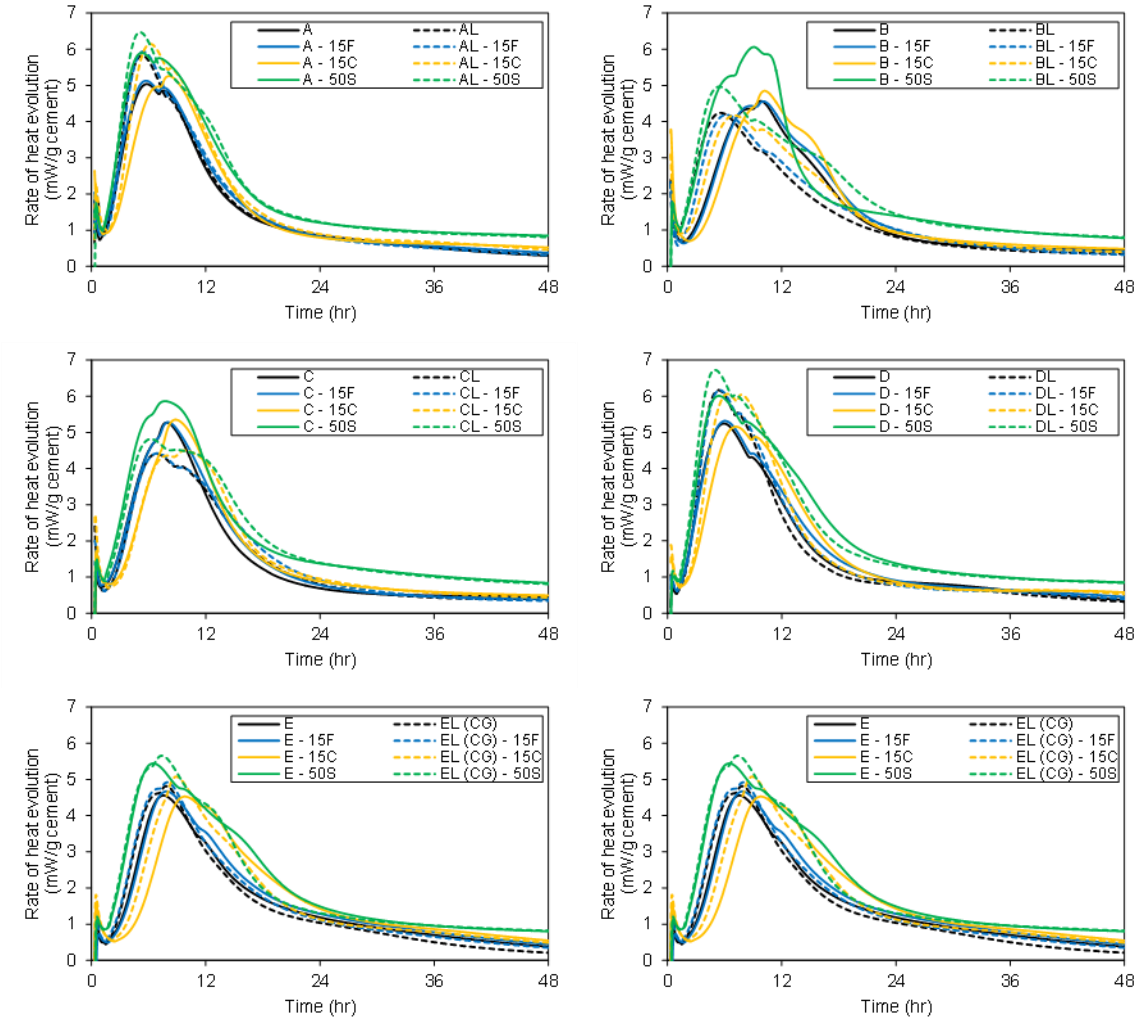

Figure 6.5. Rate of heat evolution for SCM-blended cement pastes, normalized by the mass of cement.

Comparing the Type I/II and Type IL cements to one another, it can be observed that the finer Type IL cements from sources A, D, and E again increase the heat released when combined with SCMs, while the coarser Type IL cements from sources B and C again decrease the heat released when combined with SCMs. The accelerating and decelerating effects of the SCMs were generally found to follow the particle size trends previously observed for the neat cement pastes, with slightly shorter delays (or more rapid accelerations) seen for finer cements AL, DL, and EL, and greater retardation (or

less rapid accelerations) seen for coarser cements BL and CL. Additionally, while the shapes of the heat release curves for the Type I/II cement pastes were generally consistent with one another – aside from stretching or compressing as dictated by retardation and acceleration, respectively – the shapes of the heat release curves for the Type IL blends were found to change depending on the type of SCM used. In particular, blends of Type IL cement with Class C fly ash generally showed a broadening of the peak typically associated with C_3A hydration, while the blends of Type IL cements with slag showed a third peak between 2 and 24 hr of hydration suggesting possible changes to the hydration of the C_3S and C_3A – or possibly other – phases. No significant changes in the shape of the heat evolution curves were observed for the mixtures containing Class F fly ash, suggesting that the limestone interactions with Class F fly ash are not as pronounced during the first 3 days of hydration.

Degree of hydration was computed from the cumulative heat results for the 33 cement paste mixtures to determine if the limestone-SCM interactions had any significant effects on cement hydration over the first 72 hr. It can be seen from the results in Figure 6.6 that by 72 hr of hydration, a 15% substitution of cement by Class F fly ash increases degree of hydration by an average of 4.0% (SD = 3.0%), a 15% substitution of cement by Class C fly ash reduces degree of hydration by an average of 6.1% (SD = 3.3%), and a 50% substitution of cement by slag reduces degree of hydration by 26.8% (SD = 3.2%). As with heat of hydration, there were no significant differences between the Type I/II and Type IL cement blends at 72 hr of hydration; however, for both cement sources, the Class C fly ash increased degree of hydration for the Type IL cement paste relative to the Type I/II cement paste, regardless of cement fineness.

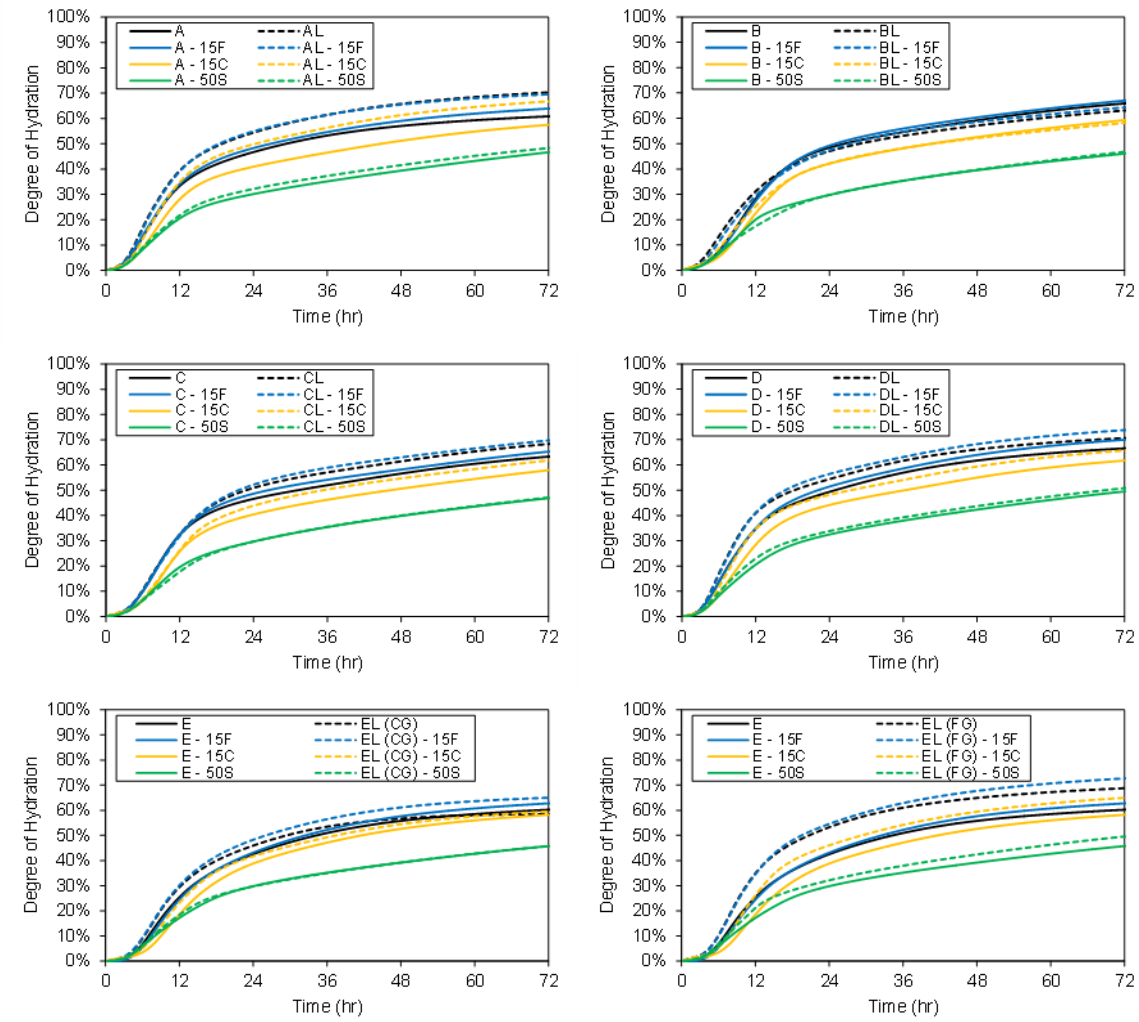

Figure 6.6. Degree of hydration for SCM-blended cement pastes.

6.4.2 Chemical shrinkage

The results of the chemical shrinkage test, normalized with respect to the starting volume of cement paste, are shown in Figure 6.7. Error bars are omitted for clarity, but the average coefficient of variation over the 7 day period for each of the 33 tests did not exceed 6% for any mix.

The shapes of the chemical shrinkage curves are generally consistent with the degree of hydration curves of Figure 6.6, as would be expected given the hydration-rate-

dependence of chemical shrinkage. The relative magnitudes of the chemical shrinkage for SCM blended cement pastes were greater than the relative magnitudes of degree of hydration for the same SCM blended pastes, suggesting that the SCM interactions contribute more to chemical shrinkage than they do to degree of hydration. In particular, it was observed after 72 hr of hydration that 15% Class F fly ash increased degree of hydration by 4%, 15% Class C fly ash decreased degree of hydration by 6%, and 50% slag decreased degree of hydration by 27%. By contrast, after 72 hr of hydration, 15% Class F fly ash reduced chemical shrinkage by an average of 12.0% (SD = 3.9%), 15% Class C fly ash reduced chemical shrinkage by an average of 1.5% (SD = 3.0%), and 50% slag reduced chemical shrinkage by 22.2% (SD = 3.3%). Similar reductions were also observed prior to normalizing the results by the starting volume, indicating that the differences between the degree of hydration and chemical shrinkage are not due to the different volumes of the pastes, but are more likely a function of the secondary hydration of the SCMs.

By 7 days, the secondary reactions of the SCMs appear to introduce even more chemical shrinkage of the paste, reducing the shrinkage-mitigating effects seen at earlier ages in the SCM blends. While the more slowly reacting Class F fly ash mixtures continued to show approximately a 10% reduction in chemical shrinkage by 7 days (10.5%, SD = 4.5%), the hydraulically reactive slag only reduced chemical shrinkage by 9.0% (SD = 3.8%), and the Class C fly ash was found to actually increase chemical shrinkage by 3.7% (SD = 3.6%). Between 3 and 7 days of hydration, then, the chemical reactivity of the SCMs appears to play a significant role in increasing the chemical shrinkage of mixtures containing Class C fly ash and slag.

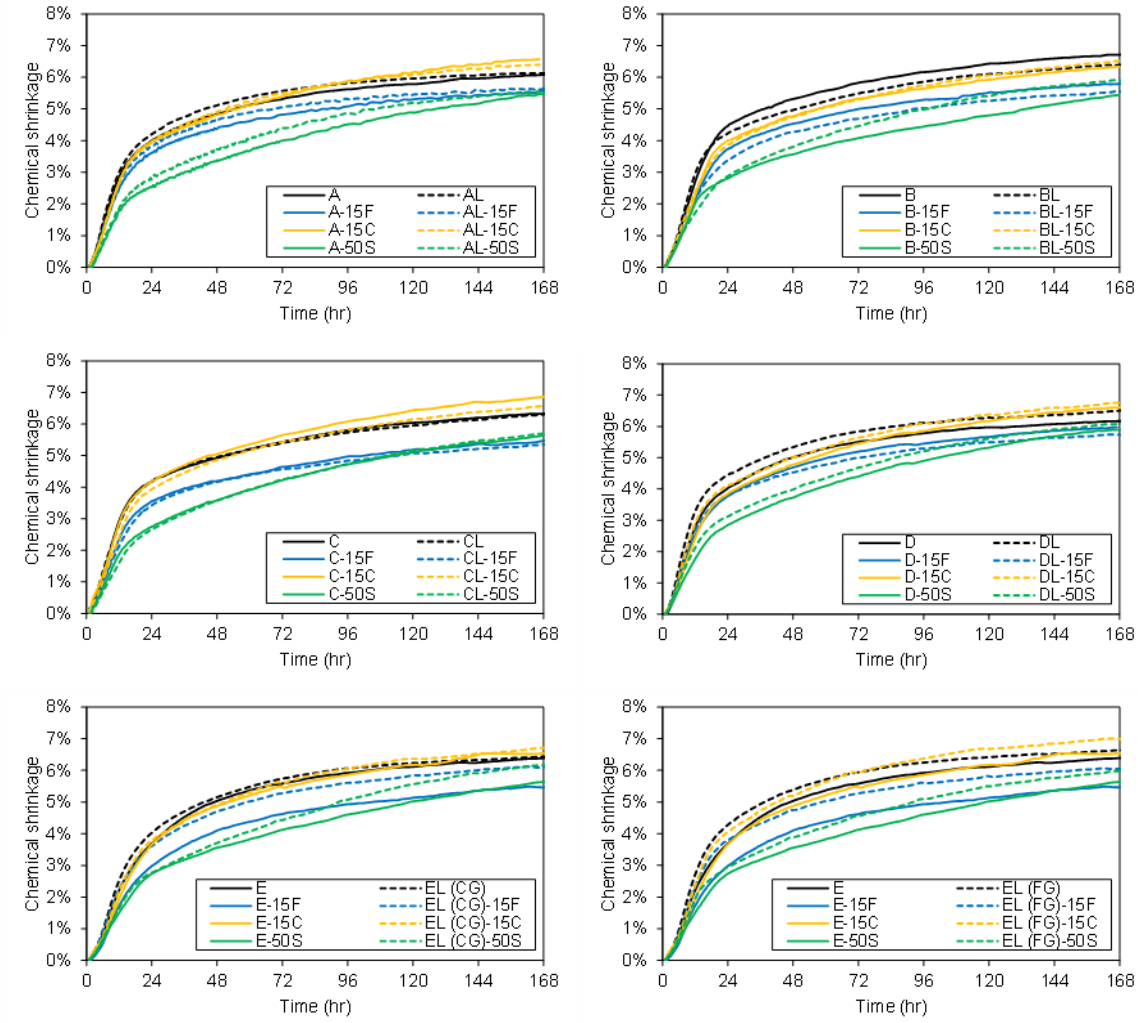

Figure 6.7. Chemical shrinkage for SCM blended cement pastes at *w/cm* = 0.40, as a fraction of the initial paste volume.

The changes in chemical shrinkage relative to the neat cement pastes were generally consistent between Type I/II and Type IL cements, but small differences could be discerned for the mixtures containing 15% Class F fly ash and 50% slag. The Type I/II blends containing Class F fly ash reduced chemical shrinkage by approximately 1.5% more than the corresponding Type IL cement pastes did, or 11.2% compared to only 9.8% for the Type IL mixtures. Similarly, the Type I/II blends containing slag reduced chemical shrinkage by approximately 3% more than the corresponding Type IL cement

pastes, or 10.7% compared to only 7.6% for the Type IL mixtures. It would be logical to attribute such differences to the secondary reactions between the limestone and alumina phases in the SCMs; however, for both the Class F fly ash and the slag, the differences between the two cement types were within one standard deviation of the mean for the eleven cements. This suggests that – for the Class F fly ash blends, in particular – the effect of the limestone-SCM synergies on chemical shrinkage is still small after 7 days of hydration. Longer duration studies encompassing more of the secondary reactions may be required to fully investigate the influence of limestone-SCM synergies on the early-age chemical shrinkage of SCM-blended PLC pastes.

6.4.3 Autogenous shrinkage

The autogenous shrinkage results are shown in Figure 6.8 for the SCM blends with cements from source A and in Figure 6.9 for the SCM blends with cements from source C. Figure 6.8b and Figure 6.9b are normalized with respect to the cement factor, CF, of the binder; that is, the proportion of cement in the binder (1.0 for neat cement pastes, 0.85 for blends with fly ash, and 0.5 for blends with slag). Error bars are removed for clarity.

During the first 7 days of hydration, the autogenous shrinkage of all six SCM-blended cement pastes was found to be lower than the companion Type I/II and Type IL neat cement pastes, due primarily to the dilution of the cement by the more slowly reacting SCMs. Such a decrease suggests that SCM-blended cement pastes may be effective at reducing shrinkage at early ages, when less strength has been developed and the potential for cracking is higher. However, as the primary hydration of the cement

slows and the secondary hydration of the SCMs becomes more dominant, significant changes in autogenous shrinkage can be observed. These changes appear to be sensitive to both the type of SCM used and the type of cement used, indicating potential effects from limestone-SCM interactions.

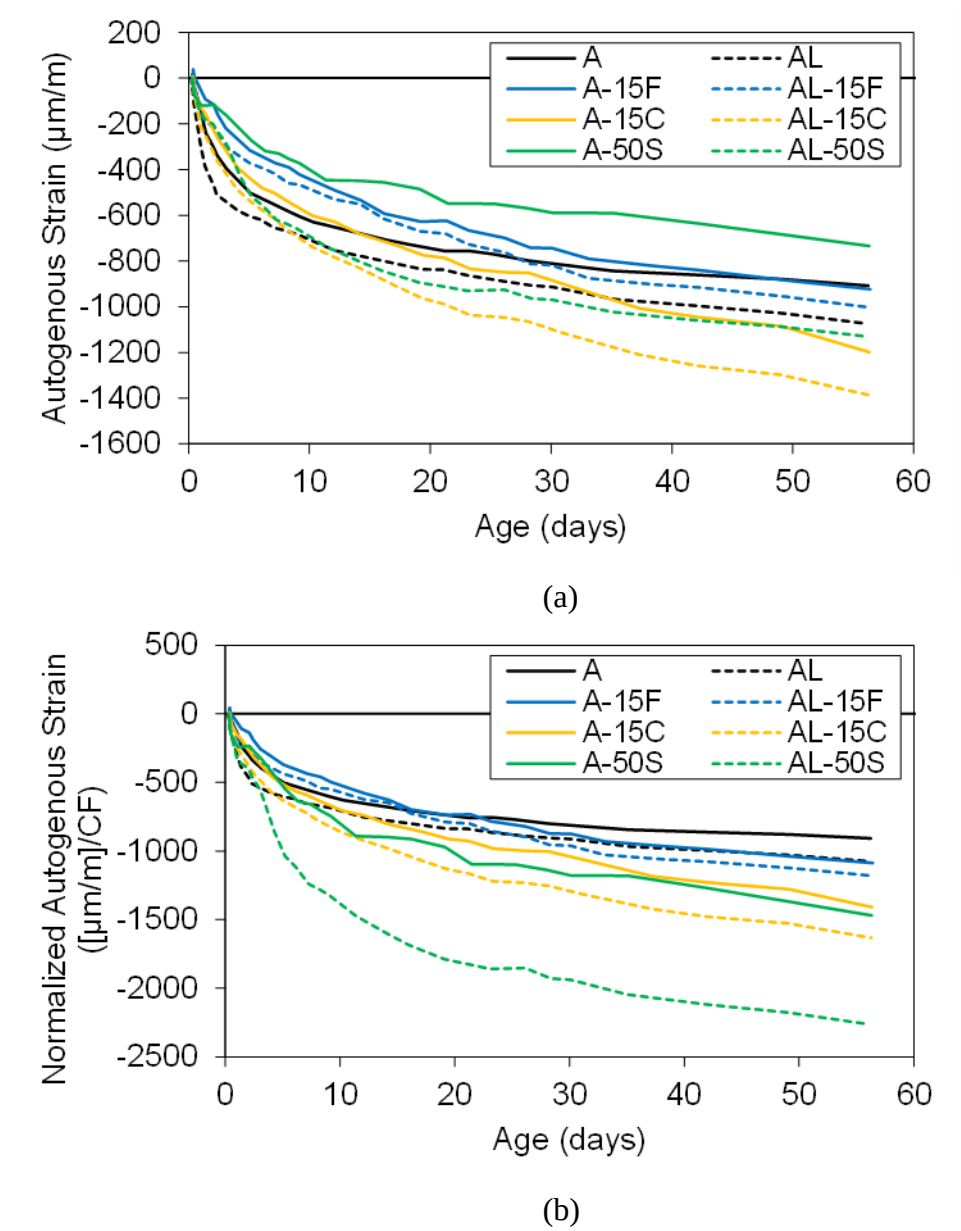

Figure 6.8. Autogenous deformation of SCM blended cement pastes at *w/cm* = 0.40, prepared with cements from source A. (a) Results as measured. (b) Results normalized by cement factor (CF). Error bars are removed for clarity.

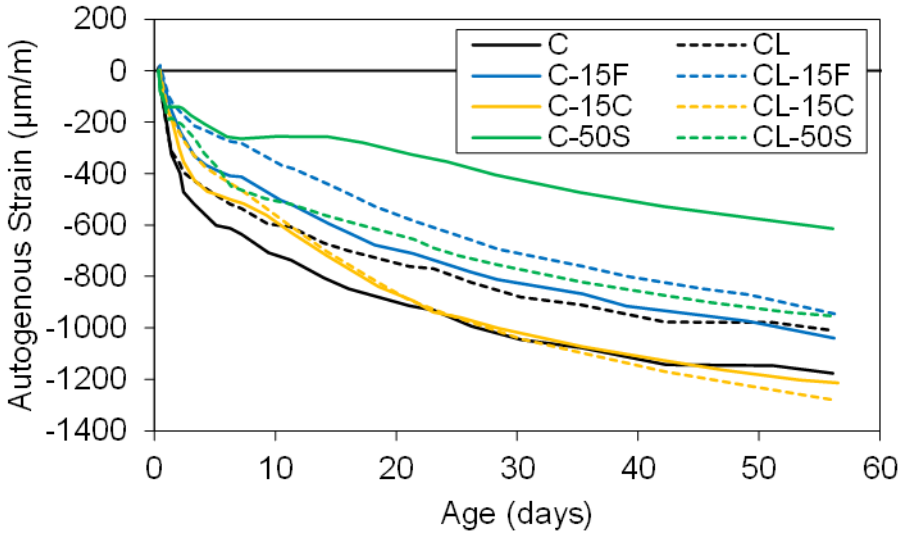

(a)

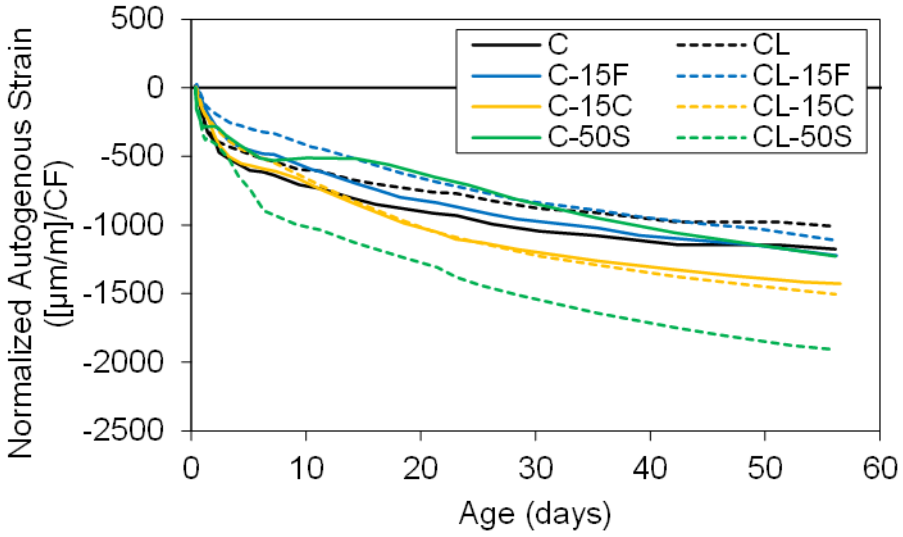

(b)

Figure 6.9. Autogenous deformation of SCM blended cement pastes at *w/cm* = 0.40, prepared with cements from source C. (a) Results with standard deviation error bars shown. (b) Results with error bars removed for clarity.

The 50% replacement of cement with slag had the most extreme effects on autogenous shrinkage of the Type I/II and Type IL cement pastes. Even at early ages, the autogenous deformation of the Type IL cement-slag mixes was more than 50% larger than the autogenous deformation of the Type I/II cement-slag mixes, and by 56 days, it was observed that the shrinkage of the AL and CL blends exceeded that of the A and C blends by 72% and 56%, respectively. Comparing the slag mixes to their neat cement paste counterparts, it can additionally be observed that the 50% slag replacement for the Type I/II blends reduced autogenous deformation by an average of 38% (48% for cement A and 28% for cement C) at 56 days, but only reduced autogenous deformation in the Type IL blends by a combined 1% (5% increase for cement AL, 6% decrease for cement CL) at that same age. The substantial increase in autogenous deformation for the Type IL cement-slag relative to their Type I/II-slag counterparts suggests extensive pore refinement in those blends as a result of the limestone-slag synergies, but also indicates that a 50% replacement of Type IL cement by slag may not have the same shrinkage-mitigating effects as the same replacement level would for a more traditional Type I/II cement.

Additional – albeit smaller – differences were observed in the autogenous shrinkage results for the two fly ash blends. After about 7 days of hydration, the Class C fly ash blends begin to show steeper increases in autogenous shrinkage compared to the neat cement paste control mixtures, which suggest that pozzolanic activity initiating around 7 days of hydration leads to greater pore refinement in Class C fly ash blends. The autogenous shrinkage of the Class C fly ash blends continues to increase through 56 days, leading to a 56 day autogenous shrinkage, on average, 23% greater than for the neat

cement paste controls. Separating by cement type, it can be seen that the Type I/II cement blends increase autogenous shrinkage by an average of 18%, while the Type IL cement blends increase autogenous shrinkage by an average of 28%, further suggesting reductions in average pore size due to interactions between the limestone and fly ash. Overall, the blend of Type IL cement with Class C fly ash had the largest autogenous shrinkage observed for both cement sources by 28 days, indicating that such a combination may not be desirable if shrinkage is to be limited during the first 28 days of hydration.

Finally, it was observed that the Class F fly ash blends undergo autogenous deformations more similar in magnitude to the neat cement paste controls, despite continued pore refinement as a result of their secondary hydration reactions. On average, the substitution of cement by 15% Class F fly ash reduced the 56 day autogenous shrinkage by 6%, with little differences observed between the Type I/II and Type IL mixtures beyond what was already observed for the control mixtures. Although the Class F fly ash is slower to react due to its low CaO content and coarser particle size, it is anticipated that beyond 56 days, the ongoing secondary reactions of the Class F fly ash will continue to refine the porosity, leading to greater autogenous shrinkage for those cement pastes relative to the neat cement paste mixtures.

6.4.4 Compressive strength development

The measured compressive strengths for the 12 SCM-blended Class AA concrete mixtures are shown in Figure 6.10; strengths of companion concretes prepared without

SCMs but with otherwise the same mixture proportions are shown for comparison.[12] With respect to the neat concrete mixtures, the data show that the more finely ground Type IL cement from source A produces concrete with early-age (< 28 days) strengths comparatively higher than those made from the companion Type I/II cement, consistent with the more rapid rates of hydration and microstructural development observed at those ages in Chapter 3 and 4. As the dilution effects begin to supersede the early-age nucleation effects, the compressive strengths of the A and AL mixtures become more similar to one another, and are statistically indistinguishable by 90 days. The mixtures from source C also show rates of compressive strength evolution consistent with the early-age hydration and microstructural development characterized in Chapters 3 and 4. The more similar particle size distributions for the two cements led to more similar rates of hydration and microstructural development at all ages, which can be observed in the statistically similar compressive strengths measured at all ages for the two concrete mixtures. Since the compressive strength development of the neat concrete mixtures was consistent with the rates microstructural evolution characterized for the neat cement pastes, it is assumed that the compressive strength development of the SCM-blended mixtures is likewise consistent with the microstructural evolution for the SCM-blended cement pastes – even if the microstructure was not directly characterized for such mixtures.

[12] Compressive strength measurements for mixtures without SCMs were generously provided by Ahmad Shalan. A complete discussion of his results can be found in the final report for GDOT Project No. 02-127, Assessment of Limestone Blended Cements for Transportation Applications, currently in preparation.

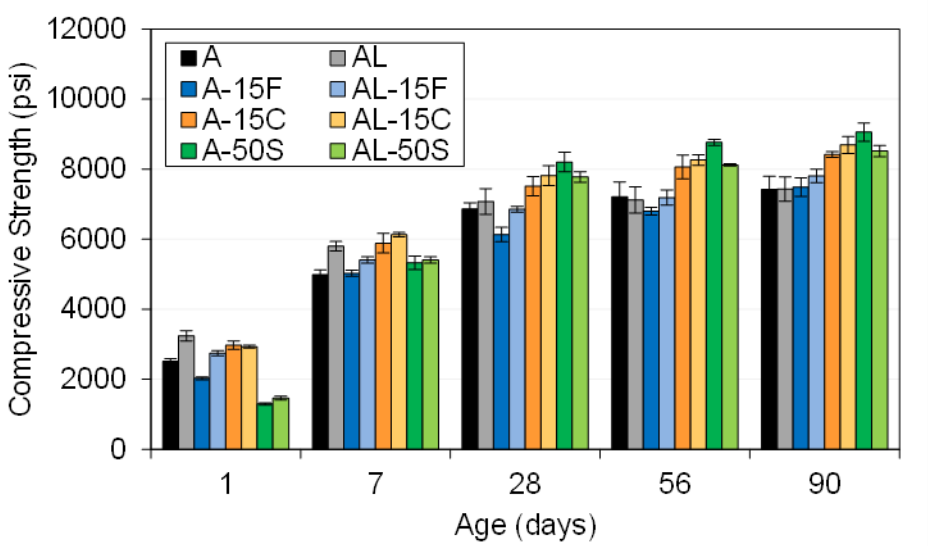

(a)

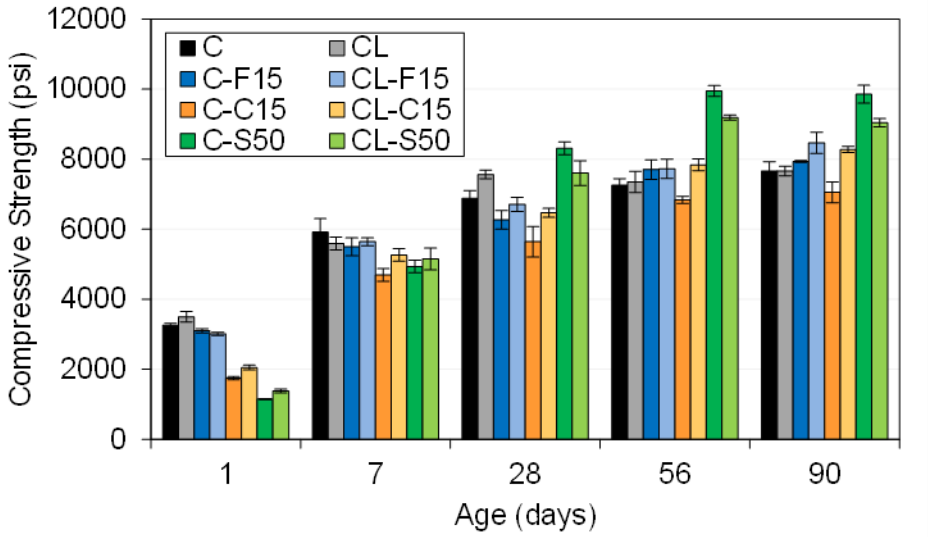

(b)

Figure 6.10. Compressive strength development for concrete mixtures from sources (a) A and (b) C, each containing SCMs at *w/cm* = 0.445.

Mixtures containing SCMs were generally found to have lower strengths than the control mixtures at 1 day of age as a consequence of the dilution of the cement by the more slowly reacting SCMs, but over time, the secondary pozzolanic and latent hydraulic reactions produced concretes with equivalent or higher compressive strengths relative to the control mixtures by 90 day. By 28 days, although some of the Type I/II-SCM blends still exhibited lower compressive strengths compared to the Type I/II control, all 6 mixtures containing Type IL cements had statistically equivalent or greater compressive strengths, indicating that blends of Type IL cements with SCMs can be used to overcome dilution effects and achieve functionally equivalent strengths by 28 days [84].

Blends with 15% Class F fly ash developed strengths at rates most similar to the control mixtures, and by 90 days hydration were found for both sources to increase compressive strength by up to 10% (800 psi) relative to the neat concrete mixtures. Blends of Class F fly ash with Type IL cements, on average, exhibited strengths 500 psi greater at 90 days than the blends of Class F fly ash with Type I/II cements, suggesting a supplementary strengthening effect caused by interactions between the limestone fillers and the fly ash [49, 51]. The 500 psi difference, however, falls within the expected variability of the test results [112], so it cannot be concluded on the basis of compressive strength alone that the limestone has a synergetic interaction with the Class F fly ash.

Blends containing 15% Class C fly ash yielded inconsistent results between the two cement sources, with the two blends from source A showing similar or increased compressive strengths at all ages and the two blends from source C showing similar or *decreased* compressive strengths at all ages relative to the neat concrete controls. In both cases, it was observed that the Type IL-blended concretes had higher compressive

strengths at all ages than the Type I/II-blended concretes – 300 psi at 90 days for cements from source A and 1200 psi at 90 days for cements from source C – further suggesting a synergetic strengthening relationship as reported previously in the literature [49, 51]. The differences between mixes C-15C and CL-15C was more than 3 standard deviations, providing strong evidence for a synergetic strengthening of the Class C fly ash blends by interactions with the limestone filler.

The blends containing 50% slag exhibited the greatest strength gains over the first 90 days of hydration, reaching more than 9000 psi for mixes from both sources. While the dilution of the cement by the more slowly reacting SCM reduced the compressive strength of the mixtures by more than 50% (and as much as 65%) relative to the neat concrete controls, by 7 days, the hydraulic reactivity of the slag increased the strength of the mixtures to within 10% (~500 psi) of the control strengths, and by 90 days, had exceeded the control strengths by an average of 20% (~1500 psi). At a 50% slag replacement level, no synergetic increases in compressive strength were observed for the Type IL mixes; instead, the Type IL-slag mixes were found to be, on average, 700 psi weaker 90 days compared to the Type I/II-slag blends.

6.5 Discussion

The primary objective of this research effort was to better understand how interactions between limestone and alumina-containing SCMs affect the early-age hydration processes and microstructural development of PLC-SCM blended systems. The results indicate that each SCM interacts with limestone in a way that uniquely affects the hydration and microstructural development of the PLC-SCM blend.

The Class F fly ash was observed to have the smallest effect on hydration, early-age shrinkage, and compressive strength development. Aside from a slight 10 min retardation, which can be attributed a dilution effect and to the coarser particle size distribution of the fly ash, the differences between the rates of hydration of the fly ash-blended and the neat cement pastes over the first 72 hr were found to be minimal. The primary difference observed was a slight increase in the isothermal heat released by the C_3A hydration and a general extension of the reaction time by 1-2 hr, but the same effect was observed for both the Type I/II and Type IL blends. Cumulative heat and chemical shrinkage for the Class F fly ash blends were both reduced by 10% at 3 and 7 days, respectively, indicating that the 15% replacement of cement by Class F fly ash had a primarily diluting role during the first 7 days of hydration. It was not until 14 days that the normalized autogenous began to differ significantly from the control pastes, indicating that the secondary pozzolanic reaction of the Class F fly ash does not initiate – and therefore does not have any effect on microstructural development – until that age. Based on the relative autogenous deformations and compressive strengths, it is believed that the extent of the pore refinement in the Class F fly ash-blended materials is small, as the increases in normalized autogenous deformation and compressive strength were within the expected variability of each test performed. Synergetic interactions between the limestone and Class F fly ash were likewise considered to have a minimal effect on the hydration and microstructural development of the PLC blends at the particular *w/cm* and fly ash dosage investigated, based on the observation that differences between the Type I/II and Type IL blends were either within the expected variability of the test

methodologies or were consistent with the differences already observed for the neat cement mixtures. Overall, it was found that substituting either cement with 15% Class F fly ash was an effective method of decreasing the early-age heat of hydration and chemical and autogenous shrinkage while still producing concrete of equivalent compressive strength to the control mixtures.

Compared to the Class F fly ash, the Class C fly ash was observed to have a more pronounced effect on hydration, early-age shrinkage, and compressive strength development as a result of its pozzolanic and hydraulic reactivity. Blends containing Class C fly ash released more heat and exhibited significantly more chemical shrinkage in the first 3-7 days of hydration compared to the blends containing Class F fly ash, suggesting that even at early ages, the hydraulic properties of the Class C fly ash enable it to participate in the hydration and microstructural development of the cement pastes. Between 7 and 14 days of hydration, the pozzolanic reactivity of the Class C fly ash initiates, as evidenced by a relative increase in the normalized autogenous deformation for those cement pastes. The pozzolanic reaction appears to occur 3-7 days sooner for the Type IL pastes than for the Type I/II pastes, suggesting that chemical interactions between the limestone and the fly ash accelerate the onset of secondary reactions in PLC-fly ash blends and produce concretes with more refined porosities at earlier ages than PC-fly ash blends do. While refinements in porosity were observed to contribute to increases in the rate of compressive strength development, they were also observed to contribute to significant increases in autogenous deformation, such that blends of PLCs with Class C fly ashes may be less desirable than blends of PLCs with Class F fly ashes for applications where early-age cracking is to be avoided.

With respect to the slag replacement, it was observed that the 50% replacement of both cements with blast furnace slag had significant – and significantly varied – impacts on the hydration, early-age shrinkage, and compressive strength development of the PC and PLC blends. The hydraulic reactivity of the slag was observed within just a few hours of hydration in the normalized calorimetric heat profiles, which indicated significant increases in the rate and amount of heat evolved in blends containing 50% slag. These hydraulic effects led to an increase in the relative rate of chemical shrinkage within the first few days of hydration, such that the 50% reduction in cement content only reduced chemical shrinkage by 9% at 7 days, compared to the 50% reduction that would be expected from substitution with a chemically inert filler. Changes to the intensity and shape of the calorimetric C_3A peak in blends containing Type IL cements pointed to limestone-slag interactions occurring within the first few hours of hydration, which resulted in a more than two-fold increase in autogenous deformation for Type IL blends compared to the Type I/II blends when normalized by the cement fraction in the binder. Such increases suggest substantial reductions in the average pore size of Type IL-slag blends as a result of these chemical interactions, but these hypothesized reductions did not result in further increases in compressive strength. Instead, it was observed that the Type IL-slag concretes had slightly reduced compressive strengths when compared to their Type I/II counterparts, possibly indicating that the extent of their microstructural development is less than is suggested by their autogenous deformation. Since autogenous deformation additionally depends on the surface tension of the pore solution (Equation 4.2), it is possible that the changes to the pore solution by the substitution of cement with

10% limestone and 50% slag had a significant impact on its surface tension, as well, but further investigation is required.

Finally, it appears as though the different alumina loadings of the SCMs had no direct relationship to the synergetic limestone-SCM interactions observed. It had been predicted that the Class F fly ash and slag, which added the largest amounts of alumina to the cementitious binder, would have a more noticeable interaction with the limestone than the Class C fly ash, which added 20% less alumina. However, while all three SCMs exhibited some synergetic interaction with the limestone, the relative magnitudes of the increased strengths and autogenous shrinkage were greater for the mixes containing slag and Class C fly ash than for the mixes containing Class F fly ash. One possible explanation for these observed differences could be that the limestone synergies are not strictly related to the amount of reactive alumina in the SCMs, but also to their relative rates of reaction. The slag, which showed significant hydraulic reactivity within the first few hours, also showed the clearest differences between the hydration and early-age shrinkage of the Type I/II and Type IL blends, while the Class F fly ash, which showed slow pozzolanic reactivity only after 14 days of hydration, also showed the smallest differences in autogenous deformation and compressive strength development for the Type I/II and Type IL blends. Recent research by Puerta-Falla, et al., [109] supports this hypothesis by demonstrating that the source of the alumina plays a significant role in the synergetic interactions exhibited between limestone and SCMs. The results of this study propose an extension to their findings, suggesting that it is not strictly the source of the alumina but also the reactivity of the source that influences the nature of the limestone-SCM interactions. Further research looking at the reaction rates of limestone with

alumina sourced from various SCMs would be needed to investigate this hypothesis more fully.

6.6 Conclusions

The results of this study demonstrate that blends of Type IL cements with SCMs can be suitably used as replacements for Type I/II cements in construction applications. Despite the dilution of the cement by the limestone filler, equivalent or more refined porosities – resulting in equivalent or higher strengths – can be achieved when Type IL cements are partially substituted with 15% fly ash or 50% slag, by mass. Chemical interactions between the PLCs and fly ash were found to increase compressive strength by 56 days relative to blends of ordinary portland cement and fly ash, supporting the "synergetic" PLC-SCM interactions previously established in the literature. While blends of Type IL cements with 15% Class C fly ash were able to achieve higher strengths at 56 days when compared to the Type I/II control mixtures, the increases in strength came at the expense of increased chemical and autogenous shrinkage at early-ages, which could increase cracking in structural applications. By contrast, blends of Type IL cements with 15% Class F fly ash were found to provide the best balance in properties, slightly increasing compressive strength by 56 days, while still reducing early-age chemical and autogenous shrinkage. Such mixes are recommended for use in construction applications, pending further investigating into their long-term durability (Chapter 7).

Blends of PLCs with 50% slag did not show the same synergetic increases in compressive strength as the blends with 15% fly ash did, but still showed substantial increases in compressive strength relative to the neat Type I/II control concretes. While

blends of Type I/II cements with slag were found to dramatically reduce the autogenous deformation exhibited by the cement paste, no such shrinkage-mitigating effects were found for blends of Type IL cements with slag, believed to be due to the chemical interactions between the limestone and the slag. Based on the pronounced influence of the limestone on the autogenous deformation of the 50% slag mixes, it is recommended that lower slag replacement levels be considered for structural concretes containing Type IL cements.

CHAPTER 7

DURABILITY OF PLC-BASED MATERIALS: ELECTRICAL INDICATORS OF PERMEABILITY

7.1 Introduction

The transport properties of concrete control many aspects of its durability, from resistance to chloride and sulfate ion penetration to resistance to damage by freezing and thawing cycles or by internal salt crystallization, among others. The most commonly characterized transport properties for concrete are permeability (the rate of pressure-driven fluid flow through the material) and diffusivity (the rate of concentration-driven ion flow through saturated porosity), but other transport processes such as electromigration (flow of ions under an electric field) and thermal migration (flow of fluids and ions under a temperature gradient), may also influence the long-term durability of the concrete [113]. The concrete's transport properties are a function of several microstructural parameters, including the size, interconnectivity, and tortuosity of the porosity. Materials with large pore volumes are more likely to have larger and more interconnected pores through which water and ionic species can flow [42, 113]. Likewise, materials with low porosity are more likely to have more tortuous, less interconnected pore networks, which could help to protect against damage caused by transport-related phenomena.

It was established in the previous chapters that limestone substitutions to portland cement can have significant impacts on microstructural development. In particular, dilution effects were found to reduce the total volume of hydration products formed,

thereby increasing the total porosity of the cement paste matrix, while filler and ancillary specific gravity effects were found to improve the efficiency of particle packing within the matrix, thereby reducing the average size of the pores. The balance between these two competing microstructural effects has important implications for the transport processes – and therefore the long-term durability – of PLC-based materials and warrants further investigation. Specifically of interest is whether the overall increase in porosity dominates the behavior such that permeability and diffusivity are also increased, or whether the reduction in average pore size dominates such that the interconnectivity and therefore the permeability and diffusivity are instead reduced.

To that end, this chapter focuses on the links between the microstructural development and the permeability and diffusivity of PLC-based materials. Twenty-three concrete mixtures containing various combinations of PLCs and SCMs are assessed using the ASTM C1202/AASHTO T277 [114, 115] rapid chloride permeability test (RCPT) and the AASHTO TP95 [11] surface resistivity (SR) test. These two tests use the electrical properties of concrete – conductivity (σ) and resistivity (ρ), respectively – as indirect indicators of the concrete's permeability, where here, "permeability" is used to collectively refer to the water permeability, electrical permeability, and ionic diffusivity of the concrete[13]. The two tests are commonly used in practice to quickly assess the transport properties of concrete structures and are employed in this study to better understand the evolution of microstructure and impermeability in PLC-based materials over time.

[13] In the analysis that follows, the term "permeability" will be used in this collective sense, as is common practice in industry [2].

7.2 Theoretical background

To understand why and how electrical measurements can be used as indicators of permeability and microstructural development in concrete, it is first necessary to understand how electrical properties such as conductivity and resistivity are related to microstructure. Conductivity is an intrinsic property of a material that describes how easily current can flow through it. It is defined mathematically as the inverse of resistivity, which can be measured directly by applying a voltage *V*, measuring the induced current *I* (or vice versa), and normalizing by the geometry of the specimen, as shown:

$$\sigma = \frac{1}{\rho} \tag{7.1}$$

$$\rho = \frac{VA}{IL} \tag{7.2}$$

where *A* is the cross-sectional area through which the current passes and *L* is the length of the specimen. Practically, Equation 7.2 can only be applied if the measurement is conducted *through* some depth *L* of the concrete, but in the case of the SR test, resistivity is only measured on one surface of the concrete, using a four-probed "Wenner array" [116]. As illustrated in Figure 7.1, the two outer probes of the Wenner array apply a current to the concrete, while the two inner probes measure the voltage difference induced by the current flow. Since the measurements are performed on a single surface of the concrete, the cross-sectional area and length required for Equation 7.2 are ill-defined. A different equation, which assumes a semi-infinite geometry, is instead employed to compute the resistivity near the probed surface [117]:

$$\rho = 2\pi a \frac{V}{I} \tag{7.3}$$

where *a* is the spacing between probes.

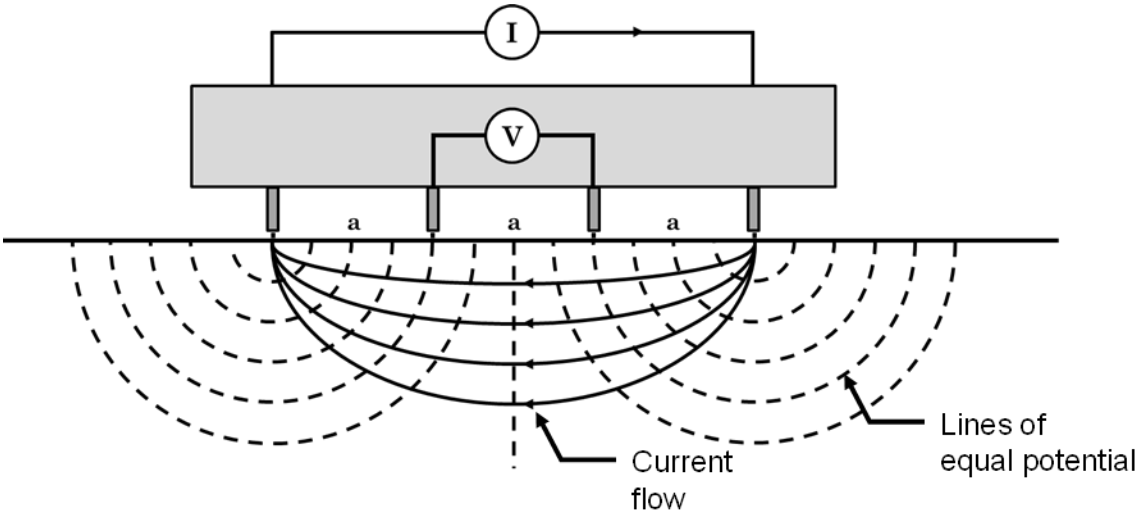

Figure 7.1. Schematic representation of surface resistivity as measured by a four-probed Wenner array.

Current flows through concrete primarily within the pore solution, which contains dissolved species of hydroxyl (OH-), potassium (K+), and sodium (Na+) ions that make it a favorable pathway for electric current [113, 118]. While current flow through solids such as aggregates and hydrated cement paste is also possible, flow through these materials typically plays a much smaller role due to their comparatively higher electrical resistivities [119]. When the path of the current (or inversely, electrons) through the pore network is made more difficult by a more tortuous – or twisting – path, as illustrated in Figure 7.2b, the concrete is said to have a higher electrical resistivity, since it is more resistant to the flow of electrons. This is analogous to when the path of water is made more difficult by a more tortuous path, in which case the concrete is said to have a lower permeability. Thus, measurements of electrical resistivity can provide a reasonable

indicator of the concrete's permeability, since both properties are controlled, in part, by the tortuosity of the pore network.

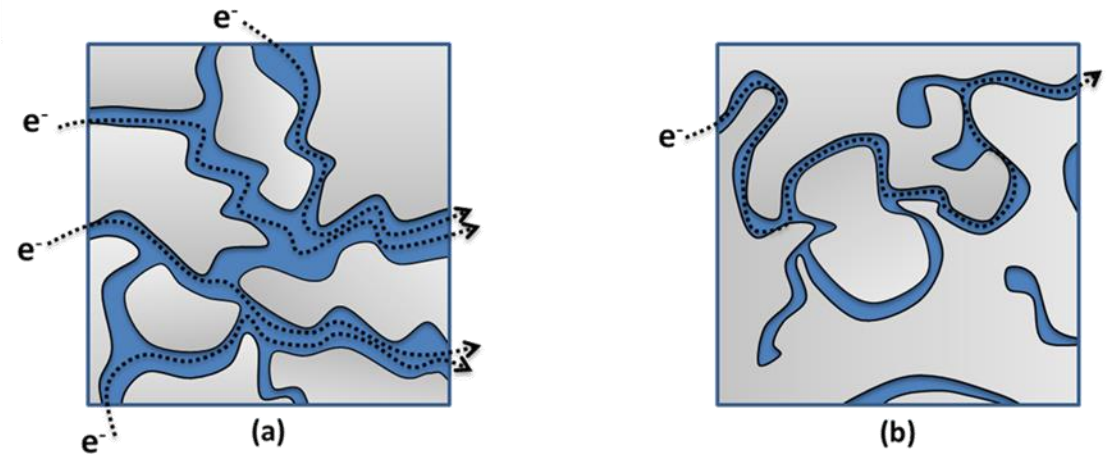

Figure 7.2. Electron flow through (a) a highly porous microstructure and (b) a denser, more tortuous microstructure.

The tortuosity of the pore network, in turn, is determined by the microstructure of the concrete. Denser microstructures, such as those resulting from pozzolanic reaction of SCMs or higher degrees of hydration, tend to have more complex and refined pore networks, giving the concrete a higher tortuosity and a lower permeability. By contrast, less dense microstructures, such as those resulting from the dilution of the cement by less reactive fillers, tend to have greater porosity, lower tortuosity, and higher permeability. Since electrical resistivity is controlled, in part, by the tortuosity of the pore network, it is proposed that measurements of concrete surface resistivity can be used to indirectly assess not only the permeability of the concrete at specific ages but also the rate of its microstructural development over time.

7.3 Materials and methods

Twenty-three concrete mixtures were prepared for this investigation: 11 neat cement mixtures using each of the commercially-produced cements characterized in Chapter 3, and 12 SCM-blended mixtures using the cements from sources A and C combined with each of the three SCMs characterized in Chapter 6. All 23 mixtures were prepared to meet Georgia Department of Transportation (GDOT) Section 500 specifications for Class AA concrete [110], a class of concrete specified for use in bridge superstructures which may therefore require low permeability to aggressive environments such as sea water and sulfate exposure [120]. To investigate the "worst-case" permeability for this class of concrete, the maximum permitted water-to-cementitious-materials ratio (*w/cm* = 0.445) and the minimum permitted cementitious materials content (635 lb/yd^3, or 375 kg/m^3) were selected for each mix. SCMs, when used, were substituted for cement at the maximum allowed replacement levels, as in Chapter 6: 15% for Class F and Class C fly ashes, and 50% for slag. The compositions of the binder phases for each mix are shown in Table 7.1, in lb/yd^3. Since the SCMs were dosed at a 1:1 mass replacement ratio, their lower specific gravities (Section 6.2.3) slightly increased the yield of each mixture, reducing the total cementitious content to 632 lb/yd^3 for mixes containing fly ash and to 630 lb/yd^3 for mixes containing slag.[14]

Table 7.1. Binder compositions for permeability study, lb/yd^3.

Mixture	Cement sources used	Water	Cement	Fly Ash	Slag
No SCMs	A-E	283	635	0	0
15% Fly Ash (Class F)	A and C only	281	537	95	0

[14] The difference between the cementitious content used (e.g., 630 lb/yd^3) and the cementitious materials content required (635 lb/yd^3) is within the ±1% tolerance permitted by GDOT Section 500 specifications.

15% Fly Ash (Class C)	A and C only	281	537	95	0
50% Slag	A and C only	280	315	0	315

The aggregates consisted of a #67 crushed granite coarse aggregate (Lithia Springs, GA; dry-rodded unit weight = 98 lb/ft^3, SG = 2.61) proportioned at 1889 lb/yd^3, and a natural sand fine aggregate (Byron, GA; fineness modulus = 2.4, SG = 2.65) proportioned at 1260 lb/yd^3; the same proportions were used for each mixture. A mid-range water reducer (Sika SikaPlast-300GP) was also used to ensure adequate workability during mixing and casting. Dosages of 8 fl.oz./cwt (100 lb. cementitious material) were used for mixtures without SCMs, 10 fl.oz./cwt were used for mixtures containing fly ash, and 14 fl.oz./cwt were used for mixtures containing slag. Slumps between 3 and 5 inches were typically obtained.

Five 4 in. by 8 in. cylinders were cast for each mixture for use in permeability testing. After 24 hours, the cylinders were stripped from their molds, and an initial surface resistivity measurement was made on three of the specimens using a four-probed Wenner array, in accordance with AASTHO TP95-11 [11]. Measurements were made along lines drawn lengthwise at quarter-points around the circumference of the cylinders, with eight measurements being made for each cylinder (two measurements per line), as depicted in Figure 7.3. The five samples were placed into a saturated calcium hydroxide (limewater) solution maintained at 70 ± 3°F. After 3, 7, 14, 28, 56, and 90 days of hydration, the surface resistivity was measured again on the same three specimens used for the 1 day measurement to obtain SR-development curves for each mix. SR values for limewater-cured specimens were multiplied by a factor of 1.1, as specified by the

AASHTO provisional standard, to account for an assumed 10% decrease in pore solution resistivity caused by the limewater [11].

After 56 days of hydration, the two samples not used for resistivity testing were removed from the limewater bath, and a 2 in. disk was cut from near the top of each cylinder. The disks were vacuum-saturated for 18 ± 2 hr, and the rapid chloride permeability test was performed the following day in accordance with ASTM C1202/AASHTO T277 [114, 115] (Figure 7.4).

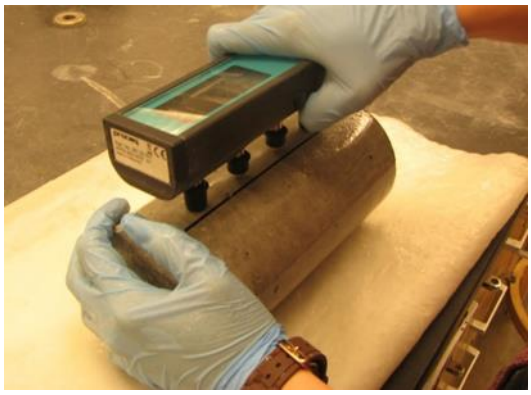

Figure 7.3. Surface resistivity test performed using four-probed Wenner array in accordance with AASHTO TP95-11.

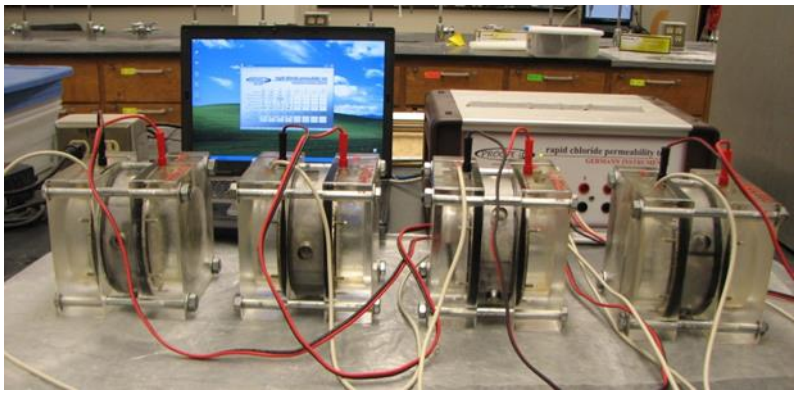

Figure 7.4. RCP test conducted in accordance with ASTM C1202/AASHTO T277.

7.4 Results

The two electrical indicator tests – SR and RCPT – were performed on the neat and SCM-blended concrete specimens in order to obtain greater insights into the influence of interground limestone and limestone-SCM synergies on the microstructural development and long-term durability of PLC-based materials. The non-destructive SR test was used to indirectly monitor the rates of microstructural development in the 23 concrete mixtures [121], and the destructive RCP test was used to assess their relative permeabilities at 56-days. Service lives were predicted for the 23 mixtures using the results of the RCP test and a modified Nernst-Einstein relationship [122]; results were compared to glean better insights into how limestone-induced microstructural changes affect the serviceability of PLC-based concrete structures.

7.4.1 Surface resistivity

The evolution of surface resistivity over the first 90 days of hydration is shown in Figure 7.5 for the 11 concrete mixtures without SCMs, and in Figure 7.6 for the 12 concrete mixtures with SCMs; control mixtures not containing SCMs are also shown in Figure 7.6 for comparison. To aid in the interpretation of the results, horizontal dashed lines are shown in all figures to indicate the permeability classifications defined by the standard (Table 7.2).

Approximately 4 months after the first samples had been cast, the temperature of the curing room was reduced by an estimated 6-8°F while maintenance was performed on the thermal control unit. While most of the specimens tested had either reached 90 days of age by that time or had not yet been cast, the 56 and 90 day measurements for mix CL

and the 90 day measurements for mix EL (FG) were performed under these lower temperature conditions. It was estimated based on an empirically-derived equation by Castellote, et al., [123] that such a temperature reduction increases SR values by approximately 10%;[15] the three affected SR values were therefore reduced by 10% to compensate for the thermal effect, and the adjusted values are reflected in Figure 7.5.

Table 7.2. Permeability classifications for concrete tested according to the AASHTO TP95 surface resistivity test.

Classification	SR limits (kOhm-cm)
High	< 12
Moderate	12 – 21
Low	21 – 37
Very Low	37 – 254
Negligible	> 254

[15] Castellote, et al., conducted temperature-dependence studies on 14 saturated concrete and mortar mixtures with similar w/cm (0.45-0.5) to the mixtures considered in this study. They found that, for tests conducted below 25°C (77°F), the thermal adjustment factor, α, is approximately:

$$\alpha \approx (1 + 0.664 \cdot \Delta T - 0.825 \cdot W_g \cdot \Delta T)^{-1}$$

where ΔT is the temperature change (in °C) and W_g is the fraction of aggregates in the solids (cement + SCMs + aggregates). For ΔT = 4°C and W_g = 0.832, $\alpha \approx 1.10$.

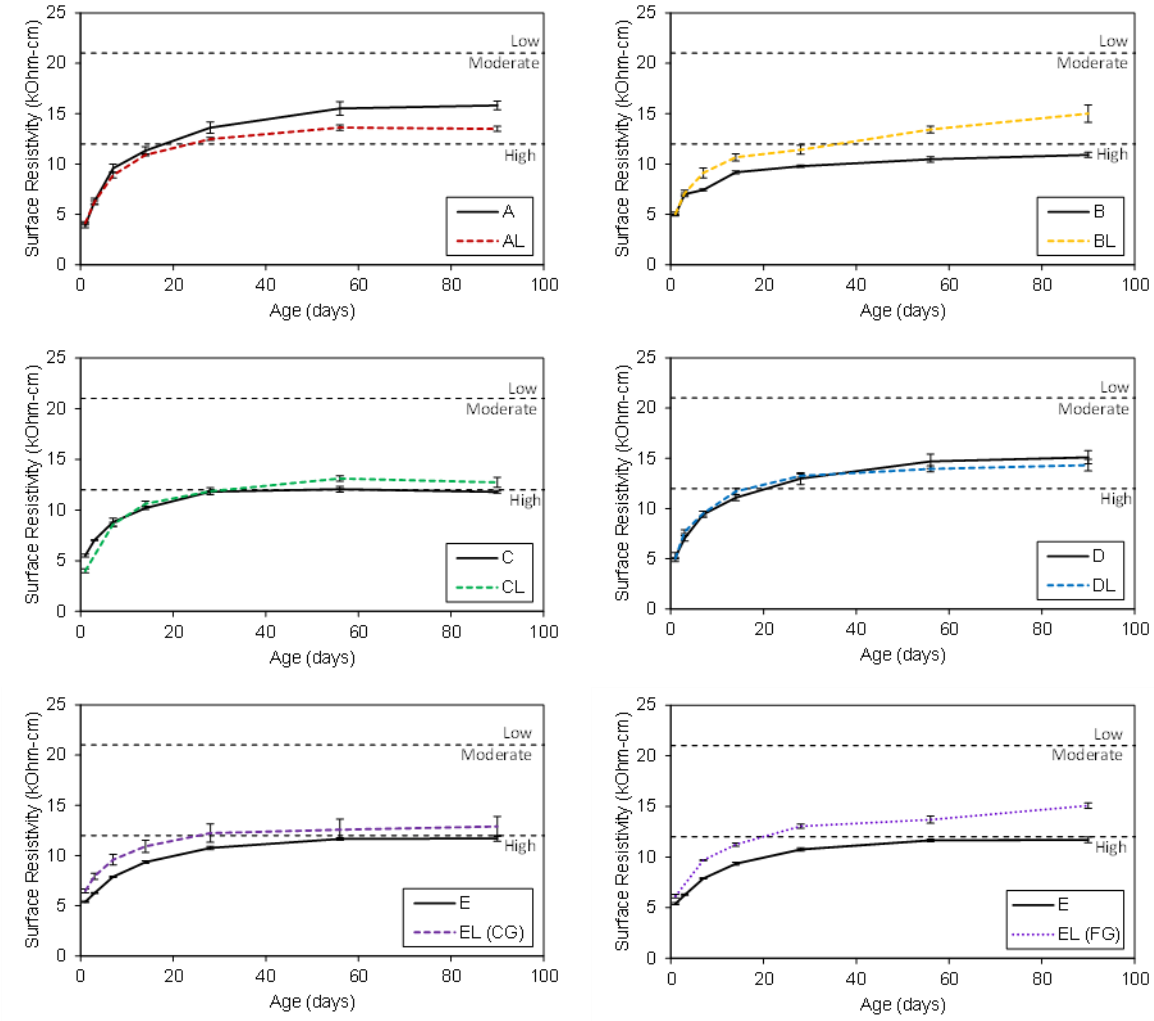

Figure 7.5. Surface resistivity measurements over the first 90 days of hydration for neat concretes A-E. Permeability classifications, as specified by AASHTO TP95-11, are indicated by horizontal dashed lines in each figure.

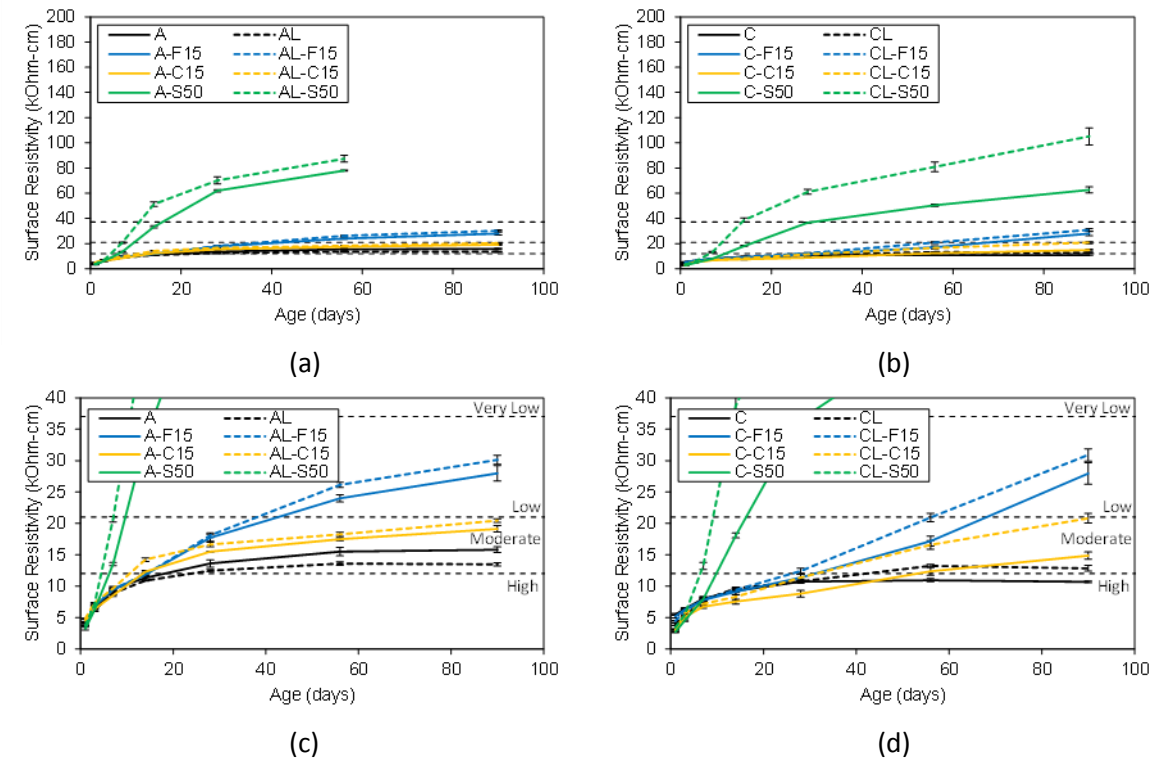

Figure 7.6. Surface resistivity measurements over the first 90 days of hydration for concretes blended with SCMs. Mixes containing cements A and AL are shown in (a) and (c). Mixes containing cements C and CL are shown in (b) and (d). Figures (c) and (d) are zoomed in versions of figures (a) and (b) so that differences between fly ash mixes can be seen. Permeability classifications, as specified by AASHTO TP95-11, are indicated by horizontal dashed lines in each figure.

In general, the 23 mixtures each show increasing resistivity with time as the primary hydration of the cement and the secondary hydration of the SCMs reduce and refine the porosity. While the neat OPC and PLC mixtures all tend to reach a plateau after about 28 days of hydration – consistent with their slower rates of hydration and microstructural development at that time [2] –, the mixtures containing SCMs continue to show further SR development up to and even beyond 90 days of hydration, which suggests continued microstructural development due to secondary pozzolanic and latent hydraulic reactions of the SCMs. The onset of these secondary SCM reactions is suggested in the SR-development curves by relative increases in slope [121, 124], the

most obvious of which can be observed between 3 and 7 days for the four mixtures containing 50% cement replacement with slag. Upticks in slope for the four fly ash-blended systems were found to occur within the first 7-14 days for blends with Class C fly ash and 14-28 days for blends with Class F fly ash, which is generally consistent with the current understanding of reaction rates for those SCMs in traditional OPC systems [2, 31].

Comparing the neat Type I/II and Type IL mixtures to one another, no consistent trends were observed based on limestone dosage or fineness. Cement AL, which had shown the greatest increases in hydration rate relative to its Type I/II counterpart (Figure 3.7), actually yielded consistently lower concrete surface resistivity values at all ages, by comparison. At 90 days, mix AL exhibited a SR reduction of 15% compared to mix A – greater, even, than the 8% dilution of the cement by the incorporation of limestone filler. By contrast, cement BL, which had shown reduced degrees of hydration compared to its Type I/II counterpart, was observed to yield concrete with consistently higher surface resistivities at all ages. At 90 days, it exhibited a 37% increase in SR relative to mix B. Cements from the other three sources also yielded inconsistent results based on limestone dosage and cement fineness, with the cements from source E producing the only mixtures to consistently show increases in degree of hydration, early-age shrinkage, and surface resistivity. Such generally inconsistent behavior suggests that the surface resistivity measurements may be additionally affected by changes to the pore solution chemistry caused by the limestone inclusion, and that therefore the permeability classifications indicated in Table 7.2 may not be applicable to PLC systems.

Comparing the Type I/II and Type IL SCM-blended systems to one another, it can be seen that the upticks in slope indicating the onset of secondary SCM reactions consistently occur first in the limestone-blended mixtures and are followed 3-7 days later by the Type I/II mixtures. This behavior indicates that the limestone accelerates the onset of secondary reactions in alumina-bearing SCMs [121, 124], as had also been suggested by the relative rates of autogenous deformation in the PLC-SCM blended systems of Chapter 6. Not only do these synergetic interactions accelerate the onset of the SCM reaction in PLC-blended systems, however, but they also appear to increase SR at faster rates than in OPC-blended systems. As a result, the PLC-SCM concretes exhibit greater increases in SR after 90 days than their companion OPC-SCM concretes do.

Overall, the greatest SR values and lowest AASHTO permeability classifications ("very low") were obtained for mixtures containing 50% slag, with the Type IL mixtures generating SR values up to 60% higher than the Type I/II mixtures by 56 days. The Class F fly ash and Class C fly ash also showed marked improvements in permeability classification compared to the neat concrete control mixtures, with the Class F fly ash blends achieving "low" permeability status by 90 days and the Class C fly ash blends achieving "moderate" permeability status by 90 days. For both fly ash sources, the Type IL blends generated SR values approximately 10% higher than the Type I/II mixtures at 90 days. While the high SR values for the SCM (and in particular, PLC-SCM) blends suggest more refined microstructures compared to the neat concrete controls, such increases in resistivity could also arise from incidental reductions in the ionic conductivities of the pore solution as a consequence of the dilution of the cement by the SCMs [125-127]. A de-coupling of the pore solution and microstructural effects is

therefore necessary in order to adequately compare the "permeabilities" of mixtures having different chemical compositions.

7.4.2 RCPT

The results of the rapid chloride permeability test are shown in Figure 7.7 for concretes without SCMs and in Figure 7.8 for concretes with SCMs. As was done for the SR results, the permeability classifications defined by the ASTM and AASHTO standards (Table 7.3) are indicated in each figure by horizontal dashed lines. It is important to note that unlike in the SR test, where greater resistivity indicates lower permeability concrete, in the RCP test, a lower total charge passed (which can be directly related to conductivity [122]) indicates lower permeability concrete.

The results of the RCP test again indicate that there is little difference between the electrical properties for the Type I/II and Type IL concretes without SCMs. Slight reductions in total charge passed were observed for the more finely ground cements from sources D and E, but the cements from sources A, B, and C all yielded concretes having similar charges passed – suggesting similar permeabilities – to one another. In blends with SCMs, the Type IL cements showed slightly greater reductions in total charge passed when blended with 15% Class F fly ash or 50% slag, but the magnitude of the reduction was, in general, not statistically significant. Mixed results were obtained for the concretes containing 15% Class C fly ash, where there was essentially no difference at 56 days between mixes A and AL, but a more than 30% reduction in charge passed for mix CL versus C. It is believed that the inconsistent behavior of the Class C fly ash blends could be related to the small sampling size of the tests and the greater compositional

variability of the Class C fly ash. Additional tests averaged over more samples could provide a better indicator of the behavior of the Class C fly ash blends.

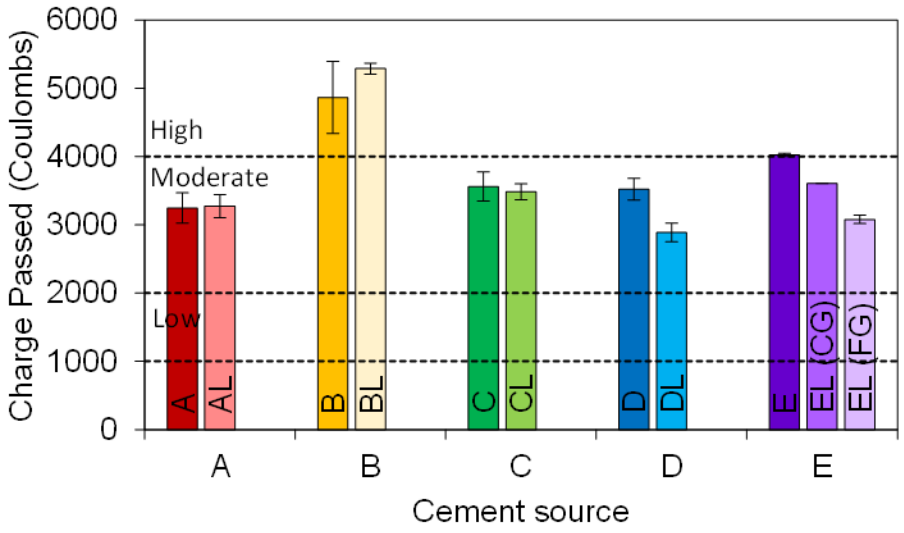

Figure 7.7. Total charge passed by RCPT for concretes A-E, after 56 days of hydration. Error bars indicate the range of values obtained for each mixture.

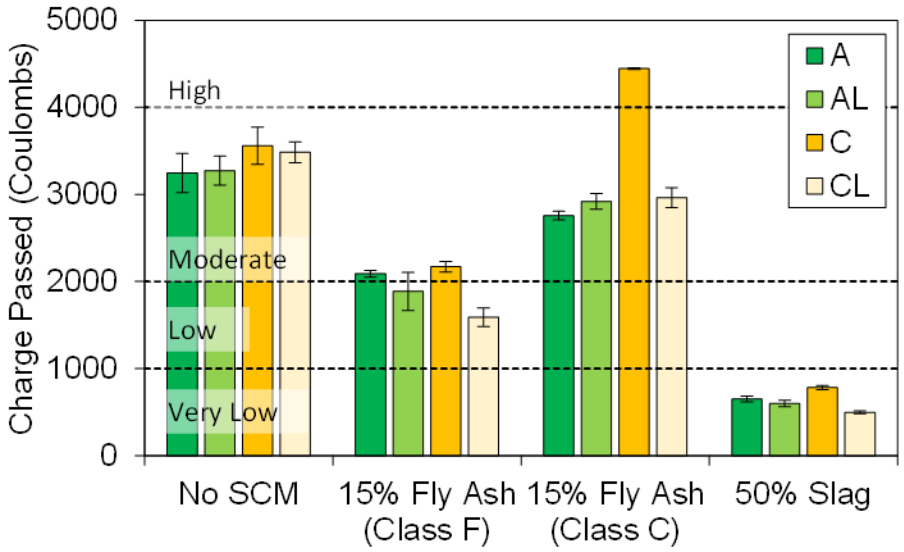

Figure 7.8. Total charge passed by RCPT for concretes containing SCMs, after 56 days of hydration. Error bars indicate the range of values obtained for each mixture.

Table 7.3. Permeability classifications for concrete tested according to the ASTM C1202/AASHTO T277 rapid chloride permeability test.

Classification	Charge Passed (Coulombs)
High	> 4000
Moderate	2000-4000
Low	1000-2000
Very Low	100-1000
Negligible	< 100

Comparing the 56 day SR and RCPT results to one another (Figure 7.9), it can be observed that the two tests have a nearly perfect inverse relationship to one another, as would be expected given the inverse relationship of conductivity (on which RCPT depends) and resistivity (measured directly by the SR test). Similar inverse relationships have been found by other authors [128-130], although the line of best fit varies among studies. The results of this particular study are consistent with those obtained by Chini, et al., [128], on which the AASHTO TP95 guidelines for permeability classification are based. Since the two test methods yield consistent results to one another, it is proposed that factors that affect the interpretation of results for the SR test (e.g., pore solution chemistry) equally affect the interpretation of results for the RCP test, such that the low total charges passed by the SCM-blended mixes may be due to a combination of microstructural and pore solution effects [126, 127], which must also be de-coupled.

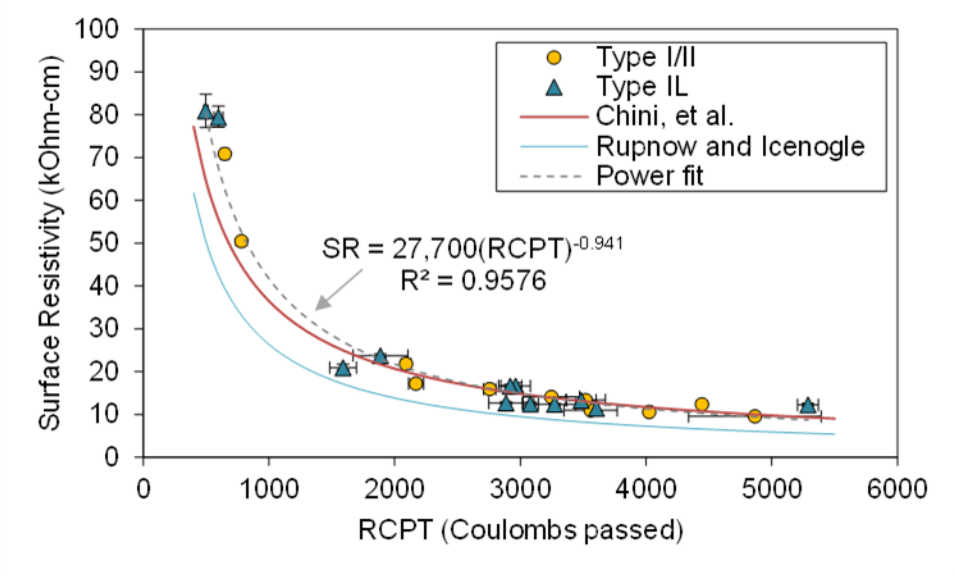

Figure 7.9. Correlation between SR and RCPT results. Fits obtained by Chini, et al., [128] and Rupnow and Icenogle [129] are shown for comparison.

7.4.3 Diffusion coefficient and service-life prediction

In addition to providing an indirect indicator of concrete's permeability, the results of the RCP test can also be used to predict its apparent diffusion coefficient, D_a. The apparent diffusion coefficient describes the ease of ionic diffusion through a porous material, with ionic species, such as chloride ions, diffusing more rapidly through materials with high D_a values. In the context of the long-term durability of cement-based materials, concretes with higher D_a values will be more susceptible to damage by chloride-induced corrosion, since shorter times are required for the chloride ions to penetrate to the level of the steel reinforcement.

For this study, the results of the rapid chloride permeability test were used to predict the apparent chloride ion diffusivity (D_a) of the 23 concrete mixtures by means of the Nernst-Einstein equation [122, 131]. A simplified expression for the Nernst-Einstein equation is given by Equation 7.4:

$$D_{a,i} = K_i \sigma_i \tag{7.4}$$

where σ_i is the conductivity of a charged species i through the concrete, and K_i is a constant which depends on the temperature of the porous material and the charge and concentration of the species i. For the diffusivity of chloride ions through concrete during an RCP test conducted at 70°F (21°C), the constant K_i takes on a value of 2.75 E-4 $lb \cdot in^4/C^2$.

If it is assumed that only chloride ions are passed during an RCP test [122, 131, 132], then the conductivity of the chloride ions can be computed directly from the total charge passed during the RCP test, using the definition of conductivity (Equations 7.1 and 7.2):

$$\sigma = \frac{LI}{AV} \tag{7.5}$$

where L is the length of the sample (2 in), A is its cross-sectional area (12.19 in^2), V is the applied voltage (60 V), and I is the initial current flow through the specimen.[16] The initial current flow was found experimentally by Barde, et al. [122] to be approximately 75% of the total average flow through the specimen, or:

$$I = 0.75 \frac{Q_t}{t} \tag{7.6}$$

where Q_t is the total charge passed, and t is the duration of the test (6 hr). Combining Equations 7.4-7.6, it can then be shown that for the specimen geometries and testing conditions specified by the ASTM and AASHTO standards, the apparent chloride diffusivity constant can be approximated from the RCPT results as:

---

[16] This assumption means that contributions of other ionic species dissolved within the pore solution – which also flow under an applied electric field – are ignored. This assumption has significant implications for the accuracy of the service life prediction model, as will be discussed further in Section 7.5.2.

$$D_a \approx 2.87 \times 10^{-12} Q_t \quad (7.7)$$

where Q_t is given in coulombs and D_a is in units of in^2/s.

Since the values of D_a are proportional to the total charge passed by RCPT, the trends for the 23 concrete mixtures considered in this test are identical to those previously observed for the RCPT results. The usefulness of such diffusion coefficient estimations is that enables the prediction of service lives for concrete structures exposed to chloride ions. The computed 56-day diffusion coefficients can be used as inputs into the Life 365 [133] service life prediction model to estimate the service lives of *uncracked* sections of concrete exposed to various temperature and chloride exposures. For this study, the service life is assumed to be the time to initiation of corrosion in the reinforcing steel, which occurs when the concentration of chloride ions at the level of the reinforcement reaches a critical concentration threshold of 0.05% by weight of concrete [133].

One-dimensional chloride ingress was simulated through the depth of a hypothetical 8-inch thick concrete slab, assuming concrete mixtures having the 56-day diffusion coefficients computed by Equation 7.7 and a 2-inch cover depth for the steel reinforcement. Two exposure conditions were modeled: the first assuming an urban highway bridge deck in Atlanta, GA, with "low" exposure to chloride ions, and the second assuming a coastal bridge deck located in a marine spray zone in Savannah, GA, subject to "extreme" chloride exposures. The predicted service lives of the 23 concrete mixtures are shown in Figure 7.10 for the low-chloride exposure and in Figure 7.11 for the extreme-chloride exposure; service lives exceeding 150 years could not be computed by the model, and are indicated as "150+" in the figures.

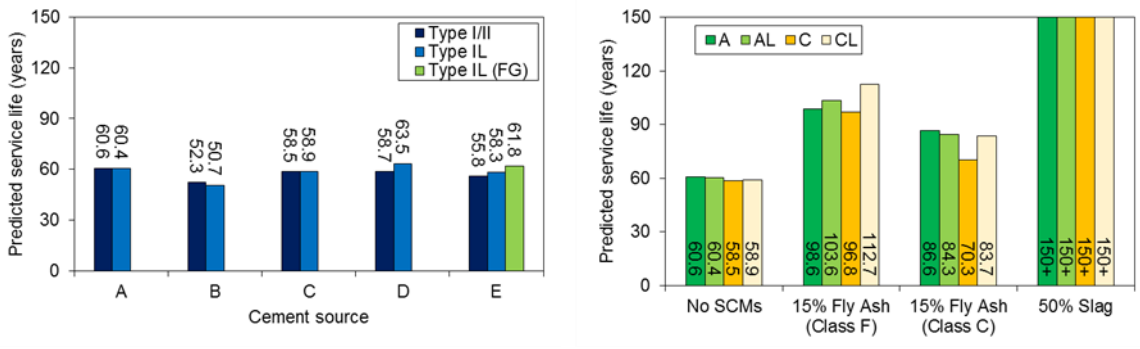

(a) (b)

Figure 7.10. Service-life prediction for concretes from (a) sources A-E, without SCMs and (b) sources A and C, with SCMs, assuming low chloride exposure (Atlanta urban highway bridge deck).

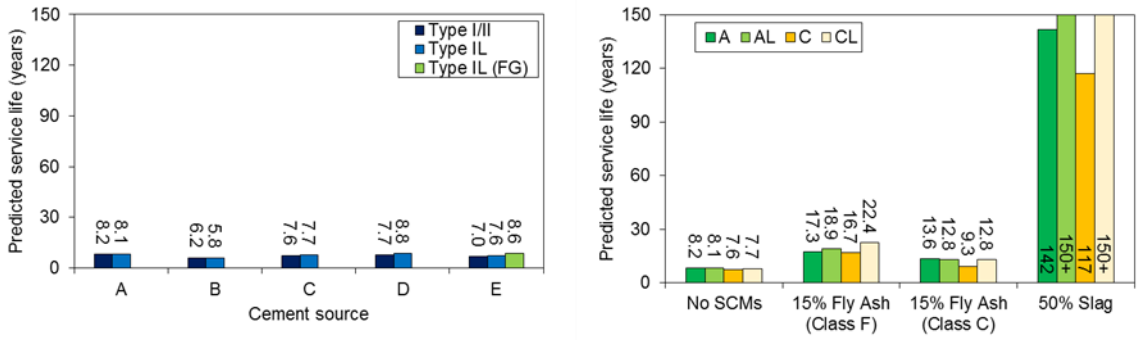

(a) (b)

Figure 7.11. Service-life prediction for concretes from (a) sources A-E, without SCMs and (b) sources A and C, with SCMs, assuming extreme chloride exposure (Savannah marine spray zone bridge deck).

In general, it was observed that the mixtures containing SCMs were predicted to have significantly longer service lives than the mixtures containing only portland or portland limestone cements, which follows directly from their lower charges passed during the RCP test. The "very low" permeability 50% slag mixtures were found by service life prediction to have 150+ year service lives under normal exposures and 120+ year service lives under extreme exposures, while the "moderate/high" permeability neat concrete mixtures were found by service life prediction to have only 60-year service lives under normal exposures and 8-year service lives under extreme exposures.

Only marginal differences were observed between the service lives predicted for the neat OPC and PLC systems. While limestone fillers were found to increase the service life of neat concrete by an average of 21 months under normal exposures and 5 months under extreme exposures, these improvements accounted for less than 1% of the total expected service life of the structure. By contrast, synergies between the limestone and the SCMs were found to increase the service life by an additional 5-10% for normal chloride exposures and 7-15% for extreme chloride exposures, or about 4-10 years for blends containing Class F fly ash and 1-5 years for blends containing Class C fly ash. No conclusions could be made regarding the influence of the limestone-slag synergies on service life estimates, since 6 of the 8 slag blends exceeded the 150-year upper limit for the model, but it is similarly anticipated that the limestone-slag synergies would contribute to extended service lives in the PLC-slag blended systems.

7.5 Discussion

The results of the electrical permeability tests indicated that the Type I/II and Type IL concretes, in general, have similar permeability to one another at *w/cm* = 0.445. No significant differences were observed in either the permeability classification or the predicted service lives for the Type I/II and Type IL concretes without SCMs, which all yielded permeability classifications in the "high" to "moderate" range by 56 days and an expected 60 year service life, on average, under normal chloride exposures. In mixtures containing SCMs, acceleration of the pozzolanic and latent hydraulic reactions of the SCMs by the limestone filler led to a greater increase in surface resistivity and – in general – a greater reduction in total charge passed by 56 days, yielding instead

permeability classifications of “moderate” (15% Class C fly ash), “low” (15% Class F fly ash), or “very low” (50% slag) for SCM-blended mixtures, and service lives averaging 81, 103, and 150+ years, respectively, under normal chloride exposure levels. The lower permeability designations of the Type IL-SCM blends, in particular, suggest that the synergies between the SCMs and the limestone could lead to greater pore refinement and reduced permeabilities in Type IL-SCM blended concretes, thereby extending the service lives of PLC concrete structures. It is important to note, however, that the service life predictions obtained by Life 365 apply only to uncracked concrete specimens and do not account for the increased rates of chloride ingress in cracked concrete. Since it was previously found in Sections 4.3.2 and 6.3.3 that mixtures containing the more finely ground Type IL cements and mixtures containing 15% Class C fly ash exhibit increased early-age shrinkage, the true service lives of these blends may, in fact, be reduced by the increased cracking potential of the cement paste matrix.

In addition to neglecting the influence of increased cracking potential on permeability and ultimate service life, the simulated service lives are also based on the assumption that the apparent chloride diffusivity through the concrete can be directly determined from the results of the RCP test. One fundamental problem with using electrical properties as surrogates for permeability, however, is that the electrical properties of concrete are not solely a function of microstructure. Other factors, including the composition of the pore solution, the temperature at which the test is conducted, the moisture content of the sample during testing, and the types of raw materials (e.g., aggregates, fibers, or admixtures) used, can all have a noted effect on the values of conductivity or resistivity measured for a particular concrete [38, 134-138]. While

moisture- and temperature-related effects were controlled externally in this study by using saturated specimens stored at a relatively constant temperature, and material-related effects were controlled – in part – by using the same aggregates and admixtures for all 23 mixtures, the composition of the pore solution could not be controlled, and in fact, varied considerably between mixtures due to the different compositions of the binder phases. Such variation in pore solution composition could explain the substantial increases in surface resistivity observed for the slag – and especially slag-limestone – blended concretes, and should therefore be accounted for when evaluating the concrete's permeability.

7.5.1 Formation factor

In order to separate the effect of pore solution electrochemistry from the microstructural component of conductivity and resistivity, the concept of formation factor, *F*, is employed. Formation factor is defined as the ratio of the pore solution conductivity (σ_p) to the bulk, or measured, conductivity (σ_b), or inversely, the ratio of bulk resistivity (ρ_b) to pore solution resistivity (ρ_p):

$$F = \frac{\sigma_p}{\sigma_b} = \frac{\rho_b}{\rho_p} \tag{7.8}$$

It essentially functions as a global or collective "microstructural" conductivity or resistivity term, which – with additional research – can be directly related to microstructure-dependent properties such as permeability [138-140].

To determine the formation factor of a concrete specimen, the conductivity (or resistivity) of its pore solution must be known. Measurement of pore solution conductivity typically requires extraction of the solution by means of expression [141],

which is often impractical or impossible for concretes having highly refined or discontinuous porosities [118]. For this study, the pore solution conductivities were modeled using the National Institute of Standards and Technology (NIST) pore solution conductivity estimator [142]. The NIST tool assumes that pore solution conductivity is a function of the Na+, K+, and OH- concentration in the pore solution, which are primarily governed by the Na_2O and K_2O loadings of the concrete mixture and the degree of hydration of the cementitious materials [118]. Inputs into the model include the proportions of water, cement, fly ash, slag, and silica fume (if used) in the concrete, their respective Na_2O and K_2O contents (% by mass), the SiO_2 contents of the fly ash and silica fume (if used), and the estimated degree of hydration of the concrete. SiO_2 contents for fly ash and silica fume are used to implicitly reduce the amount of alkalis available in the pore solution because of increased absorption by pozzolanic C-S-H [142].

The pore solution conductivities (σ_p) estimated for the 23 concrete mixtures at a constant 75% degree of hydration are shown in Figure 7.12 for the 11 neat concrete mixes and in Figure 7.13 for the 12 SCM-blended mixes. The relative binder proportions and alkali contents are given in Table 7.1 and Table 7.4, respectively. It can be seen in the figures that although the eleven cements all yield neat concretes with similar pore solution conductivities to one another (Figure 7.12), the different alkali concentrations within the Type I/II and the Type IL cements generate different pore solution properties, even within pairs of cements produced from the same clinker source. For mixtures containing 15% fly ash, the model calculates higher σ_p values due to the higher alkali contents of the two fly ashes relative to the cements (Figure 7.13), while for the mixtures

containing 50% slag, the model calculates substantially lower σ_p values due to the extreme dilution of alkali and OH- species by the 50% slag substitution.

Table 7.4. Alkali and SiO_2 contents, as applicable, for cements and SCMs.

Material	Na_2O	K_2O	SiO_2
Cement A	0.09	0.60	N/A
Cement AL	0.07	0.48	N/A
Cement B	0.09	0.50	N/A
Cement BL	0.04	0.43	N/A
Cement C	0.15	0.51	N/A
Cement CL	0.14	0.45	N/A
Cement D	0.14	0.45	N/A
Cement DL	0.15	0.42	N/A
Cement E	0.06	0.61	N/A
Cement EL (CG)	0.07	0.61	N/A
Cement EL (FG)	0.06	0.67	N/A
Class F Fly Ash	0.82	2.43	51.30
Class C Fly Ash	1.92	0.47	34.57
Slag	0.19	0.48	N/A

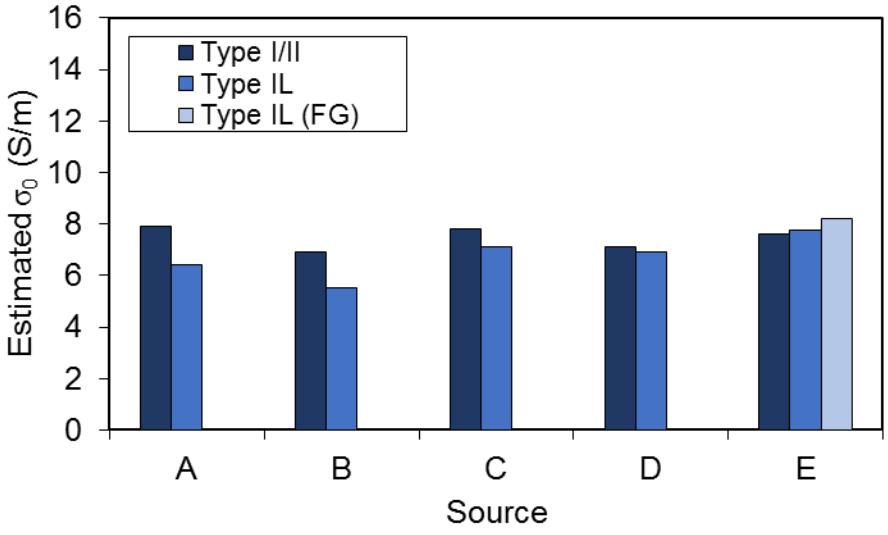

Figure 7.12. Pore solution conductivity estimated at 75% degree of hydration for concrete mixtures without SCMs.

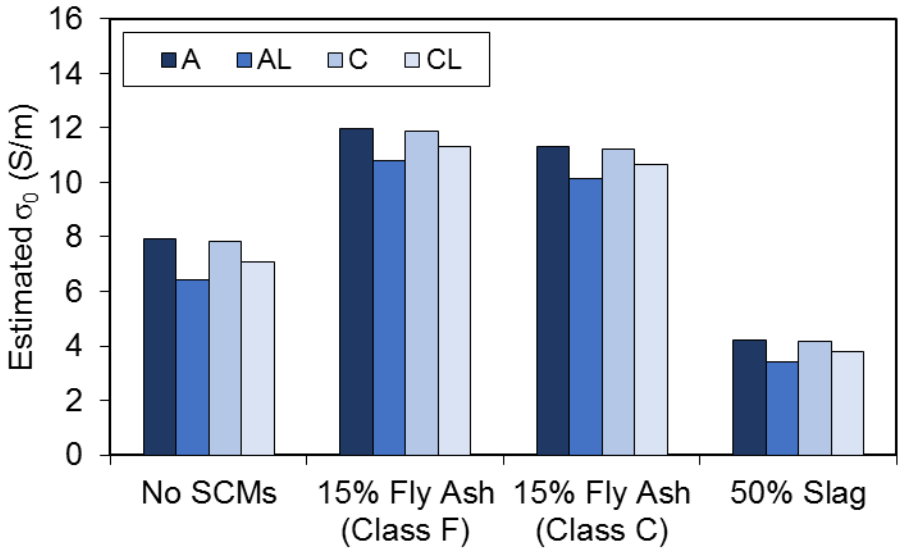

Figure 7.13. Pore solution conductivity estimated at DOH = 75% for concrete mixtures with SCMs.

Based on the widely varying pore solution conductivities of the 23 concrete mixtures, it was determined that pore solution conductivity may have a significant impact on the measured values of electrical resistivity and conductivity. Thus, if the mixtures are to be compared to one another and accurate assessments of relative permeability are to be made, then the pore solution effects must be de-coupled from the microstructural effects. To that end, formation factor was computed over the first 90 days of hydration for each of the 23 concrete mixtures, using the results of the surface resistivity test.

Bulk resistivity (ρ_b) was computed from the measured surface resistivity values by multiplying by a geometric correction factor, *k*, which accounts for the finite geometry of the cylindrical test specimen [117, 140, 143]:

$$k = 1.09 - \frac{0.527}{d/a} + \frac{7.34}{(d/a)^2} = 1.09 - \frac{0.527}{2.67} + \frac{7.34}{(2.67)^2} = 1.92 \quad (7.9)$$

where *d/a* is the ratio of the diameter of the test specimen (4 in.) to the spacing of the probes (1.5 in.). Pore solution resistivity (ρ_p) was computed as the inverse of the conductivity simulated using the NIST tool, using the relative binder proportions and alkali contents given in Table 7.1 and Table 7.4.

Although the preliminary investigation into pore solution conductivity had assumed a constant 75% degree of hydration for each mixture, variable degrees of hydration were considered for this second investigation of formation factor evolution in order to more accurately estimate the conductivity of the pore solution at each age of interest. The degrees of hydration assumed for each testing age are indicated in Table 7.5 for the 11 neat concrete mixtures, and in Table 7.6 for the 12 SCM-blended concrete mixtures. The degrees of hydration for the neat concrete mixtures were estimated from a three-parameter exponential function fitted to the degree of hydration data presented in Chapter 3 (Figure 3.7) [64, 144, 145]. The same approach could not be applied to the estimates for the SCM-blended mixtures (Figure 6.6), as the duration over which degree of hydration was measured did not extend long enough for the secondary SCM reactions to be observed. Instead, a hybrid estimation method was employed for the SCM-blended concretes, in which the fitted exponential equations obtained for cements A, AL, C, and CL, were modified to account for the influence of fly ash and slag using the model of Schnidler and Folliard [64] for guidance. A complete discussion of the methods used to obtain the degree of hydration estimates is included in Appendix B.

Since the cement paste mixtures used for degree of hydration estimates were prepared at a lower *w/cm* (0.40) than the concrete mixtures tested (*w/cm* = 0.445), it is predicted that the true degree of hydration of the concrete specimens is slightly higher

than was estimated. To account for this discrepancy – and for any other potential estimation errors resulting from the curve-fitting methods employed –, the pore solution conductivities and formation factors were also computed for degrees of hydration within ± 5% of the values assumed in the tables. These values are indicated as error bars in the figures that follow, and typically lie within 2.0-2.5% of the estimated formation factor.

Table 7.5. Estimated degrees of hydration for neat concrete mixtures, used to calculate pore solution conductivity.

Mix	1 d	3 d	7 d	14 d	28 d	56 d	90 d
A	47%	62%	67%	69%	71%	71%	72%
AL	56%	71%	77%	79%	80%	81%	81%
B	48%	66%	74%	77%	79%	80%	81%
BL	47%	65%	74%	77%	80%	81%	82%
C	47%	66%	74%	78%	80%	82%	82%
CL	50%	69%	78%	81%	83%	84%	85%
D	49%	66%	72%	75%	76%	77%	78%
DL	54%	70%	76%	78%	80%	80%	80%
E	45%	63%	69%	71%	72%	72%	73%
EL (CG)	50%	67%	72%	74%	75%	76%	76%
EL (FG)	54%	70%	75%	76%	77%	77%	78%

Table 7.6. Estimated degrees of hydration for concrete mixtures containing SCMs, used to calculate pore solution conductivity.

Mix	1 d	3 d	7 d	14 d	28 d	56 d	90 d
A-15F	51%	68%	74%	77%	78%	79%	79%
AL-15F	60%	78%	84%	86%	88%	89%	89%
A-15C	44%	64%	72%	76%	77%	78%	79%
AL-15C	51%	73%	82%	85%	87%	88%	89%
A-50S	28%	51%	64%	72%	77%	81%	83%
AL-50S	33%	59%	73%	81%	87%	91%	92%
C-15F	50%	71%	80%	85%	87%	89%	90%
CL-15F	53%	75%	84%	88%	90%	92%	92%
C-15C	44%	73%	84%	87%	89%	90%	90%
CL-15C	46%	76%	86%	90%	92%	92%	93%
C-50S	27%	50%	65%	75%	82%	87%	90%
CL-50S	28%	53%	69%	78%	85%	90%	93%

The estimated formation factors for the 11 neat concrete mixtures are shown in Figure 7.14. While the SR values had shown no clear patterns for the Type I/II and Type IL cements, the formation factors of the mixtures show trends more consistent with the relative fineness of the cements. With the exception of cements from source A, the more finely ground Type IL cements tended to yield concretes with slightly higher formation factors at early ages (< 28 days), while the more coarsely ground Type IL cements tended to yield concretes with slightly lower formation factors at the same ages. These trends were consistent with the changes to hydration rate previously observed in cement pastes with w/b = 0.40, suggesting that the increased rates of hydration seen for finely ground Type IL cements subsequently decrease permeability at early ages, while the decreased rates of hydration seen for coarsely ground Type IL cements subsequently increase permeability at early ages. At later ages, the dilution effects appear to negate some of the decreases in permeability obtained by filler and nucleation effects, slowing the rates of microstructural development in the Type IL mixtures. This is especially evident for mix DL, but can also be seen in the shallower slopes for mixes AL and EL, as well. Overall, the differences between the 90-day formation factors of the Type I/II and Type IL mixtures appear to be small, suggesting that the microstructural developments of Type I/II and Type IL concrete mixtures are similar to one another at w/cm = 0.445.

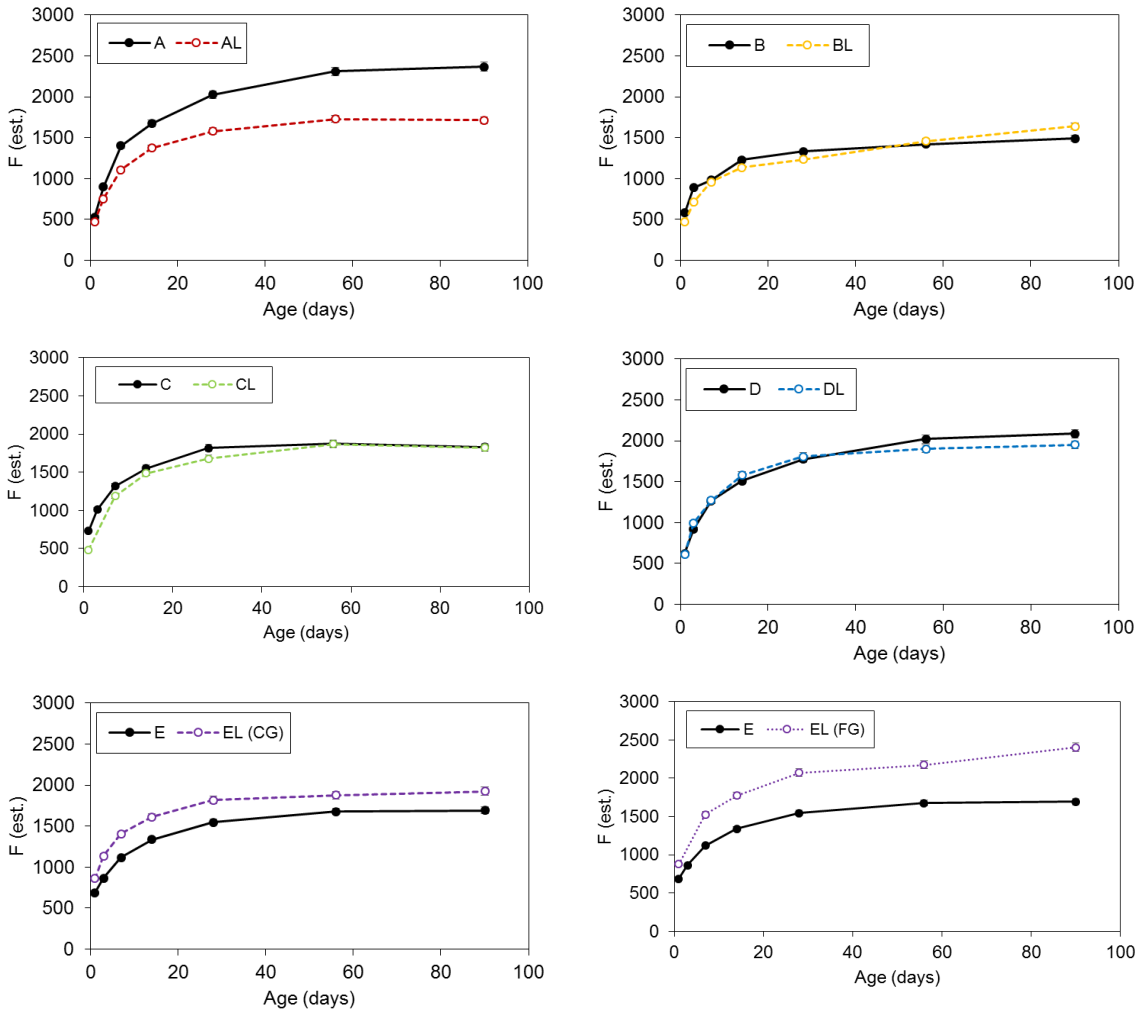

Figure 7.14 Estimated formation factor evolution for neat concrete mixtures A-E. Error bars indicate formation factors for degrees of hydration ± 5% from assumed value.

The main exception to these overall trends was observed for mixes A and AL. Although cement AL was shown in previous investigations to exhibit more rapid reaction rates, higher degrees of hydration, and greater early-age chemical and autogenous shrinkage as a result of its significantly finer particle size, the formation factors for the concrete mixes containing cements A and AL suggest that the limestone has more of a diluting effect on the long-term microstructural development of mix AL than for any other Type IL cement investigated. The cause for this surprising dilution-dominated

microstructural evolution cannot be explained based on the current understanding of cement AL's hydration and microstructural development rates, since all prior testing would suggest that mix AL should have a higher formation factor than mix A. It is possible that the differences observed are related to the higher dosages of water-reducing admixtures (not included in the NIST conductivity model) needed to achieve adequate workability for mixes A and AL, and further research is needed to better understand the influence of chemical admixtures on pore solution conductivity estimates. However, since the admixture was dosed at the same nominal level for both mixes A and AL, it is not expected that the resulting differences in pore solution conductivity would yield the stark differences in formation factor observed; some additional factor likely contributed to the differences, as well.

Figure 7.15 shows the estimated formation factor evolution for mixes containing SCMs. With the pore solution effects removed, the formation factor shows that 50% replacement of cement with slag and 15% replacement of cement with Class F fly ash have similar effects on microstructural development after 56 and 90 days. The slag mixtures still maintained higher formation factors than the Class F fly ash mixtures, indicating greater refinements in porosity, but the degree of refinement is much closer than was initially suggested by the electrical SR measurement. The formation factor development curves also demonstrate that the 15% Class C fly ash addition had a meaningful influence on microstructural development, even though the SR measurements for the Class C fly ash mixtures did not differ significantly from the control mixtures.

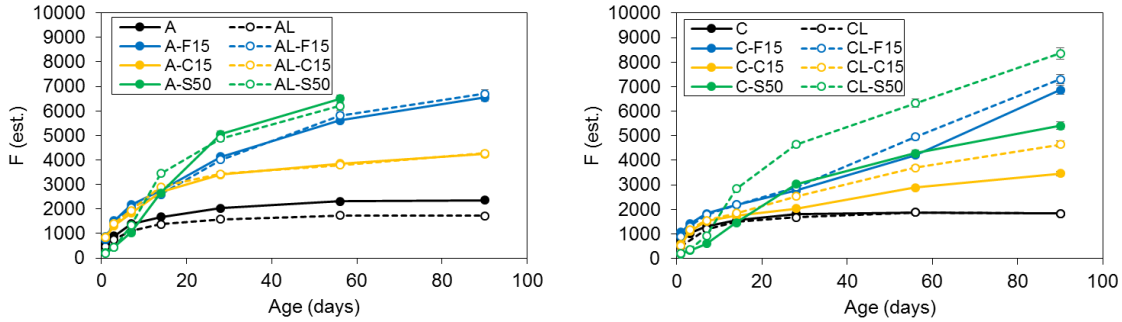

Figure 7.15. Estimated formation factor evolution for concrete mixtures from sources A and C, with SCMs. Error bars indicate formation factors for degrees of hydration ± 5% from assumed value.

For both cement sources, the blends containing Type IL cements saw greater improvements in microstructural development (as indicated by higher formation factors) than blends containing Type I/II cements did, when compared to their respective neat Type I/II or Type IL systems. Synergies between the Type IL cements and the 15% Class F and Class C fly ash additions increased the 90-day formation factor by an additional 75% in the Type IL-blended systems than in the Type I/II blended systems (a 290% vs. 225% increase in *F*, respectively, for Class F fly ash blends, and a 150% vs. 85% increase in *F*, respectively, for Class C fly ash blends). Even greater synergetic enhancements were observed in blends of Type IL cements with 50% slag, which increased the 56-day formation factor by an average of 250% in Type IL systems, but only 150% in Type I/II systems. Although further research is still required to relate formation factor directly to microstructurally-relevant parameters such as permeability or diffusion coefficient, these results demonstrate that synergetic interactions between Type IL cements and SCMs result in further microstructural development, which can substantially reduce the permeability of the concrete to water.

7.5.2 Diffusion coefficients revisited

The formation factor investigation demonstrated that pore solution composition and conductivity have a significant impact on the electrical properties of concrete, which must be accounted for in order to make accurate permeability assessments. While the follow-up study focused exclusively on surface resistivity measurements, a similar approach could also be utilized to account for the effect of pore solution conductivity on the RCPT measurements of total charge passed. However, since the Nernst-Einstein equation requires a total charge (or current) input in order to predict diffusion coefficients, the decoupled Q_t values (formation factors) would no longer be appropriate for use in the model, since they are no longer a measure of current or charge. Thus, modifications to the existing model are required in order to obtain more realistic estimates of chloride diffusion coefficients based on the results of the RCP test.

Since no such modified model currently exists, this also means that the diffusion coefficients predicted in this study are implicitly affected by changes to the pore solution conductivity, and therefore do not necessarily represent the true chloride diffusion coefficients for the concrete. More long-term study of chloride diffusion profiles in PLC- and PLC-SCM blended systems is recommended in order to better understand the true effect of the interground limestone and the limestone-SCM synergies on the diffusivity of chlorides through PLC-based materials and the consequences therein for their service lives under chloride exposure. Based on the results of the formation factor study, it can nevertheless be postulated that the greater degrees of microstructural development in PLC-SCM blended concretes will lead to similar or extended service lives in structural applications compared to OPC or OPC-SCM blended systems, provided that the typically

increased early-age shrinkage of the PLC systems does not induce extra cracking through which contaminants may easily flow.

7.6 Conclusions

This study investigated the link between microstructural development and ultimate permeability of 23 concrete mixtures, each containing various dosages of limestone and alumina-bearing SCMs. Microstructural development and permeability were found to be most appropriately characterized by the concrete's formation factor – rather than its resistivity or conductivity – due to the electrochemical influences of the concrete's pore solution. The results of the study indicate that, in general, limestone substitutions to portland cement have a small effect on the long-term microstructural development of neat concrete mixtures and ultimately yield concretes with similar permeabilities to traditional portland cement concretes. When combined with SCMs, the limestone appears to accelerate the pozzolanic and latent hydraulic reactions of the SCMs, producing concrete with generally more refined microstructures and reduced permeabilities as a result.

The service lives concrete structures produced from the neat concrete mixtures were not significantly improved by addition of limestone, but synergetic reactions between the limestone and SCMs were found to increase the expected service lives of the SCM-blended mixtures by up to 15% compared to SCM blends containing Type I/II cements. The service life estimates, however, are based on assumptions of uncracked concrete sections and no electrochemical pore solution effects, and therefore do not account for either the increased cracking potential of mixes containing finely ground

Type IL cements nor the coupled reductions in diffusion coefficient brought on by pore solution changes in SCM- and PLC-blended systems. More sophisticated models that consider both cracking and chloride ingress – and properly adjust for pore solution effects – would be required to fully characterize the relative impact of Type IL cements on the expected service life of Type IL concrete structures.

CHAPTER 8

DURABILITY OF PLC-BASED MATERIALS: PHYSICAL SALT ATTACK

8.1 Introduction

Physical salt attack refers to the mechanism by which porous materials, such as concrete, mortar, and stone, are damaged by the crystallization of salts near surfaces exposed to salt-bearing soil or groundwater [100]. The mechanism is referred to as a *physical* attack because no chemical interactions take place between the salt and the material: the damage is caused solely by the physical pressures exerted on the pores by the growing crystals. Therefore, while some of the salts involved in physical salt attack, such as sodium sulfate (Na_2SO_4) or sodium chloride (NaCl), may be involved in other types of chemical degradation (e.g., sulfate attack), the mechanisms discussed herein comprise a separate and distinct form of degradation that should not be confused with similar sounding forms of chemical attack in cement-based materials.

Signs of physical salt distress can vary depending on the type and concentration of the salt involved, but typical features include efflorescence, which is primarily cosmetic; spalling or scaling, which is similar in appearance to freeze/thaw damage; or, in the most severe cases, cracking or progressive disintegration, which can render the material structurally deficient. Such distress typically occurs near surfaces of the material that are in direct contact with soil or groundwater, and can therefore affect critical structural elements such as foundations, footings, substructures, and dams [100, 146, 147]. Not only does the type of damage depend upon the salt involved, but its severity is also directly linked to the pore structure of the material. In the context of cement-based

materials, this implies that the inclusion of filler materials like limestone, which alter the pore structure of hydrated cement paste through both chemical and physical means, could significantly affect the ability of concrete to resist damage by salt crystallization. Thus, it is necessary to investigate the implications of these limestone-altered pore structures in the context of physical salt attack.

8.2 Theoretical background: Salt crystallization in porous materials

Several mechanisms have been described in the literature to explain the distress caused by physical salt attack. Initially, distress is caused by the crystallization of salts within the pores due either to capillary rise and evaporation [148-150] or to cycles of wetting and drying [148, 151-153]. Subsequent damage may also be induced by further "hydration" of anhydrous salts, such as sodium sulfate, which undergoes a three-fold volumetric expansion when it converts from the anhydrous form, thenardite (Na_2SO_4), to its hydrated form mirabilite ($Na_2SO_4 \cdot 10H_2O$) [146, 148, 152, 153]. This research focuses primarily on damage due to capillary rise and evaporation. Thorough discussion of this underlying mechanism has been presented by Scherer [148, 154] in the context of cement-based materials, and by Rodriguez-Navarro and Doehne [155] in the context of stone. A summary of the basic principles is presented here.

When a porous material is in contact with soil or groundwater – both of which may contain dissolved salts such as sodium sulfate, sodium carbonate, and sodium chloride [100] – the dissolved salts will be drawn into the material through capillary action. The flux of the salty water into the material (J_C) is given by

$$J_C = \phi A \frac{dh}{dt} \tag{8.1}$$

where φ is the porosity of the material, A is the area of the surface in contact with the water, and h is the height of capillary rise. The driving force for this rise is capillary pressure, p_{cap}, which was shown in Chapter 4 to be a function of the pore size distribution of the material and the surface interactions between the material and the solution:

$$p_{cap} = \frac{2\gamma \cos(\theta)}{r} \tag{4.2}$$

where γ is the surface tension of the liquid at the liquid/solid interface and r is the radius of the pore containing the liquid. As the equation suggests, smaller pores generate larger capillary pressures and therefore materials with finer porosity experience a higher driving force for capillary rise.

Opposing the capillary rise into the material are the gravitational forces acting on the liquid, which increase as the height (volume) of the liquid within the material increases. Consequently, it can be shown via Darcy's law that the rate of capillary rise in the material, dh/dt, decreases as the height of the rise increases:

$$J_C = \frac{-k}{\eta}\frac{(p_{cap} + \rho_L g h)}{h} = \phi A \frac{dh}{dt} \tag{8.2}$$

where k is the permeability of the material, η is the viscosity of the solution, ρ_L is the density of the liquid, and g is the gravitational acceleration. If gravitational effects are ignored (as is often done in the analysis of short elements, such as slabs, whose geometries restrict the capillary rise to only a few inches [148]), the height of the rise h can be approximated as:

$$h \approx \sqrt{\frac{2kp_{cap}}{\eta}} = S\sqrt{t} \tag{8.3}$$

where S is the sorptivity (rate of absorption) of the material [148].

After the solution enters the material from the level of the solution, it then leaves the material from the surface at an approximately constant rate of evaporation, J_E. (J_E does not vary significantly with height, but it does vary with changes in ambient atmospheric conditions, which is important for cyclic wetting and drying or heating and cooling processes.) As a result, the salty solution exhibits a nonlinear saturation profile within the material. Near the ground, at $h = 0$, the rate of capillary rise is greater than the rate of evaporation, and a thin layer of liquid forms on the surface of the material. As h increases, the driving force for capillary rise decreases relative to the driving force for evaporation and the thickness of the liquid film decreases. At some height $h_s > 0$, the rate of evaporation becomes equal to the rate of capillary rise, and the surface of the material is saturated, but the liquid film is no longer present. Finally, at heights above h_s, the rate of evaporation exceeds the rate of capillary rise, causing the liquid-vapor interface to retreat inside the material, where the rate of evaporation is lower. The rate of evaporation, J_E, within the material is a function of pore radius, such that the equilibrium concentration of the solution is higher in small pores than it is in larger pores [148]:

$$J_E = \frac{2\gamma_{LV}\cos(\theta)}{h_S}\frac{k_S}{\eta}\left(\frac{1}{r_S} - \frac{1}{r_L}\right) \tag{8.4}$$

where γ_{LV} is the surface tension of the liquid-vapor interface, θ is the contact angle between the liquid and the solid, h_s is the width of the drying front, k_s is the permeability of the drying front, and r_s and r_L are the radii of adjoining small and large pores, respectively. A schematic depiction of a typical saturation profile is shown in Figure 8.1. Note that while there is salty liquid on the surface of the material up to a height h_s, the salty liquid actually rises to a height $h > h_s$ internally.

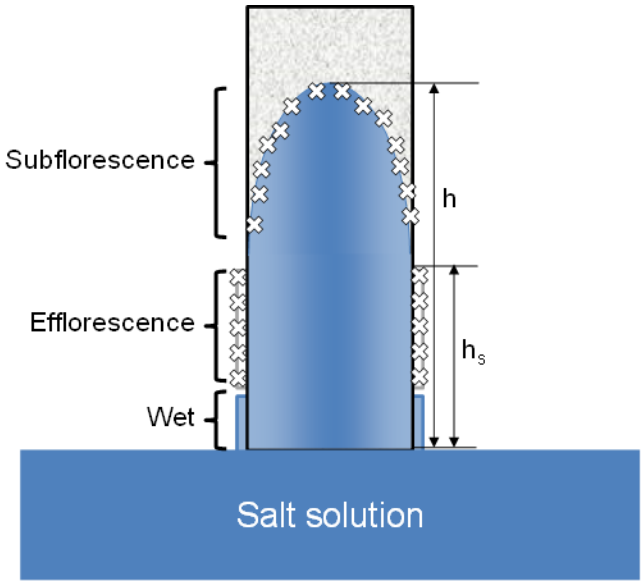

Figure 8.1. Schematic representation of salt rise, evaporation, and crystallization in a porous material (after [148] and [156]).

The internal rise of the solution to $h > h_s$ becomes significant when crystallization of the salts is considered. Recall that the evaporative flux J_E removes only water from the system, leaving the salts behind. The concentration of salt therefore increases near the evaporative surfaces, producing a gradient concentration within the solution. The gradient will cause some of the salts to diffuse back toward the source (and water to diffuse out toward the interface), but as the distance from the source increases, the driving force for that diffusion decreases. Consequently, far away from the groundwater source, supersaturated concentrations of salt may exist at the liquid-vapor interfaces, while near the groundwater source, more dilute concentrations of the salt (even below saturation) will exist. When the degree of supersaturation exceeds a critical value, salts will begin to precipitate out of the solution and crystallize at the interfaces; the higher the degree of supersaturation, the more rapidly this occurs [154]. Salts that precipitate in the film of liquid on the surface of the material is called “efflorescence”, while salts that precipitate in the pores of the material beneath the surface is called “subflorescence.” Efflorescence

is merely superficial salt crystallization, and as such, although often unsightly, it will not cause physical damage to the material. Subflorescence, on the other hand, can generate "crystallization pressures" within the pores of the material, which will induce microcracking if the pressures generate stresses exceeding the material's tensile capacity.

Crystallization pressure can be considered as a mechanical hydrostatic pressure generated by a pore wall to stop the growth of a crystal, or [148, 154]:

$$p_w = \gamma_{CL}\kappa_{CL} \tag{8.5}$$

where γ_{CL} is the surface energy and κ_{CL} is the curvature (proportional to $1/r$) of the crystal-liquid interface. While the pore wall exerts a pressure p_w to stop the crystal from growing, the crystal, meanwhile, generates its own hydrostatic pressure, p_c, as it grows. The pressure p_c is related to the supersaturation of the solution, C/C_0, by Correns' equation [157],:

$$p_c = \frac{RT}{V_C}\ln\left(\frac{C}{C_0}\right) \tag{8.6}$$

where R is the ideal gas constant (8.314 J/mol·K), T is the temperature, and V_C is the specific volume of the crystal. Under mechanical equilibrium, the pressures exerted by the growing crystal (p_c) must be equal and opposite to the pressure exerted by the pore wall (p_w), such that a crystal will only enter a pore of radius r if the degree of supersaturation is large enough that $p_c = p_w$. This means that although the smallest pores generate the largest pressures (Equation 8.5), these pressures will only exist if the degree of supersaturation is high enough that salts can crystallize within them (Equation 8.6). Thus, for a porous material, there exists a practical lower bound on the size of pores that

will become affected by physical salt attack. For portland cement-based materials, this lower bound is believed to occur at water-to-cement ratios (*w/c*) below about 0.45 [100].

In the context of portland limestone cement-based materials, the pore-size dependence of crystallization pressures implies that the pore refinement obtained through filler, nucleation, and chemical effects could cause PLC-based materials to experience increased crystallization pressures – and, by extension, increased tensile "hoop" stresses [148] – thereby reducing their resistance to physical salt attack. The purpose of this research effort is therefore to understand how changes to pore structure induced by the limestone addition will affect the resistance of PLC-based materials to damage by physical salt attack. Two salts will be considered: sodium sulfate, which has been previously identified as a leading source of deterioration by physical salt attack in field observations [151, 152, 158], and calcium nitrate, which has been shown to exhibit particularly severe cracking despite minimal surface efflorescence [159].

8.3 Experimental program

8.3.1 Materials

Six different mortar mixtures were investigated in this study to better understand how modifications to the pore structure of PLC-based materials affect their resistance to physical salt attack. Three different cements of varying fineness were considered: an ASTM C150 Type I/II ordinary portland cement (Cement E), and two ASTM C595 Type IL portland limestone cements with nominally 10 wt.% limestone, produced from the same clinker as the Type I/II cement and ground to different finenesses (a more coarsely ground and a more finely ground cement, Cements EL-CG and EL-FG, respectively).

The chemical and physical properties of the three cements can be found in Table 3.1 to Table 3.4.

For each of the three cements, two mortar mixes were prepared with water-to-binder ratios (*w/b*) of 0.40 and 0.60 – on either side of the $w/b \leq 0.45$ limit recommended by the American Concrete Institute to protect concrete against physical salt attack damages [100]. A high-range water reducer (Grace ADVA 455) was used for the 0.40 *w/b* mixtures, at dosages of 0.2-0.4% by weight of cement, to ensure adequate flowability when filling the molds. All mixtures contained a 50% volume fraction of standard graded Ottawa sand conforming to ASTM C778 [160]. Batches were mixed in a 5 qt. stand mixer according to ASTM C305 standard mixing procedures for mortars [161].

Two different salt solutions, sodium sulfate (Na_2SO_4) and calcium nitrate ($Ca(NO_3)_2$), were prepared for this study, with deionized water (18.2 MΩ-cm resistivity) used as a control. Sodium sulfate was selected due to its common occurrence in soils and groundwater and its lengthy history of aggressive physical attack in concrete structures [100, 147, 151, 152, 158]. Calcium nitrate was selected due to its hygroscopic properties, which cause it to take in additional moisture from the environment upon crystallization [162, 163]. The sodium sulfate solution was prepared from sodium sulfate decahydrate ($Na_2SO_4 \cdot 10H_2O$, Fisher, >99% purity) at a concentration of 15% by mass (0.5 M), and the calcium nitrate solution was prepared from calcium nitrate tetrahydrate ($Ca(NO_3)_2 \cdot 4H_2O$, Acros, >99% purity) at a concentration of 30% by mass (1.5 M). The two concentrations were consistent with those used in prior studies by Lee [156] and Scherer [148]. Fresh solutions were prepared every 28 days.

8.3.2 Salt-exposure testing

Mortar cylinders were cast in 0.8" (2.0 cm, inner diameter) by 8" (20.3 cm, length) plastic tubes, which had been coated with a thin layer of form release agent prior to casting. Three mortar cylinders were cast for each mix. Specimens were cured in sealed conditions at 23 ± 2°C for 24 hr, then removed from their molds and placed in saturated limewater solution until 7 days of age. At that time, each of the specimens was cut with a wet saw to 6" (15.2 cm) in length by removing the bottom and top 1" (2.5 cm) of material. The cut specimens were then stored in air at 50% relative humidity and 23 ± 2°C until 28 days of age. The specimens were exposed to the test solutions beginning at 28 days of age. One 6" specimen per mix was exposed to each of the test solutions.

The exposure chamber itself was modeled after Lewin [164], Scherer [148], and Lee [159] and consisted of a sealed, glass-walled container with a saturated magnesium chloride ($MgCl_2$) solution at its base to provide a constant 33% relative humidity during testing [165]. The test solutions were housed in separate, closed containers above the $MgCl_2$ solution, and holes just wide enough for the mortar specimens to pass through were cut into the tops of the containers, so that evaporation from the test solutions could be minimized. The mortar specimens were placed on platforms inside the test solution containers, such that their bases were submerged approximately 0.5" (1.3 cm) into the solution. Back-up solutions were connected by siphon to the test solution containers in order to maintain a constant solution height and immersion depth. The experimental set-up is shown in Figure 8.2.

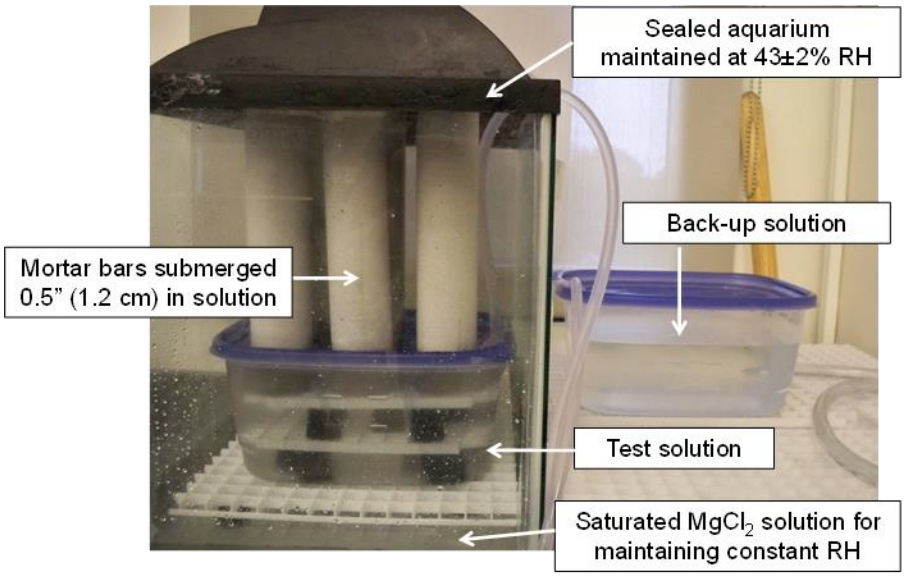

Figure 8.2. Experimental set-up for salt crystallization testing. Mortar bars shown have a different geometry from the specimens used in the present study, but the experimental set-up otherwise remained unchanged.

Every 7 days, the specimens were removed from the chamber. Efflorescence and spalled material were gently removed from the sample surfaces with a soft-bristled brush and weighed. The brushed samples were then also weighed and immediately returned to the salt solutions. Back-up reservoirs were replenished weekly, as needed, and all containers were completely refilled with fresh solutions every 28 days. Magnesium chloride was also added to the chamber every 28 days, or as needed, to maintain an approximately constant relative humidity inside the chamber. Despite the narrow openings in the test solution lids, some evaporation of the test solutions was found to occur, causing the relative humidity of the chamber to stabilize at 43 ± 2%, rather than 33%, during testing.

8.3.3 Supplemental testing

Additional mortar specimens were cast for supplemental characterization of mechanical properties and microstructure. Three 2” (5.1 cm) cubes were cast for compressive strength testing, three 3” by 6” (7.6 cm by 15.2 cm) cylinders were cast for tensile strength testing, and one 4” by 8” (10.1 cm by 20.3 cm) cylinder was cast for sorptivity testing. All supplemental test specimens were cured under identical conditions as the salt-exposed specimens. After 7 days curing in limewater, the 4” by 8” cylindrical specimens were cut with a wet saw to 2” (5.1 cm) in height by removing the bottom 1” (2.5 cm) and top 5” (12.7 cm) of the cylinder. All specimens were then stored in ambient conditions at 50 ± 4% relative humidity and 23 ± 2°C until 28 days of age.

Mechanical properties were measured at 28 days according to ASTM standard procedures: ASTM C109 [166] for compressive strength of 2” (5.1 cm) cubes and ASTM C496 [167] for splitting tensile strength of 3” by 6” (7.6 cm by 15.2 cm) cylinders. Sorptivity testing was also performed at 28 days using the 2” (5.1 cm) disks cut from the 4” by 8” (10.1 cm by 20.3 cm) cylinder. The sides of the 2” specimens were sealed with aluminum tape, and a sheet of plastic film was loosely affixed to the top cut surface with a rubber band prior to testing. Measurements were performed following ASTM C1585 [168], but the standard curing regime was not used, since it was desired to know the sorptive properties of the specimens under their actual curing conditions.

Microstructure was characterized for the specimens using nitrogen adsorption testing. One additional 0.8” by 8” (2.0 cm by 20.3 cm) cylinder of *cement paste* was cast for this purpose. The composition of the cement paste was identical to that of the mortars, but contained no fine aggregate, because the aggregates were of similar size to the

fragments examined by the adsorption analyzer. The paste cylinders were cured under identical conditions as the mortar specimens. At 28 days, fragments of paste were removed from each cylinder and crushed to pass the No. 18 (1.00 mm) sieve and be retained on the No. 30 sieve (0.595 mm). Hydration was halted by soaking the fragments in isopropanol for 30 minutes, followed by drying over vacuum for 5 minutes. Pore size distributions were measured by nitrogen gas adsorption at 77 K (-196°C) in a Micromeritics ASAP 2020 surface area and pore size analyzer, after degassing at 105°C and 10 μmHg for 12 hr.

8.4 Experimental results

The tests conducted in this study serve two primary purposes toward better understanding the influence of limestone-induced pore structure changes on the resistance of PLC-based materials to physical salt attack. The first set of results presented characterize the physical and mechanical properties of the six mortar mixtures. The results are then used to inform the interpretation of the second set of tests presented, which comparatively assess damages induced by the internal crystallization of sodium sulfate and calcium nitrate salts within the mortars. In all results presented, a consistent nomenclature is used, which first designates mixtures by their *w/b* (0.4 or 0.6) and then by their cement type ("I", "C", or "F"). Type I/II cements are specified by the letter "I", while the coarsely ground and finely ground Type IL cements are specified by the letters "C" and "F", respectively.

8.4.1 Mortar characterization

8.4.1.1 Porosity

One of the primary factors influencing the magnitude of crystallization pressures is the size of the pore in which the crystal is growing. As it was shown in Equation 8.5, crystallization pressure is inversely proportional to pore radius, such that crystals growing in smaller pores exert larger pressures – and therefore larger stresses – than crystals growing in larger pores. Thus, materials with narrower pore sizes are more likely to generate larger crystallization pressures, provided that the degree of supersaturation occurring at the evaporation front is large enough that the crystals can enter the pores.

The pore size distributions for the six mortar mixtures obtained by nitrogen gas adsorption are shown in Figure 8.3 (differential) and Figure 8.4 (cumulative). A comparison of pore sizes in the ranges of 1-10 nm and 10-100 nm for each mixture (Figure 8.5) reveals that – as expected [40, 42] – the mixtures prepared at *w/b* = 0.40 have less porosity than those prepared at *w/b* = 0.60, and a greater portion of their porosity confined to pores less than 10 nm in diameter. While the reduction in total porosity could reduce the amount of capillary rise and evaporation experienced by the 0.40 *w/b* mortars, the smaller pore sizes could also generate greater crystallization pressures, depending on the degree of supersaturation achieved by the salt solution. These larger pressures, however, may be compensated for by increases in the tensile capacities of the mortars at the 0.40 *w/b*, as will be investigated in Section 8.4.1.3.

Minor differences in pore size distributions can be observed with respect to cement type. Primarily, it was observed that at both *w/b*'s, the incorporation of limestone fillers slightly increases the volume of pores between 10 and 100 nm in diameter due to

apparent dilution effects. The differences between pore volumes in the 1-10 nm range were negligible by comparison.

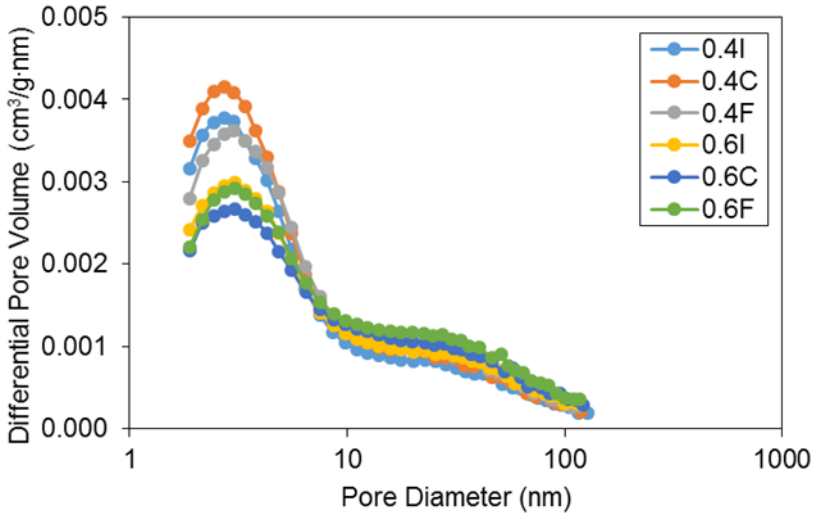

Figure 8.3. Differential pore size distributions for mortar specimens at onset of salt exposure (28 days).

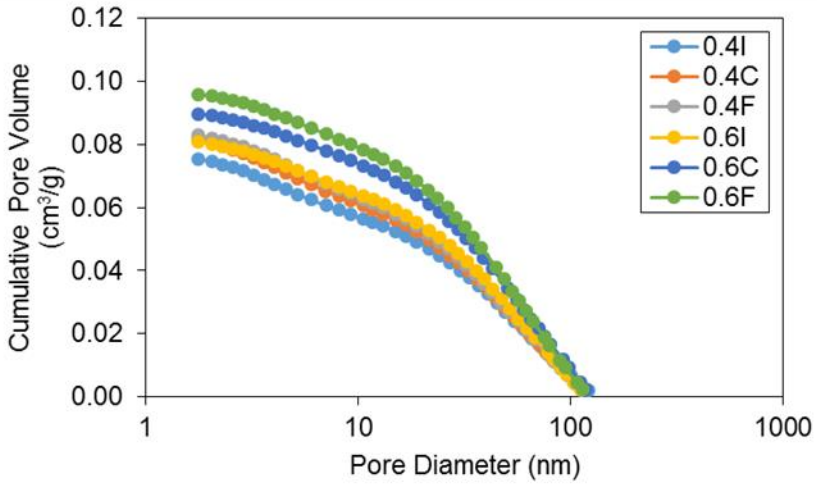

Figure 8.4 Cumulative pore size distribution for mortar specimens at onset of salt exposure (28 days).

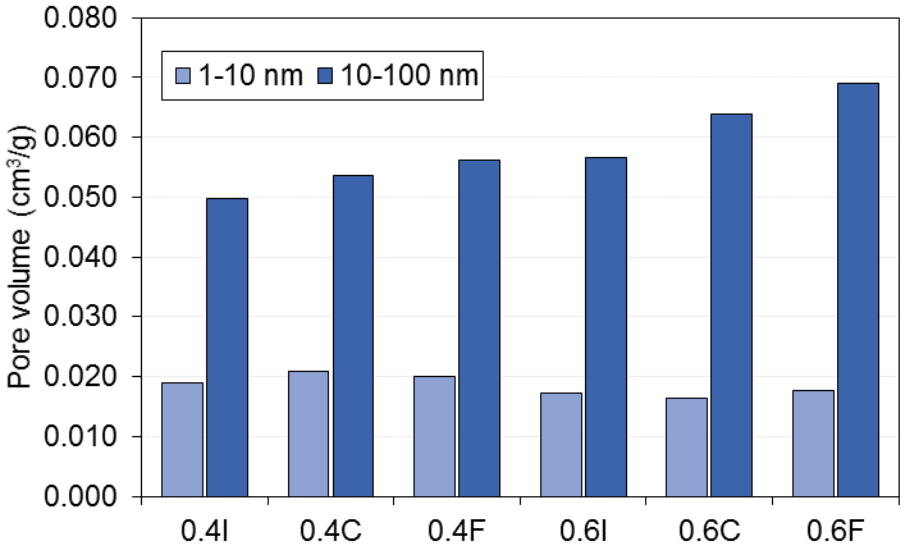

Figure 8.5. Comparison of pore volumes in 1-10 nm range and 10-100 nm range for mortar specimens at 28 days.

8.4.1.2 Sorptive properties

The sorptive properties of the mortar specimens govern the capillary rise within the material. Materials with more rapid rates of capillary absorption will take in more of the salt solution and are therefore more likely to exhibit efflorescence on their surfaces [148]. The rate of the initial absorption is primarily governed by capillary rise through the largest pores of the material, while the rate of secondary absorption is primarily governed by transport through the smaller pores [168-171]. Secondary absorption may become restricted if the tortuosity and interconnectivity of the pore space is such that the permeability of the mortars is reduced [113, 169].

The initial (≤ 6 hr) and secondary (> 24 hr) rates of water absorption for the six mortar mixtures, as determined by a modified ASTM C1585 test, are shown in Figure 8.6. The results indicate that the three mixtures at *w/b* = 0.60 are 2-5 times more absorbent in their first 24 hr of exposure when compared to the mixtures at *w/b* = 0.40, suggesting that they will experience greater amounts of efflorescence as a result. The

differences in initial sorptivity between the two *w/b*'s can be attributed to the larger volumes of capillary pores and more interconnected porosities of the *w/b* = 0.60 mixtures, which were not only observed via nitrogen adsorption, but are also well-established in the literature [2, 42, 169]. At both *w/b*'s, mortars made from the Type IL cements were found to have lower initial rates of water absorption than mortars made from the Type I/II cement, despite having similar measured porosities at each *w/b*. Such results suggest the possibility that filler effects in the Type IL blends did, in fact, contribute to reductions in the size and interconnectivity of the larger capillary pores at both *w/b*'s, although no such reductions could be observed experimentally (although capillary porosity extends into micron-sized pore diameters [40], the capillary condensation of nitrogen gas only occurs in pores below about 200 nm in diameter, limiting the range of pore sizes that can be characterized by nitrogen gas adsorption [80]).

After 24 hr, the rates of water absorption for the six mortar mixtures dropped by 70-90% (75-80%, typically), indicating that most of the capillary rise will occur within the first 24 hr of exposure. Since secondary absorption is primarily a function of the smaller pore sizes – which can be characterized by nitrogen adsorption – the secondary rates of absorption tended to follow the same trends observed by nitrogen adsorption – namely, that at low *w/b*, filler effects slightly reduce sorptivity (porosity), while at high *w/b*, dilution effects increase sorptivity (porosity).

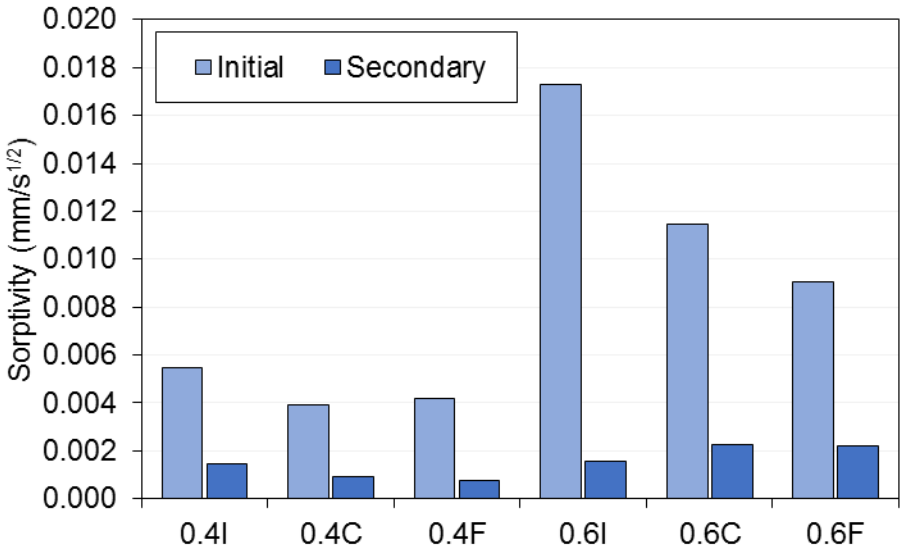

Figure 8.6. Initial and secondary rates of absorption of water for mortar mixes tested at 28 days.

The total absorption, *I*, exhibited by the six mortar specimens is shown in Figure 8.7. Total absorption is defined as the volume of solution absorbed, divided by the cross-sectional area of the specimen, *A*, and can be related to the average height of the capillary rise through the material, if the porosity of that material, φ, is known:

$$I = \frac{m}{A\rho} = h_{ave}\varphi \tag{8.7}$$

where *m* is the mass of solution absorbed and ρ is the density of the solution (assumed to be 1.00 g/cm^3 for water). Since the porosities of the mortars vary with time it and moreover could not be measured by nitrogen gas adsorption, absorption indices were compared, instead, as a surrogate for the height of the capillary rise.

The mixes prepared at *w/b* = 0.60 were found to have absorption indices between 3-5 mm (0.1-0.2 in) by 8 days, while the mixes prepared at *w/b* = 0.40 were only found to have indices of 2 mm (0.08 in) or less. In fact, if the same trends were to continue for 91 days (the duration of the salt exposure test), the total absorption by mixes 0.4I, 0.4C, and

0.4F would only be expected to be 5.0 mm (0.2 in), 3.3 mm (0.13 in), and 2.8 mm (0.11 in), respectively – approximately the same absorption indices measured for the 0.60 *w/b* mortars after only 8 days. Extrapolating the same trends to 91 days exposure for the 0.60 *w/b* specimens, it can be predicted that the total absorption by mixes 0.6I, 0.6C, and 0.6F will be roughly double that expected for the 0.40 *w/b* mixtures, at 7.8 mm (0.31 in), 8.3 mm (0.33 in), and 7.7 (0.30 in) mm, respectively. Since the 0.40 *w/b* mixes are expected to absorb less solution than the 0.60 *w/b* mixes, it is hypothesized that the 0.60 *w/b* mixes will exhibit substantially more efflorescence than the 0.40 *w/b* mixtures.

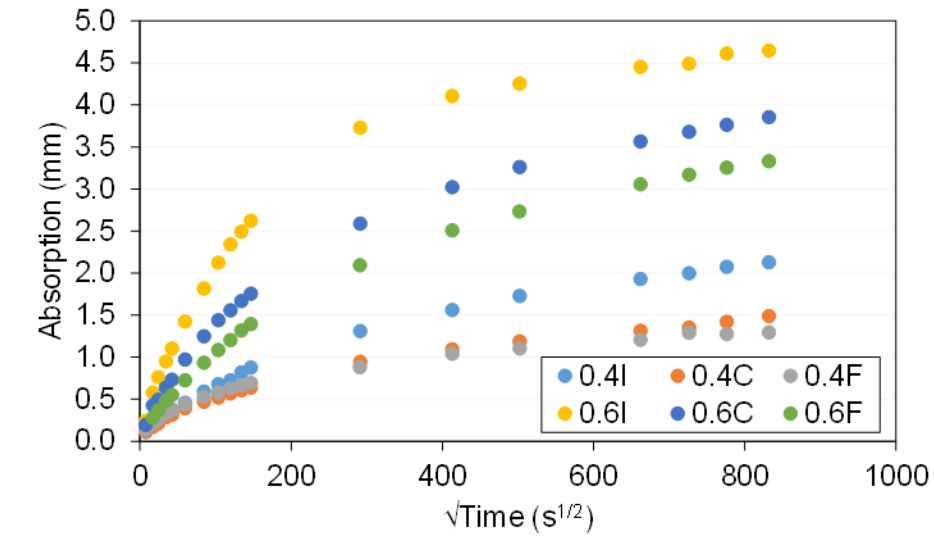

Figure 8.7. Total absorption of mortar mixtures during sorptivity test conducted at 28 days.

8.4.1.3 Mechanical properties

The mechanical properties of the six mortar specimens primarily govern their ability to resist damage by physical salt attack. Pressures can only be exerted by the pore wall to suppress crystal growth (Equation 8.5) while they do not exceed the compressive

strength of the material. Likewise, tensile hoop stresses induced by the compressive restraining forces cannot be resisted if they exceed the tensile strength of the material.

Measured values of compressive and tensile strength are indicated in Figure 8.8. The results show that tensile strength is approximately 7% of compressive strength for the six mortar mixtures tested, and therefore will likely govern the materials' ability to resist damages due to physical salt attack. Tensile strength is moderately affected by the *w/b* of the mix, with the 0.40 *w/b* mixes exhibiting slightly higher (~90 psi) tensile strengths than the 0.60 *w/b* mixes. Tensile strength does not appear to be influenced by the type of cement used, indicating that at a particular *w/b*, each mortar mixture has approximately the same mechanical resistance to physical salt attack and therefore, any observed differences in damage are due to changes to the pore size distribution of the mortar.

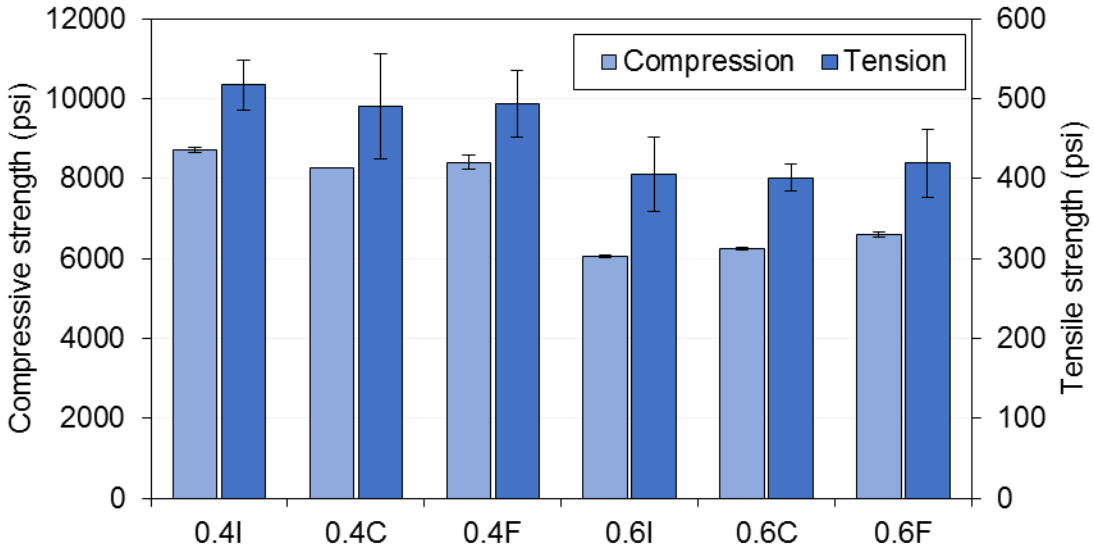

Figure 8.8. Compressive and tensile strengths measured for mortar specimens at 28 days.

8.4.2 Resistance to damage by physical salt attack

The damages induced by the internal crystallization of salts were comparatively assessed for each of the six mortar mixtures. One set of specimens was exposed to a solution of deionized (DI) water to establish the baseline absorptive behavior of the specimens. A second set of specimens was exposed to a 15 wt.% sodium sulfate solution to evaluate the influence of limestone fillers on efflorescence and crystallization-induced damages. Finally, a third set of specimens was exposed to a 30 wt% calcium nitrate solution to evaluate the influence of limestone fillers on a system that does not effloresce but is known to induce expansive cracking damage within cement-based materials [156].

8.4.2.1 Deionized (DI) water exposure

The change in mass measured for the DI-water-exposed specimens over the 91-day exposure period is shown in Figure 8.9. Since mass change depends in part on the density of the solution, an effective absorption index, I_{eff}, was also computed using Equation 8.7 in order to compare results from the specimens exposed to DI water to results from specimens exposed to the other two test solutions. A was assumed to be a constant 0.5 in^2 (3.24 cm^2) for all specimens, and ρ was assumed to be 1.00 g/cm^3 for water. The I_{eff} values corresponding to the measured mass changes for each specimen are also shown in Figure 8.9. The computed values at 91 days are given in Table 8.1.

Since no damage or efflorescence occurred in the DI-water control mixtures, the mass change indicated can be assumed to be the net water imbibed in the specimens due

to capillary rise and evaporation. In general[17], it can be observed that the three *w/b* = 0.60 mixtures imbibed more water than the three *w/b* = 0.40 mixtures, as would be expected based on their relative sorptivity values. More water was imbibed during the first week (and presumably during the first day) as a result of the higher rate of water absorption at early times of exposure. Small differences between the amounts of water absorbed by each cement type were also observed, and were generally consistent with the differences in secondary absorption rates measured in Section 8.4.1.2.

The effective absorption indices measured at 91 days were found to be 10-15% lower than the predicted absorptions for all mixes except for 0.4I. The decrease in absorption is likely due to the evaporation of water from the outer surfaces of the specimens, which was not considered in the sorptivity test. A larger I_{eff} reduction was observed for mix 0.4I (55%) than was observed for the other five mixtures, but it is believed that the larger reduction was due to the presence of a large void on the surface of the specimen, which reduced the volume of material that could absorb water in the capillary rise-affected region. Since the calculation of I_{eff} assumes a constant cross-sectional area, the amount of capillary absorption should be greater than what was computed from the mass change data. In general, the mass change of the DI water samples was found to be primarily a function of the sorptivities of each mixture, indicating that sorptivity will also drive the uptake of salts in samples exposed to sodium sulfate and calcium nitrate solutions.

[17] A slight increase in mass for samples 0.6C, 0.6F, and 0.4F between 28 and 35 days occurred due to the repositioning (and slight tilting) of the specimen container and does not suggest a sudden uptake in moisture at that time.

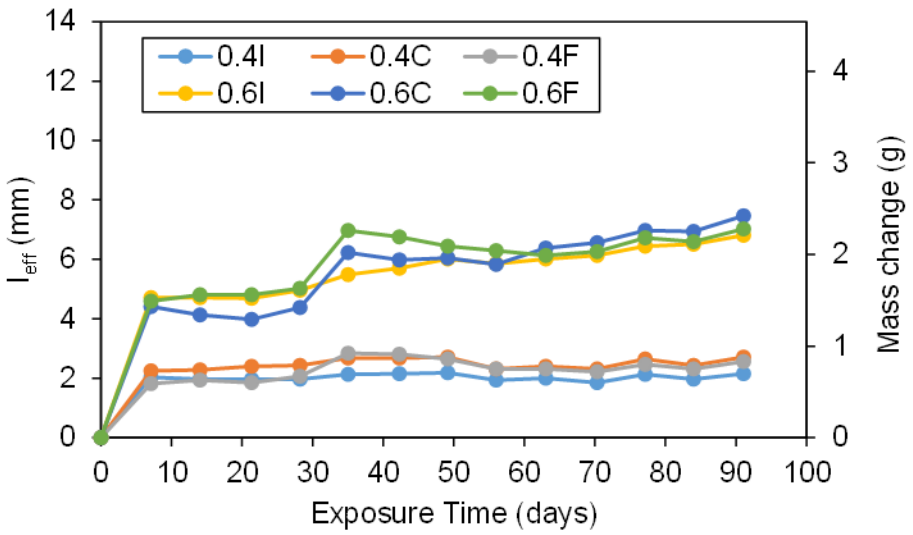

Figure 8.9. Computed effective absorption index, I_{eff}, and measured mass change for mortar specimens exposed to deionized water for 91 days.

Table 8.1. Predicted and measured effective absorption indices for mortar specimens exposed to water and salt solutions, mm.

	0.4I	**0.4C**	**0.4F**	**0.6I**	**0.6C**	**0.6F**
Predicted (DI water)	5.0	3.3	2.8	7.8	8.3	7.7
DI Water	2.2	2.7	2.6	6.8	7.5	7.0
Na_2SO_4	5.2	3.6	3.4	7.3	4.2	5.9
$Ca(NO_3)_2$	3.6	3.9	3.0	10.3	13.5	11.5

8.4.2.2 Sodium sulfate exposure

The mass change measurements and their equivalent effective absorption indices for the specimens exposed to 15 wt.% sodium sulfate solution are shown in Figure 8.10. A measured value of 1.06 g/cm^3 was assumed for the density of the solution in the I_{eff} calculations. Efflorescence and damage in the form of micro-scale surface spalling ("microspalling") were observed for all specimens under the sodium sulfate exposure. Measurements of the efflorescence and microspalled masses are given in Figure 8.11 and Figure 8.12, respectively, and photographs of the specimens after 91 days exposure (following the removal of efflorescence) are shown in Figure 8.13.

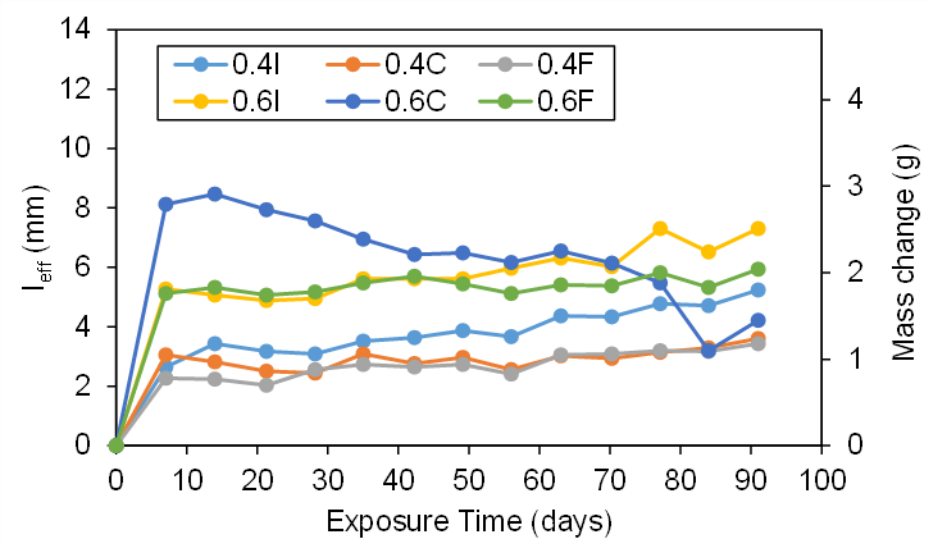

Figure 8.10. Computed effective absorption index, I_{eff}, and measured mass change for mortar specimens exposed to 15 wt.% sodium sulfate solution for 91 days.

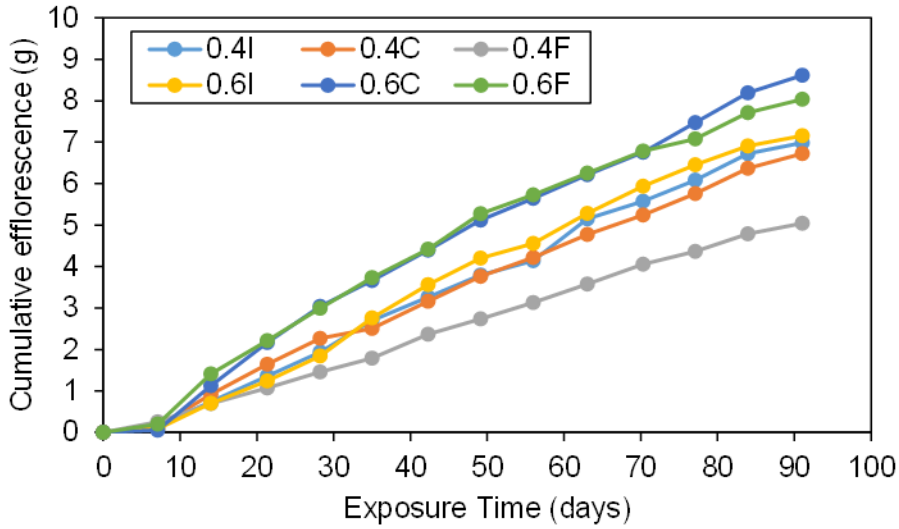

Figure 8.11. Cumulative amount of efflorescence removed from mortar specimens exposed to 15 wt.% sodium sulfate solution.

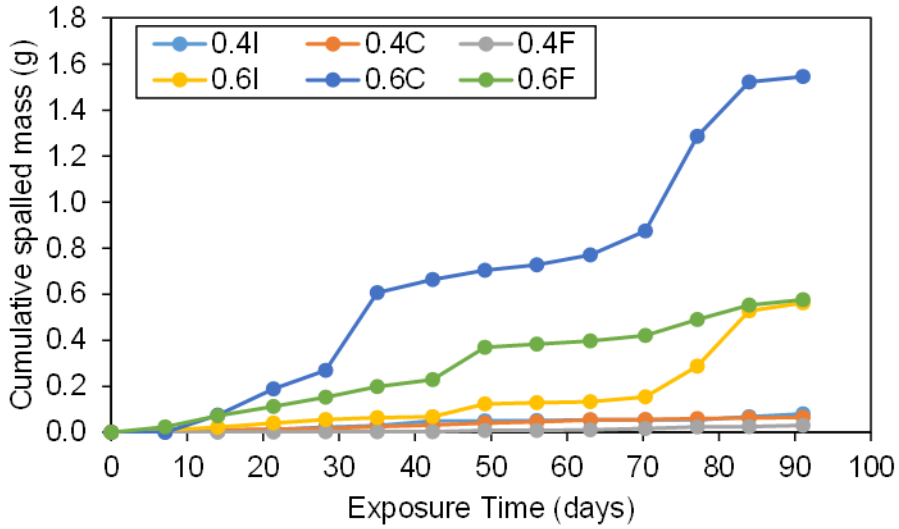

Figure 8.12. Cumulative mass removed due to surface spalling in mortar specimens exposed to 15 wt.% sodium sulfate solution.

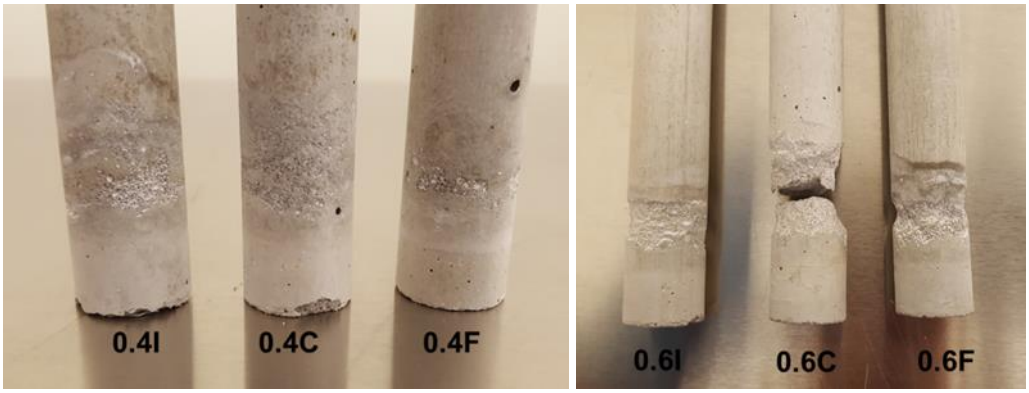

Figure 8.13. Microspallation and disintegration of the surfaces of specimens exposed to 15 wt.% sodium sulfate solution for 91 days. Efflorescence was removed by gentle brushing prior to photographing specimens. Specimen 0.6C fractured upon removal of salts at 91 days, and was not fractured during the exposure.

The absorption of the sodium sulfate solution by the six mortar specimens was found to be significantly different than their absorption of the DI water. After only 7 days of exposure, most of the sodium sulfate-exposed specimens imbibed between 10-30% more sodium sulfate solution than they had DI water, and small amounts of efflorescence were noted to be precipitating on their surfaces. While most of the efflorescence could be

removed by gentle brushing for quantification (Figure 8.11), a thin scale of efflorescence could not be removed from the surface of mix 0.6C, which resulted in an 85% increase in the apparent absorption index of that mix compared to the DI water controls. It is therefore hypothesized that the increase in effective absorption index for the sodium sulfate-exposed specimens is related to precipitation of salts in voids near the surface, which could also not be removed by gentle brushing.

Over time, continued absorption and evaporation of the sodium sulfate solution resulted in the precipitation of large quantities of efflorescence on the surfaces of the specimens. In mixes at *w/b* = 0.60, the efflorescence was frequently accompanied by microspalled flakes of material, typically less than 1 mm in thickness, which progressively exfoliated off of the surfaces of the specimens and reduced the effective absorption index for those mixtures. The typical damage patterns exhibited for the 0.60 *w/b* mixtures are shown in Figure 8.14, which demonstrates the progressive exfoliation and microspalling of a samples 0.6C and 0.6F. A large surface spall can be seen separating from mix 0.6F in the figure, but more typical flakes, less than 5 mm in their maximum dimension, were typically encountered, as shown in Figure 8.15.

The damage caused by the progressive exfoliation of the 0.60 *w/b* mixtures led to a significant weakening of the mortar such that specimen 0.6C eventually fractured under its own weight once the efflorescence had been removed at 91 days (Figure 8.13). Based on their similar modes of microspallation, such a failure would also be anticipated to occur in mixes 0.6I and 0.6F after longer exposure times. Overall, mixes 0.6C and 0.6F exhibited the greatest amounts of microspalling and disintegration among the six mixtures examined (as can be seen in Figure 8.13), suggesting that the filler and dilution-

induced changes to pore size and sorptivity by the interground limestone increased the likelihood of physical salt attack damage at the 0.60 *w/b*.

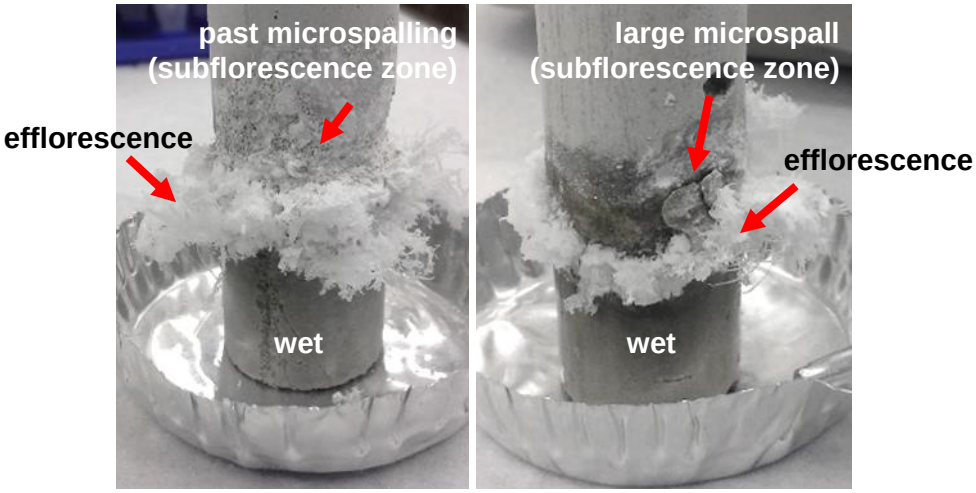

Figure 8.14. Photographs of specimens 0.6C (left) and 0.6F (right) taken at 49 days of exposure, showing typical efflorescence and spalling patterns for sodium sulfate-exposed specimens. Microspalls occur above the level of the efflorescence, in the subflorescence zone. No damage is observed in the "wet" zone, where the mortar is in direct contact with the test solution.

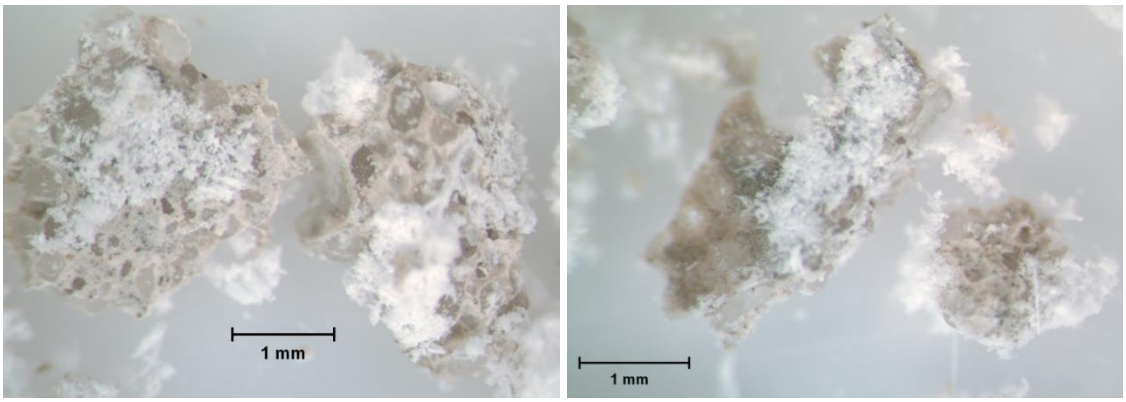

Figure 8.15. Typical microspalled flakes, as viewed under optical microscopy. Flakes were typically found to be < 5 mm in their maximum dimension and < 1 mm in thickness.

In mixes at *w/b* = 0.40, although comparable amounts of efflorescence were produced (Figure 8.11), very little microspalling was observed (Figure 8.12).

Microspalling was typically confined to the efflorescence zone in regions where thick scales of salt had deposited, as illustrated in Figure 8.13. While the spallation of the 0.60 *w/b* specimens caused severe loss of cross-section and a consequential decrease in the load-bearing capacity of the specimens, spallation of the 0.40 *w/b* specimens only minimally penetrated the surface and would therefore not be expected to cause loss of structural integrity in real-world applications. It is more likely that the 0.40 *w/b* mixtures would suffer loss of structural integrity due to *chemical* – rather than physical – attack by the sodium sulfate solution. In fact, after 11 weeks of exposure, evidence of chemical sulfate attack – namely exfoliation in the wet region around the base of the specimens [172] – was visually identifiable for all six sodium sulfate-exposed specimens. Thus, while it appears as though interground limestone increases the potential for physical sulfate attack at *w/b* = 0.60, it does not have the same detrimental effect at *w/b* = 0.40, where average pore sizes are likely too small for the crystals to precipitate in and cause damage.

8.4.2.3 Calcium nitrate exposure

Mass change measurements and corresponding I_{eff} estimates for the specimens exposed to a 30 wt.% calcium nitrate solution are shown in Figure 8.16. For the purposes of I_{eff} calculations, the density of the calcium nitrate solution was measured to be 1.16 g/cm^3. Compared to the other two test solutions, the mortar specimens imbibed significantly more of the calcium nitrate solution, even after differences in solution densities were accounted for. The trends in total mass change were consistent with trends in water sorptivity, but the effective absorption index was much greater than was

predicted for water sorptivity – by as much as 50% for the 0.60 *w/b* specimens (Table 8.1). It is believed that the increased absorption of the calcium nitrate specimens is due to the hygroscopic properties of calcium nitrate salts, which enable it to absorb additional water from the atmosphere in their amorphous solid state [162, 163], thereby inducing swelling in the mortar specimens. Swelling was visually observed in samples 0.4I, 0.6I, 0.6C, and 0.6F during testing (as shown in Figure 8.17), and was followed by surface cracking (0.4I and 0.6C) and ultimately fracture through the entire specimens (0.6F).

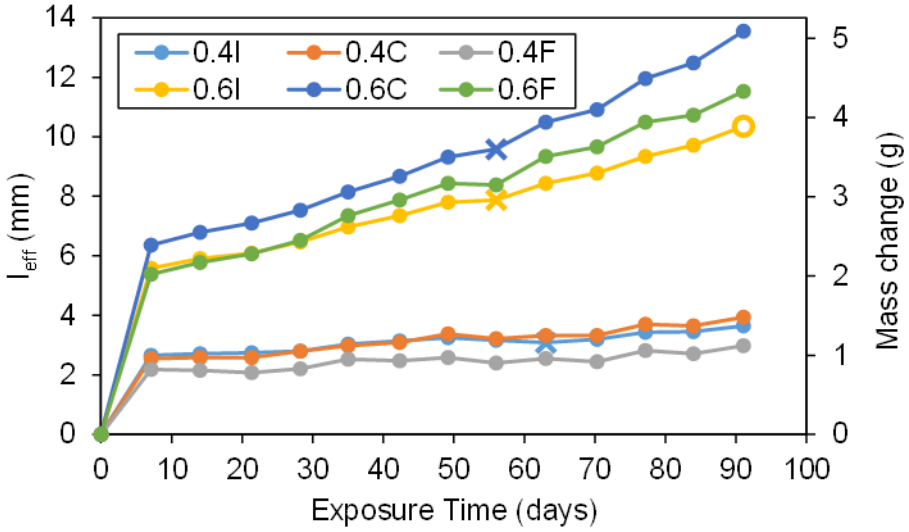

Figure 8.16. Computed effective absorption index, I_{eff}, and measured mass change for mortar specimens exposed to 30 wt.% calcium nitrate solution for 91 days. Initiation of surface cracking in samples 0.6I, 0.6C, and 0.4I is denoted by ×. Failure of sample 0.6I is denoted by ○.

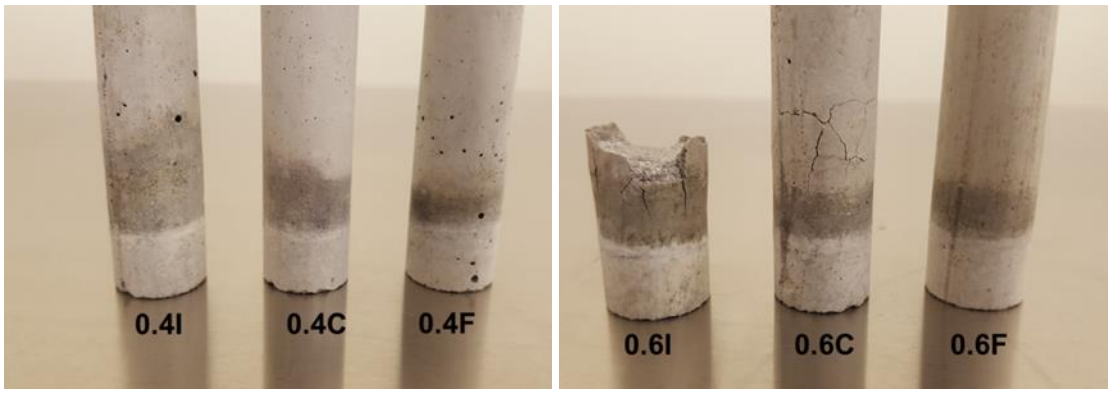

Figure 8.17. Discoloration, swelling, and cracking on the surfaces of specimens exposed to 30 wt.% calcium nitrate solution for 91 days. The light-colored region below the discoloration corresponds to the part of the specimen submerged in the test solution.

Instead of showing efflorescence like the sodium sulfate-exposed specimens had done, the surfaces of the samples showed a dark discoloration, believed to be caused by calcium nitrate salts that initially precipitated on the surface but then absorbed water from the atmosphere and re-dissolved into new supersaturated salt solutions at the surface [162]. Swelling was typically observed in or above this discolored zone, suggesting that it may have been caused by the deliquescence of calcium nitrate salts precipitating near the surface or internal to the mortar specimens. Precipitated salts were clearly visible in the fracture surfaces of sample 0.6I, as can be seen in Figure 8.18, but no salts were observed in the region approximately 0.05 in. (1.2 mm) in thickness around the perimeter of the specimen, where the discoloration and most extreme cracking occurred. It is therefore proposed that the mechanism of physical salt attack by calcium nitrate salts is the hygroscopic swelling of precipitated salts just beneath the surface of the material, where it is possible for moisture from the atmosphere to be absorbed by the salts.

Figure 8.18. Fracture surface of specimen 0.6I after 91 days exposure to 30 wt.% calcium nitrate solution, showing the precipitation of salts internally and the re-dissolution into an aqueous solution near the surface.

8.5 Discussion

The results of this study provide greater insights into the factors influencing physical salt attack in cement-based materials. Capillary rise and evaporation appear to be governed primarily by a material's sorptivity, such that materials with higher initial and secondary (steady-state) sorptivities imbibe more salt solution and are consequently more susceptible to efflorescence, spalling, and cracking than are materials with lower sorptivity values. For all three solutions examined, the total amount of solution absorbed and retained by the material after 91 days of exposure was found to directly correlate with the material's secondary rate of absorption. The secondary rate of absorption for mortars prepared at *w/b* = 0.40 were lower in mixtures containing interground limestone (0.4C and 0.4F) due to the reduction in average pore size caused by dominant filler effects, leading to less uptake of the three test solutions by the Type IL cement mortars. By contrast, the secondary rate of absorption for mortars prepared at *w/b* = 0.60 were higher in mixtures containing interground limestone (0.6C and 0.6F) due to the increases

in overall porosity caused by dominant dilution effects, leading to greater uptake of the three test solutions compared to the Type I/II control mix (0.6I).

Once the solution is imbibed by the material, it begins to precipitate salts onto the surfaces and within the pores located near the liquid-vapor interfaces. In the case of the 15 wt.% sodium sulfate solution, this precipitation results in large quantities of efflorescence forming on the surfaces of the mortar specimens and a progressive disintegration of mortars at high *w/b*'s due to damage by microspalling. The amount of efflorescence again followed similar trends with sorptivity, with highly sorptive materials producing greater amounts of efflorescence with time. Since the total absorption, *I*, is proportional to the height of the capillary rise within the material, *h*, and all six materials were exposed to the same ambient evaporative forces (albeit, internally through different pore structures), then the height of the subflorescence region should also follow trends in total absorption. Thus, materials with higher total absorption indices *I* at a given time are more likely to exhibit more efflorescence due to increases in height of the efflorescence-affected zone.

Increases in efflorescence, however, did not necessarily correlate with increases in damage. Although unsightly, the efflorescence itself only caused minor surface scaling, localized to regions where large deposits of salt scales were observed. Otherwise, the damage was primarily confined to the region just above the efflorescence zone, where the internal subflorescence occurs [148, 156]. Damages within the subflorescence are governed by the size of the pores in which the salts are crystallizing and the overall tensile capacity of the material. Interground limestone did not significantly affect the tensile capacity of the mortar specimens at each *w/b*. As a result, differences in the

amount of damage observed in the sodium sulfate-exposed specimens were related primarily to changes in their pore size distributions. Although the incorporation of limestone fillers increased the total porosity of the mortars, the particle-packing filler effects reduced the average size of the pores, thereby increasing the pressures exerted by crystals growing within them. At the low *w/b*, the driving force for crystallization did not permit the crystallization of salts within these smaller pores; however, at the high *w/b*, salts were able to penetrate the smaller pores of the Type IL mortars, which consequently exhibited greater magnitudes of damage than the Type I/II companion specimen. Damage occurred as progressive exfoliation of the mortar, in flakes typically less than 1 mm in thickness, which suggests that the highest levels of supersaturation occur just beneath the surfaces of the mortars.

The precipitation of calcium nitrate salts caused damage by a different mechanism than did the precipitation of the sodium sulfate salts. No efflorescence was observed in the specimens exposed to the 30 wt.% calcium nitrate solution; rather, the surfaces became coated with a thin, translucent film, which darkened and discolored the mortar beneath it. The film is believed to be caused by the deliquescence of calcium nitrate salts precipitated as "efflorescence" on the surfaces of the mortar specimens; upon crystallization, these salts immediately imbibe additional water from the atmosphere and become a supersaturated liquid, which coats the surface of the mortar. Such deliquescent behavior is well-established in the literature for calcium nitrate salts [162, 163], and is proposed here as the primary mechanism governing physical salt attack damages by calcium nitrate salts in mortars. When these hygroscopic salts precipitate in the interior of the mortar, they also absorb moisture from the environment, causing the mortars to swell

and eventually crack due to the increased uptake of water. Since the pressures exerted on the mortar by the swelling liquid are *not* crystallization pressures, the pore-size dependence is not the same as for non-swelling salts. In fact, the extent of damage occurring in the six mortar specimens investigated in this study trended instead with the total measured porosity. More research is required to fully understand the damage mechanism of these calcium nitrate salts, but it is possible that the swelling behavior elicits more of a bulk response in the material such that the relative pore volumes, rather than relative pore sizes, are the dominant predictor of damage.

8.6 Conclusions

This research investigated the influence of the microstructural changes induced by limestone fillers on the ability of mortar specimens to resist damages caused by physical salt attack due to capillary rise and evaporation. Two salts, each having different damage mechanisms, were considered: sodium sulfate, which exhibited excessive efflorescence and induced progressive surface spallation due to crystallization pressures; and calcium nitrate, which is proposed to exhibit swelling and induce cracking due to the internal deliquescence of precipitated calcium nitrate salts.

With respect to the limestone fillers, it was determined that at high *w/b* (0.60), use of limestone fillers increased salt crystallization damages as a result of the reduced average pore sizes caused by the filler effect. At low *w/b* (0.40), no such increase in damages were observed despite more substantial reductions in average pore size. This apparent protection from salt crystallization damage at *w/b* = 0.40 was attributed to the inability of the salts to penetrate the smaller pores of the material. It is therefore proposed

that filler effects may, in fact, help to protect low-*w/b* concretes from damage due to physical salt attack by requiring excessive driving forces for crystallization that are often not encountered in field exposure conditions. However, if such driving forces are achieved, as in high-*w/b* concretes, the use of fillers can significantly increase the probability of crystallization-induced damages, and additional protections may be required. The precise *w/b* at which mortars and concrete become protected requires additional study over a wider range of *w/b*'s and material compositions, but preliminary evidence from this study suggests that a *w/b* of 0.40 may provide adequate protection from capillary rise and evaporation-induced salt crystallization. While the driving forces for damaging crystallization pressures were not encountered during study for the 0.40 *w/b* mixes, further study is also required to determine if they may be achieved under more aggressive cycles of wetting and drying or hot and cold temperatures.

CHAPTER 9

CONCLUSIONS AND RECOMMENDATIONS

9.1 Conclusions

The primary objective of this research was to understand how the chemical and physical properties of finely divided limestone inclusions influence the early-age hydration and structure and the long-term durability of portland limestone cement (PLC)-based materials, particularly in comparison to ordinary portland cement. As stated in Chapter 1, the specific objectives were:

1. To understand the influence of finely divided limestone inclusions on the hydration and microstructural development of cement-based materials,
2. To examine the relative influences of limestone composition and fineness on cement hydration and microstructural development,
3. To investigate the interactions between limestone and aluminum-rich supplementary cementitious materials (SCMs), and
4. To relate changes in early-age microstructural development to the long-term durability of portland limestone cement concretes.

Experimental and computational investigations into several commercially-available and laboratory-produced PLC systems yielded insights into the relative influences of the limestone's composition, blending rate with portland cement, and particle size distribution on the hydration and microstructural development of PLC-based materials. These insights provided the context for subsequent analysis of the long-term

durability of PLC-based systems as it relates to shrinkage, permeability, and salt crystallization resistance. The following sections present the key findings of this research effort.

9.1.1 Physical effects of limestone fillers

Based on the literature review presented in Chapter 2, it was established that interground limestone can affect cement hydration through three primary physical mechanisms: (1) dilution, (2) heterogeneous nucleation, and (3) improvements in particle packing (filler effect). This study investigated the relative influence of each of these effects on the hydration and microstructural development of six commercially-produced Type IL portland limestone cement pastes. It was concluded that:

- Type IL cements ground to similar fineness as Type I/II cements produced from the same clinker (typically with median particle size $D_{50} \approx 10$ μm) exhibited dilution-dominated hydration behavior, which was characterized by slower rates of hydration and increased total porosity, but also by reductions in early-age chemical and autogenous shrinkage. Such behavior was primarily attributed to the reduced clinker content of the cement, which, in turn, reduced the volume of hydration products formed (dilution effect) and the amount of chemical shrinkage experienced by the paste. Additional decreases in hydration rate and increases in porosity were attributed to the coarser size of the clinker fractions in the Type IL cements compared to the Type I/II cements, which resulted from the relatively finer grinding of the soft limestone during finishing.

- Type IL cements ground significantly finer than Type I/II cements produced from the same clinker (typically with D_{50} < 10 μm) exhibited nucleation- and filler-dominated hydration behavior, which was characterized by more rapid rates of hydration and decreased average pore sizes, but also by increases in early-age chemical and autogenous shrinkage. This behavior was primarily attributed to the enhanced nucleation of hydration products on the surfaces of the limestone particles (heterogeneous nucleation) and the improved space-filling efficiency of the finer particle size distributions (filler effects). In the most finely ground Type IL cements (typically with D_{50} < 9 μm), a finer grind of the clinker fraction further contributed to more rapid rates of hydration and increases in chemical and autogenous shrinkage, which could increase the potential for cracking at early-ages.

9.1.2 Chemical effects of limestone fillers

Investigations into the chemical effects of limestone fillers on the hydration and microstructural development of commercially- and laboratory-produced portland limestone cements yielded the following conclusions:

- For the particular cement compositions, limestone sources, and 0.40 *w/b* investigated, it was found that approximately 10-20% of the calcium carbonate ($CaCO_3$) in the limestone becomes available to participate in cement hydration within the first few days of hydration. The availability of the $CaCO_3$ shifts the thermodynamic balance of the system such that ettringite is no longer converted into the AFm phase monosulfate, but rather becomes indirectly stabilized as the

$CaCO_3$ and any remaining C_3A (and at later ages, C_4AF) react with one another to produce the carbonate-AFm hydration products, hemi- and monocarbonate.

- Limestone contents as low as 3% by weight are sufficient to form carbonate-AFm phases, and hemi- and monocarbonate were detected after about 3 days of hydration in all of the limestone-containing Type I/II and the Type IL cement pastes investigated.
- Analysis by the modified Powers' model reveals that formation of carbonate-AFm increases the chemical shrinkage experienced by limestone-containing Type I/II and Type IL cement pastes. These increases are not properly accounted for by the model, leading to the conclusion that Powers' model is not appropriate for the prediction of chemical shrinkage in limestone-containing Type I/II or Type IL cement systems. Comparison of experimental data to Powers' model predictions can, however, illustrate the chemical effects of reactive fillers on the hydration of blended cement pastes.
- While the particular mineralogical composition of the limestone slightly influences the amount of $CaCO_3$ available for reaction and the degree of hydration and chemical shrinkage exhibited by the paste, the effects of geological source are minimal in comparison to the other physical and bulk chemical ($CaCO_3$-related) effects previously discussed.

9.1.3 Interactions with supplementary cementitious materials

Synergetic interactions between limestone and alumina-containing SCMs were investigated in this study to determine how the alumina source (SCM type) and its

interaction with the limestone affected the hydration, microstructural development, and early-age shrinkage of PLC-SCM blended systems. Investigations of PLC-SCM synergies in systems blended with either 15% Class F fly ash, 15% Class C fly ash, or 50% slag, by total mass of cementitious material, led to the conclusions that:

- An underlying mechanism of the limestone-SCM "synergy" is the acceleration of the secondary hydraulic and pozzolanic SCM reactions by the limestone filler. Blends of PLCs with SCMs were found to exhibit secondary SCM-induced pore refinements an average 3-7 days earlier than blends of ordinary portland cements (OPCs) with SCMs did.
- PLC-SCM synergies are not strictly related to the alumina content of the SCM, but also to the relative reactivity of the SCM. The hydraulically reactive SCMs, Class C fly ash and slag, reacted more rapidly and showed greater limestone synergies than did the more slowly reacting pozzolanic Class F fly ash, despite having comparatively lower total alumina contents.
- Although the purported "synergies" between PLCs and SCMs beneficially increase the compressive strength and further refine the microstructure of PLC-SCM blended systems, they also negatively increase the chemical and autogenous shrinkage experienced by the PLC-blended systems at early-ages, thereby increasing the potential for cracking in structural applications.

9.1.4 Durability implications

The implications of limestone-induced microstructural changes on the permeability of PLC-blended systems were indirectly assessed using electrical test

methods (surface resistivity [SR] and rapid chloride permeability [RCP] tests). It was concluded that:

- Formation factor – rather than the measured values of resistivity (SR) or total charge passed (RCP test) – provides a more reliable indicator of microstructural development and permeability in blended cement systems. Changes to pore solution composition caused by the incorporation of limestone and/or SCMs artificially increases the resistivity and decreases the total charge passed by OPC- and PLC-blended systems, which may lead to erroneous lower permeability classifications under current testing protocols.
- Interground limestone has no significant effect on the permeability of neat PLC systems. Changes in permeability were primarily affected by the relative grind of the clinker particles within the cement, rather than by the physical or chemical effects of the limestone particles.
- Synergetic interactions between SCMs and limestone fillers produced PLC-blended concretes with equivalent or reduced permeabilities compared to OPC-blended concretes. 50% cement replacement with slag offered the greatest improvements in permeability at 56 days, followed closely by the 15% replacement with Class F fly ash, and less closely by the 15% replacement of cement by Class C fly ash.
- Service life predictions indicated that neat PLC concretes do not have significantly different expected service lives than neat OPC concretes, but when blended with SCMs, the synergetic reductions in permeability may extend the service lives of PLC-blended mixes by up to 15% compared to OPC-blended

mixes. The predictions, however, rely upon the underlying assumptions (1) that the service life is governed by the ingress of chloride ions and subsequent corrosion of the reinforcing steel, (2) that the diffusion coefficient of concrete is directly proportional to the total charge passed during an RCP test, and (3) that the concrete is uncracked. The use of PLCs (and combinations of PLCs with SCMs) in concrete applications challenges the validity assumptions (2) and (3), as it was determined that PLCs (and PLC-SCM blends) may alter the total charge passed by the RCP test through electrochemical means and may also increase the potential for early-age cracking in structural applications.

The implications of limestone-induced microstructural changes on the resistance of neat PLC systems to physical salt attack were also assessed in mortars exposed to sodium sulfate (Na_2SO_4) and calcium nitrate ($Ca(NO_3)_2$) solutions. Based on the results, it was proposed that Na_2SO_4 salts induce damage to the mortar as a direct result of pressures exerted on the pore walls during their crystallization, while $Ca(NO_3)_2$ salts induce damage indirectly through hygroscopic swelling beneath the surface of the mortar after their crystallization. With respect to the influence of PLCs, it was additionally concluded that:

- The effects of finely ground PLCs on physical salt attack resistance are limited by the *w/b* of the material. At low *w/b* ($\leq$ 0.40), the finer microstructures of PLC systems appear to offer increased protection against physical salt attack damages due to the higher driving forces required to initiate salt precipitation in smaller pores. At high *w/b* ($\geq$ 0.60), the finer microstructures of PLC systems appear to

increase damages caused by physical salt attack due to the higher pressures exerted by salts crystallizing in the smaller pores of the PLC pastes.

- More coarsely ground PLCs may induce the opposite effects at high and low *w/b*'s due to the comparatively coarser porosities exhibited by those materials. Coarsely ground PLCs may offer increased protection at high *w/b* due to the decreased crystallization pressures exerted by salts precipitating within the larger pores, but they may also remove the protections at low *w/b*'s by reducing the required driving force for salt crystallization to an attainable level.

9.2 Recommendations for practice

9.2.1 Early-age behavior

Based on the results of the present study, it was concluded that the relative fineness of a portland limestone cement has the most significant impact on its rate of hydration and extent of chemical and autogenous shrinkage at early ages. Consequently, PLCs may be selected based on their fineness in order to obtain a certain combination of desired early-age properties. In applications where more rapid hydration and strength development rates are required, a fine PLC is recommended, but such selection comes at the expense of increased early-age shrinkage. In applications where early-age shrinkage is to be limited, use of a coarse PLC or a fine PLC in combination with 15% Class F fly ash is recommended instead.

Determination of whether a Type IL cement is "fine" or "coarse", however, is not a trivial task. While Blaine fineness is widely considered the industry standard for characterizing the fineness of a cement, it was found to be relatively insensitive to

differences in the particle size distributions of the Type IL cements considered in this study, such that the largest Blaine "fineness" values were actually obtained for the most dilution-dominated cements. These insensitivities in Blaine fineness can be related to the particle-packing and specific gravity assumptions implicit in the calibration of the Blaine fineness test. Since Type IL cements have typically lower densities (due to the limestone inclusion) and improved particle packing efficiencies (due to broader particle size distributions) compared to ordinary portland cements, the mass of sample that is used based on standard calibration procedures yields a lower porosity than is assumed by the standard, which, in turn, results in higher Blaine fineness values [59]. Instead, fineness parameters obtained by laser diffraction analysis were found to be comparatively more sensitive to changes in the particle size distributions and correlated well with the resulting dilution- or nucleation-dominated behaviors. Based on this preliminary study, it is recommended that "fine" Type IL cements be classified as those cements having median particle sizes $D_{50} < 10$ μm or 90^{th} percentile particle sizes $D_{90} < 30$ μm. But, further characterization of a larger selection of portland and portland limestone cements would be required to set accurate limits on the classification.

9.2.2 Use with SCMs

When combined with SCMs, PLCs were found to exhibit equivalent or greater compressive strengths and equivalent or reduced permeabilities when compared to neat OPC mixtures. These higher strengths and lower permeabilities occurred irrespective of the fineness of the Type IL cement, suggesting that coarsely ground PLCs may be

beneficially combined with SCMs in order to counter some of the strength reductions and porosity increases attributed to the dilution of the clinker.

The increases in compressive strength and reductions in permeability also tended to be greater in blends of SCMs with PLCs than in blends of SCMs with OPCs due to the synergetic interactions between the limestone and the alumina within the SCM. While the synergetic interactions beneficially refined the porosity of the systems, these refinements were accompanied by often substantial increases in early-age shrinkage in PLC-SCM blended systems. In applications where low shrinkage is required, it is *not* recommended that combinations of PLCs with Class C fly ash or high volumes of slag be used. Further research is recommended to determine if the current GDOT limits on slag replacement in structural concrete should be reduced for blends containing PLCs due to the significant increases in early-age shrinkage observed at the present 50% maximum replacement level.

9.2.3 Use in aggressive environments

The results of this study indicate that PLC and PLC-SCM blended systems have comparable or slightly improved resistance to the ingress of contaminants when compared to neat OPC and OPC-SCM blended systems at *w/cm* = 0.445. Similar or greater improvements in permeability would be expected at even lower *w/cm*'s, where the dilution of the clinker by the limestone has a less impactful role in hydration and microstructural development due to the inability of the clinker to fully hydrate [37]. Therefore, PLCs may be used as a suitable alternative to OPCs in structural applications

requiring low permeability to contaminants, provided that the potential increases in early-age shrinkage cracking are also controlled.

In applications where concrete or mortar may be susceptible to physical salt exposures (e.g., foundations, slabs on grade, or bridge substructures in direct contact with soil or groundwater), it is recommended that finely ground PLCs be used only at low *w/b* (e.g., ≤ 0.40), where the driving force for crystallization is so high that salts cannot form within the damagingly small pores of the material. If higher *w/b*'s (e.g., ≥ 0.60) are to be used, only coarsely ground PLCs are recommended, as the increase in average pore size due to dilution effects will reduce the crystallization pressures exerted on the pore walls within the PLC system.

9.2.4 Methods for characterizing and modeling PLC systems

The research presented in this study also revealed several areas where conventional approaches to characterizing and modeling neat OPC systems did not suitably apply to PLC or PLC-SCM blended systems. In addition to the insufficiencies with the Blaine fineness test previously discussed, the study also indicated that Powers' model for chemical shrinkage under-predicts the amount of chemical shrinkage occurring in PLC (and limestone-containing OPC) systems due to its inability to account for the secondary hydration of carbonate-AFm species. It is therefore not recommended that Powers' model be used for the prediction of early-age shrinkage in PLC-based materials.

Furthermore, the influence of pore solution conductivity on SR and RCPT measurements was found to have a significant impact on the perceived permeability classifications of both OPC and PLC systems – especially those containing blends with

SCMs. Formation factor was determined to provide a more reliable and realistic indicator of microstructural development in both systems and is recommended for use as a more appropriate indicator of concrete's ability to resist the ingress of contaminants such as chloride ions. Further research is required to determine what values of formation factor correspond to acceptable chloride diffusion parameters, not only so that appropriate limits may be set for concrete specifications, but also so that more accurate estimates of expected service life may be predicted. Until such research is done, it is recommended that the SR and RCPT tests only be used in quality control applications where samples of field-batched concrete are compared to laboratory-prepared reference samples having similar compositions and pore solution chemistries. Use of either test with strictly defined performance requirements (e.g., a maximum permitted chloride permeability of 2000 coulombs at 56 days to provide adequate impermeability) is not recommended due to the conflating influence of pore solution composition.

9.3 Recommendations for future research

The research presented in this dissertation provides further insights into the chemical and physical influences of limestone fillers on the hydration and microstructural development of PLC-based materials. However, the research also demonstrates the need for additional research related to the optimization of limestone-blended systems for use in structural applications. Specific areas for future research are recommended as follows:

- The research conducted in this study – for most considerations – only considered *w/cm*'s of either 0.40 or 0.445. While the *w/cm*'s selected provided substantial insights into the influence of limestone fillers on the hydration and

microstructural development of PLC systems compared to those of OPC systems, they were still among the highest *w/cm*'s permitted by GDOT for structural concrete applications and only provide an "upper-bound" on the behavior of PLC systems. A wider range of *w/cm*'s should also be examined to more fully understand the balance between dilution-dominated behavior (which is more pronounced at higher *w/cm*'s) and nucleation- and filler-dominated behavior (which is more pronounced at lower *w/cm*'s) at other *w/cm*'s that may be encountered in engineering applications.

- The research conducted in this study also only considered PLC systems with 8-12% replacement of clinker with limestone. While the dosage rates examined encompassed the typical range of limestone contents expected for Type IL cements produced within the United States (based on a 15% limit set in current American [10] and Canadian [16] cement specifications), higher dosages of up to 35% are permitted in other parts of the world, including Europe [13]. Additional research is needed to characterize the early-age hydration and microstructural development – and their long-term durability implications – for PLC-based systems at these yet higher limestone dosages.
- With respect to SCM synergies, this research only considered binary blends of PLCs with either 15 wt.% replacement Class F fly ash, 15 wt.% replacement Class C fly ash, or 50 wt.% replacement slag. Further research is recommended over a wider range of SCM dosages in order to determine the minimum replacement level for each SCM required to overcome dilution-induced reductions in compressive strength and impermeability and the maximum

replacement level for each SCM such that early-age shrinkage is reduced. Additional research considering ternary blends of PLCs with both fly ash and slag is also recommended in order to investigate how PLC-SCM synergies affect hydration, microstructural development, and long-term durability in ternary blended systems.

- Finely ground PLC systems were found to exhibit particularly pronounced increases in early-age chemical and autogenous shrinkage at the 0.40 *w/cm* investigated in this study. Since autogenous shrinkage, in particular, becomes more pronounced at lower *w/cm*'s, further research is needed to determine whether there should be an upper limit on the fineness of the Type IL cements used at low *w/cm*'s in order to protect concrete structures from detrimental increases in early-age chemical and autogenous shrinkage.
- Through studies of laboratory-blended PLCs containing custom blends of limestone powders, it was demonstrated that limestone mineralogy has a small effect on the early-age hydration and chemical shrinkage of PLC-based materials, but that ultimately it is the physical and bulk-chemical properties of the limestone that contribute most to the early-age properties. The four limestone powders investigated, however, all had relatively similar mineralogical compositions to one another. Further research should also examine a wider array of limestone sources, to better understand how mineralogical impurities such as amorphous silica or clay affect the hydration and property development of PLC-based materials.

- Limestone was found to interact with both C_3A and C_4AF phases to produce carbonate-AFm phases. While much has already been published in the literature about C_3A interactions with limestone [19, 20], less is known about the C_4AF interactions. Thus, further study into carbonate-AFm reactions from C_4AF hydration is recommended.
- Powers' model was shown to be inappropriate for predicting the chemical shrinkage of PLC- and limestone-containing OPC-based materials due to its inability to account for secondary formation of carbonate-AFm phases. Additional study considering hydration over a wider range of *w/b*'s, cement compostitions, and degrees of hydration is necessary to develop a modified model which adequately accounts for the interactions between the limestone and the clinker phases. In particular, it is necessary to understand how the initiation of AFm formation relates to degree of hydration, and by what order it increases the chemical shrinkage of the paste relative to the clinker phases already accounted for by the model.
- The diffusion coefficients for OPC and PLC concretes were estimated from the RCP test results using the Nernst-Einstein equation, following the model of Barde, et al. [122]. The model implicitly normalizes the total charge passed during the RCP test by an *average* pore solution conductivity for neat OPC concretes, and therefore does not adequately account for the effect of pore solution conductivity on the total charge passed by the SCM-blended systems. Predicted diffusion coefficients are consequently lower and expected service lives consequently longer due to the inability of the model to separate the structural

diffusion parameters from the electrochemical artifacts. Thus, additional research is needed to develop a more appropriate relationship between the total charge passed by RCP and the ionic conductivity of the chloride ions, so that the Nernst-Einstein equation may be more appropriately used to characterize diffusion coefficients and predict service lives of OPC-SCM and PLC-SCM blended systems.

- Finally, a testing protocol was developed based on the research of Scherer [148], Lee [156], and Lewin [164], to comparatively assess the resistance of PLC-based mortars to damage by physical salt attack. While the test results elicited greater insights into the effect of fine limestone inclusions on the crystallization resistance of PLC-based materials, several opportunities for further study remain:
    - The laboratory study was conducted for salt concentrations significantly higher than would be expected in field exposures. Time to damage initiation under laboratory concentrations should be related to time to damage initiation under field concentrations.
    - The laboratory study only considered capillary rise and evaporation under approximately constant temperature and relative humidity profiles. Studies considering capillary rise and evaporation under thermal cycles, moisture cycles, and combined thermal and moisture cycles, should also be conducted on PLC-based materials to determine if the smaller average pore sizes at a 0.40 *w/b* continue to offer increased protection against physical salt attack damages under more realistic exposures.

- The salt crystallization study also only considered mortar specimens prepared at two discrete *w/b*'s. A broader range of *w/b*'s should be investigated for both mortars and concretes to determine (1) at what *w/b* the concrete becomes protected by the smaller pore sizes of the finer PLCs, and (2) whether the threshold *w/b* applies to both mortar and concrete or if interfacial transition zone (ITZ)-effects in the concrete change the recommended *w/b* limit.
- Finally, additional studies should be conducted on coarsely ground PLCs to determine if the coarser particle sizes and pore size distributions provide protections from damage at higher *w/b*'s.

APPENDIX A

DERIVATION AND SENSITIVITY ANALYSIS OF POWERS' MODEL FOR INERT FILLERS

A.1 Powers' model for portland cement pastes

Powers' model for portland cement hydration gives predicted volumes of water-filled capillary porosity, unhydrated cement, hydration product, and chemical shrinkage as a linear function of the degree of hydration, α, of the cement, and the initial porosity, p, of a cement and water system. Commonly used expressions for each of the terms, based on experimental fits to Powers' original model [33], are given in Equation A.1 [35]:

Unhydrated cement: $V_{uc} = (1-p)(1-\alpha)$ (A.1a)

Capillary water: $V_{cw} = p - 1.32(1-p)\alpha$ (A.1b)

Hydration product: $V_{hp} = 2.12(1-p)\alpha$ (A.1c)

Chemical shrinkage: $V_{cs} = 0.20(1-p)\alpha$ (A.1d)

Volume balance: $V_{cw} + V_{uc} + V_{hp} + V_{cs} = 1$ (A.1e)

Parsing these equations, the following observations can be made:

1. The volume fraction of unhydrated cement, V_{uc} (Equation A.1a), is defined as the product of the initial volume fraction of cement in the paste (1-p) and the fractional amount of cement that has not yet reacted (1-α).
2. The initial porosity, p, is equivalent to the initial volume fraction of water in the system (Equation A.1e, with $\alpha = 0$).

3. Approximately 1.00 cm^3 of cement (Equation A.1a) reacts with 1.32 cm^3 of water (Equation A.1b) to produce 2.12 cm^3 of hydration product (Equation A.1c) and 0.20 cm^3 of chemical shrinkage (Equation A.1d).
4. The total system volume is conserved (Equation A.1e).

These four observations form the foundation of the original Powers' model and will enable the derivation of a modified Powers' model for inert fillers.

A.2 Powers' model for inert fillers

Consider a system containing water, cement, and an inert filler, each occupying an initial volume V_w, V_c, and V_f, respectively, and having an initial mass M_w, M_c, and M_f, respectively, as illustrated in Figure A.1. If p is defined as the initial volume fraction of water in the paste, then by definition:

$$p = \frac{V_w}{V_w + V_c + V_f} \tag{A.2}$$

Assuming that the cement and filler are combined in a single "binder" phase, then Equation A.2 can be rewritten as:

$$p = \frac{V_w}{V_w + V_b} \tag{A.3}$$

where V_b is the total volume of binder = $V_c + V_f$.

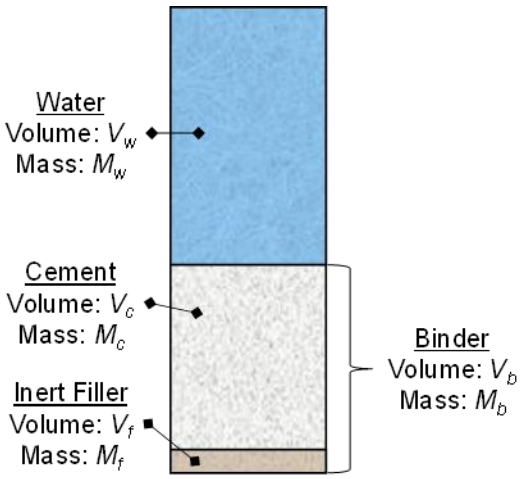

Figure A.1 Schematic representation of cement paste containing inert filler.

In the case where cement pastes are batched by mass rather than by volume, the volume terms V_i may be determined from the masses M_i if the densities ρ_i are known for each phase *i*. In such a case, Equation A.3 may be rewritten as:

$$p = \frac{\dfrac{M_w}{\rho_w}}{\dfrac{M_w}{\rho_w} + \dfrac{M_b}{\rho_b}} \tag{A.4}$$

Algebraic manipulation of Equation A.4 yields a simple expression for *p*:

$$p = \frac{\dfrac{M_w}{M_b}}{\dfrac{M_w}{M_b} + \dfrac{\rho_w}{\rho_b}} = \frac{w/b}{w/b + \dfrac{1}{SG_b}} \tag{A.5}$$

where *w/b* is the water-to-binder ratio of the cement paste (by mass) and SG_b is the specific gravity of the binder.

For a system containing an inert filler, the quantity 1-*p* no longer represents the volume fraction of cement in the system, but rather the volume fraction of *binder* in the system. To obtain the volume fraction of unreacted cement in the system, the binder

fraction 1-p must be multiplied by the volume fraction of cement in the binder, 1-f_v, where f_v is the volume fraction of filler in the binder:

V_{uc} = (volume fraction of cement)×(1-α)

= (volume fraction of binder)×(volume fraction of cement in binder)×(1-α)

$$V_{uc} = (1-p)(1-f_v)(1-\alpha) \tag{A.6}$$

If the filler is dosed as an equivalent mass of cement (i.e., if 10% filler means that 10% of the cement by mass has been replaced by an equivalent mass of filler), then f_v can be determined from f_m, the mass fraction of filler in the binder (i.e., the mass substitution rate), as follows:

$$f_v = \frac{V_f}{V_b} = \frac{\frac{M_f}{\rho_f}}{\frac{M_b}{\rho_b}} = \frac{M_f}{M_b} \times \frac{SG_b}{SG_f}$$

$$f_v = f_m \times \frac{SG_b}{SG_f} \tag{A.7}$$

Finally, if the fraction of unhydrated cement remaining is given by (1-p)(1-f_v)(1-α), then it follows that a fraction (1-p)(1-f_v)(α) of the original volume contained cement that has been hydrated. Since the filler is assumed to be inert and have no influence on cement hydration, the other relationships assumed by Powers' model should still hold: namely, 1.00 cm^3 of cement will react with 1.32 cm^3 of water to yield 2.12 cm^3 of hydration product and 0.20 cm^3 of chemical shrinkage. In other words, any time the term (1-p)α appears in the original Powers' model, it can simply be replaced by (1-p)(1-f_v)(α).

Thus, the modified Powers' model for inert fillers, dosed on an equivalent mass basis, can be written as:

Capillary water: $$V_{cw} = p - 1.32(1-p)(1-f_v)\alpha \quad \text{(A.8a)}$$

Unhydrated cement: $$V_{uc} = (1-p)(1-f_v)(1-\alpha) \quad \text{(A.8b)}$$

Inert filler: $$V_f = (1-p)f_v \quad \text{(A.8c)}$$

Hydration product: $$V_{hp} = 2.12(1-p)(1-f_v)\alpha \quad \text{(A.8d)}$$

Chemical shrinkage: $$V_{cs} = 0.20(1-p)(1-f_v)\alpha \quad \text{(A.8e)}$$

Volume balance: $$V_{cw} + V_{uc} + V_{hp} + V_{cs} + V_f = 1 \quad \text{(A.8f)}$$

where p is given by Equation A5 and f_v is given by Equation A.7. It can be confirmed through simple algebra that the total system volume is conserved (Equation A.8f).

A.3 Sensitivity analysis

Powers' model is primarily used to predict the maximum possible degree of hydration for a particular cement paste and to understand how porosity and chemical shrinkage evolve in a cement paste over its hydration period. For most applications, three primary inputs are required: the *w/b* of the paste, the filler content, and the specific gravity of the binder. The effect of each of these inputs is considered in detail below.

A.3.1 Variation in *w/b*

Arguably the most significant input for Powers' model is the initial *w/b* of the cement paste, as the *w/b* dictates the relative amounts of material available to react. Values for maximum degree of hydration, maximum chemical shrinkage, and total porosity predicted by Powers' model are shown in in Figure A.2 through Figure A.4 for

an ordinary portland cement paste with SG = 3.15. A summary of the results is presented in Table A.1. The most significant variations in maximum degree of hydration and maximum chemical shrinkage are observed for sealed cement pastes with *w/b* < 0.42 (threshold for complete hydration), while the most significant variations in total porosity are observed for all specimens able to achieve complete hydration.

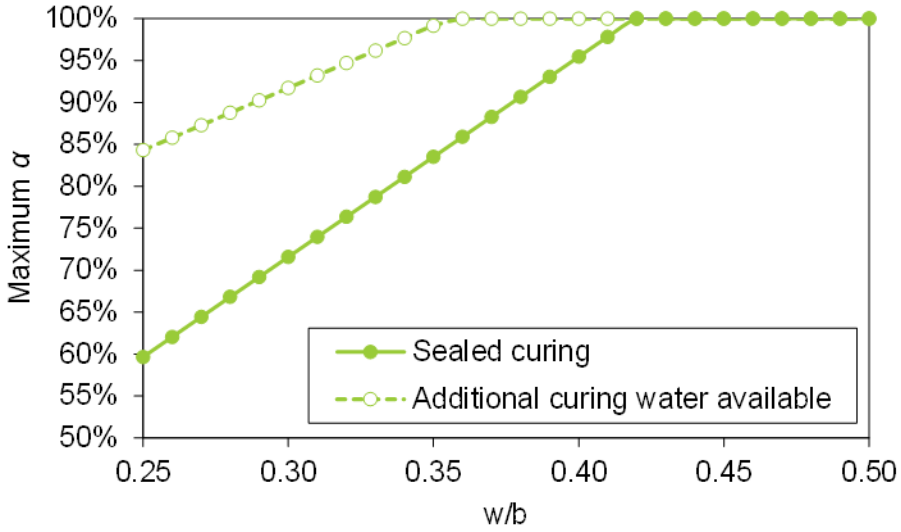

Figure A.2 Maximum degree of hydration for a portland cement paste with SG = 3.15 as a function of *w/b*.

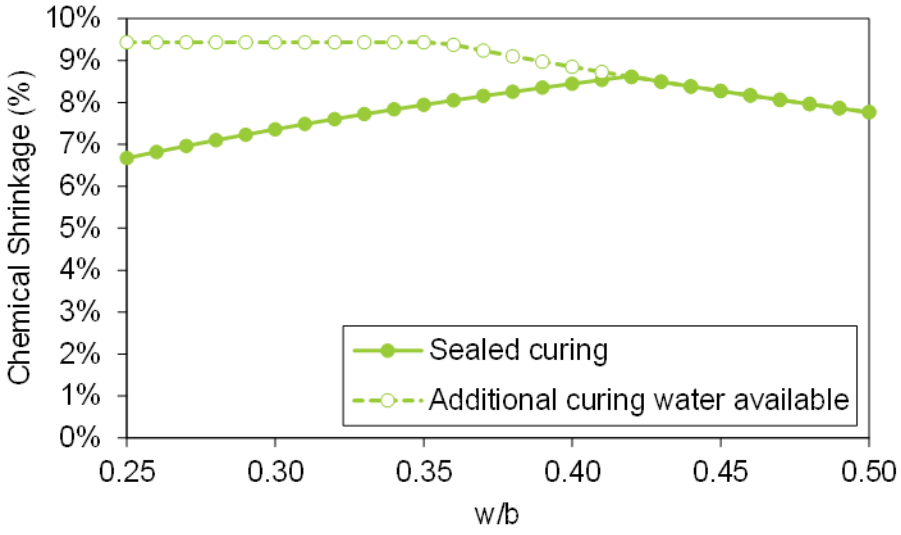

Figure A.3 Maximum chemical shrinkage for a portland cement paste with SG = 3.15 as a function of *w/b*.

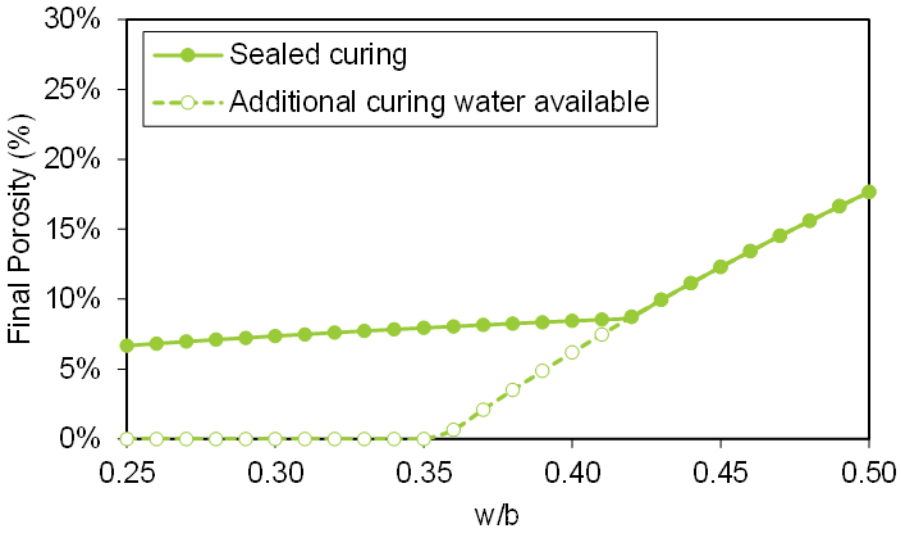

Figure A.4 Final porosity of a portland cement paste with SG = 3.15 as a function of *w/b*.

Table A.1 Effect of 0.01 increase in *w/b* on maximum degree of hydration, maximum chemical shrinkage, and total porosity.

Additional curing water available?	**Threshold *w/b* for complete hydration**	***w/b***	**Effect of 0.01 increase in *w/b* on:**		
			Maximum *α*	**Maximum CS**	**Total porosity**
Yes	0.42	< 0.42	+2.4%	+0.14%	+0.14%
		≥ 0.42	-	-0.10%	+1.2%
No	0.36	< 0.36	+1.5%	-	-
		≥ 0.36	-	-0.10%	+1.2%

A.3.2 Variation in filler content

Filler content also has a significant impact on the maximum degree of hydration, maximum chemical shrinkage, and total porosity predicted by Powers' model, due to the effective increase in water-to-cement ratio. With less cement consuming the water available to hydrate, greater degrees of hydration are possible. Figure A.5 shows the chemical shrinkage predicted by Powers' model for a cement paste with *w/b* = 0.40, containing 0-25% filler substitution by mass (the cement is assumed to have SG = 3.15,

while the filler is assumed to have SG = 2.71). While complete hydration was not possible in an ordinary portland cement paste at this *w/b*, with a substitution of at least 10% inert filler, complete hydration is possible. The reduction in cement content by filler substitution additionally decreases the maximum predicted chemical shrinkage and increases the total predicted porosity of the paste (Figure A.6).

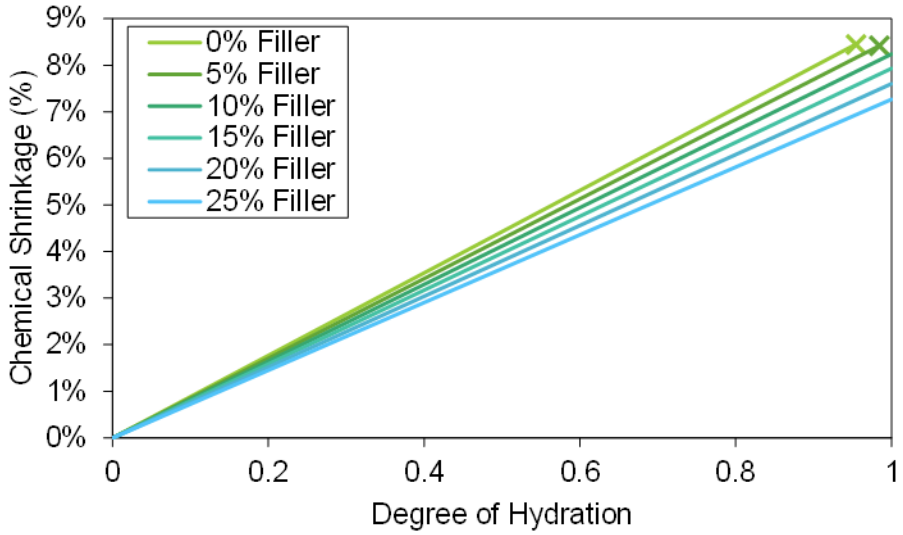

Figure A.5 Chemical shrinkage as a function of degree of hydration for a cement paste with *w/b* = 0.40 and filler dosages 0-25%, by mass.

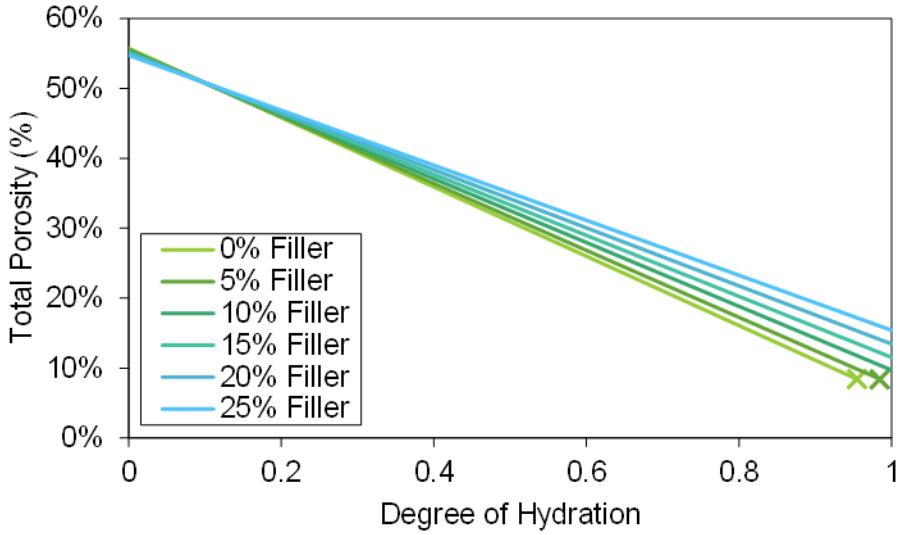

Figure A.6 Total porosity as a function of degree of hydration for a cement paste with *w/b* = 0.40 and filler dosages 0-25%, by mass.

A.3.3 Variation in specific gravity

Specific gravity of the binder has a less significant effect on the maximum degree of hydration, maximum chemical shrinkage, and total porosity, relative to the other two inputs, as long as the *w/b* of the paste is below the threshold for complete hydration. An increase in specific gravity of 0.05 results in a 1% increase in the maximum degree of hydration and a 0.06% increase in both the maximum chemical shrinkage and total porosity, as long as the *w/b* is below the threshold value. Above the threshold, there is no change in maximum degree of hydration nor maximum chemical shrinkage with changing specific gravity; however total porosity is increased by 0.8% for every 0.05 increase in specific gravity. Since the cement pastes considered in this dissertation were prepared at *w/b* = 0.40, and had typical specific gravities in the range of 3.05-3.15, variations in measured specific gravities were determined to have a comparatively less significant impact on the predictions offered by Powers' model.

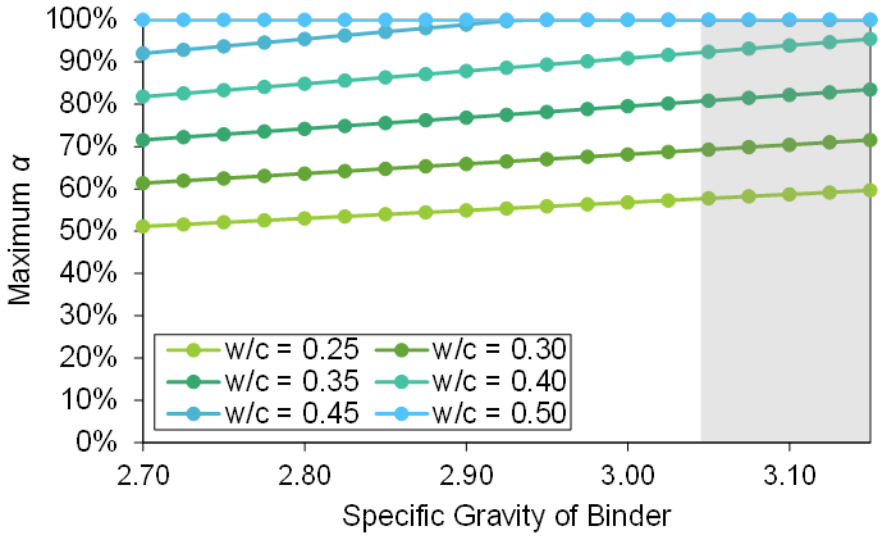

Figure A.7 Maximum degree of hydration for a portland cement paste as a function of specific gravity and *w/b*. Shaded region indicates typical range of specific gravities for blended cements.

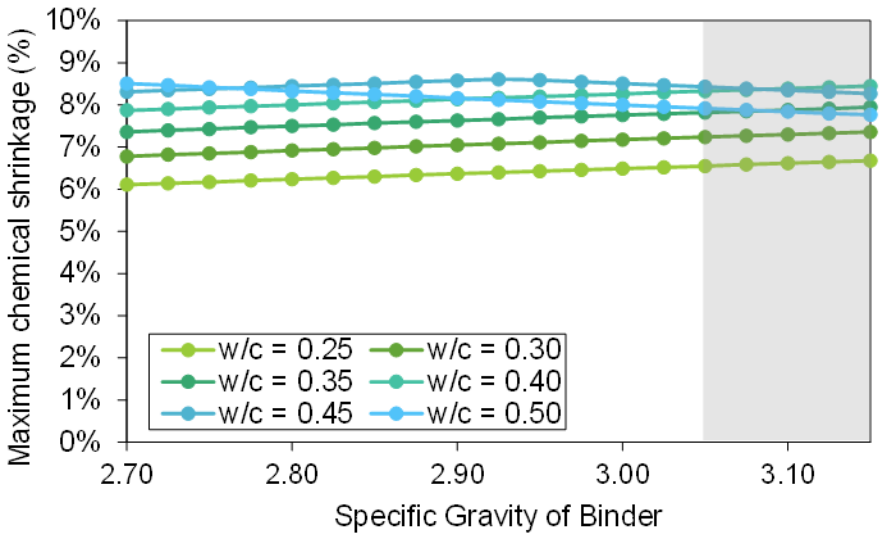

Figure A.8 Maximum chemical shrinkage for a portland cement paste as a function of specific gravity and *w/b*. Shaded region indicates typical range of specific gravities for blended cements.

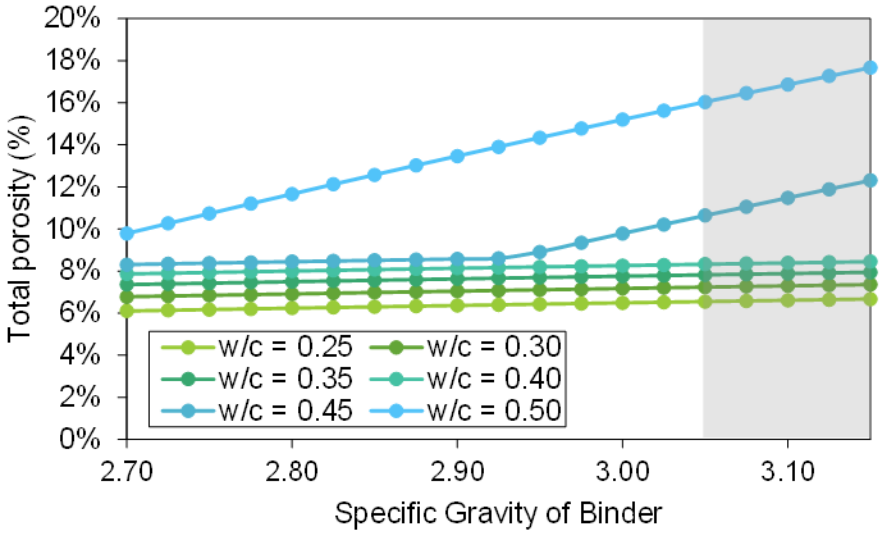

Figure A.9 Total porosity for a portland cement paste as a function of specific gravity and *w/b*. Shaded region indicates typical range of specific gravities for blended cements.

APPENDIX B

EMPIRICAL METHODS FOR ESTIMATING DEGREE OF HYDRATION

B.1 Three-parameter exponential model

Three-parameter exponential models have been recently proposed and utilized to characterize and predict the hydration behavior of cement-based materials [64, 144, 145]. The three-parameter model takes the form:

$$\alpha(t) = \alpha_u \cdot \exp\left[-\left(\frac{\tau}{t}\right)^{\beta}\right] \tag{B.1}$$

where $\alpha(t)$ is the degree of hydration of the cementitious binder at time t, $\alpha_u \leq 1$ is the ultimate degree of degree of hydration of the binder, τ is a characteristic time parameter that defines the relative rate of the acceleration, and β is a shape parameter that describes the general slope of the hydration curve. Knowing the three parameters α_u, β, and τ for a given cement system enables the prediction of the degree of hydration of that system at any age t.

The three-parameter model was fit to the degree of hydration estimates obtained for the cement pastes from sources A-E at w/b = 0.40 over the first 7 days of hydration (Figure 3.7). The fit parameters that were obtained are given in Table B.1. A comparison of the model fits for cement pastes from source A (Figure B.1) show that the three-parameter accurately characterizes the degree of hydration over the first 7 days, and provides reasonable estimates of the ultimate degree of hydration, α_u, for each of the cement pastes analyzed.

Table B.1 Three-parameter exponential fit for estimating degree of hydration of cement pastes A-E at *w/b* = 0.40.

Parameter	A	AL	B	BL	C	CL	D	DL	E	EL (CG)	EL (FG)
α_u (-)	0.72	0.82	0.81	0.83	0.83	0.86	0.78	0.81	0.73	0.76	0.78
τ (hr)	9.6	8.8	11.8	11.9	12.3	12.0	10.3	9.0	12.4	10.9	10.0
β (-)	0.94	0.95	0.87	0.79	0.81	0.87	0.92	0.94	1.10	1.11	1.17

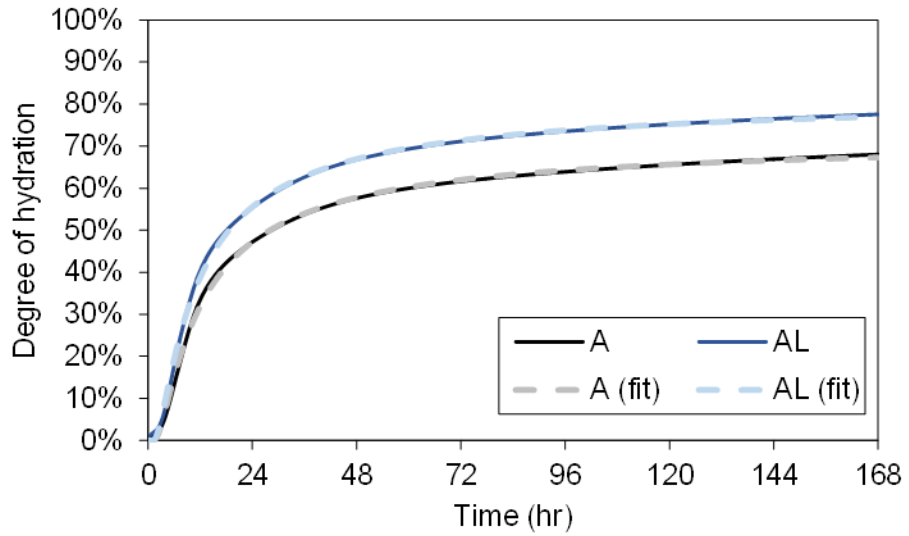

Figure B.1 Degree of hydration as measured (solid lines) and as fit (dashed lines) by three-parameter exponential model for cement pastes A and AL.

The three-parameter model was also preliminarily fit to the degree of hydration estimates for the SCM-blended cement pastes from sources A and C, which were instead determined over the first 3 days of hydration at *w/cm* = 0.40 (Figure 6.6). The fitted parameters for the SCM blends are given in Table B.2 and Table B.3. As the comparison of experimental and fitted values for blends of SCMs with cement A indicates (Figure B.2), the three-parameter model under-predicts the degree of hydration of the SCM-blended pastes by as little as 72 hr. The ultimate degree of hydration is estimated to be

less for the SCM-blended cement pastes than for the neat cement paste controls, which is inconsistent with the current understanding of SCM hydration; SCMs are expected to increase, rather than decrease, the ultimate degree of hydration of the system [2]. The under-prediction of ultimate degree of hydration is based in part on the fact that degree of hydration was only estimated for these mixtures over 72 hrs, prior to any secondary reactions of the SCMs, thereby rendering the three-parameter fit incapable of accurately accounting for the influence of the SCMs at later ages.

Table B.2 Three-parameter exponential fit for estimating degree of hydration of cement pastes from source A, blended with SCMs at *w/cm* = 0.40.

Parameter	A-15F	AL-15F	A-15C	AL-15C	A-50S	AL-50S
α_u (-)	0.72	0.76	0.66	0.75	0.68	0.66
τ (hr)	9.42	8.54	11.00	9.77	17.20	14.75
β (-)	0.99	1.11	0.95	1.03	0.63	0.69

Table B.3 Three-parameter exponential fit for estimating degree of hydration of cement pastes from source C, blended with SCMs at *w/cm* = 0.40.

Parameter	C-15F	CL-15F	C-15C	CL-15C	C-50S	CL-50S
α_u (-)	0.70	0.76	0.65	0.68	0.67	0.67
τ (hr)	9.95	10.54	11.77	11.68	17.58	18.21
β (-)	1.14	1.17	1.05	1.12	0.69	0.72

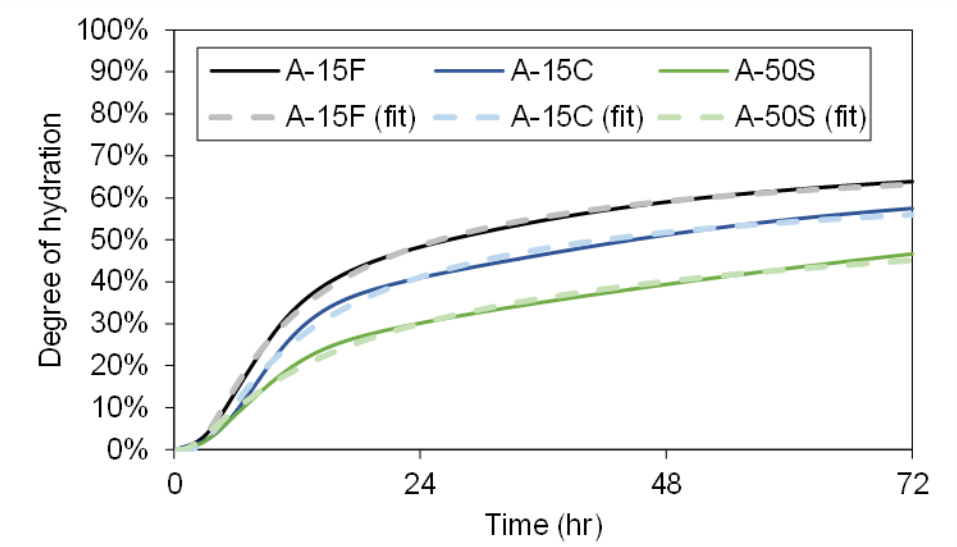

Figure B.2. Degree of hydration as measured (solid lines) and as fit (dashed lines) by three-parameter exponential model for pastes of cement A, combined with 15% Class F fly ash (15F), 15% Class C fly ash (15C) or 50% slag (50S).

B.2 Model of Schindler and Folliard

Schindler and Folliard [64] developed an alternative model to predict degree of hydration of a cement system, based on the composition and fineness of the cement, and the amounts of fly ash and slag used. The model also takes the form of the three-parameter exponential Equation B.1, but the parameters α_u, β, and τ are empirically defined as:

$$\alpha_u = \frac{1.031 \cdot w/cm}{0.194 + w/cm} + 0.50\, p_{FA} + 0.30 \cdot p_{slag} \le 1.0 \tag{B.2}$$

$$\beta = 181.4\, p_{C_3A}{}^{0.146}\, p_{C_3S}{}^{0.227}\, Blaine^{-0.535}\, p_{SO_3}{}^{0.558} \exp\left(-0.647\, p_{slag}\right) \tag{B.3}$$

$$\tau = 66.78\, p_{C_3A}{}^{-0.154}\, p_{C_3S}{}^{-0.401}\, Blaine^{-0.804}\, p_{SO_3}{}^{-0.758} \cdot \exp\left(2.187\, p_{slag} + 9.50\, p_{FA}\, p_{FA\_CaO}\right) \tag{B.4}$$

where p_{FA} and p_{Slag} are the mass fractions of fly ash and slag, respectively in the total cementitious materials content; p_{C3A}, p_{C3S}, and p_{SO3}, are the mass fractions of C_3A, C_3S,

and SO_3, respectively, in the cement; *Blaine* is the Blaine fineness (m^2/kg); and p_{FA_CaO} is the mass fraction of CaO in the fly ash.

The model of Schindler and Folliard was also used to estimate the hydration parameters for the 23 cement pastes, assuming the cement compositions given in Table 3.1 and Table 3.2, the Blaine finenesses given in Table 3.4, and the fly ash CaO contents given in Table 6.1. The variables p_{FA} and p_{Slag} were assigned values of 0.15 and 0.50, respectively, when fly ash and slag were used, and 0 otherwise; a *w/cm* = 0.40 was assumed. The parameters obtained are shown in Table B.4 to Table B.6. Comparison to experimental values reveals that their model significantly underestimates the degree of hydration of neat and SCM-blended cement-paste systems at early ages (Figure B.3 and Figure B.4), but it does correctly account for increase the ultimate degree of hydration for SCM-blended systems.

Table B.4 Exponential fit parameters derived from model of Schindler and Folliard for cement pastes A-E at *w/b* = 0.40.

Parameter	**A**	**AL**	**B**	**BL**	**C**	**CL**	**D**	**DL**	**E**	**EL (CG)**	**EL (FG)**
α_u **(-)**	0.72	0.72	0.72	0.72	0.72	0.72	0.72	0.72	0.72	0.72	0.72
τ **(hr)**	15.4	11.5	16.0	11.8	15.9	13.2	13.1	11.2	13.6	12.8	12.1
β **(-)**	0.51	0.46	0.54	0.44	0.47	0.40	0.57	0.49	0.59	0.50	0.48

Table B.5 Exponential fit parameters derived from model of Schindler and Folliard for cement pastes from source A, blended with SCMs at *w/cm* = 0.40.

Parameter	A-15F	AL-15F	A-15C	AL-15C	A-50S	AL-50S
α_u (-)	0.79	0.79	0.79	0.79	0.87	0.87
τ (hr)	16.03	11.96	22.45	16.76	46.00	34.33
β (-)	0.51	0.46	0.51	0.46	0.37	0.33

Table B.6 Exponential fit parameters derived from model of Schindler and Folliard for cement pastes from source C, blended with SCMs at *w/cm* = 0.40.

Parameter	C-15F	CL-15F	C-15C	CL-15C	C-50S	CL-50S
α_u (-)	0.79	0.79	0.79	0.79	0.87	0.87
τ (hr)	16.58	13.72	23.23	19.22	47.60	39.38
β (-)	0.47	0.40	0.59	0.50	0.34	0.29

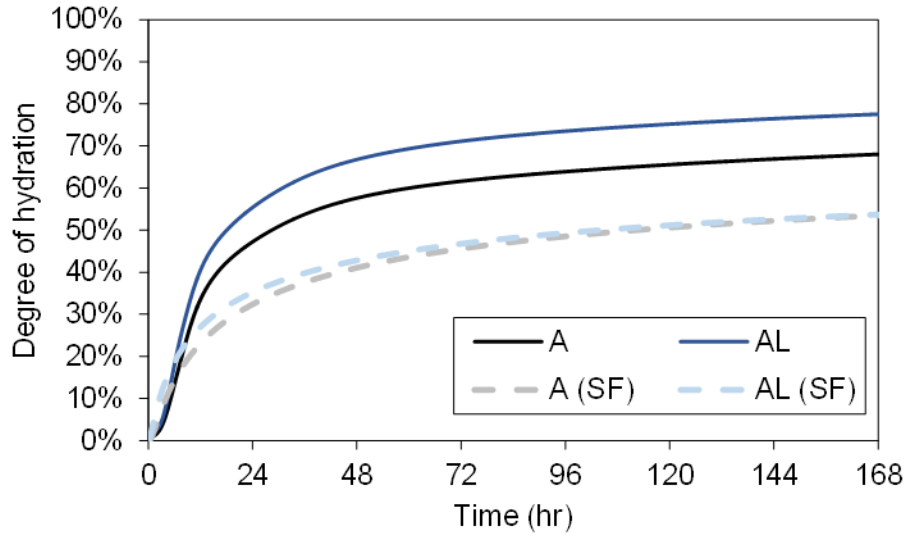

Figure B.3. Degree of hydration as measured (solid lines) and as estimated by the model of Schindler and Folliard (dashed lines) for cement pastes A and AL.

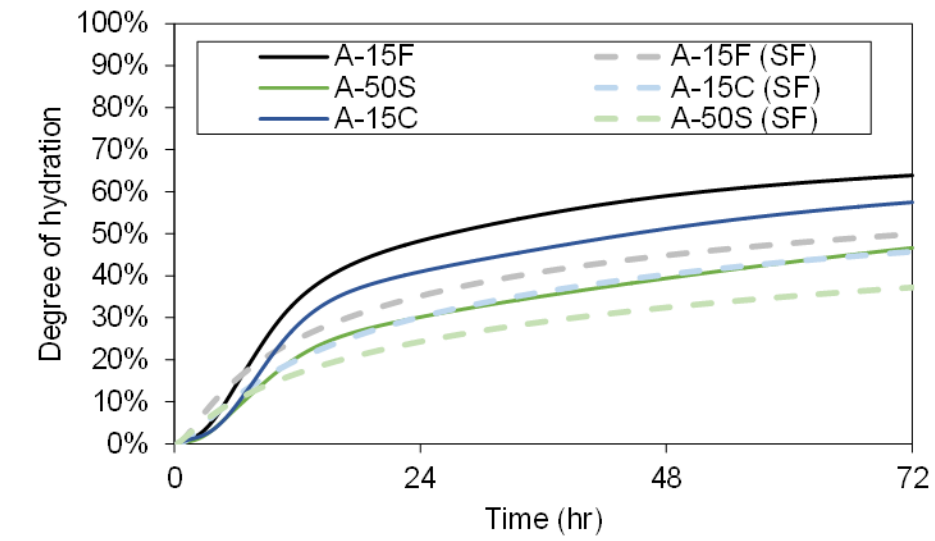

Figure B.4. Degree of hydration as measured (solid lines) and as estimated by the model of Schindler and Folliard (dashed lines) for pastes of cement A, combined with 15% Class F fly ash (15F), 15% Class C fly ash (15C) or 50% slag (50S).

B.3 Hybrid model

Based on the two model approaches, it was determined that the three-parameter fitted model provides a satisfactory estimate of the degree of hydration for neat cement systems, but that the model of Schindler and Folliard better accounts for the influence of the SCMs. In that vein, a hybrid model for estimating the degree of hydration of the SCM-blended systems was developed, which uses the empirically fitted parameters in Table B.1 for initial estimates of α_u, β, and τ, and adjusts their values for fly ash and slag content in the same way that was done by Schindler and Folliard. The adjusted parameters are calculated as:

$$\alpha_u = \alpha_u' + 0.50\, p_{FA} + 0.30 \cdot p_{slag} \leq 1.0 \tag{B.5}$$

$$\beta = \beta' \cdot \exp\left(-0.647\, p_{slag}\right) \tag{B.6}$$

$$\tau = \tau' \cdot \exp\left(2.187\, p_{slag} + 9.50\, p_{FA}\, p_{FA\_CaO}\right) \tag{B.7}$$

where α_u', β', and τ' are the values of α_u, β, and τ for the neat cement paste. The hybrid model fit parameters are given in Table B.7 and Table B.8. Comparison to experimental values (Figure B.5) reveals that the predicted early-age hydration behavior is more similar to measured values than what was predicted using the model of Schindler and Folliard, although the values tend to be over-estimated at later ages. However, the magnitude of this over-estimation is less than the under-estimation of the original model of Schindler and Folliard, and moreover has higher – and more realistic – asymptoptic ultimate degree of hydration values, which reflect the increased degree of hydration in SCM-blended systems. Based on this assessment, the hybrid model parameters will be used to estimate degree of hydration at later ages for the SCM-blended cement systems, while the empirically fit parameters will be used to estimate degree of hydration at later ages for the neat cement systems.

Table B.7 Exponential fit parameters derived from hybrid model for cement pastes from source A, blended with SCMs at *w/cm* = 0.40.

Parameter	A-15F	AL-15F	A-15C	AL-15C	A-50S	AL-50S
α_u (-)	0.79	0.89	0.79	0.89	0.87	0.97
τ (hr)	9.99	9.15	14.00	12.82	28.68	26.27
β (-)	0.94	0.95	0.94	0.95	0.68	0.69

Table B.8 Exponential fit parameters derived from hybrid model for cement pastes from source C, blended with SCMs at *w/cm* = 0.40.

Parameter	C-15F	CL-15F	C-15C	CL-15C	C-50S	CL-50S
α_u (-)	0.91	0.93	0.91	0.93	0.98	1.00
τ (hr)	12.80	12.48	17.94	17.48	36.74	35.82
β (-)	0.81	0.87	1.10	1.11	0.59	0.63

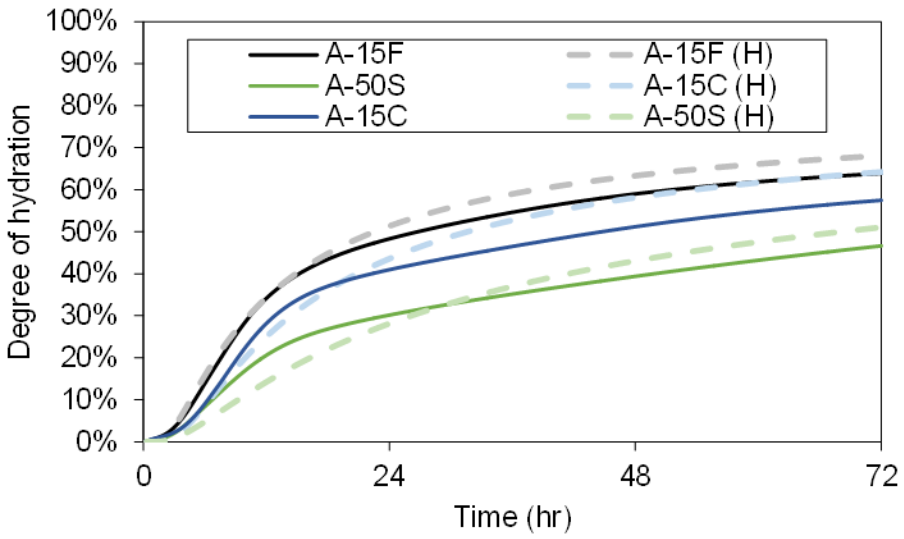

Figure B.5. Degree of hydration as measured (solid lines) and as estimated by the hybrid model (dashed lines) for pastes of cement A, combined with 15% Class F fly ash (15F), 15% Class C fly ash (15C) or 50% slag (50S).

REFERENCES

1. van Oss, H.G., *Cement*. 2016, U.S. Geological Survey: Mineral Commodity Summaries.

2. Mehta, P.K. and P.J.M. Monteiro, *Concrete : microstructure, properties, and materials*. 3rd ed. 2006, New York: McGraw-Hill. 659 pp.

3. Boden, T.A., G. Marland, and R.J. Andres, *Global, regional, and national fossil-fuel CO2 emissions*. Carbon Dioxide Information Analysis Center, U.S. Department of Energy, Oak Ridge, TN, 2010.

4. Malhotra, V.M., *Making concrete "greener" with fly ash.* Concrete International, 1999. **21**(5): p. 61-66.

5. Kelly, T.D. and G.R. Matos, *Cement statistics*, in *Historical statistics for mineral and material commodities in the United States*. 2014, U.S. Geological Survey Data Series 140.

6. Muller, N. and J. Hamisch, *A blueprint for a climate friendly cement industry*. World Wildlife Fund International, 2008. p. 101.

7. Environmental Protection Agency, *Inventory of U.S. greenhouse gas emissions and sinks, 1990-2011*. U.S. Environmental Protection Agency, EPA 430-R-13-001, 2013. p. 505.

8. Cement Sustainability Initiative, *Cement industry energy and CO2 performance: "Getting the numbers right"*. World Business Council for Sustainable Development, Cement Sustainability Initiative, 2009. p. 42.

9. AASHTO Standard M85, "Standard Specification for Portland Cement", American Association of State Highway and Transportation Officials, Washington, DC, 2014.

10. ASTM Standard C595, "Standard Specification for Blended Hydraulic Cements", ASTM International, West Conshohocken, PA, 2012, 10.1520/C0595-12E01, www.astm.org.

11. Tennis, P.D., M.D.A. Thomas, and W.J. Weiss, *State-of-the-art report on use of limestone in cements at levels of up to 15%*. Portland Cement Association, SN3148, Skokie, Illinois, 2011. p. 78.

12. Livesey, P., *Strength characteristics of Portland-limestone cements.* Construction and Building Materials, 1991. **5**(3): p. 147-150.

13. European Standard EN 197-1, "Cement - Part 1: Composition, specifications, and conformity criteria for common cements", European Committee for Standardization, Brussels, Belgium, 2011.

14. CEMBUREAU, *Cements for a low-carbon Europe*. CEMBUREAU, Brussels, 2013. p. 24.

15. ASTM Standard C150, "Standard Specification for Portland Cement", ASTM International, West Conshohocken, PA, 2004, 10.1520/C0150-04, www.astm.org.

16. CSA Standard A3001, "Cementitious materials for use in concrete", Canadian Standards Association, Mississauga, Ontario, Canada, 2013.

17. Lea, F.M. and P.C. Hewlett, *Lea's chemistry of cement and concrete*. 4th ed. 1998, New York: J. Wiley. 1053 pp.

18. Damidot, D., B. Lothenbach, D. Herfort, and F.P. Glasser, *Thermodynamics and cement science.* Cement and Concrete Research, 2011. **41**(7): p. 679-695.

19. De Weerdt, K., M. Ben Haha, G. Le Saout, K.O. Kjellsen, H. Justnes, and B. Lothenbach, *Hydration mechanisms of ternary Portland cements containing limestone powder and fly ash.* Cement and Concrete Research, 2011. **41**(3): p. 279-291.

20. Matschei, T., B. Lothenbach, and F.P. Glasser, *The role of calcium carbonate in cement hydration.* Cement and Concrete Research, 2007. **37**(4): p. 551-558.

21. Lothenbach, B., G. Le Saout, E. Gallucci, and K. Scrivener, *Influence of limestone on the hydration of Portland cements.* Cement and Concrete Research, 2008. **38**(6): p. 848-860.

22. Isaia, G.C., A.L.G. Gastaldini, and R. Moraes, *Physical and pozzolanic action of mineral additions on the mechanical strength of high-performance concrete.* Cement & Concrete Composites, 2003. **25**(1): p. 69-76.

23. Opoczky, L., *Progress of Particle-Size Distribution during the Intergrinding of a Clinker-Limestone Mixture.* Zement-Kalk-Gips, 1992. **45**(12): p. 648-651.

24. Lawrence, P., M. Cyr, and E. Ringot, *Mineral admixtures in mortars - Effect of inert materials on short-term hydration.* Cement and Concrete Research, 2003. **33**(12): p. 1939-1947.

25. Sun, H.F., B. Hohl, Y.Z. Cao, C. Handwerker, T.S. Rushing, T.K. Cummins, and J. Weiss, *Jet mill grinding of portland cement, limestone, and fly ash: Impact on particle size, hydration rate, and strength.* Cement & Concrete Composites, 2013. **44**: p. 41-49.

26. Jayapalan, A.R., B.Y. Lee, S.M. Fredrich, and K.E. Kurtis, *Influence of Additions of Anatase TiO2 Nanoparticles on Early-Age Properties of Cement-Based Materials.* Transportation Research Record, 2010(2141): p. 41-46.

27. Lee, B.Y. and K.E. Kurtis, *Influence of TiO2 Nanoparticles on Early C3S Hydration.* Journal of the American Ceramic Society, 2010. **93**(10): p. 3399-3405.

28. Thomas, J.J., H.M. Jennings, and J.J. Chen, *Influence of Nucleation Seeding on the Hydration Mechanisms of Tricalcium Silicate and Cement.* Journal of Physical Chemistry C, 2009. **113**(11): p. 4327-4334.

29. Kadri, E.H., S. Aggoun, G. De Schutter, and K. Ezziane, *Combined effect of chemical nature and fineness of mineral powders on Portland cement hydration.* Materials and Structures, 2010. **43**(5): p. 665-673.

30. Oey, T., A. Kumar, J.W. Bullard, N. Neithalath, and G. Sant, *The Filler Effect: The Influence of Filler Content and Surface Area on Cementitious Reaction Rates.* Journal of the American Ceramic Society, 2013. **96**(6): p. 1978-1990.

31. Kosmatka, S.H., B. Kerkhoff, and W.C. Panarese, *Design and Control of Concrete Mixtures*. 14th ed. 2002, Skokie, IL: Portland Cement Association.

32. Balonis, M. and F.P. Glasser, *The density of cement phases.* Cement and Concrete Research, 2009. **39**(9): p. 733-739.

33. Powers, T.C. and T.L. Brownyard, *Studies of the Physical Properties of Hardened Portland Cement Paste*. Research Laboratories of the Portland Cement Association, Chicago, IL, 1948.

34. Powers, T.C., *Physical Properties of Cement Paste*. Research Laboratory of the Portland Cement Association, Skokie, IL, 1960.

35. Jensen, O.M. and P.F. Hansen, *Water-entrained cement-based materials I. Principles and theoretical background.* Cement and Concrete Research, 2001. **31**(4): p. 647-654.

36. Bentz, D.P., E.F. Irassar, B.E. Bucher, and W.J. Weiss, *Limestone Fillers Conserve Cement; Part 1: An analysis based on Powers' model.* Concrete International, 2009. **31**(11): p. 41-46.

37. Bonavetti, V., H. Donza, G. Menendez, O. Cabrera, and E.F. Irassar, *Limestone filler cement in low w/c concrete: A rational use of energy.* Cement and Concrete Research, 2003. **33**(6): p. 865-871.

38. Jayapalan, A.R., *Properties of Cement-Based Materials in the Presence of Nano and Microparticle Additives*. 2013, Ph.D. Dissertation, Georgia Institute of Technology: Atlanta, GA.

39. Tsivilis, S., J. Tsantilas, G. Kakali, E. Chaniotakis, and A. Sakellariou, *The permeability of Portland limestone cement concrete.* Cement and Concrete Research, 2003. **33**(9): p. 1465-1471.

40. Mindess, S., J.F. Young, and D. Darwin, *Concrete*. 2nd ed. 2003, Upper Saddle River, NJ: Pearson.

41. Bentz, D.P. and M.A. Peltz, *Reducing thermal and autogenous shrinkage contributions to early-age cracking.* ACI Materials Journal, 2008. **105**(4): p. 414-420.

42. Bentz, D.P. and E.J. Garboczi, *Percolation of Phases in a 3-Dimensional Cement Paste Microstructural Model.* Cement and Concrete Research, 1991. **21**(2-3): p. 325-344.

43. Bentz, D.P., E.F. Irassar, B.E. Bucher, and W.J. Weiss, *Limestone Fillers Conserve Cement; Part 2: Durability issues and the effects of limestone fineness on mixtures.* Concrete International, 2009. **31**(12): p. 35-39.

44. Irassar, E.F., *Sulfate attack on cementitious materials containing limestone filler - A review.* Cement and Concrete Research, 2009. **39**(3): p. 241-254.

45. Ramezanianpour, A.A., E. Ghiasvand, I. Nickseresht, M. Mahdikhani, and F. Moodi, *Influence of various amounts of limestone powder on performance of Portland limestone cement concretes.* Cement & Concrete Composites, 2009. **31**(10): p. 715-720.

46. Dhir, R.K., M.C. Limbachiya, M.J. McCarthy, and A. Chaipanich, *Evaluation of Portland limestone cements for use in concrete construction.* Materials and Structures, 2007. **40**(5): p. 459-473.

47. Pipilikaki, P. and M. Beazi-Katsioti, *The assessment of porosity and pore size distribution of limestone Portland cement pastes.* Construction and Building Materials, 2009. **23**(5): p. 1966-1970.

48. Antoni, M., J. Rossen, F. Martirena, and K. Scrivener, *Cement substitution by a combination of metakaolin and limestone.* Cement and Concrete Research, 2012. **42**(12): p. 1579-1589.

49. De Weerdt, K., K.O. Kjellsen, E. Sellevold, and H. Justnes, *Synergy between fly ash and limestone powder in ternary cements.* Cement & Concrete Composites, 2011. **33**(1): p. 30-38.

50. Vance, K., M. Aguayo, T. Oey, G. Sant, and N. Neithalath, *Hydration and strength development in ternary portland cement blends containing limestone and fly ash or metakaolin.* Cement & Concrete Composites, 2013. **39**: p. 93-103.

51. Menendez, G., V. Bonavetti, and E.F. Irassar, *Strength development of ternary blended cement with limestone filler and blast-furnace slag.* Cement & Concrete Composites, 2003. **25**(1): p. 61-67.

52. Smartz, B.W., T.S. Laker, and T. VanDam, *Performance and Sustainability.* Concrete International, 2013. **35**(9): p. 39-43.

53. ASTM Standard C114, "Standard Test Methods for Chemical Analysis of Hydraulic Cement", ASTM International, West Conshohocken, PA, 2013, DOI: 10.1520/C0114-13, www.astm.org.

54. ASTM Standard C1365, "Standard Test Method for Determination of the Proportion of Phases in Portland Cement and Portland-Cement Clinker using X-Ray Powder Diffraction Analysis", ASTM International, West Conshohocken, PA, 2011, 10.1520/C1365-06R11, www.astm.org.

55. Taylor, H.F.W., *Cement chemistry*. 2nd ed. 1997, London: Thomas Telford. xviii, 459 p.

56. ASTM Standard C150, "Standard Specification for Portland Cement", ASTM International, West Conshohocken, PA, 2016, 10.1520/C0150-16, www.astm.org.

57. ASTM Standard C188, "Standard Test Method for Density of Hydraulic Cement", ASTM International, West Conshohocken, PA, 2014, 10.1520/C0188-14, www.astm.org.

58. Azari, H., C.F. Ferraris, and E.J. Garboczi, *Measuring Cement Particle Size and Surface Area by Laser Diffraction*. 2013.

59. ASTM Standard C204, "Standard Test Methods for Fineness of Hydraulic Cement by Air-Permeability Apparatus", ASTM International, West Conshohocken, PA, 2011, 10.1520/C0204-11E01, www.astm.org.

60. ASTM Standard E799, "Standard Practice for Determining Data Criteria and Processing for Liquid Drop Size Analysis", ASTM International, West Conshohocken, PA, 2015, 10.1520/E0799-03R15, www.astm.org.

61. Irassar, E.F., D. Violini, V.F. Rahhal, C. Milanesi, M.A. Trezza, and V.L. Bonavetti, *Influence of limestone content, gypsum content and fineness on early age properties of Portland limestone cement produced by inter-grinding.* Cement & Concrete Composites, 2011. **33**(2): p. 192-200.

62. Bullard, J.W., H.M. Jennings, R.A. Livingston, A. Nonat, G.W. Scherer, J.S. Schweitzer, K.L. Scrivener, and J.J. Thomas, *Mechanisms of cement hydration.* Cement and Concrete Research, 2011. **41**(12): p. 1208-1223.

63. ASTM Standard C1679, "Standard Practice for Measuring Hydration Kinetics of Hydraulic Cementitious Mixtures Using Isothermal Calorimetry", ASTM International, West Conshohocken, PA, 2009, 10.1520/C1679-09, www.astm.org.

64. Schindler, A.K. and K.J. Folliard, *Heat of hydration models for cementitious materials.* ACI Materials Journal, 2005. **102**(1): p. 24-33.

65. Taylor, H.F.W., *Cement chemistry*. 2nd ed. 1997, London: Thomas Telford. 459.

66. Lothenbach, B., P. Durdzinski, and K. De Weerdt, *Thermogravimetric analysis*, in *A Practical Guide to Microstructural Analysis of Cementitious Materials*, K. Scrivener, R. Snellings, and B. Lothenbach, Editors. 2015, CRC Press. p. 177-212.

67. Zhang, L. and G.W. Scherer, *Comparison of methods for arresting hydration of cement.* Cement and Concrete Research, 2011. **41**(10): p. 1024-1036.

68. Bentz, D.P., E.J. Garboczi, C.J. Haecker, and O.M. Jensen, *Effects of cement particle size distribution on performance properties of Portland cement-based materials.* Cement and Concrete Research, 1999. **29**(10): p. 1663-1671.

69. Grazulis, S., D. Chateigner, R.T. Downs, A.T. Yokochi, M. Quiros, L. Lutterotti, E. Manakova, J. Butkus, P. Moeck, and A. LeBail, *Crystallography Open Database – an open-access collection of crystal structures.* Journal of Applied Crystallography, 2009. **42**: p. 726-729.

70. Grazulis, S., A. Daskevic, A. Merkys, D. Chateigner, L. Lutterotti, M. Quiros, N.R. Serebryanaya, P. Moeck, R.T. Downs, and A. LeBail, *Crystallography Open Database (COD): an open-access collection of crystal structures and platform for world-wide collaboration.* Nucleic Acids Research, 2012. **40**: p. D420-D427.

71. Downs, R.T. and M. Hall-Wallace, *The American Mineralogist Crystal Structure Database.* American Mineralogist, 2003. **88**: p. 247-250.

72. Potgieter-Vermaak, S.S., J.H. Potgieter, and R. Van Grieken, *The application of Raman spectrometry to investigate and characterize cement, Part I: A review.* Cement and Concrete Research, 2006. **36**(4): p. 656-662.

73. Bensted, J., *Uses of Raman-Spectroscopy in Cement Chemistry.* Journal of the American Ceramic Society, 1976. **59**(3-4): p. 140-143.

74. Lazic, B., H. Kruger, V. Kahlenberg, J. Konzett, and R. Kaindl, *Incommensurate structure of Ca2Al2O5 at high temperatures - structure investigation and Raman spectroscopy.* Acta Crystallographica Section B, 2008. **64**(4): p. 417-425.

75. Martinez-Ramirez, S., M. Frías, and C. Domingo, *Micro-Raman spectroscopy in white portland cement hydration: long-term study at room temperature.* Journal of Raman Spectroscopy, 2006. **37**(5): p. 555-561.

76. Renaudin, G., R. Segni, D. Mentel, J.M. Nedelec, F. Leroux, and C. Taviot-Gueho, *A Raman study of the sulfated cement hydrates: Ettringite and monosulfoaluminate.* Journal of Advanced Concrete Technology, 2007. **5**(3): p. 299-312.

77. Torrens-Martin, D., L. Fernandez-Carrasco, S. Martinez-Ramirez, J. Ibanez, L. Artus, and T. Matschei, *Raman Spectroscopy of Anhydrous and Hydrated Calcium Aluminates and Sulfoaluminates.* Journal of the American Ceramic Society, 2013. **96**(11): p. 3589-3595.

78. Brunauer, S., P.H. Emmett, and E. Teller, *Adsorption of Gases in Multimolecular Layers.* Journal of the American Chemical Society, 1938. **60**(2): p. 309-319.

79. Barrett, E.P., L.G. Joyner, and P.P. Halenda, *The Determination of Pore Volume and Area Distributions in Porous Substances. I. Computations from Nitrogen Isotherms.* Journal of the American Chemical Society, 1951. **73**(1): p. 373-380.

80. Palacios, M., H. Kazemi-Kamyab, S. Mantellato, and P. Bowen, *Laser diffraction and gas adsorption techniques*, in *A Practical Guide to Microstructural Analysis of Cementitious Materials*, K. Scrivener, R. Snellings, and B. Lothenbach, Editors. 2015, CRC Press. p. 445-484.

81. Scrivener, K., A. Bazzoni, B. Mota, and J. Rossen, *Electron microscopy*, in *A Practical Guide to Microstructural Analysis of Cementitious Materials*, K. Scrivener, R. Snellings, and B. Lothenbach, Editors. 2015, CRC Press. p. 351-418.

82. Scrivener, K.L., *Backscattered electron imaging of cementitious microstructures: understanding and quantification.* Cement and Concrete Composites, 2004. **26**(8): p. 935-945.

83. Kjellsen, K.O., A. Monsøy, K. Isachsen, and R.J. Detwiler, *Preparation of flat-polished specimens for SEM-backscattered electron imaging and X-ray microanalysis—importance of epoxy impregnation.* Cement and Concrete Research, 2003. **33**(4): p. 611-616.

84. Barcelo, L., M.D.A. Thomas, K. Cail, A. Delagrave, and B. Blair, *Portland Limestone Cement Equivalent Strength Explained.* Concrete International, 2013. **35**(11): p. 41-47.

85. ASTM Standard C1608, "Standard Test Method for Chemical Shrinkage of Hydraulic Cement Paste", ASTM International, West Conshohocken, PA, 2012, 10.1520/C1608-12, www.astm.org.

86. ASTM Standard C1698, "Standard Test Method for Autogenous Strain of Cement Paste and Mortar", ASTM International, West Conshohocken, PA, 2009, 10.1520/C1698-09, www.astm.org.

87. ASTM Standard C191, "Standard Test Methods for Time of Setting of Hydraulic Cement by Vicat Needle", ASTM International, West Conshohocken, PA, 2013, 10.1520/C0191-13, www.astm.org.

88. Bouasker, M., P. Mounanga, P. Turcry, A. Loukili, and A. Khelidj, *Chemical shrinkage of cement pastes and mortars at very early age: Effect of limestone filler and granular inclusions.* Cement and Concrete Composites, 2008. **30**(1): p. 13-22.

89. Sant, G., P. Lura, and J. Weiss, *Measurement of Volume Change in Cementitious Materials at Early Ages - Review of Testing Protocols and Interpretation of Results.* Transportation Research Record, 2006. **1979**: p. 21-29.

90. Jensen, O.M. and P.F. Hansen, *Autogenous deformation and RH-change in perspective.* Cement and Concrete Research, 2001. **31**(12): p. 1859-1865.

91. Lura, P., O.M. Jensen, and K. van Breugel, *Autogenous shrinkage in high-performance cement paste: An evaluation of basic mechanisms.* Cement and Concrete Research, 2003. **33**(2): p. 223-232.

92. Hansen, T., *Physical structure of hardened cement paste. A classical approach.* Materials and Structures, 1986. **19**(6): p. 423-436.

93. Brouwers, H.J.H., *The work of Powers and Brownyard revisited: Part I.* Cement and Concrete Research, 2004. **34**(9): p. 1697-1716.

94. Neville, A.M., *Properties of concrete*. 4th ed. 2009, New York: Pearson. 846.

95. Lothenbach, B. and F. Winnefeld, *Thermodynamic modelling of the hydration of Portland cement.* Cement and Concrete Research, 2006. **36**(2): p. 209-226.

96. Kakali, G., S. Tsivilis, E. Aggeli, and M. Bati, *Hydration products of C(3)A, C3S and Portland cement in the presence of CaCO3.* Cement and Concrete Research, 2000. **30**(7): p. 1073-1077.

97. Bonavetti, V.L., V.F. Rahhal, and E.F. Irasser, *Studies on the carboaluminate formation in limestone filler-blended cements.* Cement and Concrete Research, 2001. **31**(6): p. 853-859.

98. Sprung, S. and E. Siebel, *Assessment of the Suitability of Limestone for Producing Portland Limestone Cement (PKZ).* Zement-Kalk-Gips, 1991. **44**(1): p. 1-11.

99. Tsivilis, S., E. Chaniotakis, E. Badogiannis, G. Pahoulas, and A. Ilias, *A study on the parameters affecting the properties of Portland limestone cements.* Cement & Concrete Composites, 1999. **21**(2): p. 107-116.

100. American Concrete Institute Committee 201, *Guide to Durable Concrete (ACI201.2-R08)*. American Concrete Institute, 2008.

101. Thomas, M.D.A., B. Fournier, and K.J. Folliard, *Alkali-Aggregate Reactivity (AAR) Facts Book*. Federal Highway Administration, FHWA-HIF-13-019, 2013.

102. Jin, W.H., C. Meyer, and S. Baxter, *"Glascrete" - Concrete with glass aggregate.* ACI Materials Journal, 2000. **97**(2): p. 208-213.

103. Shao, Y.X., T. Lefort, S. Moras, and D. Rodriguez, *Studies on concrete containing ground waste glass.* Cement and Concrete Research, 2000. **30**(1): p. 91-100.

104. Krinsley, D.H. and J.C. Doornkamp, *Atlas of quartz sand surface textures*. 1973, Cambridge Eng.: University Press. 91 p.

105. Norvell, J.K., J.G. Stewart, M.C.G. Juenger, and D.W. Fowler, *Influence of clays and clay-sized particles on concrete performance.* Journal of Materials in Civil Engineering, 2007. **19**(12): p. 1053-1059.

106. Fernandes, V.A., P. Purnell, G.T. Still, and T.H. Thomas, *The effect of clay content in sands used for cementitious materials in developing countries.* Cement and Concrete Research, 2007. **37**(5): p. 751-758.

107. American Concrete Institute Committee 318, *Building Code Requirements for Structural Concrete (ACI 318-14)*. American Concrete Institute, 2014.

108. ASTM Standard C618, "Standard Specification for Coal Fly Ash and Raw or Calcined Natural Pozzolan for Use in Concrete", ASTM International, West Conshohocken, PA, 2015, 10.1520/C0618-15, www.astm.org.

109. Puerta-Falla, G., M. Balonis, G. Le Saout, G. Falzone, C. Zhang, N. Neithalath, and G. Sant, *Elucidating the Role of the Aluminous Source on Limestone Reactivity in Cementitious Materials.* Journal of the American Ceramic Society, 2015. **98**(12): p. 4076-4089.

110. Georgia Department of Transportation, *Standard Specifications for Construction of Transportation Systems, Section 500 - Concrete Structures*. 2015, Georgia Department of Transportation.

111. ASTM Standard C192, "Standard Practice for Making and Curing Concrete Test Specimens in the Laboratory", ASTM International, West Conshohocken, PA, 2016, 10.1520/C0192_C0192M-16, www.astm.org.

112. ASTM Standard C39, "Standard Test Method for Compressive Strength of Cylindrical Concrete Specimens", ASTM International, West Conshohocken, PA, 2016, 10.1520/C0039_C0039M-16, www.astm.org.

113. Claisse, P., *Transport Properties of Concrete.* Concrete International, 2005. **27**(1): p. 43-48.

114. ASTM Standard C1202, "Standard Test Method for Electrical Indication of Concrete's Ability to Resist Chloride Ion Penetration", ASTM International, West Conshohocken, PA, 2012, 10.1520/C1202-12, www.astm.org.

115. AASHTO Standard T277, "Standard Method of Test for Electrical Indication of Concrete's Ability to Resist Chloride Ion Penetration", American Association of State Highway and Transportation Officials, Washington, DC, 2011.

116. Wenner, F., *A method of measuring earth resistivity.* Bulletin of the National Bureau of Standards, 1915. **12**(4): p. 469-478.

117. Morris, W., E.I. Moreno, and A.A. Sagues, *Practical evaluation of resistivity of concrete in test cylinders using a Wenner array probe.* Cement and Concrete Research, 1996. **26**(12): p. 1779-1787.

118. Snyder, K.A., X. Feng, B.D. Keen, and T.O. Mason, *Estimating the electrical conductivity of cement paste pore solutions from OH−, K+ and Na+ concentrations.* Cement and Concrete Research, 2003. **33**(6): p. 793-798.

119. Whittington, H.W., J. Mccarter, and M.C. Forde, *The Conduction of Electricity through Concrete.* Magazine of Concrete Research, 1981. **33**(114): p. 48-60.

120. Holland, R.B., *Durability of Precast Prestressed Concrete piles in Marine Environments*. 2012, Ph.D. Dissertation, Georgia Institute of Technology.

121. Nadelman, E.I. and K.E. Kurtis, *A Resistivity-Based Approach to Optimizing Concrete Performance.* Concrete International, 2014. **36**(5): p. 50-54.

122. Barde, V., A. Radlinska, M. Cohen, and W.J. Weiss, *Relating Material Properties to Exposure Conditions for Predicting Service Life in Concrete Bridge Decks in Indiana*. Indiana Department of Transportation, Purdue University, West Lafayette, IN, 2009.

123. Castellote, M., C. Andrade, and M.C. Alonso, *Standardization, to a Reference of 25 °C, of Electrical Resistivity for Mortars and Concretes in Saturated or Isolated Conditions.* ACI Materials Journal, 2002. **99**(2): p. 119-128.

124. Kurtis, K.E., L.F. Kahn, and E.I. Nadelman, *Viability of Concrete Performance Based Specification for GDOT Projects*. Georgia Department of Transportation, RP 12-08, 2013.

125. Nokken, M.R. and R.D. Hooton, *Electrical Conductivity Testing.* Concrete International, 2006. **28**(10): p. 58-63.

126. Shi, C.J., *Effect of mixing proportions of concrete on its electrical conductivity and the rapid chloride permeability test (ASTM C1202 or ASSHTO T277) results.* Cement and Concrete Research, 2004. **34**(3): p. 537-545.

127. Shi, C., J.A. Stegemann, and R.J. Caldwell, *Effect of supplementary cementing materials on the specific conductivity of pore solution and its implications on the rapid chloride permeability test (AASHTO T277 and ASTM C1202) results.* ACI Materials Journal, 1998. **95**(4): p. 389-394.

128. Chini, A.R., L.C. Muszynski, and J. Hicks, *Determination of Acceptance Permeability Characteristics for Performance-Related Specifications for Portland Cement Concrete*. Florida Department of Transportation, BC 354-41, Tallahassee, FL, 2003.

129. Rupnow, T. and P. Icenogle, *Surface Resistivity Measurements Evaluated as Alternative to Rapid Chloride Permeability Test for Quality Assurance and Acceptance.* Transportation Research Record: Journal of the Transportation Research Board, 2012. **2290**: p. 30-37.

130. Kessler, R.J., R.G. Powers, E. Vivas, M.A. Paredes, and Y.P. Virmani, *Surface Resistivity as an Indicator of Concrete Chloride Penetration Resistance*, in *Concrete Bridge Conference*. 2008.

131. Lu, X.Y., *Application of the Nernst-Einstein equation to concrete.* Cement and Concrete Research, 1997. **27**(2): p. 293-302.

132. Andrade, C., *Calculation of Chloride Diffusion-Coefficients in Concrete from Ionic Migration Measurements.* Cement and Concrete Research, 1993. **23**(3): p. 724-742.

133. Bentz, E.C. and M.D.A. Thomas, *Life-365 Service Life Prediction Model, Version 2.2*. 2013, Life-365 Consortium III.

134. Sengul, O. and O.E. Gjorv, *Electrical Resistivity Measurements for Quality Control During Concrete Construction.* ACI Materials Journal, 2008. **105**(6): p. 541-547.

135. Monfore, G.E., *Electrical Resistivity of Concrete.* Journal of the Pca Research and Development Laboratories, 1968. **10**(2): p. 35-&.

136. Gowers, K.R. and S.G. Millard, *Measurement of Concrete Resistivity for Assessment of Corrosion Severity of Steel Using Wenner Technique.* ACI Materials Journal, 1999. **96**(5): p. 536-541.

137. Nadelman, E.I., B.H. Zaribaf, L.E. Burris, and K.E. Kurtis, *What does surface resistivity really tell us about permeability?*, in *American Concrete Institute Concrete Convention and Exposition - Spring 2016*. 2016: Milwaukee, WI.

138. Spragg, R., C. Villani, K. Snyder, D. Bentz, J.W. Bullard, and J. Weiss, *Factors That Influence Electrical Resistivity Measurements in Cementitious Systems.* Transportation Research Record, 2013(2342): p. 90-98.

139. Snyder, K.A., *The relationship between the formation factor and the diffusion coefficient of porous materials saturated with concentrated electrolytes: theoretical and experimental considerations.* Concrete Science and Engineering, 2001. **3**(12): p. 216-224.

140. Spragg, R., C. Villani, and J. Weiss, *Electrical Properties of Cementitious Systems: Formation Factor Determination and the Influence of Conditioning Procedures.* Advances in Civil Engineering, 2016. **5**(1): p. 124-148.

141. Barneyback, R.S. and S. Diamond, *Expression and Analysis of Pore Fluids from Hardened Cement Pastes and Mortars.* Cement and Concrete Research, 1981. **11**(2): p. 279-285.

142. Bentz, D.P. *Estimation of pore solution conductivity*. [cited 2016 April 19]; Available from: http://ciks.cbt.nist.gov/poresolncalc.html.

143. Spragg, R., Y. Bu, K. Snyder, D. Bentz, and J. Weiss, *Electrical Testing of Cement-Based Materials: Role of Testing Techniques, Sample Conditioning, and Accelerated Curing*. Joint Transportation Research Program, Indiana Department of Transportation and Purdue University, FHWA/IN/JTRP-2013/28, West Lafayette, Indiana, 2013.

144. Pane, I. and W. Hansen, *Concrete Hydration and Mechanical Properties under Nonisothermal Conditions.* ACI Materials Journal, 2002. **99**(6): p. 534-542.

145. Riding, K.A., J.L. Poole, K.J. Folliard, M.C.G. Juenger, and A.K. Schindler, *Modeling Hydration of Cementitious Systems.* Materials Journal, 2012. **109**(2): p. 225-234.

146. Haynes, H., R. O'Neill, and P.K. Mehta, *Concrete Deterioration From Physical Attack By Salts.* Concrete International, 1996. **18**(1): p. 63-68.

147. Hime, W.G., R.A. Martinek, L.A. Backus, and S.L. Marusin, *Salt Hydration Distress.* Concrete International, 2001. **23**(10): p. 43-50.

148. Scherer, G.W., *Stress from crystallization of salt.* Cement and Concrete Research, 2004. **34**(9): p. 1613-1624.

149. Espinosa-Marzal, R.M. and G.W. Scherer, *Crystallization Pressure Exerted by in-Pore Confined Crystals.* Poro-Mechanics IV, 2009: p. 1013-1018.

150. Espinosa-Marzal, R.M. and G.W. Scherer, *Advances in Understanding Damage by Salt Crystallization.* Accounts of Chemical Research, 2010. **43**(6): p. 897-905.

151. Folliard, K.J. and P. Sandberg, *Mechanisms of Concrete Deterioration by Sodium Sulfate Crystallization.* Special Publication, 1994. **145**.

152. Haynes, H., R. O'Neill, M. Neff, and P.K. Mehta, *Salt Weathering Distress on Concrete Exposed to Sodium Sulfate Environment.* ACI Materials Journal, 2008. **105**(1): p. 35-43.

153. Haynes, H., R. O'Neill, M. Neff, and P.K. Mehta, *Salt Weathering of Concrete by Sodium Carbonate and Sodium Chloride.* ACI Materials Journal, 2010. **107**(3): p. 258-266.

154. Scherer, G.W., *Crystallization in pores.* Cement and Concrete Research, 1999. **29**(8): p. 1347-1358.

155. Rodriguez-Navarro, C. and E. Doehne, *Salt weathering: Influence of evaporation rate, supersaturation and crystallization pattern.* Earth Surface Processes and Landforms, 1999. **24**(3): p. 191-209.

156. Lee, B.Y., *Effect of titanium dioxide nanoparticles on early age and long term properties of cementitious materials*. 2012, PhD Dissertation, Georgia Institute of Technology: Atlanta, GA.

157. Correns, C.W., *Growth and Dissolution of Crystals under Linear Pressure.* Discussions of the Faraday Society, 1949(5): p. 267-271.

158. Haynes, H. and M.T. Bassuoni, *Physical Salt Attack on Concrete.* Concrete International, 2011. **33**(11): p. 38-42.

159. Lee, B.Y., *Effect of titanium dioxide nanoparticles on early age and long term properties of cementitious materials*. 2012, PhD Dissertation, Georgia Institute of Technology: Atlanta, GA.

160. ASTM Standard C778, "Standard Specification for Standard Sand", ASTM International, West Conshohocken, PA, 2013, 10.1520/C0778-13, www.astm.org.

161. ASTM Standard C305, "Standard Practice for Mechanical Mixing of Hydraulic Cement Pastes and Mortars of Plastic Consistency", ASTM International, West Conshohocken, PA, 2014, 10.1520/C0305-14, www.astm.org.

162. Tang, I.N. and K.H. Fung, *Hydration and Raman scattering studies of levitated microparticles: Ba(NO(3))(2), Sr(NO3)(2), and Ca(NO3)(2).* Journal of Chemical Physics, 1997. **106**(5): p. 1653-1660.

163. Liu, Y.J., T. Zhu, D.F. Zhao, and Z.F. Zhang, *Investigation of the hygroscopic properties of Ca(NO3)(2) and internally mixed Ca(NO3)(2)/CaCO3 particles by micro-Raman spectrometry.* Atmospheric Chemistry and Physics, 2008. **8**(23): p. 7205-7215.

164. Lewin, S.Z., *The Mechanism of Masonry Decay Through Crystallization*, in *Conservation of Historic Stone Buildings and Monuments*, N.R. Council, Editor. 1982, The National Academic Press: Washington, DC. p. 120-144.

165. ASTM Standard E104, "Standard Practice for Maintaining Constant Relative Humidity by Means of Aqueous Solutions", ASTM International, West Conshohocken, PA, 2012, DOI: 10.1520/E0104-02R12, www.astm.org.

166. ASTM Standard C109, "Standard Test Method for Compressive Strength of Hydraulic Cement Mortars (Using 2-in. or [50-mm] Cube Specimens)", ASTM International, West Conshohocken, PA, 2013, 10.1520/C0109_C0109M-13E1, www.astm.org.

167. ASTM Standard C496, "Standard Test Method for Splitting Tensile Strength of Cylindrical Concrete Specimens", ASTM International, West Conshohocken, PA, 2011, 10.1520/C0496_C0496M-11, www.astm.org.

168. ASTM Standard C1585, "Standard Test Method for Measurement of Rate of Absorption of Water by Hydraulic-Cement Concretes", ASTM International, West Conshohocken, PA, 2013, 10.1520/C1585-13, www.astm.org.

169. Martys, N.S. and C.F. Ferraris, *Capillary transport in mortars and concrete.* Cement and Concrete Research, 1997. **27**(5): p. 747-760.

170. Hall, C., *Water Sorptivity of Mortars and Concretes - a Review.* Magazine of Concrete Research, 1989. **41**(147): p. 51-61.

171. Hall, C., W.D. Hoff, and M.R. Nixon, *Water-Movement in Porous Building-Materials .6. Evaporation and Drying in Brick and Block Materials.* Building and Environment, 1984. **19**(1): p. 13-20.

172. Stock, S.R., N.K. Naik, A.P. Wilkinson, and K.E. Kurtis, *X-ray microtomography (microCT) of the progression of sulfate attack of cement paste.* Cement and Concrete Research, 2002. **32**(10): p. 1673-1675.